AD-A173 976 GENERALIZED PHENOMENOLOGICAL CYCLIC STRESS-STRAIN-STRENGTH CHARACTERIZATI (U) FLORIDA UNIV GAINESVILLE DEPT OF CIVIL ENGINEERING M C MCVAY ET AL. 1/4

UNCLASSIFIED 02 SEP 84 AFOSR-TR-86-0918 AFOSR-84-0108 F/G 8/13 NL

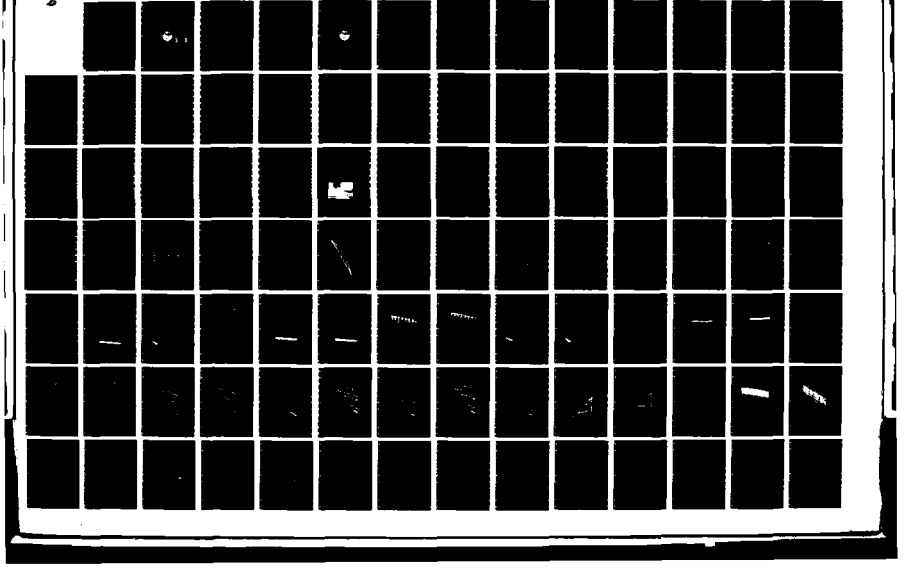

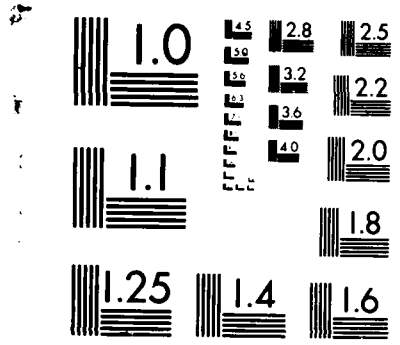

MICROCOPY RESOLUTION TEST CHART
NATIONAL BUREAU OF STANDARDS-1963-A

AFOSR-TR- 86-0918

"GENERALIZED PHENOMENOLOGICAL CYCLIC STRESS-STRAIN-STRENGTH CHARACTERIZATION OF GRANULAR MEDIA"

SECOND YEAR

FINAL REPORT

AFOSR - 84 - 0108

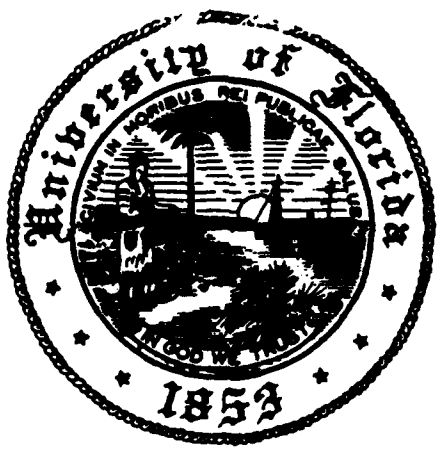

Submitted by: M.C. Mcvay
D. Seereeram
P.F. Linton
D.B. Bloomquist

DEPARTMENT OF CIVIL ENGINEERING
DIVISION OF SOIL MECHANICS
UNIVERSITY OF FLORIDA
GAINESVILLE

SECURITY CLASSIFICATION OF THIS PAGE AD-A172976

REPORT DOCUMENTATION PAGE

1a REPORT SECURITY CLASSIFICATION: Unclassified	1b RESTRICTIVE MARKINGS
2a SECURITY CLASSIFICATION AUTHORITY	3 DISTRIBUTION/AVAILABILITY OF REPORT: Approved for public release distribution unlimited
2b DECLASSIFICATION/DOWNGRADING SCHEDULE	
4 PERFORMING ORGANIZATION REPORT NUMBER(S)	5 MONITORING ORGANIZATION REPORT NUMBER(S): AFOSR-TR- 86-0918
6a NAME OF PERFORMING ORGANIZATION: University of Florida; 6b OFFICE SYMBOL (If applicable)	7a NAME OF MONITORING ORGANIZATION: AFOSR/NA
6c ADDRESS (City, State and ZIP Code): Department of Civil Engineering, 346 Weil Hall, University of Florida, Gainesville, FL 32611	7b ADDRESS (City, State and ZIP Code): AFOSR/NA, Building 410, Bolling AFB, DC 20332-6448
8a NAME OF FUNDING/SPONSORING ORGANIZATION: U.S. Air Force Office of Scientific Research; 8b OFFICE SYMBOL (If applicable): AFOSR/NA	9 PROCUREMENT INSTRUMENT IDENTIFICATION NUMBER: AFOSR-84-0108
8c ADDRESS (City, State and ZIP Code): AFOSR/NA, Building 410, Bolling AFB, DC 20332-6448	10 SOURCE OF FUNDING NOS: PROGRAM ELEMENT NO. 6110?F; PROJECT NO. 2302; TASK NO C1; WORK UNIT NO

11 TITLE (Include Security Classification): Generalized Phenomenological Cyclic Stress-Strain-Strength Characterization of Granular Media

12 PERSONAL AUTHOR(S): M. McVay, D. Seereeram, P. Linton and D. Bloomquist

13a TYPE OF REPORT	13b TIME COVERED	14 DATE OF REPORT (Yr., Mo., Day)	15 PAGE COUNT
Final Report	FROM 5/1/84 TO 8/1/86	9/2/84	304

16 SUPPLEMENTARY NOTATION

17 COSATI CODES: FIELD	GROUP	SUB GR

18 SUBJECT TERMS (Continue on reverse if necessary and identify by block number): Stress-Strain-Strength Granular Media, Hollow Cylinder, Cyclic Triaxial Test, Plasticity, Prediction Expanding Cavity Cyclic CTC Tests

19 ABSTRACT (Continue on reverse if necessary and identify by block number)

This report presents the results of a generalized laboratory and phenomenological investigation of granular media subject to a variety of stress states. Emphasis was given to ress states which involved rotations of principal planes as found below a flexible pavement.

From an extensive study of hollow cylinder and triaxial experimental response, a number observations were evident: 1) isotropic behavior for monotonic loading was observed, where as anisotropic response for cyclic loading was noted; 2) membrane penetration influences for hydrostatic loading are significant; 3) stress-strain response is significantly effected by ress path, i.e. characterization of a moving wheel (hollow cylinder) in a triaxial device not possible; and 4) assuming that the yield surface is attached to the stress point is not a bad first approach.

The generalized phenomenological plasticity model developed herein, incorporates some the classical aspects: yield surface, and a flow rule (normality is maintained); (see back)

20 DISTRIBUTION/AVAILABILITY OF ABSTRACT	21 ABSTRACT SECURITY CLASSIFICATION
UNCLASSIFIED/UNLIMITED ☐ SAME AS RPT ☐ DTIC USERS ☐	

22a NAME OF RESPONSIBLE INDIVIDUAL	22b TELEPHONE NUMBER (Include Area Code)	22c OFFICE SYMBOL
Michael McVay	904-392-0958	

DD FORM 1473, 83 APR EDITION OF 1 JAN 73 IS OBSOLETE

19. Continued from reverse side

however, unlike many formulations, the consistency condition is automatically satisfied, and plays no role in determination of the plastic modulus. For the non-hardening version, K_p depends solely on the current stress state, whereas with the hardening modification, stress history effects are manifested by the evolution of an independent hardening control surface.

The developed model was used to successfully predict the stress-strain response of: 1) hollow cylinder data under different principal plane orientations, 2) expanding cavity (pressuremeter data), 3) cyclic conventional triaxial compression (CTC) results, and 4) a combination of loading, unloading, and hydrostatic compression. Further research of stress paths which replicate a moving wheel is recommended.

"GENERALIZED PHENOMENOLOGICAL CYCLIC STRESS-STRAIN-STRENGTH CHARACTERIZATION OF GRANULAR MEDIA"

SECOND YEAR

FINAL REPORT

AFOSR - 84 - 0108

Submitted by: M.C. Mcvay
D. Seereeram
P.F. Linton
D.B. Bloomquist

DEPARTMENT OF CIVIL ENGINEERING
DIVISION OF SOIL MECHANICS
UNIVERSITY OF FLORIDA
GAINESVILLE

TABLE OF CONTENTS

LIST OF TABLES

LIST OF FIGURES

KEY TO SYMBOLS

b	parameter controlling shape of dilation portion of yield surface
C_c, C_s	compression and swell indices
$d\underline{\varepsilon}$, $d\underline{\varepsilon}^e$, $d\underline{\varepsilon}^p$	total, elastic, and plastic (small) strain increments
$d\underline{e}$, $d\underline{e}^e$, $d\underline{e}^p$	deviatoric components of $d\underline{\varepsilon}$, $d\underline{\varepsilon}^e$ & $d\underline{\varepsilon}^p$ respectively
$d\bar{\varepsilon}$, $d\bar{\varepsilon}^e$, $d\bar{\varepsilon}^p$	equal to $\sqrt{(\frac{3}{2}\, d\underline{e}:d\underline{e})}$, $\sqrt{(\frac{3}{2}\, d\underline{e}^e:d\underline{e}^e)}$ & $\sqrt{(\frac{3}{2}\, d\underline{e}^p:d\underline{e}^p)}$ respectively
$d\varepsilon_{kk}$	incremental volumetric strain
$d\varepsilon^e_{kk}$, $d\varepsilon^p_{kk}$	incremental elastic and plastic volumetric strains
$d\underline{s}$	deviatoric components of $d\underline{\sigma}$
$d\underline{\sigma}$	stress increment
D_r	relative density in %
$\underline{e}$	deviatoric components of strain $\underline{\varepsilon}$
e_o	initial voids ratio
E	elastic Young's modulus
$f(\underline{\sigma})$	failure or limit surface in stress space
$F(\underline{\sigma})$	yield surface in stress space
$F_p(\bar{\underline{\sigma}})$	bounding surface in stress space
G	elastic shear modulus
$g(\theta)$	function of Lode angle θ used to normalize $\sqrt{J_2}$
I_1, I_2, I_3	first, second & third invariants of the stress tensor $\underline{\sigma}$
$(I_1)_i$	initial magnitude of I_1 for virgin hydrostatic loading

I_o	intersection of yield surface with hydrostatic axis (the variable used to monitor its size)
$(I_o)_p$	magnitude of I_o for the largest yield surface established by the prior loading
$\sqrt{J_2}$	square root of second invariant of $\underline{s}$
$\sqrt{J_2^*}$	equivalent octahedral shear stress = $\sqrt{J_2}/g(\theta)$
k	parameter controlling size of limit or failure surface
k_{mem}	maximum magnitude of k_{mob} established by the prior loading
k_{mob}	current mobilized stress ratio computed by inserting the current stress state in the function $f(\underline{\sigma})$
K	elastic bulk modulus
K_u	dimensionless elastic modulus number
K_p	plastic modulus
$\bar{K}_p$	plastic modulus at conjugate point $\bar{\underline{\sigma}}$
$(K_p)_o$	plastic modulus at the origin of mapping
m	exponent to model curvature of failure meridion
$\underline{n}$	unit normal gradient tensor to yield surface
n	exponent to control field of plastic moduli interpolation function
n^*	magnitude of n applicable to compression stress space
N	slope of zero dilatancy line in $\sqrt{J_2^*}$-I_1 stress space
N_{REP}	number of load repetitions
p	mean normal pressure ($=I_1/3$)
p_a	atmospheric pressure
p_o or p0	initial mean pressure
q	shear stress invariant, $= \sqrt{(3J_2)} = \sqrt{(\frac{3}{2} s_{ij}s_{ij})}$
q^*	equivalent shear stress invariant, $= \sqrt{(3J_2)}/g(\theta)$

Q	parameter controlling shape of consolidation portion of yield surface
r	parameter to model the influence of σ_3 on E
R	parameter to model deviatoric variation of strength envelope
$\underline{s}$	deviatoric components of $\underline{\sigma}$
S	slope of dilation portion of yield surface at the origin of $\sqrt{J_2^*}$-I_1 stress space
XN	slope of radial line in $\sqrt{J_2^*}$-I_1 stress space (below the zero dilation line of slope N) beyond which the effects of preconsolidation are neglected ($0 < X \leq 1$)
z	stress obliquity $\sqrt{J_2^*}/I_1$
β	scalar mapping parameter linking current stress state $\underline{\sigma}$ to image stress state $\underline{\bar{\sigma}}$ on hardening control surface
β'	modified magnitude of β in proposed hardening option to account for preconsolidation effects
γ	reload modulus parameter for bounding surface hardening option
γ_1, γ_2, γ_3	reload modulus parameters for proposed cyclic hardening option
Γ	Lame's elastic constant
δ	distance from current stress state to conjugate stress state
δ_0	distance from origin of mapping to conjugate or image stress state
$\underline{\delta}$	Kronecker delta
$\underline{\varepsilon}$	components of small strain tensor
$\bar{\varepsilon}$, $\bar{\varepsilon}^e$, $\bar{\varepsilon}^p$	total, elastic, and plastic shear strain invariants, $\sqrt{(\frac{3}{2} e_{ij}e_{ij})}$, etc.
ε_{kk}	total volumetric strain
ε^e_{kk}, ε^p_{kk}	elastic and plastic volumetric strains
θ	Lode's parameter

λ	plastic stiffness parameter for hydrostatic compression
μ	Lame's elastic constant
ν	Poisson's Ratio
$\underline{\sigma}$	components of Cauchy stress tensor
$\bar{\underline{\sigma}}$	stress tensor at conjugate point on bounding surface
$\sigma_1, \sigma_2, \sigma_3$	major, intermediate, and minor principal stresses
$\sigma_r, \sigma_z, \sigma_\theta$	radial, axial, and hoop stress components in cylindrical coordinates
ϕ	Mohr-Coulomb friction angle or stress obiliquity
ϕ_c	Mohr-Coulomb friction angle observed in a compression test (i.e., one in which $\sigma_2 = \sigma_3$)
ϕ_e	Mohr-Coulomb friction angle observed in an extension test (i.e., one in which $\sigma_1 = \sigma_2$)
ϕ_{cv}	friction angle at constant volume or zero dilatancy
χ	ratio of the incremental plastic volumetric to shear strain ($= \sqrt{3}\, d\varepsilon^p_{kk}/d\bar{\varepsilon}^p$)

ACKNOWLEDGEMENTS

The investigators would like to thank the United States Air Force Office of Scientific Research (AFOSR) for sponsoring this research under contract AFOSR-84-0108. They are also deeply indebted to Col. Lawrence Hokanson, their technical monitor for providing insight into many aspects of the work. To Professor A. Saada for supplying excellent hollow cylinder data under various rotation of principle planes. Also, Professor Frank C. Townsend for his expertise in laboratory testing, and Professors Daniel Drucker and Lawrence Malvern for their help in characterizing soil as a continuum and/or an elastoplastic material. Finally, to Pat Cribbs for her typing and editorial skills.

FOREWORD

The research reported herein is the second year's efforts of a two year study to investigate the stress-strain-strength of granular media in the hopes of characterizing it as an elastoplastic continuum. In the development, emphasis was given to stress paths which involved rotations of the principal planes, a very real world situation, e.g., a passing moving wheel, an earthquake, etc. Also, to improve on the available data sets (hollow cylinder, and a few triaxial strength tests), a number of triaxial tests were performed in an attempt to: 1) replicate the hollow cylinder tests, 2) investigate anisotropy (both inherent and stress induced, and 3) probe the shape of the yield surface (that which separates elastic from plastic behavior).

In the first year's effort, a comphrensive review of past theoretical and laboratory investigations was undertaken. It was concluded that even though many sophisticated phenomenological plasticity representations had been developed to characterize the likes of anisotropy, and cyclic hardening, they were totally unable to simulate the stress-strain-strength response of granular media under the rotation of the principal planes.

Consequently, the second year's effort concentrated on the reevaluation of the state variables which control the stress-strain, and strength characteristics of granular soil. From this investigation, it was discovered that there existed a unique relationship between plastic modulus and stress state, and that the assumption of the yield surface being attached to the stress state was not a bad first approach.

However, the research also revealed that the significance of material anisotropy may not be as important as the type of applied surface tractions. This was concluded from the fact that the strength data from the hollow cylinder tests does not fit any of the strength criterion developed from cubical triaxial devices, and the former device appears to develop significantly more volumetric compression than its latter counterpart, for the same principal stress states. Also, from the limited test data (limited equipment), i.e., Hydrostatic Compression results, inherent anisotropy was not observed. Consequently, it was concluded that even though any two tests may have the same principal stresses applied to their respective specimens, if they employ different boundary tractions (particulary shear stresses), their response may be significantly different i.e., it violates Principle of Material Frame Indifference. This was attributed to the particulate nature of the media, in particular the rearrangement of the soil's fabric.

The report initiates with the University of Florida's laboratory experiments, followed by the basic model development. Theoretical development, and the model's prediction of the hollow cylinder results for various principal plane orientation is subsequently presented, along with the conclusions and recommendations for further research.

CHAPTER 1

LABORATORY RESULTS

1.1 Introduction

Laboratory tests evolved from the need of the designer to know the engineering properties of a soil in order that the settlements, stability or flow rates may be accurately determined. One of the standard laboratory tests used in measuring such properties is the conventional triaxial testing apparatus. Developed through the efforts of Casagrande, this simple device is routinely used to determine the stress-strain, and strength characteristics of soil. Unfortunately, the test is very limited in the stress states which may be applied to the specimen. For instance, a soil element subject to a passing moving wheel undergoes a continuous cyclic rotation of principal stress i.e., increasing levels of shear stress in combination with normal stresses. Since the triaxial device is incapable of subjecting a specimen to a shear stress, the standard test used in representing such a loading is simply a cyclic variation of the axial force (resilient modulus test). This approach has been seriously questioned (Ishihara 1983) as being highly unconservative with the possibility of catastrophic failure (liquification).

Consequently, the purpose of the tests reported herein were three-fold: 1) obtain conventional triaxial compression (increase in axial load) results for different levels of deviatoric (principal stress difference) stresses and cell pressures in order to investigate the evolution of the yield surface and plastic modulus for the model development of Chapter 3 (hollow cylinder data

wasn't available; 2) perform cyclic conventional triaxial compression and hydrostatic compression (increase in only cell pressure) tests (compliments the hollow cylinder data) to study the significance of anisotropy (inherent as well as stree-induced) on the evolution of strength and the plastic strain rate direction (i.e., associated or non-associated flow, see Chapter 3); and 3) perform special triaxial tests which bound the hollow cylinder representation of the moving wheel stress path. The latter series of tests will answer the question as to the appropriateness of the triaxial device in characterizing loading states which involve principal plane rotation (earthquake, sea beds, etc.).

However, before the results are presented, a discussion of current state of the art in triaxial deformation monitoring and data capture is given. The former was undertaken to ensure that uniform deformation fields were obtained, as well as minimizing the influence of end caps.

1.2 Deformation Measurements

In order to accurately obtain the deformation field within a triaxial specimen, one needs to monitor both the axial and lateral specimen movements. Presently, there exists within the geotechnical community a number of different measuring devices. Three of the most common are presented along with the reasons (pros and cons) for the selection of the Linear Variable Differential Transformer device.

1.2.1 Strain Gauge

One of the most common contact devices available to measure specimen deformations are of the strain gauge variety. Basically, the gauge is used to determine the flexural strains in a simply supported beam attached to the specimen. Depicted in Figure 1.1a and 1.1b is a plan and cross-sectional view of a proposed device consisting of three brackets affixed to the sample in the

vicinity of its middle one-third. Epoxied to the central aluminum beam of each bracket are two pairs of gauges (two on each side). They are subsequently wired to form an unbalanced Wheatstone bridge circuit; with the individual resistors (legs) in the bridge connected to produce the greatest imbalance for the smallest strain.

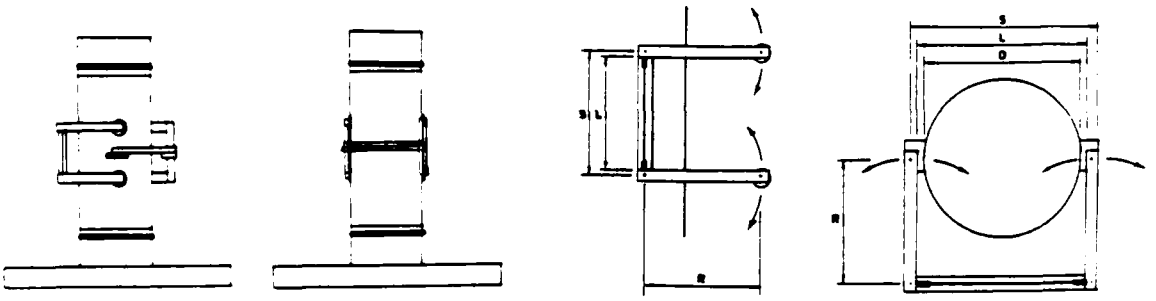

a) Plain View b) Cross-Sectional View

Figure 1.1 Proposed Strain Gauge Device.

Using an aluminum strip 0.2 in (5 mm) wide by 0.02 in. (0.5 mm) thick, specimen deformation on the order of one in ten thousandths of an inch are available, if the resolution of the voltmeter is on the order of 200 micro volts (Linton, 1986). A typical data acquisition system, eg. HP 3497A, has the capability of measuring on the micro volt scale. Cost of raw material in the brackets, gauges and calibration micrometer is on the order of

$1,500.00. Devices similar to the one discussed have been used by a number of researchers, (Boyce, 1983).

Some of the disadvantages of this form of measurement are: 1) in order to record deformation, the aluminum bar has to flex thereby applying a stress traction or the specimen on the order of 1 psi; 2) the necessity of periodic calibration: 3) the uncertainity of water proofing the gauges; and 4) the possibility of equipment destruction (induced permanent deformation) due to large specimen deformations.

1.2.2 Non-Contact Devices

Non-contact measurement instruments generally fall into one of four categories: 1) inductive, 2) ultrasonic, 3) optical, and 4) pneumatic. Possibly due to increase in demand, the accuracy of all representative devices has improved. Presently however, ultrasonic and pneumatic are generally ruled out due to a lack of sensitivity (one in five hundredths of an inch) in case of the former, and size constraints, as well as ability to perform submerged in the case of the latter. Optical techniques, such as lasers look promising with the aid of micro computers and robotics; however, the necessary capital expenditures required to develop holographic equipment is presently prohibitive. Inductive equipment, both small and fully immersible have found use in monitoring shaft or plate thickness, but only recently have there been attempts to monitor soil response (Saada, 1985). A brief discussion, as well as a representative prototype are presented.

Inductive measurement of distance uses the eddy currents generated in a metallic target through high frequency excitation to stimulate the impedance of a coil. This reaction is then conditioned and linearized to produce a direct relationship between position and output voltage (Bristol Ltd., 1985). Presented in Figure 1.2 is the plan and cross-sectional view of a

proposed inductive setup to monitor horizontal movement of a soil specimen. As depicted in the figure, the specimen is in contact with four columns of metallic plates. Each column is composed of five square plates, 1 in. by 1 in. (25 mm by 25 mm), of 0.04 in. (1 mm) thickness and separated by a 1/6 in. (4.2 mm) gap. The size of an individual plate is mandated by the inductive sensing device. The plates are curved to a 1.9 in (48 mm) radius, and are attached to the specimen by either a combination of epoxy and cyanoacrylate adhesive, or through compressive forces generated from a rubber membrane affixed between the lateral plates. A total of twenty horizontal measurements (one for each plate) would be available with this setup.

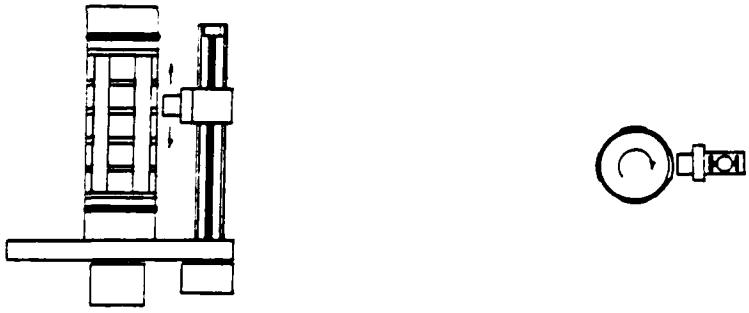

a) Plan View b) Cross-Sectional View

Figure 1.2 Inductive Set Up for Measuring Horizontal Deformations.

Because the plates are moving downward, it is necessary that the sensing device be capable of vertical motion. Moreover, if it is desired to use the same sensing device for all plates, both rotary and vertical stepping motors are suggested. The former to rotate the sensing device, and the latter to vertically align the device with an individual plate.

If vertical specimen deformation is needed, Figure 1.3 presents a suggested setup. In this approach, thin metallic plates are cantilevered to the specimen, and the sensing equipment is fixed to the base of the triaxial device.

The inductive setup was not selected for the research reported herein for two reasons: 1) even though the sensing device is non-contacting, a large metallic target must be glued to the specimen and 2) at time of selection, the sensing device was only capable of measuring one in five hundredths of an inch (0.05 mm).

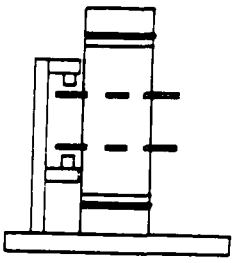

Figure 1.3 Inductive System for Measurement of Vertical Deformations.

1.2.3 Linear Variable Differential Transformers

The final option investigated to monitor specimen deformation were linear variable differential transformers (DCDTs). Available in alternating or direct current, the DCDTs work by exciting a primary coil placed between two symmetrical secondary coils which are in an opposing series circuit. The electrical potential between the primary and secondary coils is monitored and converted to deformation. However, the alternating current devices require an additional unit to convert AC to DC prior to the determination of deformation. The DCDTs have many valuable attributes for measurement: 1) near frictionless measurement, 2) infinite mechanical life, 3) extremely high resolution, 4) core and coil separation, and 5) null repeatability (Herceg, 1985).

Even though the AC devices are much smaller than their DC counterparts, previous research by the investigators found them questionable for the following reasons: 1) erratic readings often developed due to outside power sources, and 2) the necessity to continuously recalibrate the instruments due to drift. Consequently, standard DCDTs with ranges of one half inch (13 mm) and one inch (25 mm) were used. This results in a full range output of about 80V/inch and 40Vinch (3.2V/mm and 1.6V/mm). Presented in Figures 1.4a and 1.4b is a proposed DC-LVDT system to monitor vertical and horizontal deformations in a soil specimen's middle one third. Figure 1.4a depicts the cross-sectional view, whereas Figure 1.4b illustrates the plan view. It should be noted that all brackets are designed with sliding rods within stainless steel sleeves (top and bottom, Figure 1.4b) or a combination of DCDTs (middle, Figure 1.4b) to result in linear deformations and prevent the transfer of normal forces onto the specimen. The weight of the brackets and DCDTs will result in an average vertical shear stress of approximately 1 psi

(7 kPa) over the contact surface. However, this may be reduced to zero, if floatation is employed. Total cost of DCDTs, brackets and necessary machining is in the neighborhood of $1,600.00.

Due to cost, previously discussed benefits, and limited deteriments, the investigators decided to construct and compare the LVDT measuring system to the conventional burette and dial gauge system (Lambe et al., 1969)

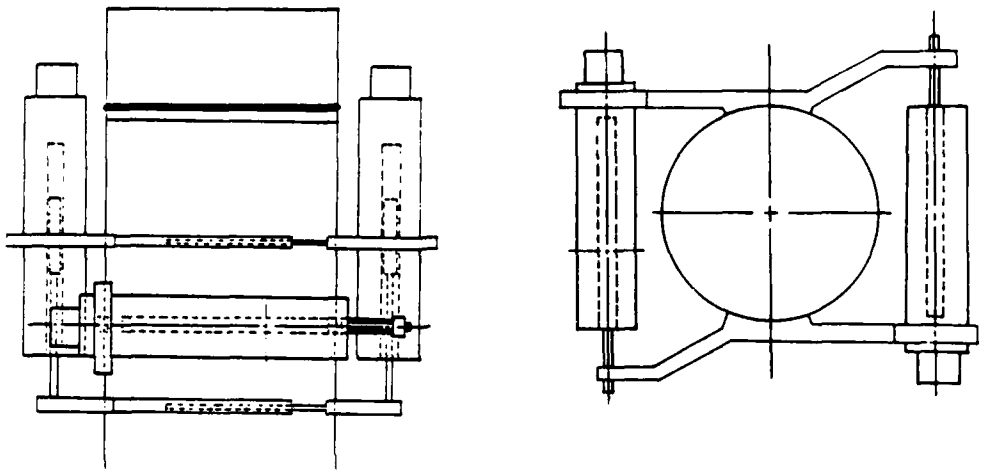

a) Plan View b) Cross-Sectional View

Figure 1.4 DCDT Measurement Device.

1.3 Data Capture and Reduction

Having to monitor both the local (DCDT) and macro (burette and dial gauge) measurements, consisting of approximately 8 instruments for 200 different load levels (cyclic testing) or 1,600 data entries, one readily sees the benefits of an automated data acquisition and reduction package. A whole slew of hardware specific software packages are commerically available for

such tasks. However, the system developed was one which incorporated hardware (equipment) most often found in and around a soil laboratory. The package depicted in Figure 1.5 consists of: 1) a micro computer and monochromatic CRT (screen), 2) a multiprogrammer and interface, 3) a 3.25 in. floppy drive unit, (4) a two pen plotter, and 5) a printer.

The multiprogrammer (voltmeter), controlled by a micro computer software package (TRITEST) developed at the University of Florida, automatically scans eight channels after the application of each load incement: four DCDTs associated with the local measurement system (Figure 1.4), one DCDT to monitor movement of top platen attached to the sample, two pore pressure transducers (one for the cell, the other for the sample), one load cell to monitor axial load, and a volumetric burette reading (inputed manually). All of the measuring devices were read every two minutes with the captured data being

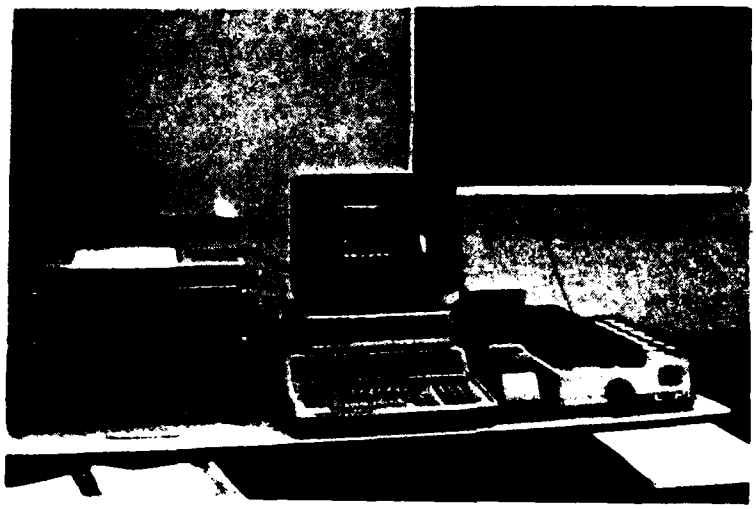

Figure 1.5 Photograph of the Computer System.

immediately reduced and stored on both hard and soft medium (floppy disk drive unit). Examples of available results are: 1) individual LVDT deformations,

2) local (Figure 1.4) and macro (computed from burette and platen movement) vertical, horizontal, and volumetric strains, 3) effective vertical and horizontal stresses, 4) Cambridge P' $((\sigma_1' + 2\sigma_3')/3)$, and Q' $(\sigma_v' - \sigma_H')$, and 5) Cambridge $\bar{\varepsilon}$ $(\varepsilon_1 - \varepsilon_H)$. Also, through the course of the test, the operator has the option of viewing the measured response by a hardcopy (printer), or by plots (CRT or plotter) or both. Moreover, multiple graphical images (eq. local and macro Q' vs $\bar{\varepsilon}$) may be viewed concurrently. These latter options were implemented to provide a means of assessing the performance of all instrumentation during the course of a test.

Two separate software packages, PRINTOUT and PLOTOUT, were coded to print or plot the output (screen or plotter) for any permanently recorded data set. Approximately twenty-five distinct graphs are available.

1.4 Soil-Sample Preparation-Back Saturation

The soil tested, commonly referred to as Reid-Bedford sand is composed of 89% quartz, 9% feldspar, 2% ferromagnesians and heavies. Particle shapes range from subrounded to subangular with a coefficient of uniformity, C_u of 1.8, and a coefficient of curvature C_c of 1.0. The Unified Soil Classification System identifies Reid Bedford as a fine sand with a group symbol of SP. The average of five relative desity tests (ASTM D-2049) indicate that the void ratio ranges from 0.59 to 0.91. These void ratios correspond to a maximum dry unit weight of 104.0 pcf and a minimum dry unit weight of 86.6 pcf respectively. All reported tests were run on samples with a void ratio of 0.67 i.e., a relative density of 75%. Testing initiated with the preparation of a specimen 5.95 in. (15.1 cm) high by 2.8 in. (7.11 cm) in diameter with a volume of 36.6 cubic inches (600 cc). The specimen was constructed through aerial pluviation with a drop height of seven to nine inches. No vibration was necessary, if the operator established a coherent

stream of falling sand particles instead of a spray. The specimen end caps depicted in Figure 1.6 were polished aluminum platens with porous steel insets for drainage. In addition each platen was coated with teflon spray to reduce the development of friction between the sand grains and the metal. Before attachment of DCDTs, the specimen mold was removed after subjecting the specimen to a vacuum of 5 psi (34 kPa).

Figure 1.6 Polished Aluminum Platen.

Attachment of the DCDTs was a three step process as depicted in Figure 1.7. First, the central bracket (local horizontal measurement device) was attached to the specimen; a quick drying epoxy was used to provide a base which molds to the specimen, then a cyanoacrylate adhesive was used to firmly attach the epoxy to the membrane (Step A Figure 1.7). Second, the bottom bracket of the vertical measuring system was affixed (Step B) through a similar process, followed by the top bracket containing the DCDTs (Step C).

Care must be exercised in aligning the vertical DCDTs with their respective cores. The whole process: placement of brackets, cementing, and hardening takes approximately 30 minutes.

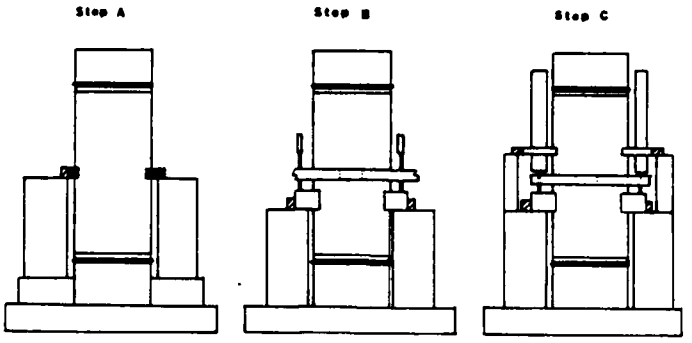

Figure 1.7 Steps for Attaching the DCDTs.

Following the placement of the local measurement system, the specimen was saturated with water by repeatedly applying vacuum to the top of the sample followed by deaired water entry through the bottom and subsequent back pressuring. Instead of checking saturation through a conventional B test (Lambe et al., 1969), saturation was determined by subjecting the specimen to an aribitrary raise in cell and back pressure such that no effective stress change occurred within the specimen. The volume of fluid entering the sample (burette) is subsequently used to determine the degree of saturation as

$$S = \frac{eV_t(P_2 - P_1) - (1 + e)\, P_1\, \Delta V}{eV_t\,(P_2 - P_1)} \qquad (1.4.1)$$

where S = Saturation at state two.

V_t = The total volume of the specimen,

ΔV = change in burette reading,

e = specimen void ratio,

P_1 = Pore pressure at state one,

and p_2 = Pore pressure at state two.

The equation was obtained from Boyle's law, as laid out in 1610, and a phase diagram. The latter approach was taken over the conventional B test (Lambe et al., 1969) until degree of saturation was at least 95% in order to minimize the influences of stress induced anisotropy. Since conventional volume measurements (burette) were to be employed, B values of at least 95% were maintained for all tests.

1.5 Triaxial Results

The triaxial results are presented by stress path: 1) Hydrostatic Compression, 2) Conventional Triaxial Compression, and 3) Triaxial Moving Wheel Representation. The first series of tests, Hydrostatic Compression, were performed to obtain data for model predictions in Chapter 3, as well as investigate anisotropy effects: inherent and stress induced. The Conventional Triaxial Compression tests were used in model predictions of Chapter 3, and for comparison of the Triaxial Moving Wheel Representation in the latter part of this chapter. All tests had both monotonic and cyclic histories. Also, many of the tests had replicate tests performed to improve the quality of the data. For all plotted data, a circle is adopted as a macro

reading (shaft displacement and burette to measure volume change) and a cross is used to characterize a local reading (data obtained from DCDTs).

1.5.1 Hydrostatic Compression

Figures 1.8 through 1.11 depict the mean pressure increase and the ensuing volumetric strain change on the Reid-Bedford sand with a nominal void ratio of 0.67. Since the hydrostatic tests were the first series of tests performed with the DCDTs attached to the specimen, it was decided to perform the first test without the DCDTs attached, Figure 1.8. The volumetric compression resulting from a change in mean pressure from 30 psi (207 kPa) to 100 psi (690 kPa) was 0.0042 in./in. The second test, Figures 1.9 and 1.10, was performed with both local and macro equipment to check the reproducibility of the equipment. The sample was observed to have a volumetric strain of 0.0040 in./in. from the macro device and a value of 0.0026 in./in. measured by the local device. Based on the macro readings of Figures 1.8 and 1.9, one can say with some degree of confidence that the DCDT brackets had miminal influence on the macro response. However, comparing the macro (.0041 in./in.) versus micro (.0026) response, the results at a first glance looked discouraging.

It was initially thought that the epoxy which held the DCDTs to the specimen may have slipped due to the surrounding cell water. Consequently, a test, Figure 1.11, was performed on a dry specimen to investigate this possibility. The local volumetric strain measured in Figure 1.11 was 0.0029 in./in. for a 70 psi (480 kPa) mean stress increase. Since this is quite close to the value of 0.0026 in./in. obtained from the previous test, slippage was ruled out.

A close scrutiny of the slopes of Figures 1.9 and 1.10 reveal that the initial slopes are quite similar, but at higher mean stresses, greater amounts

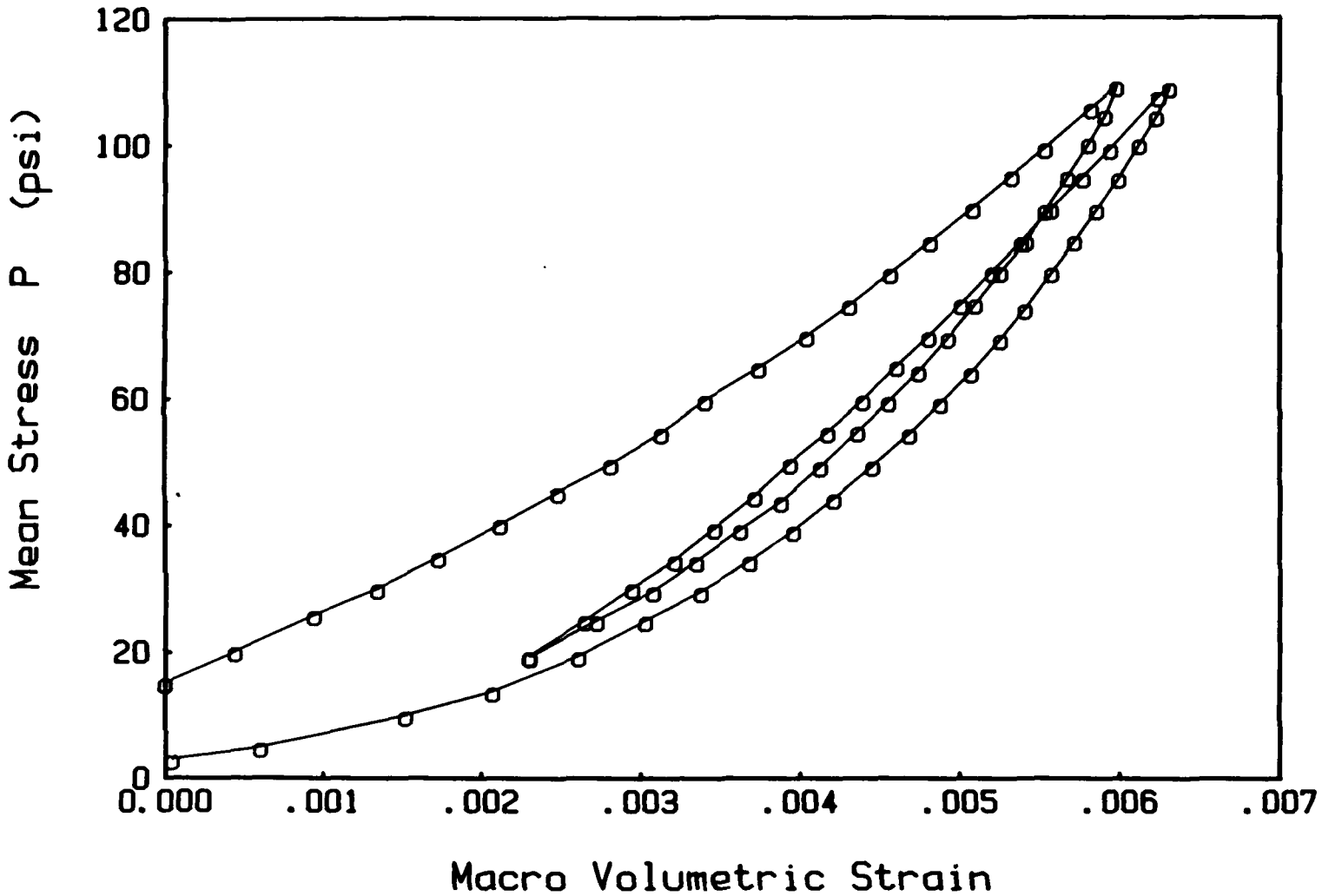

Figure 1.8 Test 1: Hydrostatic Test Without DCDT Brackets

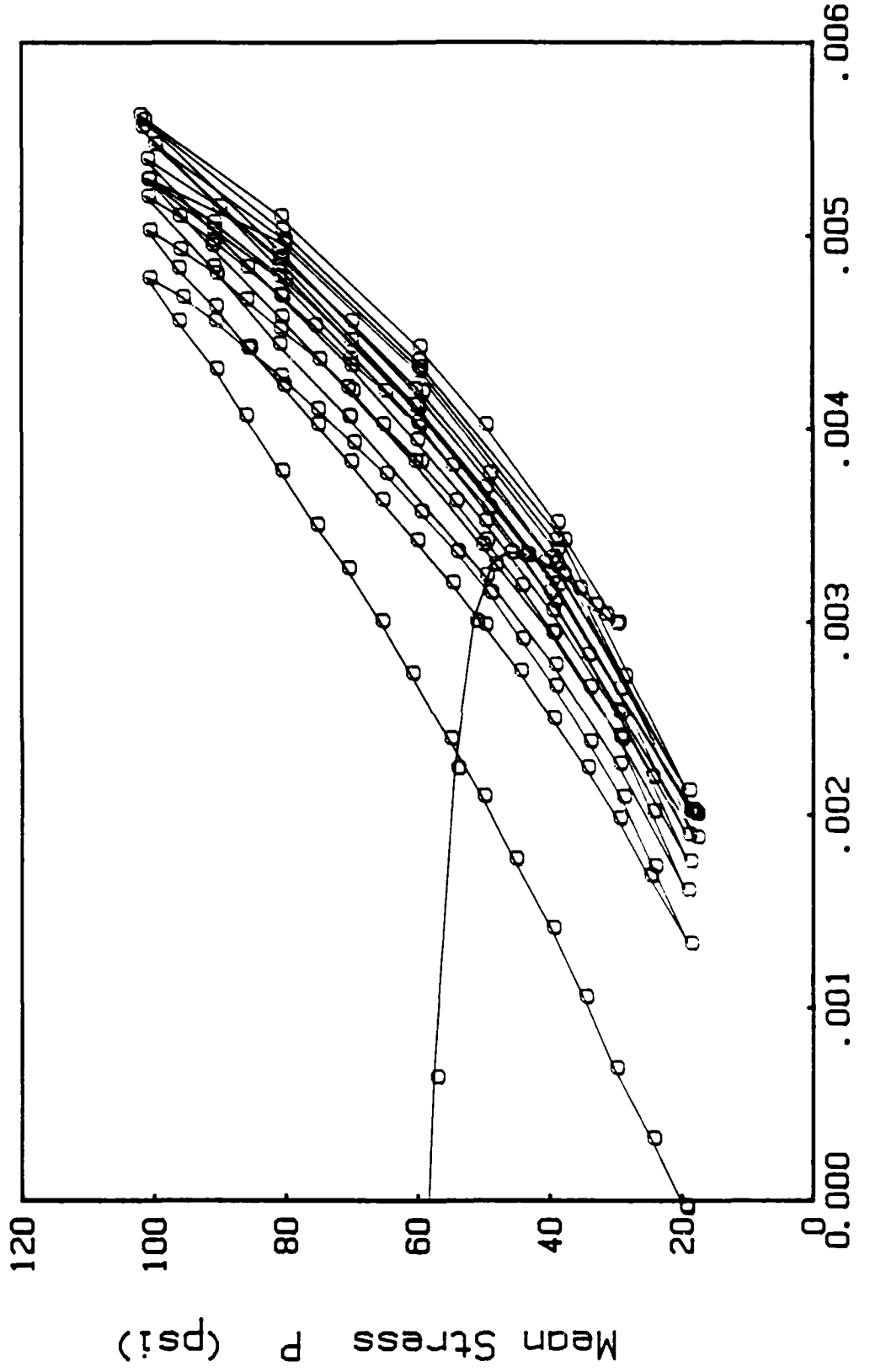

Figure 1.9 Test 2: Hydrostatic Test Using the Macro System

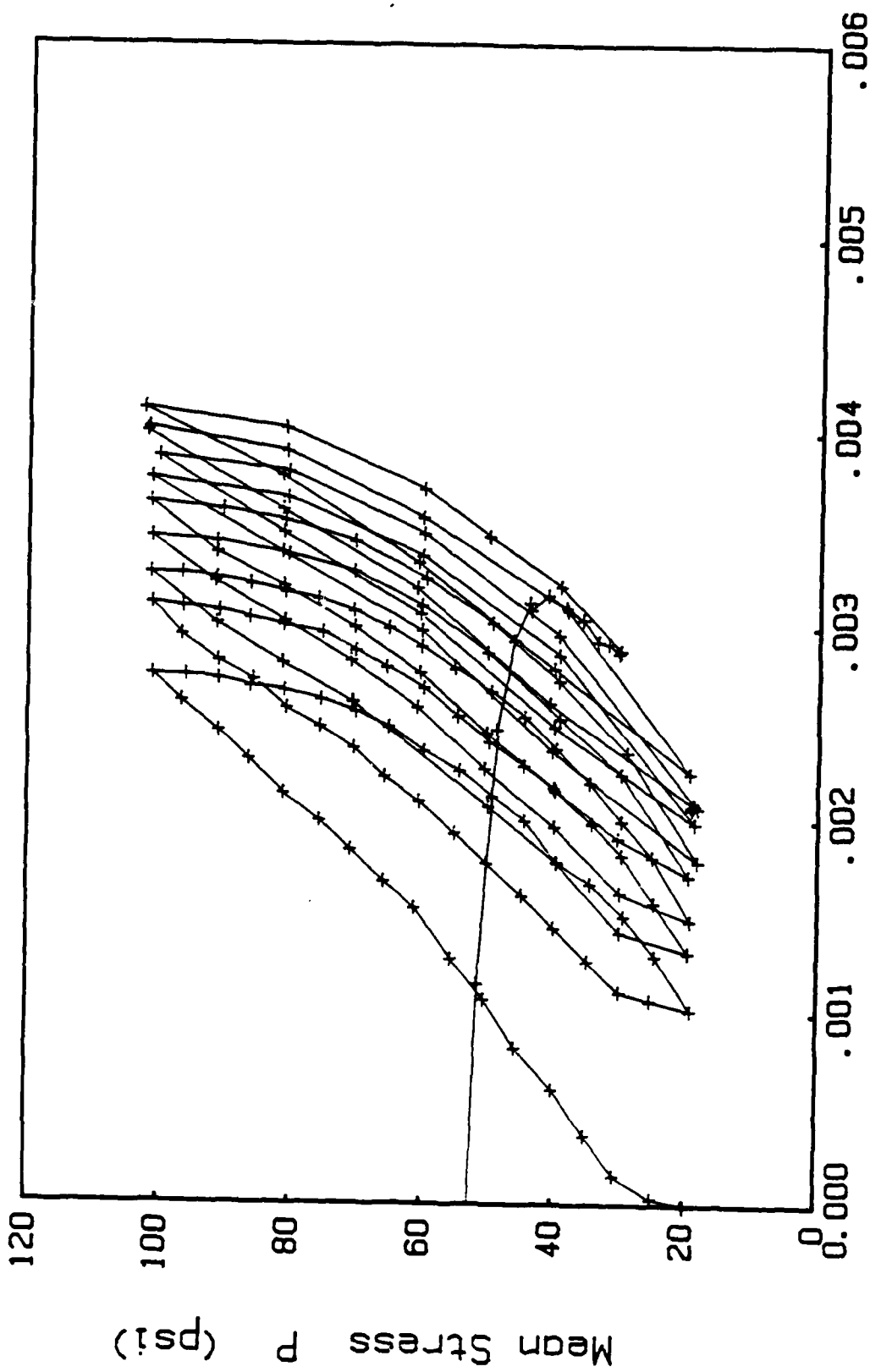

Figure 1.10 Test 2: Hydrostatic Test Using the Local Sysytem

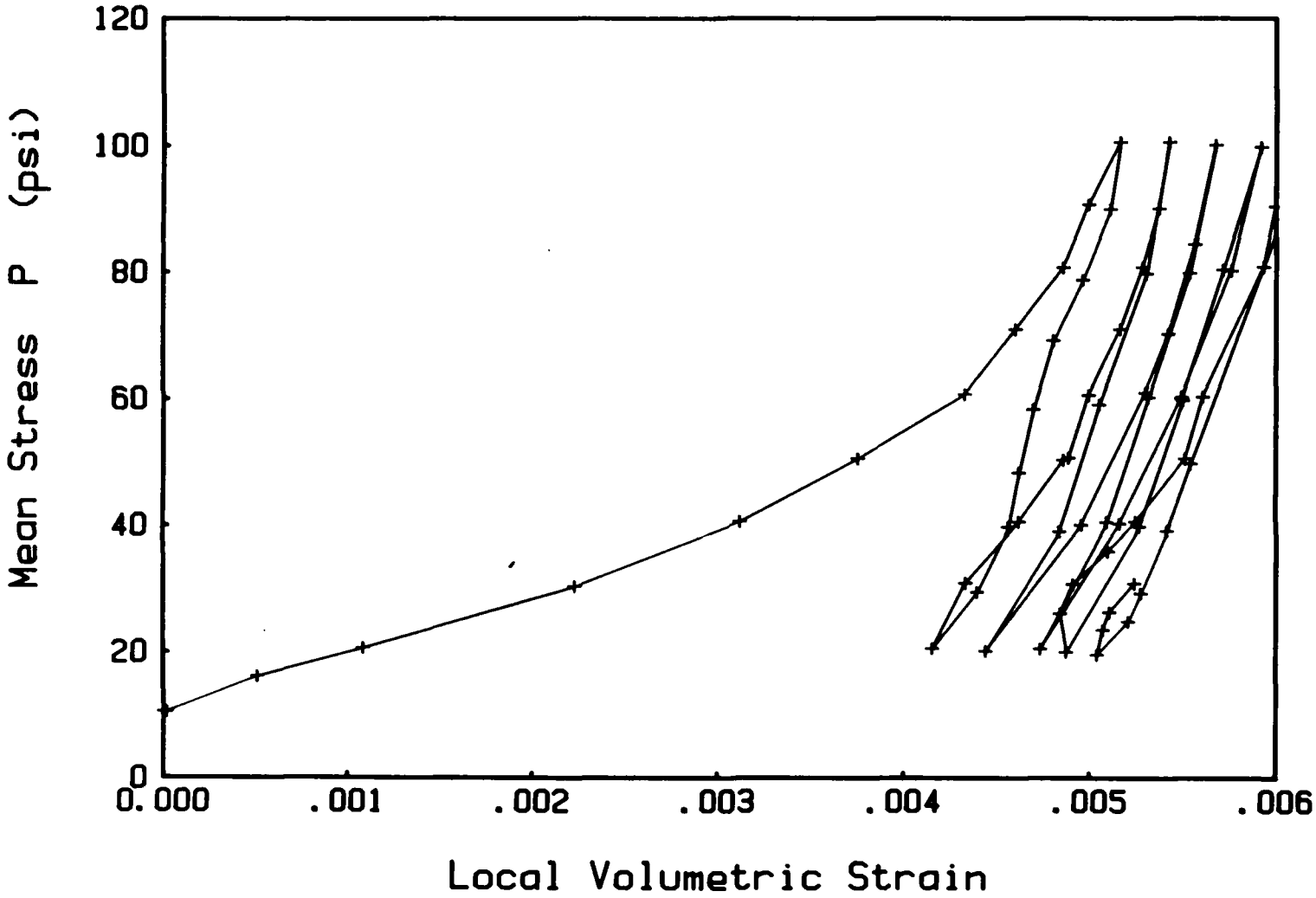

Figure 1.11 Test 3: Hydrostatic Test on a Dry Specimen

of macro volumetric strain was being generated. Based on this fact, it was readily recognized that membrane penetration may be significant.

To quantify membrane penetration, two different mathematical idealization were developed based on Figure 1.12. Starting with the triangular area trapped between the membrane and the sand particles in the left of Figure 1.12, the elemental areas (between two particles) would be:

$$A = D_{10}^2 \left\{\frac{1}{2} - \frac{\pi}{8}\right\} \qquad (1.5.1.1)$$

The number of such areas over the height of the specimen is

$$N = \frac{H}{D_{10}} \qquad (1.5.1.2)$$

and multiplying by the circumference would give the total volume change associated with the specimen as

$$\delta v = \pi D_{10} \; HD \; \left\{\frac{4 - \pi}{8}\right\} \qquad (1.5.1.3)$$

In the second approach, shown on the right of Figure 1.12, the membrane is assumed to be pushed into the space provided by four adjacent spheres to give an elemental volume of

$$v = D_{10}^2 \left\{\frac{1}{2} - \frac{\pi}{12}\right\} \qquad (1.5.1.4)$$

The number of elemental volumes contained over the surface area is

$$N = \frac{H\pi D}{a}$$

giving the total membrane penetration (volume change) for this approach as

$$\delta v = \pi \, D_{10} \, H \, D \; \frac{\{6 - \pi\}}{12} \qquad (1.5.1.6)$$

where D = diameter of specimen

D_{10} = average particle diameter

H = height of the specimen.

The volumetric strain associated with Equations 1.5.1.3 and 1.5.1.6 ranges from 0.001 in./in. to 0.002 in./in.. If the latter value was subtracted from

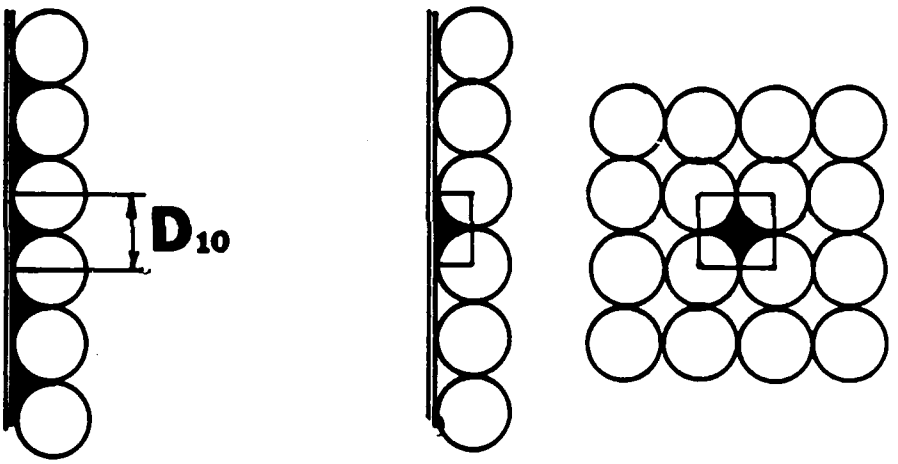

Figure 1.12 Membrane Penetration Models (Assumption Particles are Spheres)

the volumetric strains recorded in Figures 1.8, 1.9, and 1.11 volumetric strains of 0.0022 in./in,, 0.0020 in./in., and 0.0026 in./in. would be obtained respectively. Agreement with the corresponding local volumetric strains given in Figures 1.8, 1.10, and 1.11 would be excellent. Therefore, it can only be concluded that the order of error due to membrane penetration is similar in magnitude as those associated with the mean pressure change, if the standard macro measuring system is employed. Consequently, the burette measuring system of volume change is not recommended for Hydrostatic Compression tests. Since the DCDTs span the soil grains with little or no membrane influences, they are highly recommended as the alternate measuring system.

The study of anisotropy initiates with the depiction (Figure 1.13) of the hydrostatic compression's local vertical and horizontal strain reported in test two (Figure 1.9). Scrutiny of the figure reveals that the inherent anisotropy along this stress path is minimal, since the magnitudes of the horizontal and vertical strains are quite similar. However, the stress-induced effects are very significant, as seen from the cyclic response. This is more readily visible from separate plots of mean stress, P, versus the vertical and horizontal strains as shown in Figures 1.14 and 1.15. Evident from the two figures is that the vertical strain is cycling between its minimum and maximum value with little permanent strain buildup, whereas the horizontal strain component shows significant strain increase for the same mean pressure change. From a plasticity viewpoint, the above results suggests that Reid Bedford sand may have an associative yield surface during virgin loading, but a non-associative surface for cyclic response. The former will be incorporated into the proposed plasticity model developed in Chapter 3.

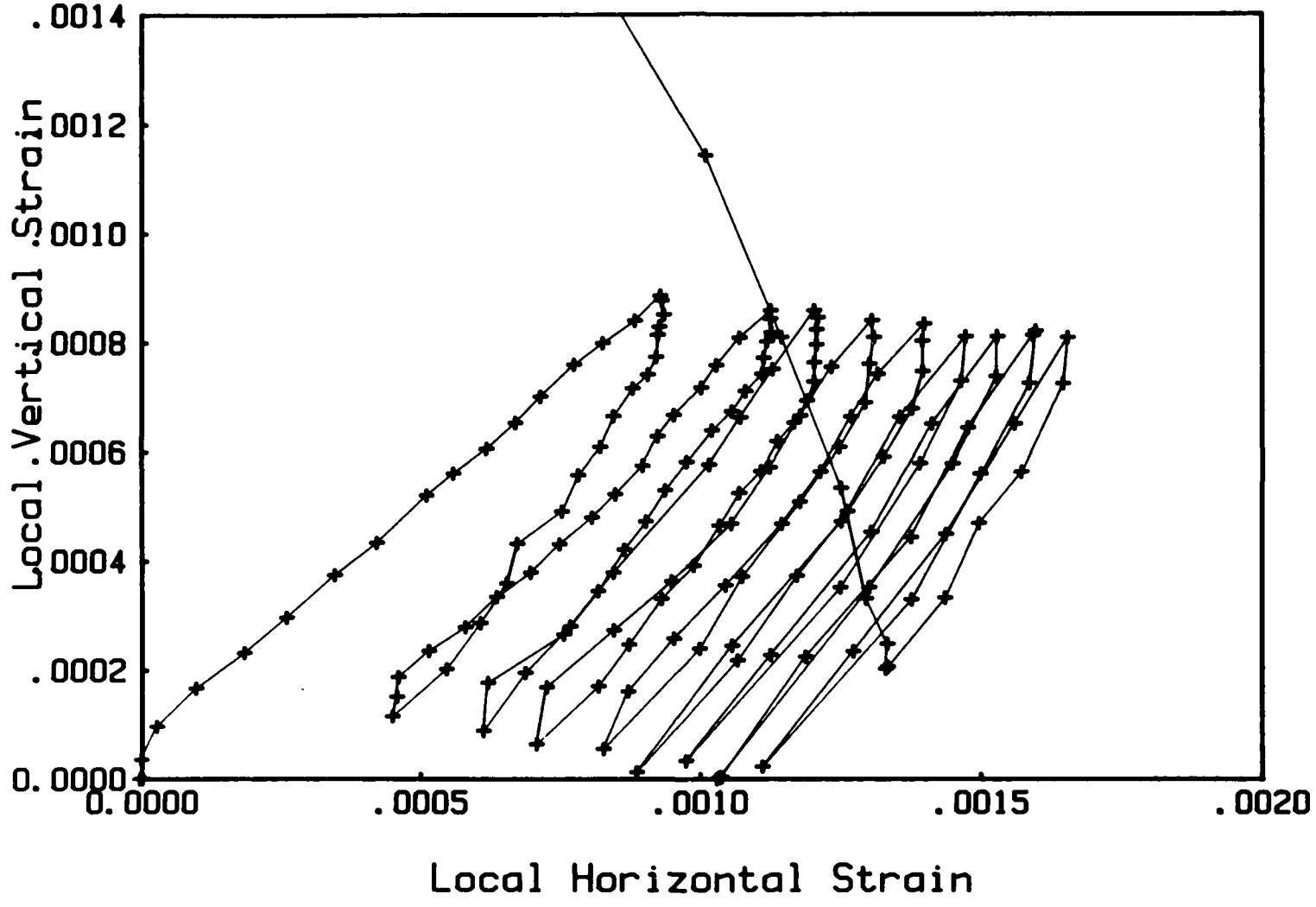

Figure 1.13 Test 2: Hydrostatic Loading, Comparison of Local Horizontal and Verticle Strains

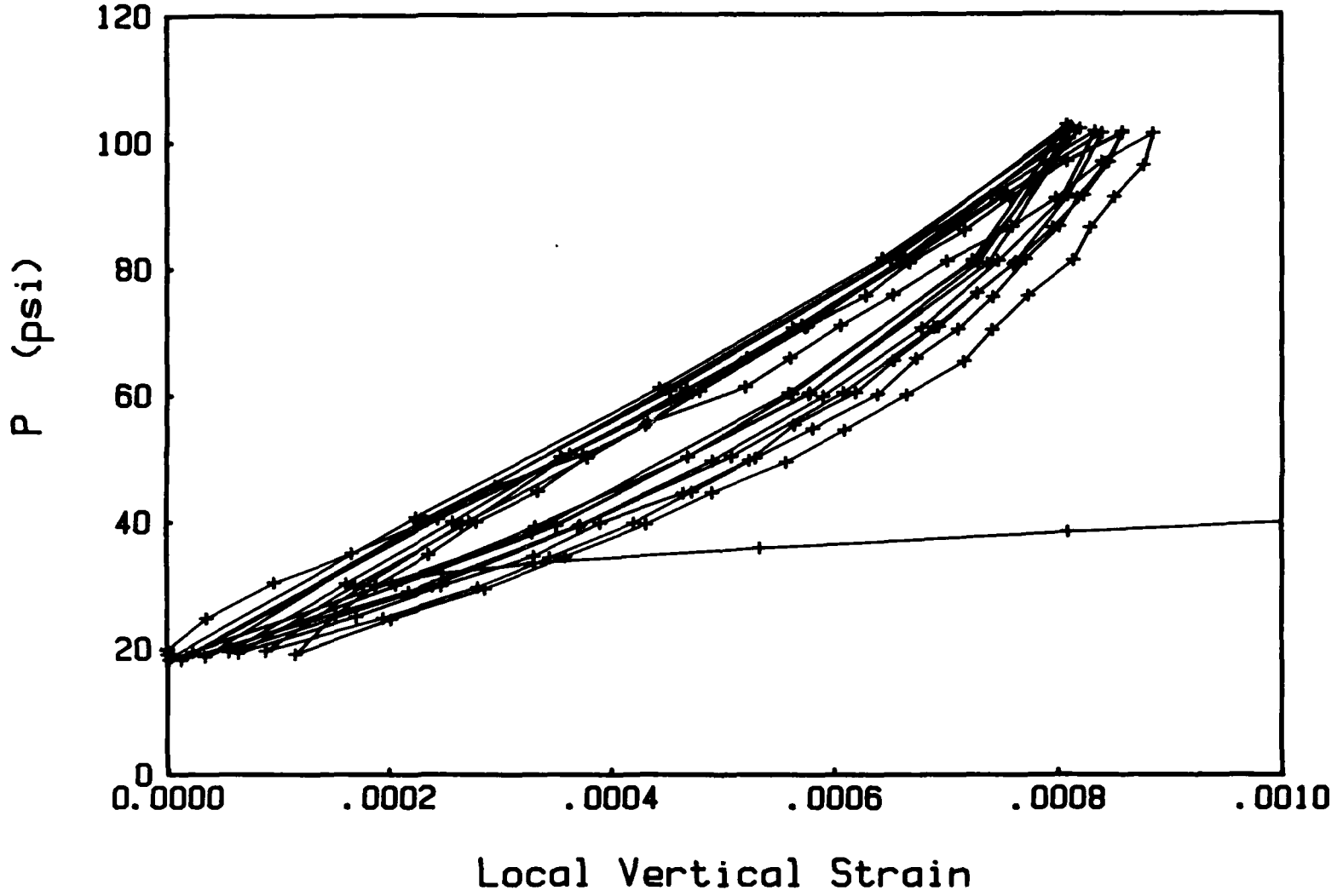

Figure 1.14 Test 2: Hydrostatic Loading, Mean Stress versus Local Verticle Strain

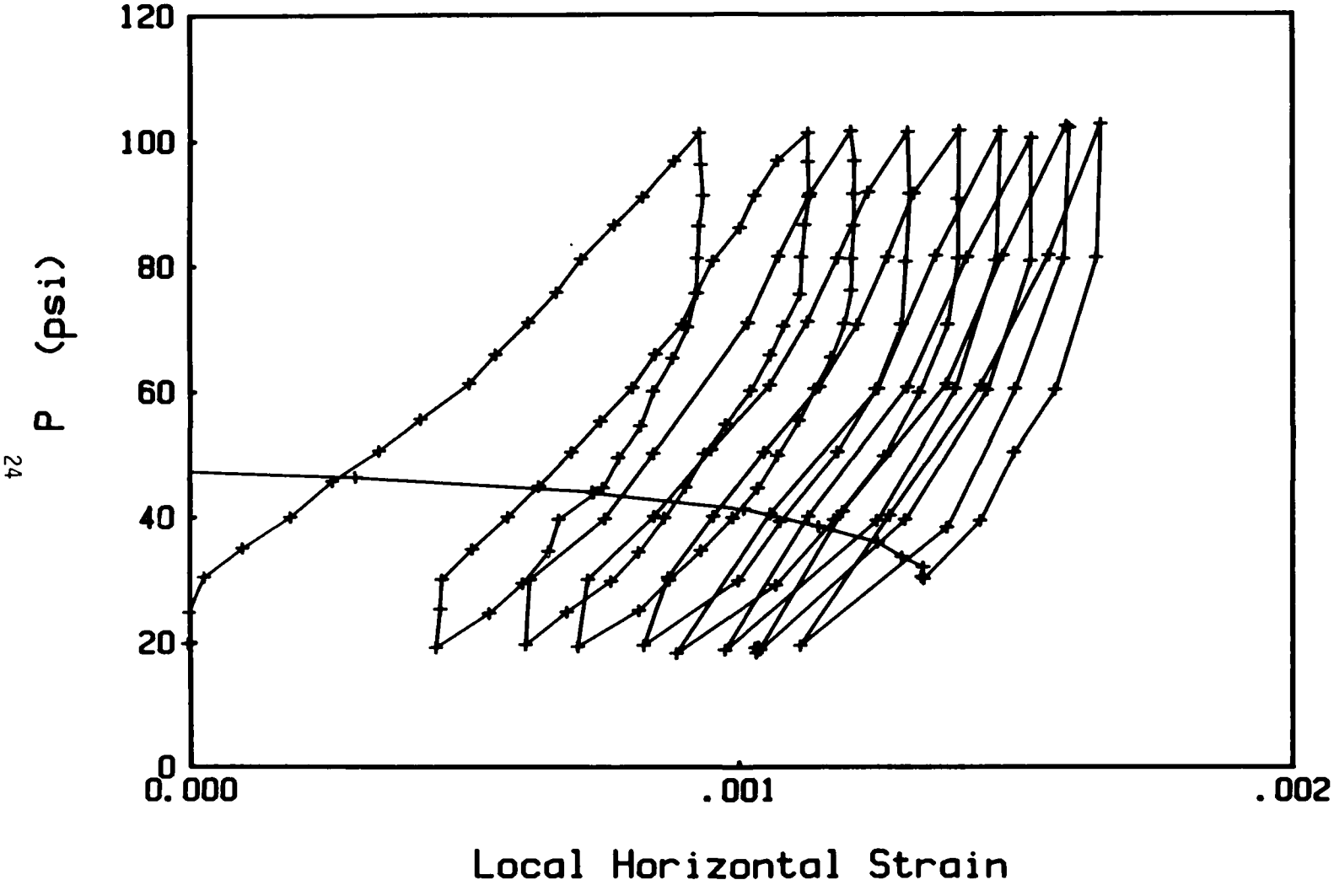

Figure 1.15 Test 2: Hydrostatic Loading, Mean Stress versus Local Horizontal Strain

To check reproducibility, presented in Figures 1.16 and 1.17 are the local horizontal and vertical strains versus the mean pressure increase for the third hydrostatic compression test, Figure 1.11. Comparing Figures 1.14 with 1.16, and Figures 1.15 with 1.17, one readily sees the excellent reproducibility of the data, and the benefits of the local measurement system (DCDTs).

To investigate the possibility of stress-induced anisotropy for other loading situations, tests two and three (Figures 1.10 and 1.11) were loaded to failure along a convention triaxial compression stress path (increase in only axial stress), Figures 1.18 - 1.21. In Figure 1.18 the invariant stress ratio, Q/P, versus the macro (shaft and burette measurements vertical strain of specimen two (Figure 1.9) is depicted. Q is defined as the vertical minus the horizontal effective stress, and P is mean effective stress $[\ (\sigma_v + 2\sigma_H) / 3\ ]$. Figure 1.19 shows the invariant stress ratio Q/P, versus the local (DCDTs measuring system $\bar{\varepsilon}\ (\varepsilon_v - \varepsilon_H)$ strains for the CTC loading portion of sample two, Figure 1.10. E bar is presented in the latter figure since it is good measure of deviatoric anisotropic strain influences. strain of specimen two (Figure 1.9) is depicted. Q is defined as the vertical minus the horizontal effective stress, and P is mean effective stress $[\ (\sigma_v + 2\sigma_H) / 3\ ]$ Figure 1.19 shows the invariant stress ratio, Q/P, loading portion of sample two, Figure 1.10. E bar is presented in the latter figure since it is good measure of deviatoric anisotropic strain influences. Figure 1.20 presents the local (DCDTs) vertical versus horizontal strains from the CTC loading portion of test two (Figure 1.10). Figure 1.21 depicts the stress invariant ratio, Q/P versus local e bar $(\varepsilon_v - \varepsilon_H)$ for specimen three (Figure 1.11). The latter results are only presented to denote the excellent reproducibility of the tests (Figures 1.19 versus 1.21). Discussion of

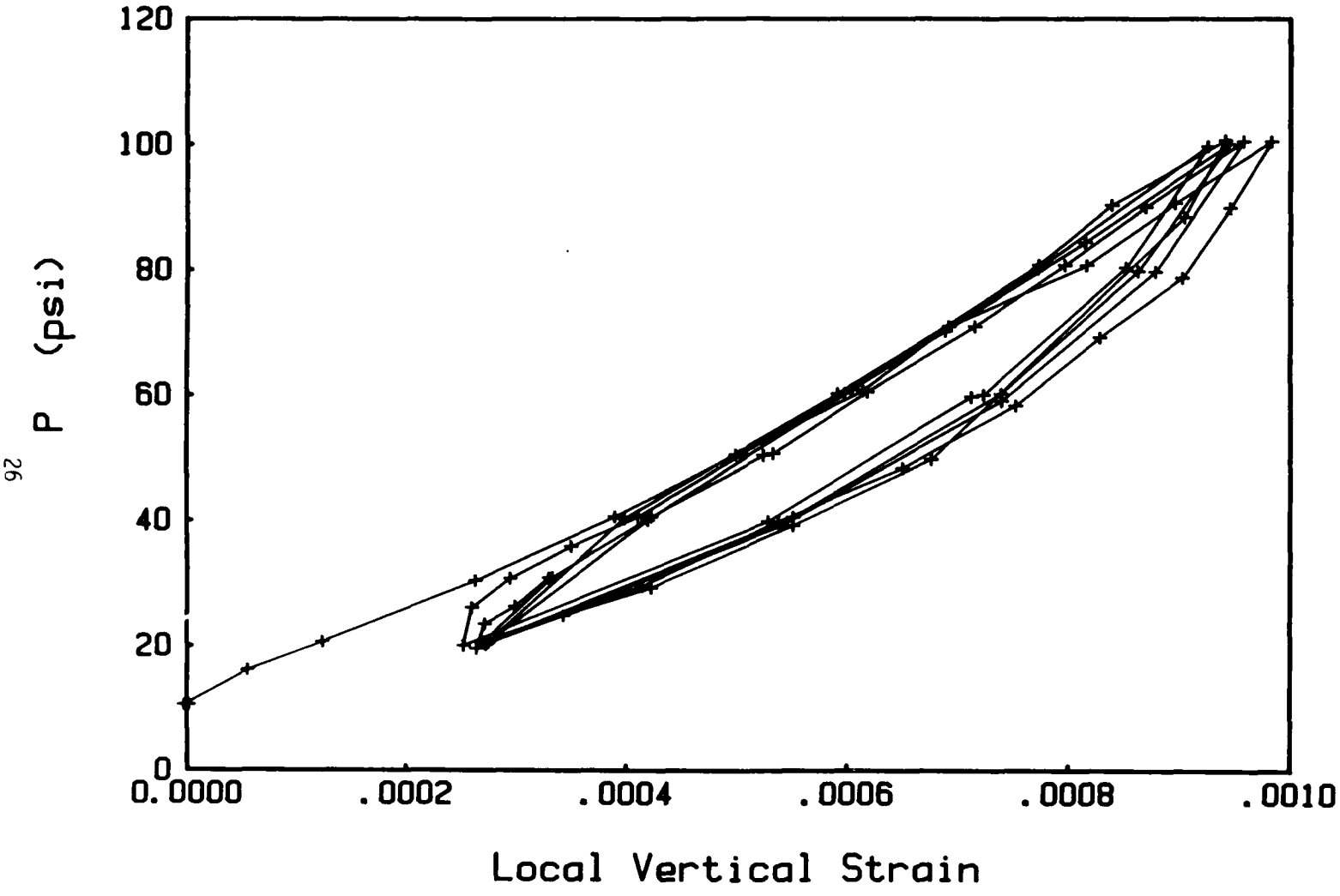

Figure 1.16 Test 3: Hydrostatic Loading, Mean Stress versus Local Verticle Strain

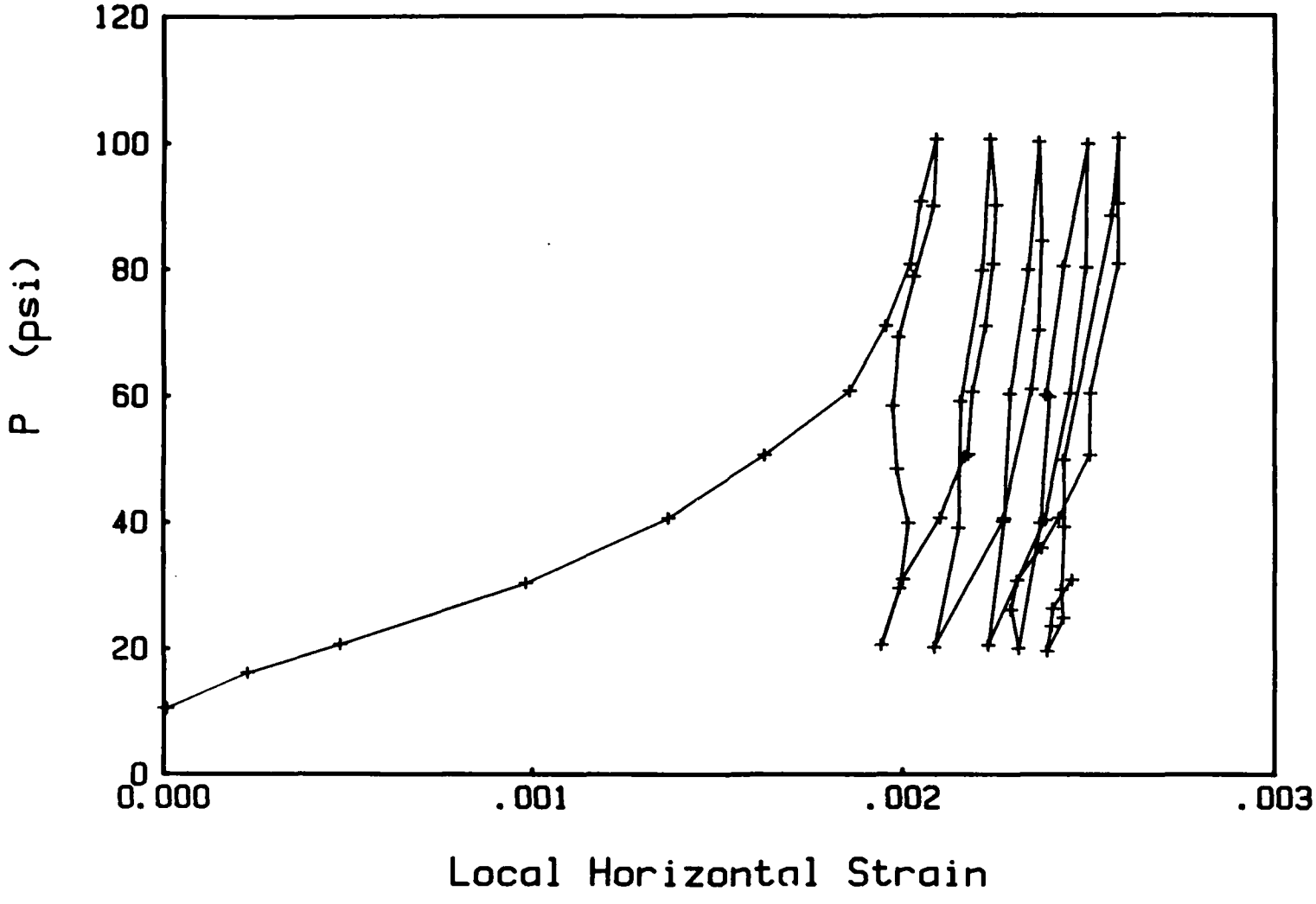

Figure 1.17 Test 3: Hydrostatic Loading, Mean Stress versus Local Horizontal Strain

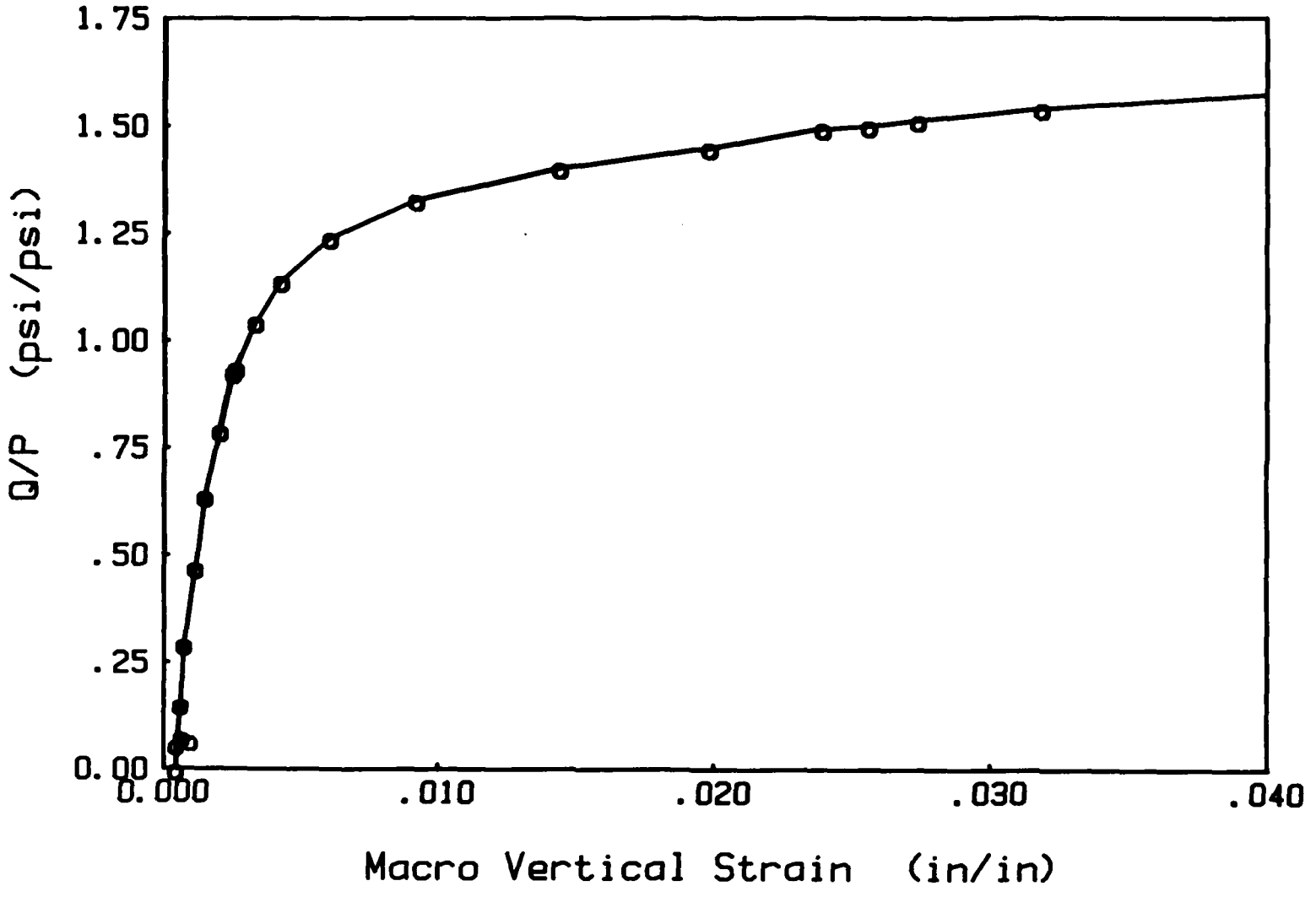

Figure 1.18 Test 2: CTC to Failure After Cyclic Hydrostatic Compression (Macro Reading)

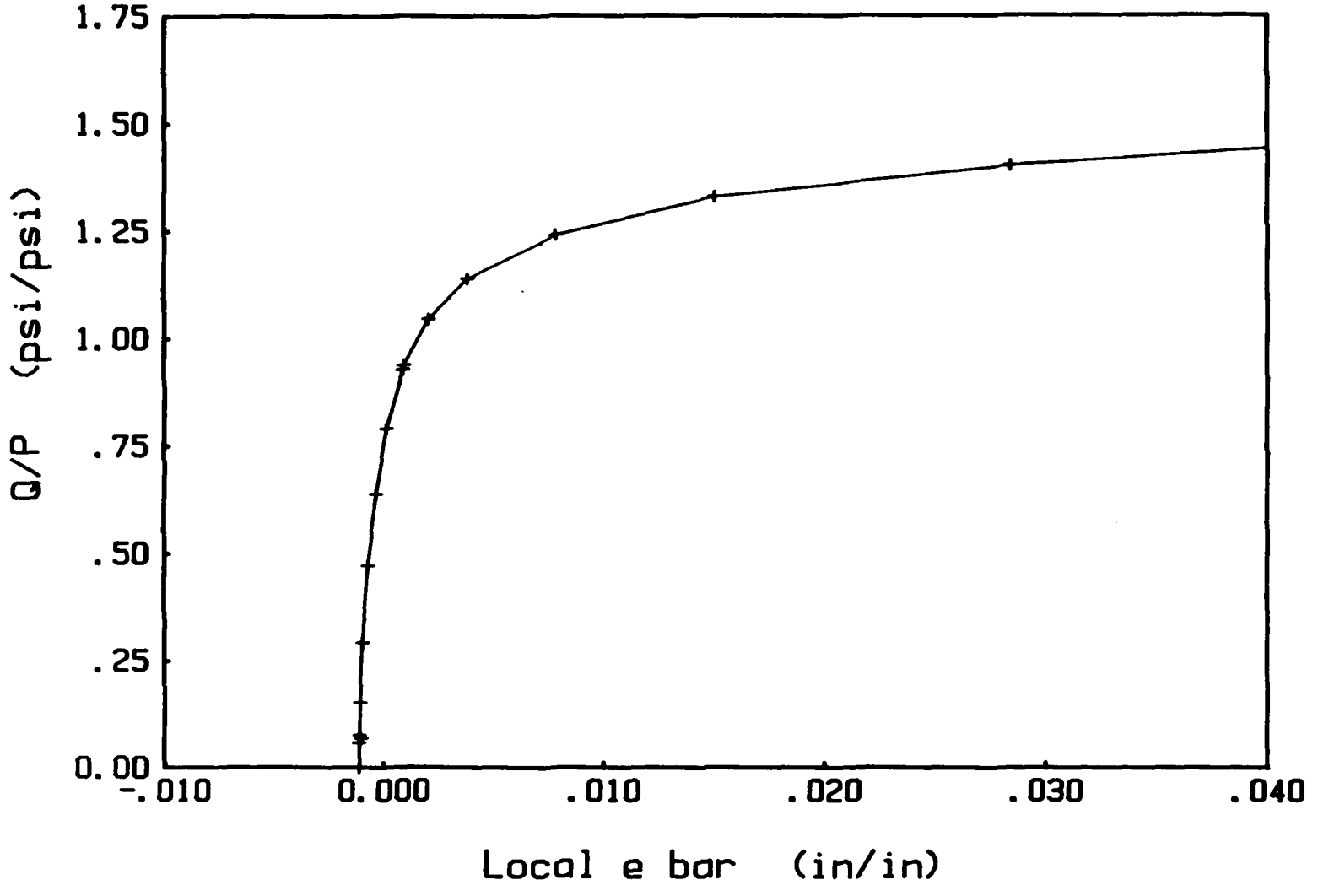

Figure 1.19 Test 2: CTC to Failure After Cyclic Hydrostatic Compression (Local Reading)

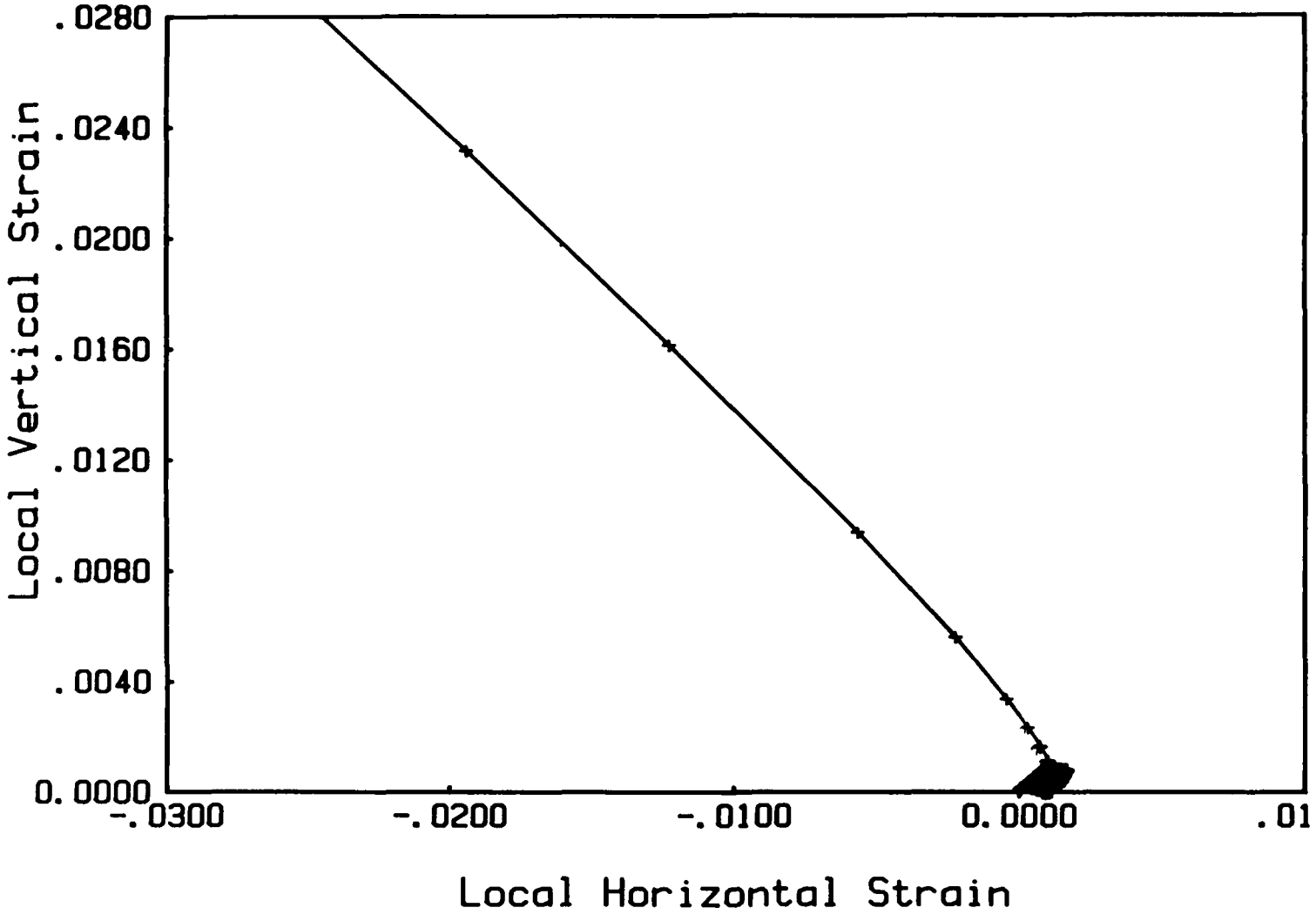

Figure 1.20 Test 2: CTC to Failure After Cyclic Hydrostatic Compression (Local Reading)

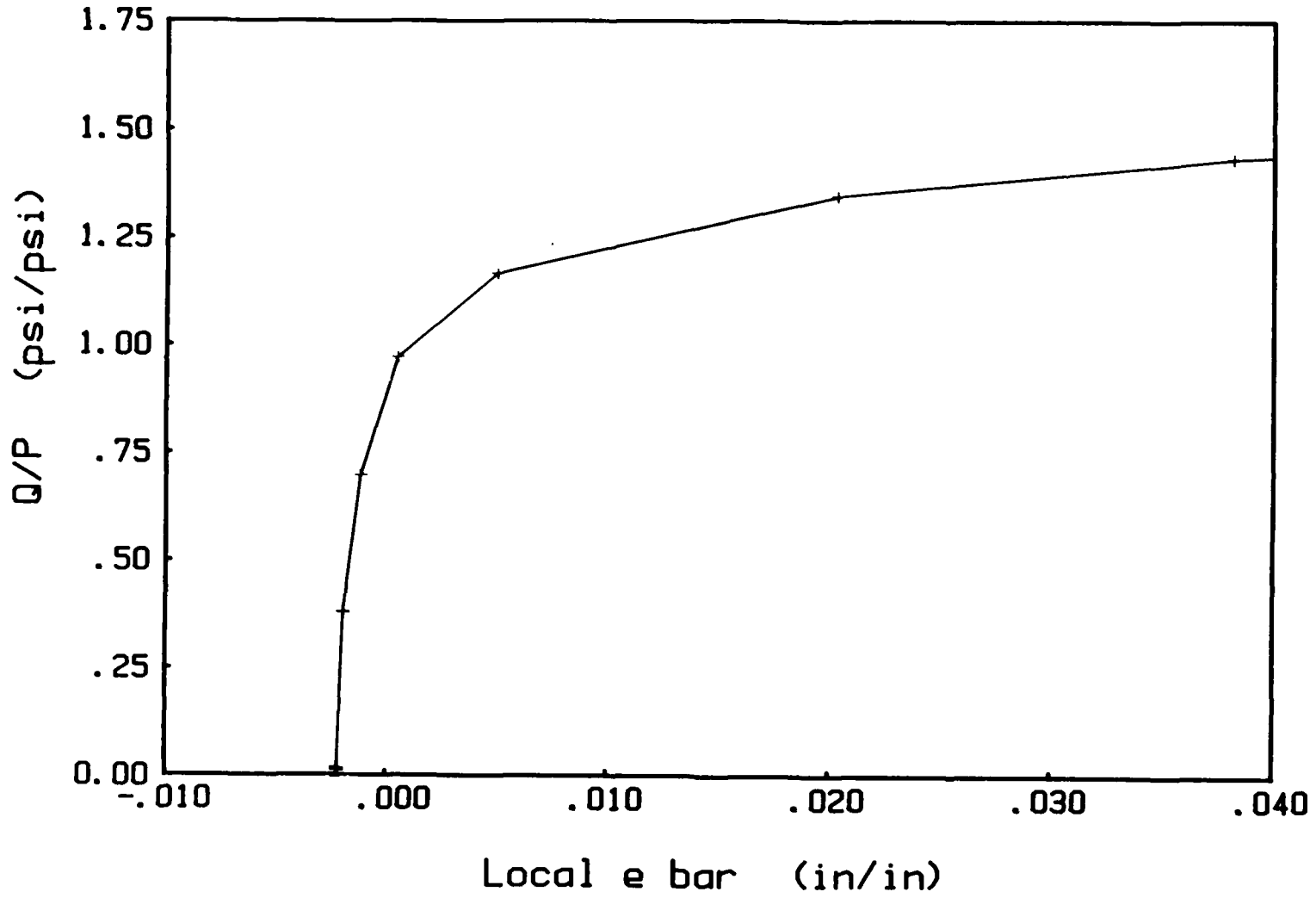

Figure 1.21 Test 3: CTC to Failure After Cyclic Hydrostatic Compression (Local Reading)

anisotropy influence in CTC tests due to prior hydrostatic loading is delayed until virgin CTC loading is presented in the next section.

1.5.2 Conventional Triaxial Compression

Since the first year's effort (Seereeram, McVay, and Linton, 1985) involved conventional monotonic compression tests to characterize strength in both the compression and extension space, the triaxial compression tests reported herein fall within two categories: 1) cyclic CTC at only one constant cell pressure and axial load, and 2) cyclic CTC at several different cell pressures and axial loads. The purpose of such a series of tests were sixfold: investigate specimen end effects (uniform deformation field), stress-induced anisotropy, growth of the yield surface and cyclic hardening (see Chapter 3), generate data to compare to other representations of the moving wheel stress path (Section 1.3.3), and study the influence of stress state on the elastic response.

Presented first are the cyclic CTC tests at a constant cell pressure of 30 psi (206 kPa) and initial void ratio of 0.67. Figures 1.22 - 1.24 and 1.25 - 1.34 are the results of two such tests. The former test employed only the macro measuring system without the micro monitoring system (DCDTs) to investigate the effects, if any of the DCDT brackets. Comparison of Figures 1.22 vs. 1.25 and Figures 1.23 vs. 1.30 reveals that there was only a slight discrepancy of approximately 10% in measured response. This difference is readily attributed to the different initial specimen conditions, i.e. uniformity of specimen, initial void ratios, etc., and not to the DCDT brackets. The influence of specimen end effects were investigated through the micro and macro measurements of Figures 1.27 and 1.28. In comparison of the axial strains for a particular principal stress difference, $Q\ (\sigma_v - \sigma_H)$, one sees that there is approximately a 10% difference in strain values which is

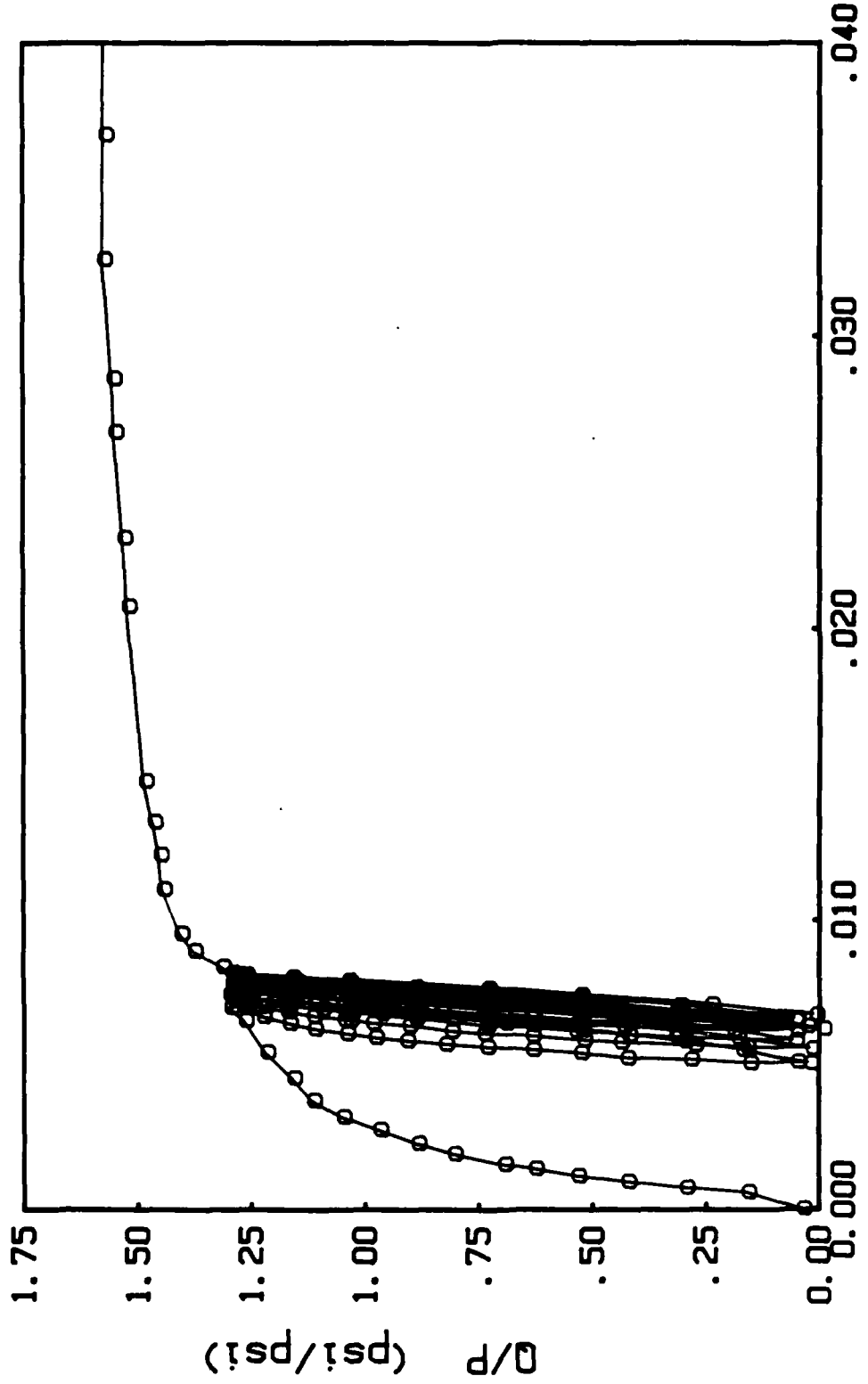

Figure 1.22 Test 4: Cyclic CTC and Subsequent Failure (Macro Reading)

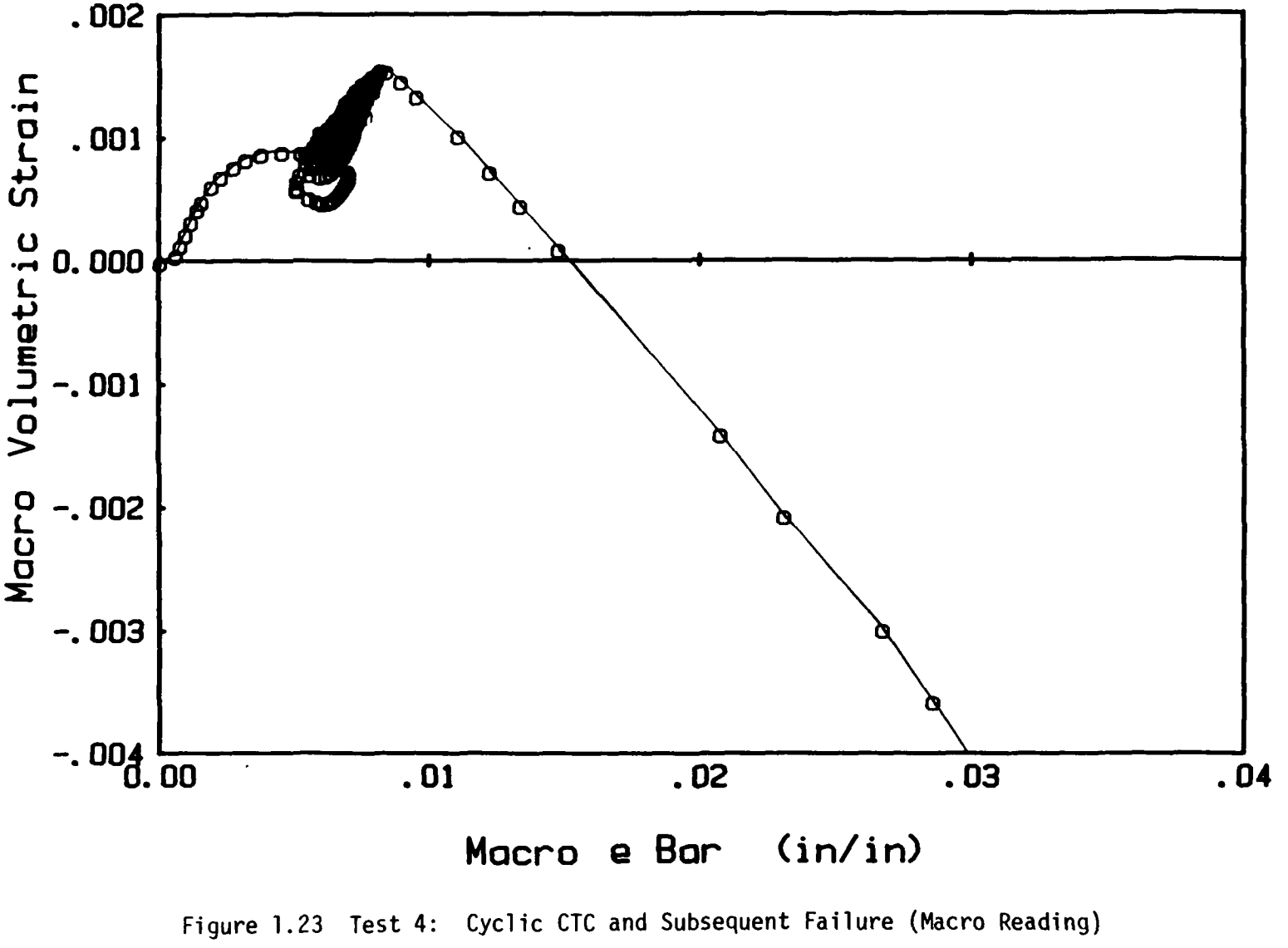

Figure 1.23 Test 4: Cyclic CTC and Subsequent Failure (Macro Reading)

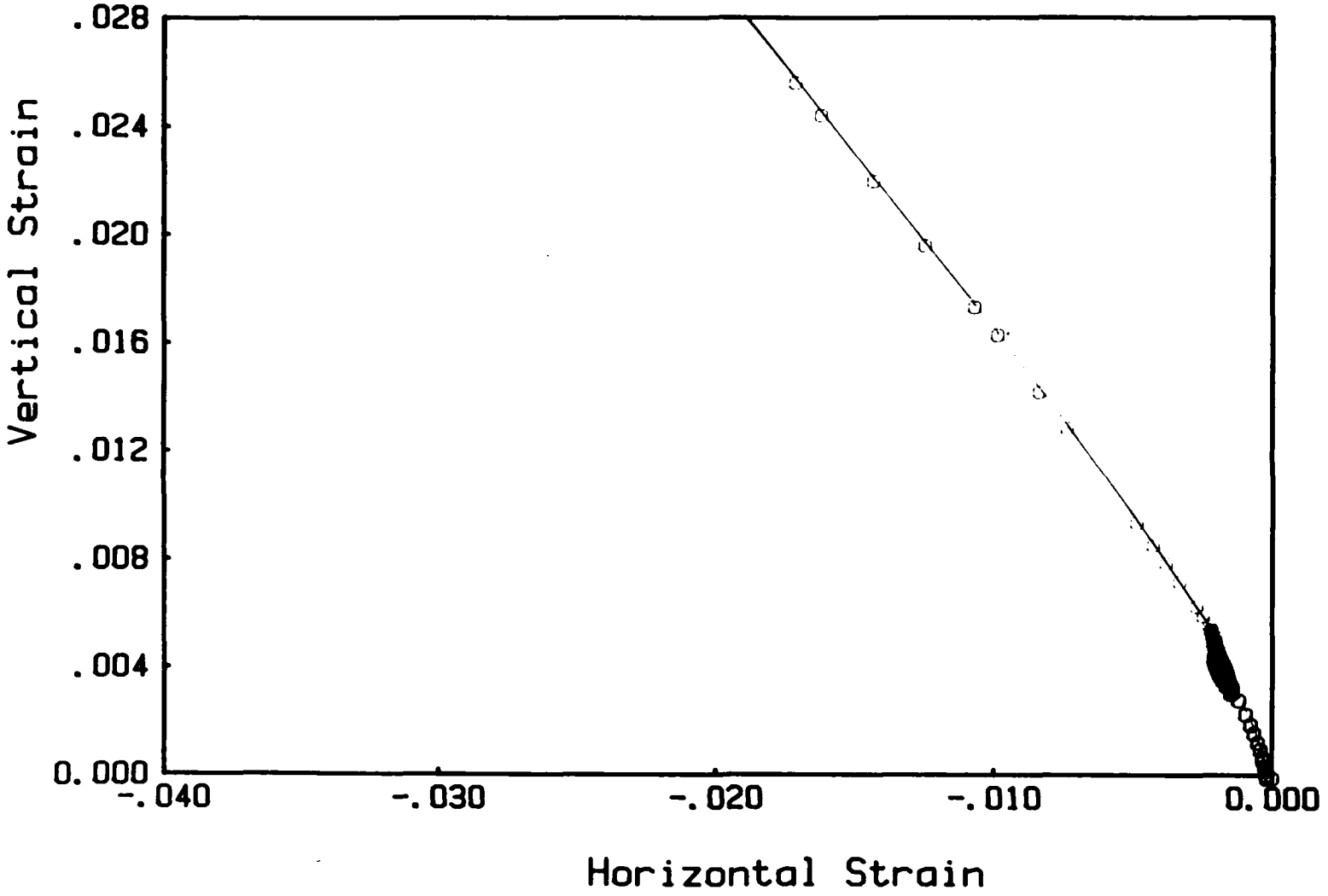

Figure 1.24 Test 4: Cyclic CTC and Subsequent Failure - Horizontal vs. Verticle Strain

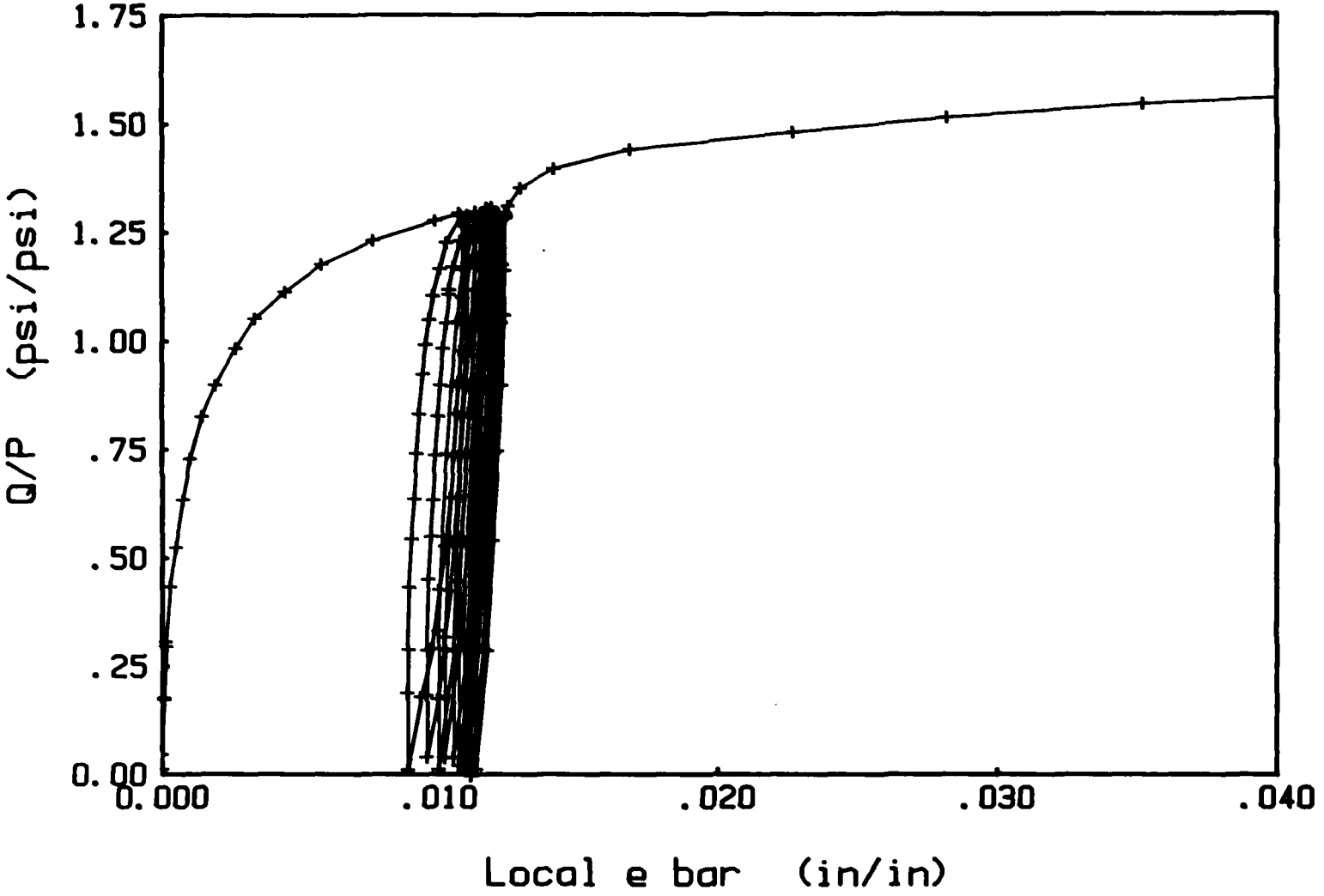

Figure 1.25 Test 5: Cyclic CTC and Subsequent Failure (Local Reading)

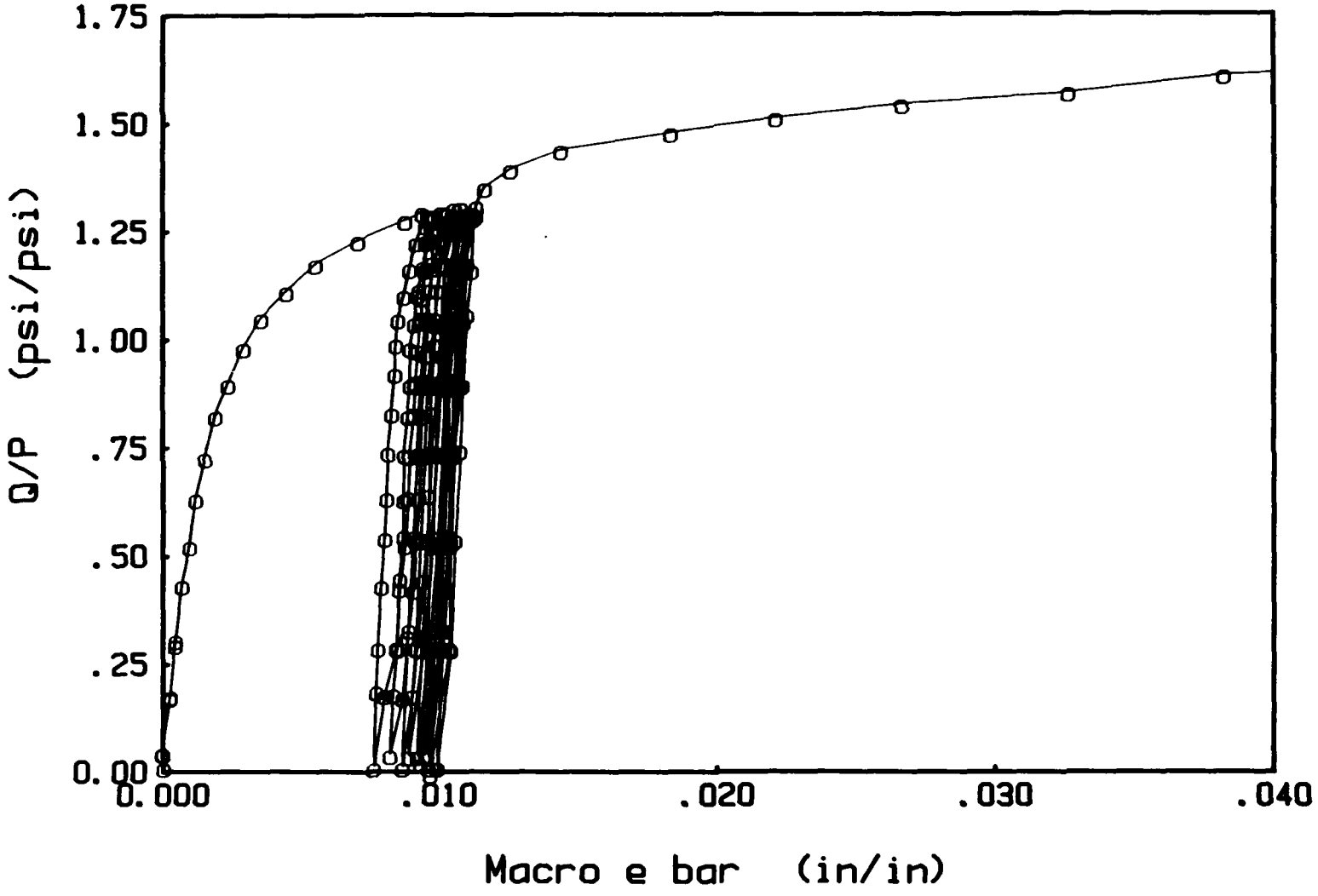

Figure 1.26 Test 5: Cyclic CTC and Subsequent Failure (Macro Reading)

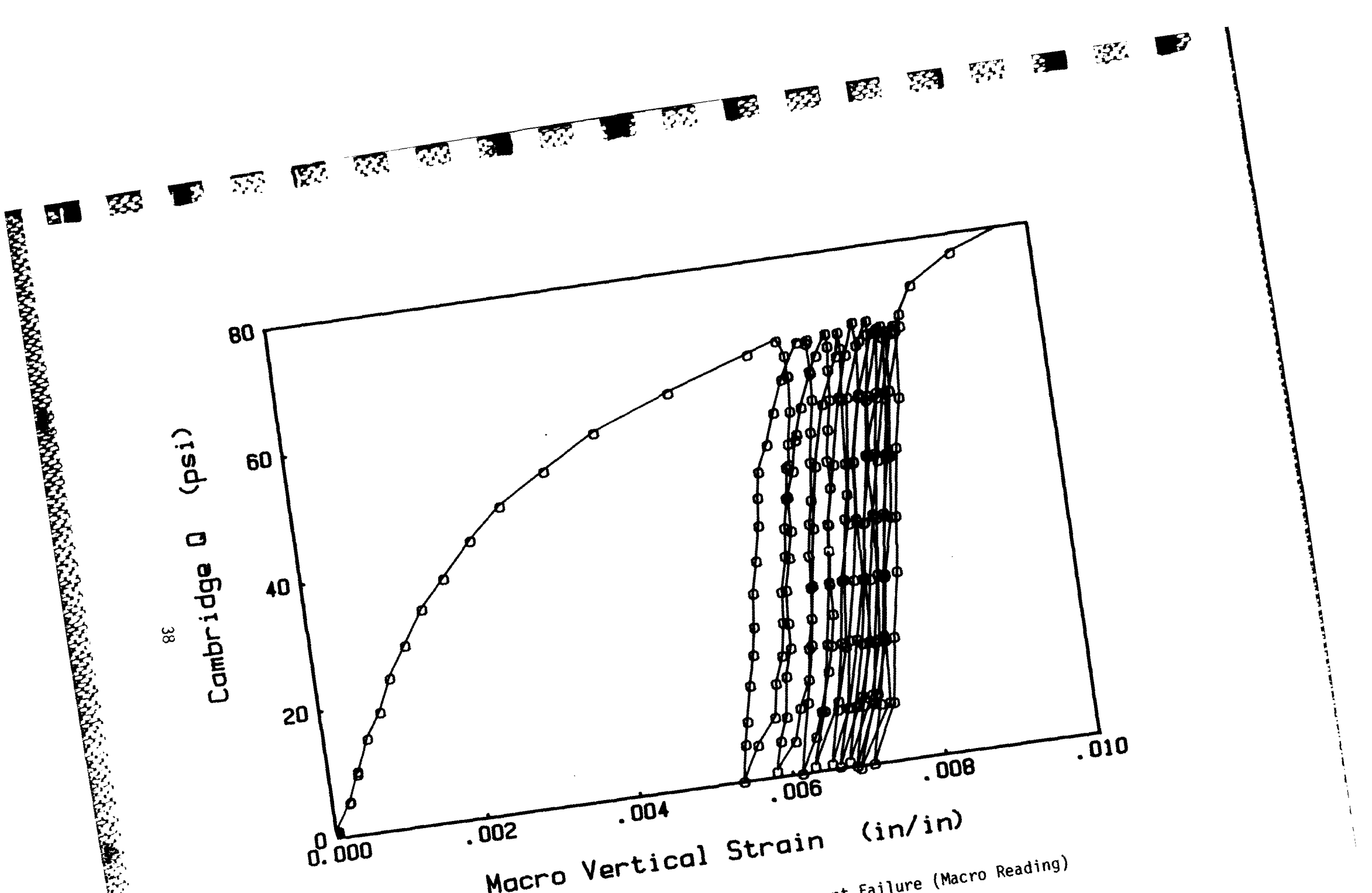

Figure 1.27 Test 5: Cyclic CTC and Subsequent Failure (Macro Reading)

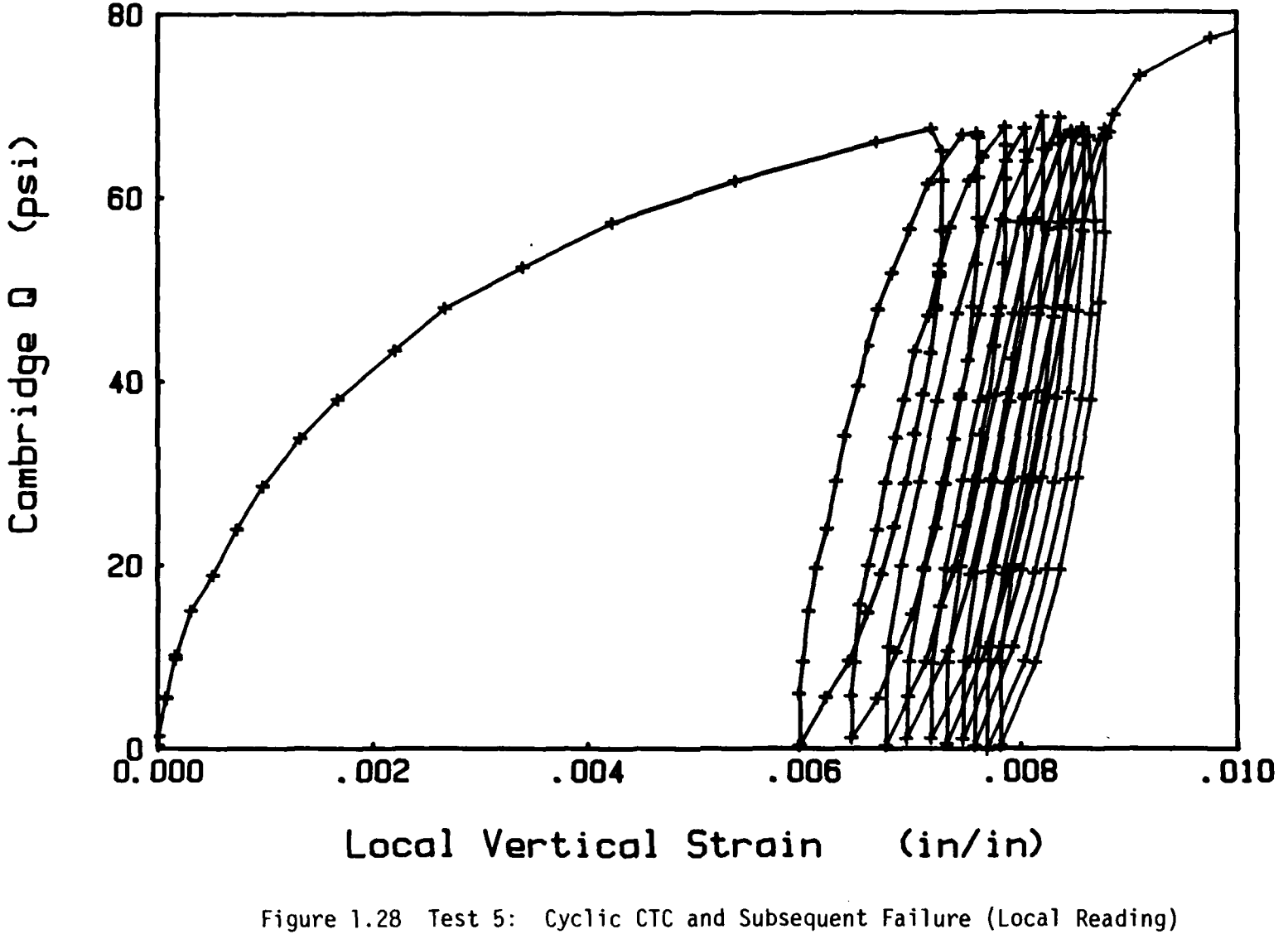

Figure 1.28 Test 5: Cyclic CTC and Subsequent Failure (Local Reading)

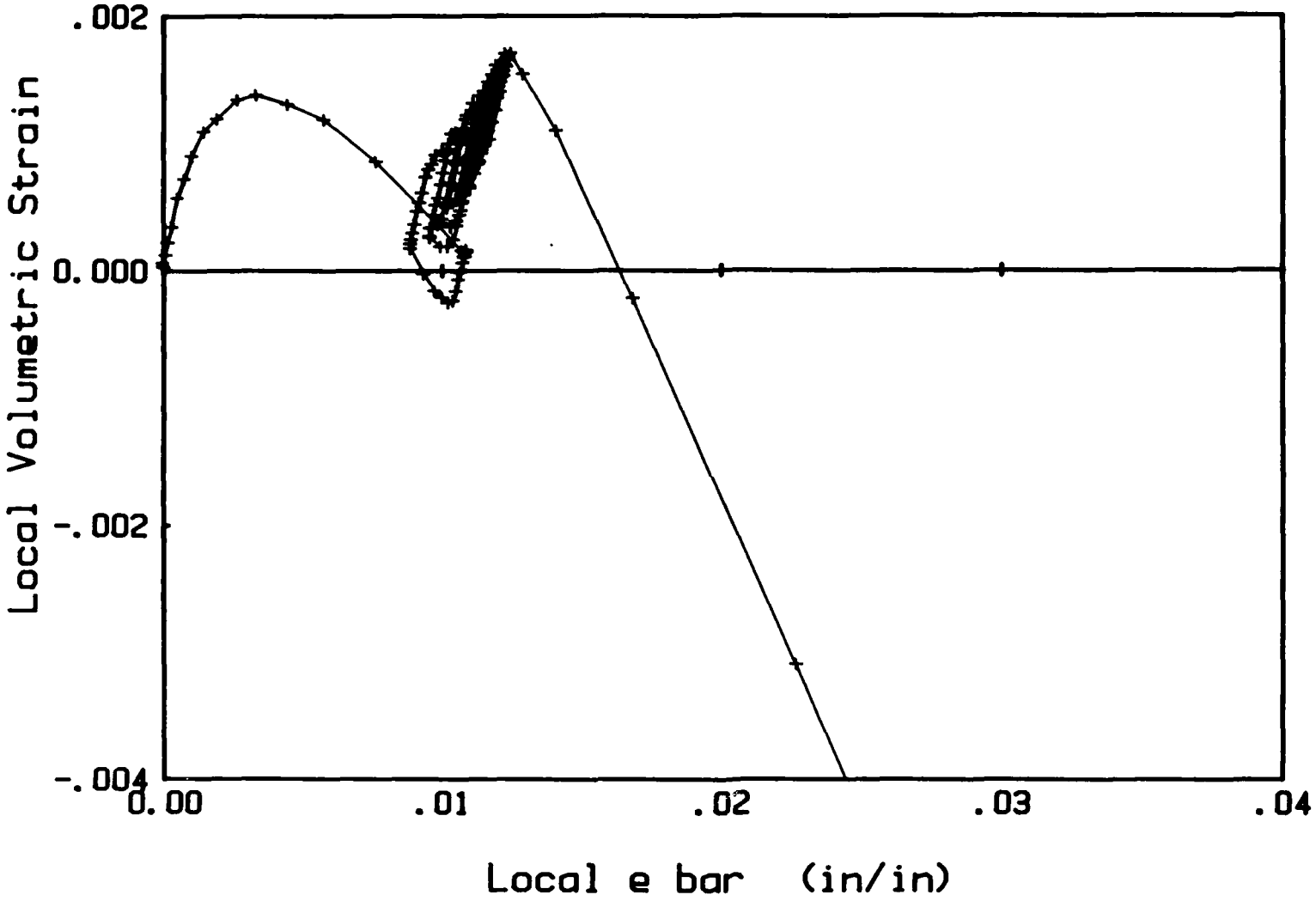

Figure 1.29 Test 5: Cyclic CTC and Subsequent Failure (Local Reading)

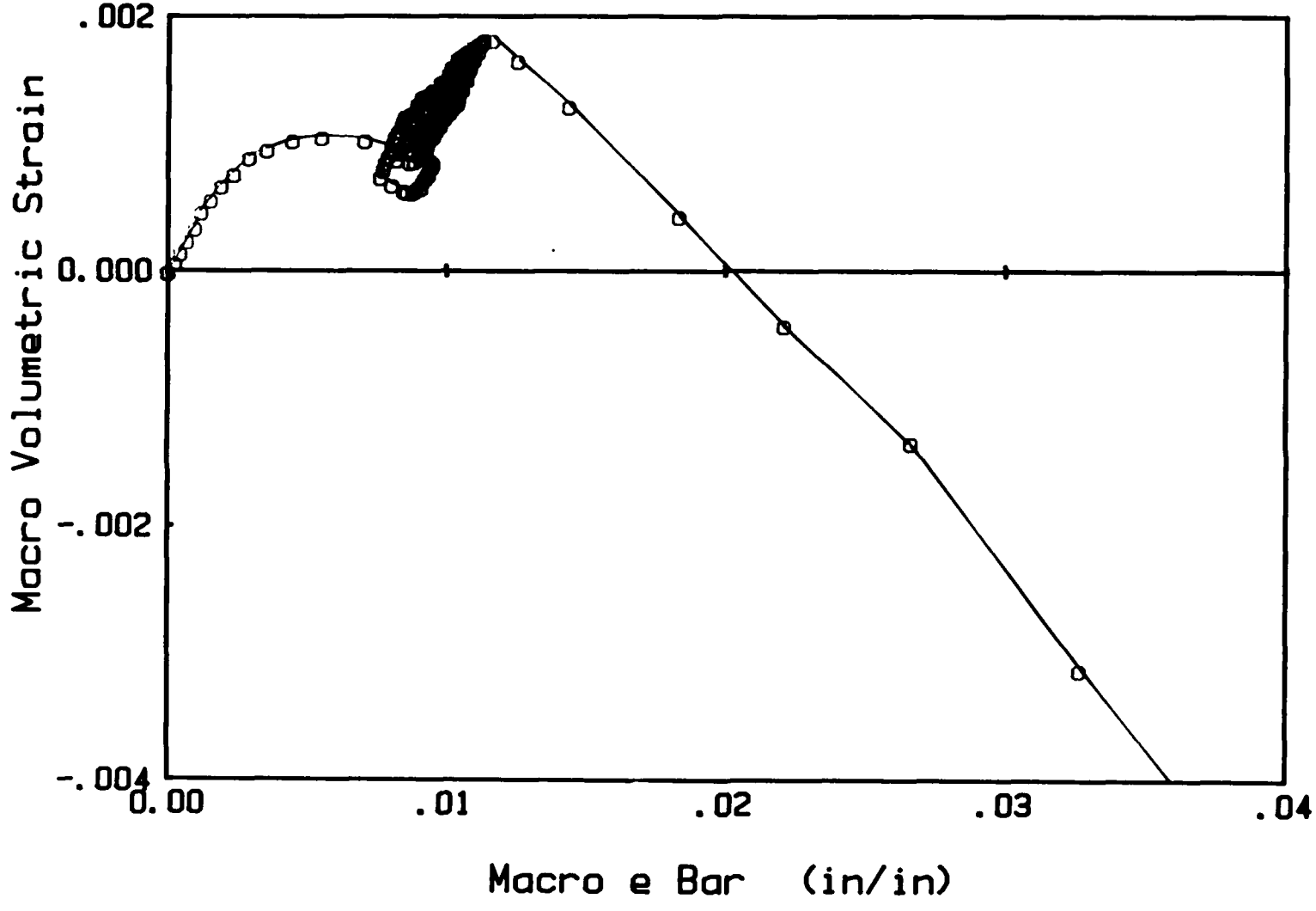

Figure 1.30 Test 5: Cyclic CTC and Subsequent Failure (Macro Reading)

reasonable considering the earlier reported reproducibility results. If one were to compare the local and macro volumetric strains versus deviatoric strains, $\bar{\varepsilon}$ $(\varepsilon_v - \varepsilon_H)$, one would readily see that the macro response both lags the micro response as well as averages out the peaks. Since membrane penetration isn't a possible issue (constant cell pressure), this latter difference can only be attributed to frictional effects (between end caps and the soil), and or nonuniform soil specimens. Given the earlier reported specimen difference (i.e. nonuniformities), the latter variations were attributed to end effects; evident in the lateral horizontal strain restrictions of the end caps shown in the correlation of Figures 1.31 and 1.32. Scrutiny of the figures reveals the mid points of the specimen are expanding outward at a faster rate than the extremities, i.e. end cap effects. However, the difference is only 15% between the two measuring systems, suggesting that the deformation fields are only slightly nonuniform and are quite acceptable for the model development undertaken in Chapter 3. These latter dispartities could be improved upon, if one were to use enlargened caps with a greased membrane separating the soil from the platens.

The study of stress induced anisotropy from prior loading initiated with a comparison of Figures 1.19 (cyclic HC followed by CTC) with 1.25 (virgin CTC). Scrutiny of the figures reveal that the agreement prior to cyclic loading in Figure 1.25 is quite close. The latter correlation is surprising, considering the stress-induced anisotropy effects which were noted during the hydrostatic portion of the loading, Figure 1.13. Not as surprising is the variation in strength as a consequence of cyclic loading as given in Figures 1.19 versus 1.25. Similar behavior is noted in the macro measurements recorded in Figure 1.26. This increase in strength is a consequence of a decrease in void ratio resulting from volumetric compression, Figures 1.23 and

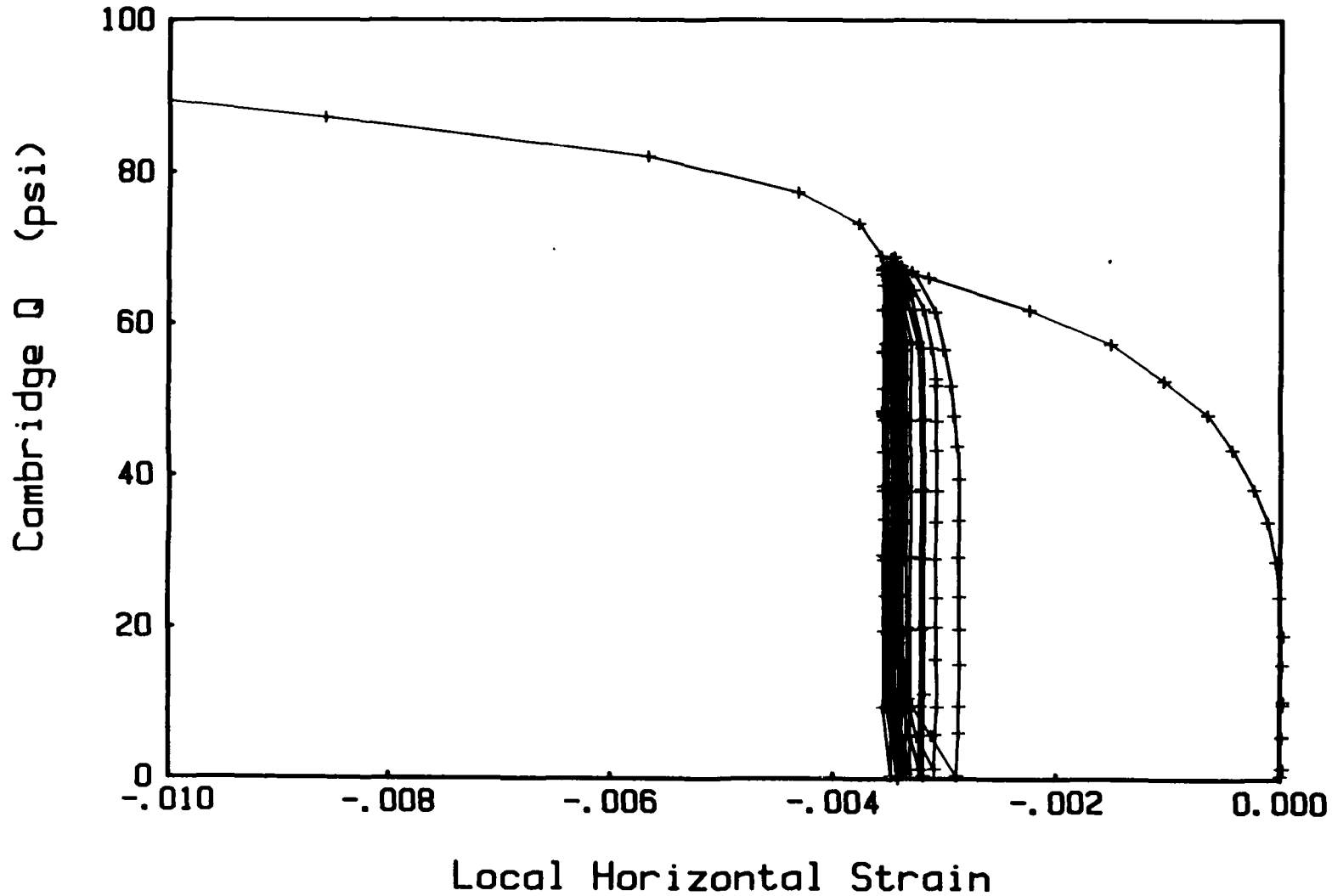

Figure 1.31 Test 5: Cyclic CTC and Subsequent Failure (Local Reading)

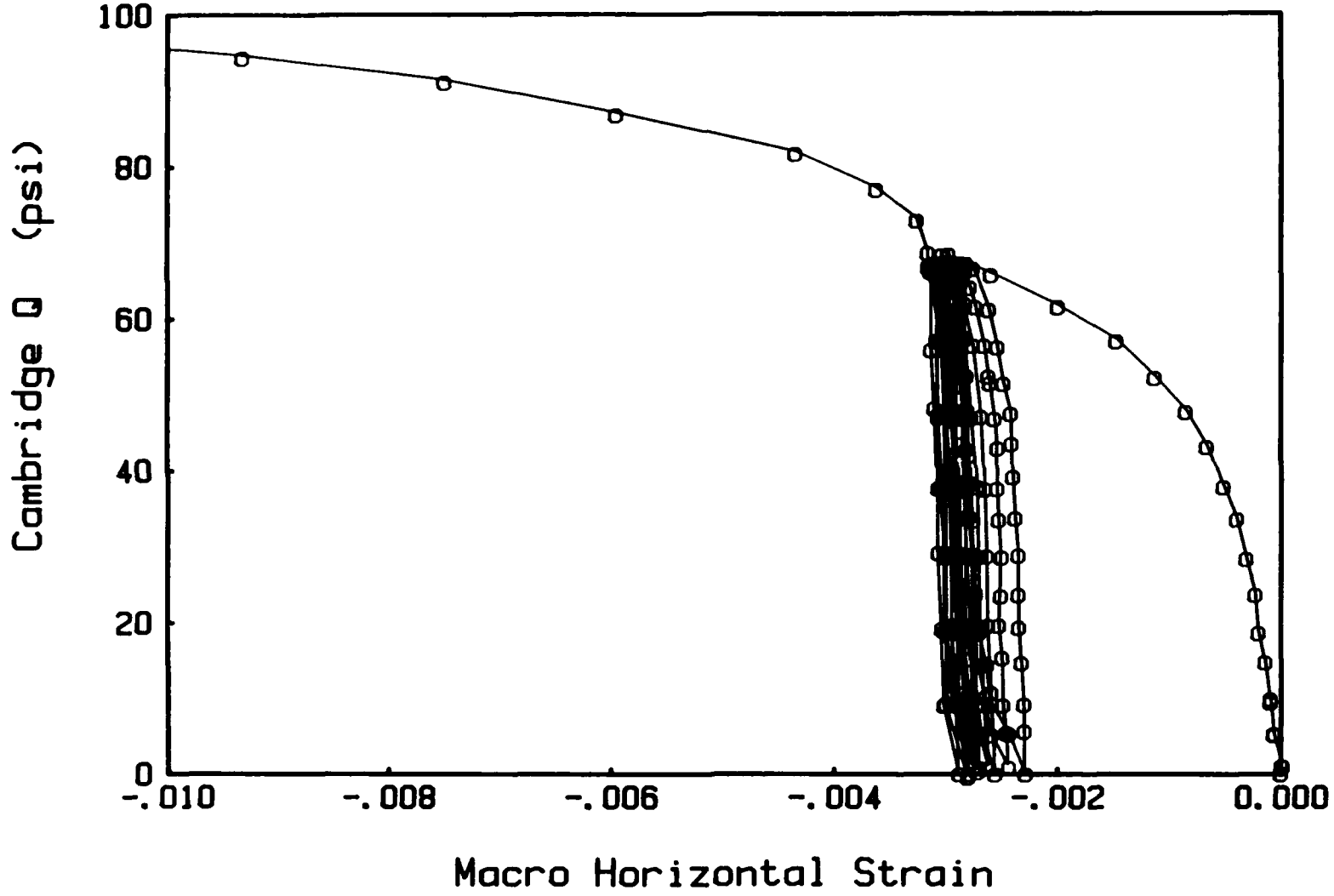

Figure 1.32 Test 5: Cyclic CTC and Subsequent Failure (Macro Reading)

1.29. As was found for the cyclic HC tests (Figure 1.13) significant anisotropy in strains were noted for the cyclic portion of the CTC, Figures 1.33 and 1.34. Also from the figures, one sees a significant buildup of axial strains with minimal change in horizontal strains (opposite of cyclic HC, Figure 1.13). As a result, the plastic deviatoric strain (see Chapter 3) rate tensor, $\dot{\bar{e}}^{p}\left(\frac{\dot{\varepsilon}^{p}_{v}}{} - \frac{\dot{\varepsilon}^{p}_{H}}{}\right)$, is rotating and becoming more vertically inclined in principal stress space than its virgin counterpart. The latter's influence on other stress path loadings is presently unknown.

The second phase of the laboratory tests reported herein is the study of the evolution of both the plastic and elastic modulus (see Chapter 3) with initial mean stress. Figures 1.35 - 1.36, 1.37, and 1.38 - 1.43 depict the stress-strain characteristics of Reid Bedford which was cyclically loaded to four different levels of deviatoric stress, $Q\ (\sigma_v - \sigma_H)$, at initial cell pressures of 5 psi (34 kPa), 10 psi (69 kPa), 20 psi (138 kPa), 30 psi (207 kPa), and 40 spi (276 kPa). Figures 1.35 and 1.36 which present deviatoric stress, Q, versus axial and deviatoric, $\tilde{\varepsilon}\ (\varepsilon_v - \varepsilon_H)$, strains were performed on a specimen without any micro measuring system, DCDTs, attached to the sample. The results in Figure 1.37 are from a repeat examination of the prior loading history with the exception of the deletion of the last initial mean state. Scrutiny of Figures 1.35 and 1.37 reveals the reproducibility of the testing technique to be quite good. However, study of the individual data points discloses a fluctuating response, especially in the cyclic regions. The latter response makes it extremely difficult to obtain material parameters. For instance the elastic shear modulus, G, is usually obtained from at CTC test, and in particular the unloading phase of cyclic phase as shown in Figure 1.36. Consequently, another test, Figures 1.38 - 1.43, was performed which employed both the DCDT monitoring system and the standard

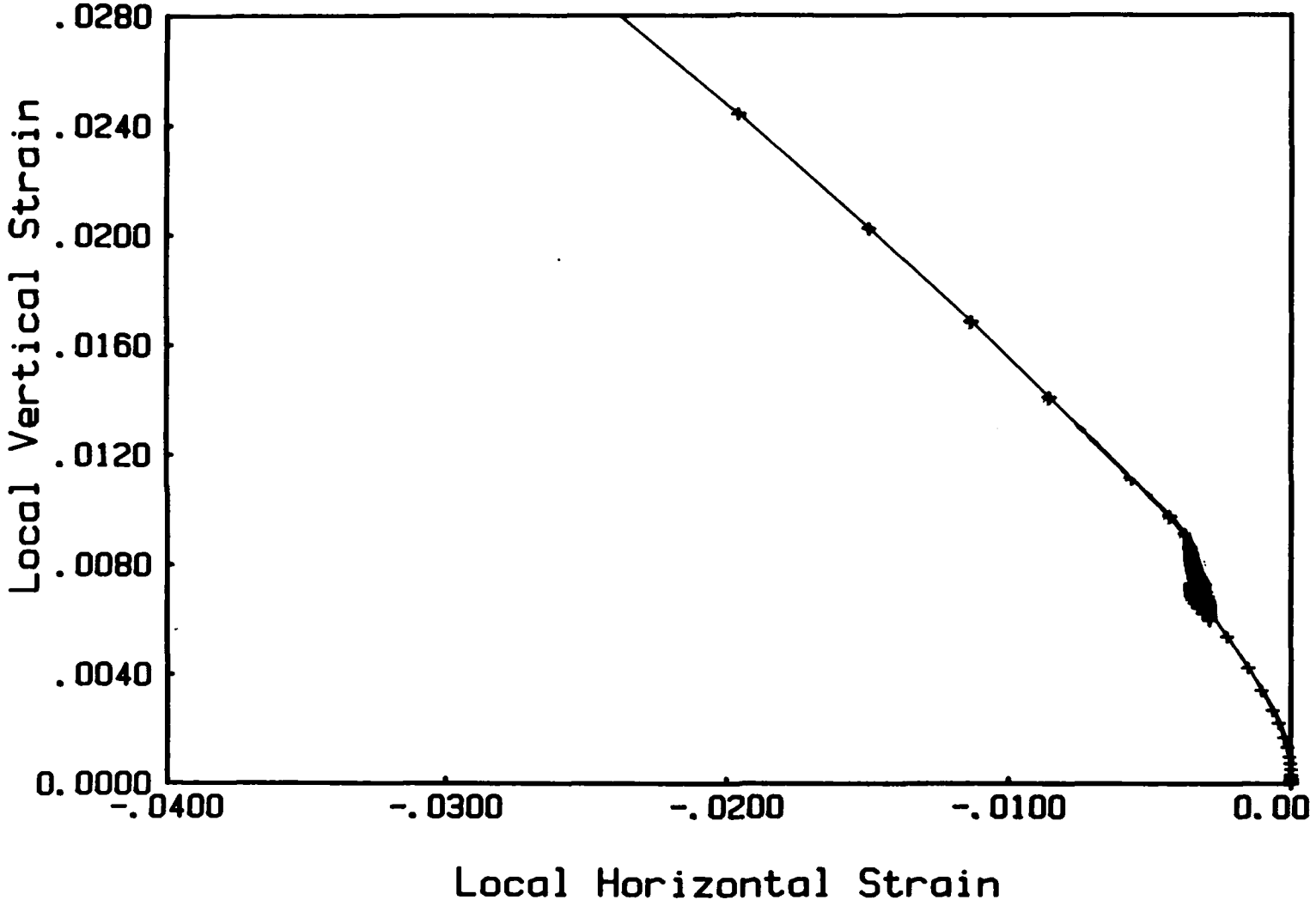

Figure 1.33 Test 5: Cyclic CTC and Subsequent Failure (Local Reading)

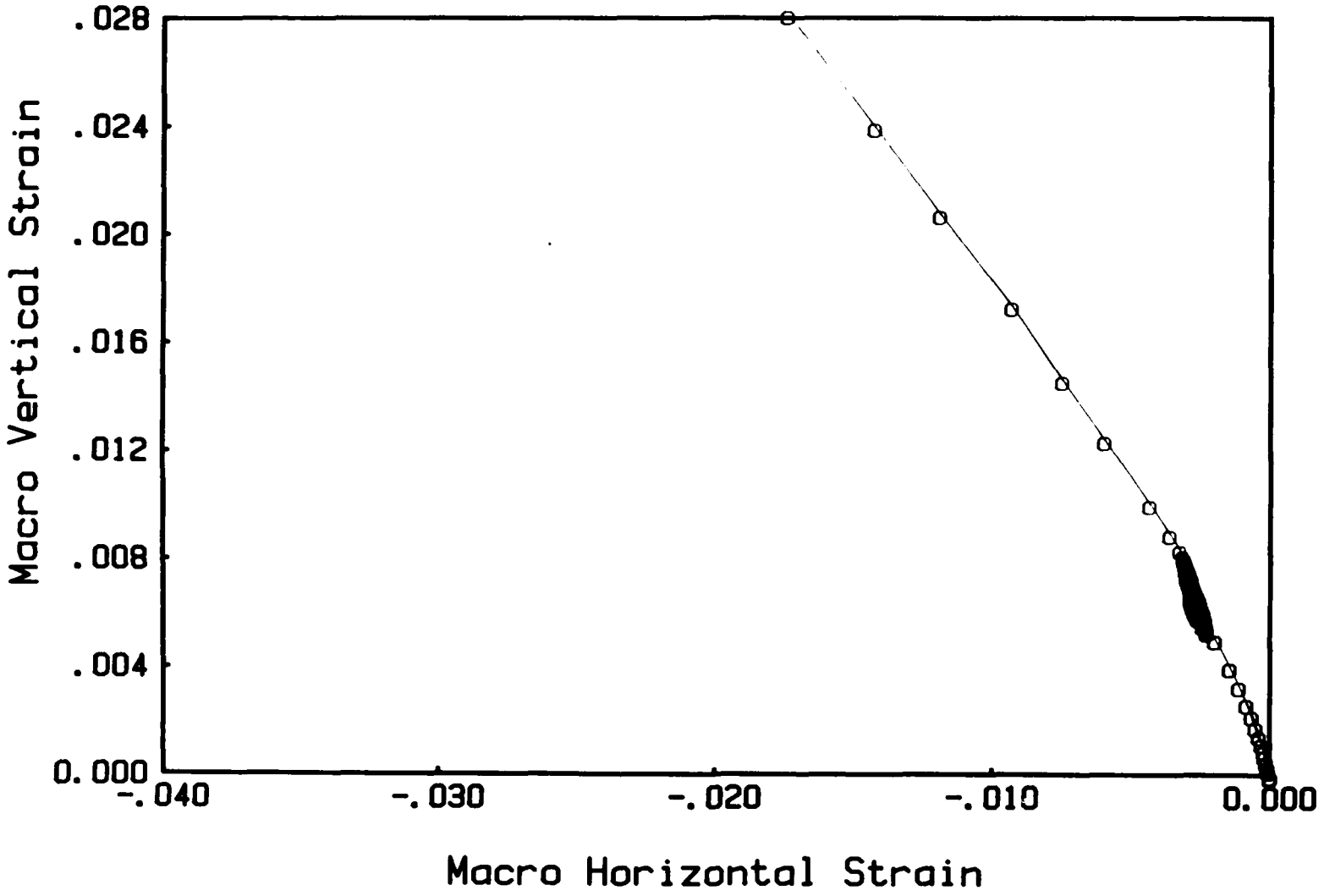

Figure 1.34 Test 5: Cyclic CTC and Subsequent Failure (Macro Reading)

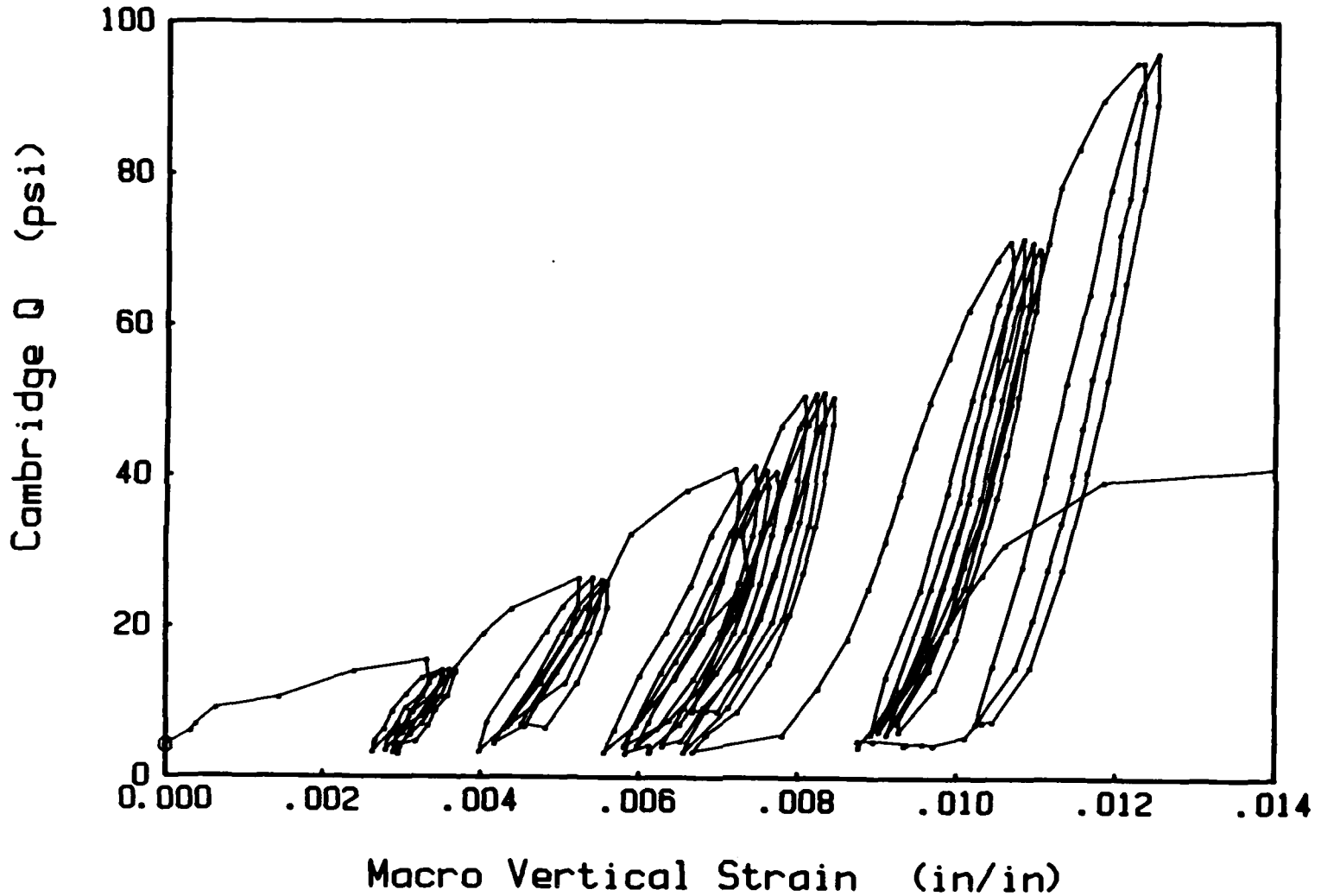

Figure 1.35 Test 6: Cyclic CTC at Different Initial Cell Pressures (Macro Reading)

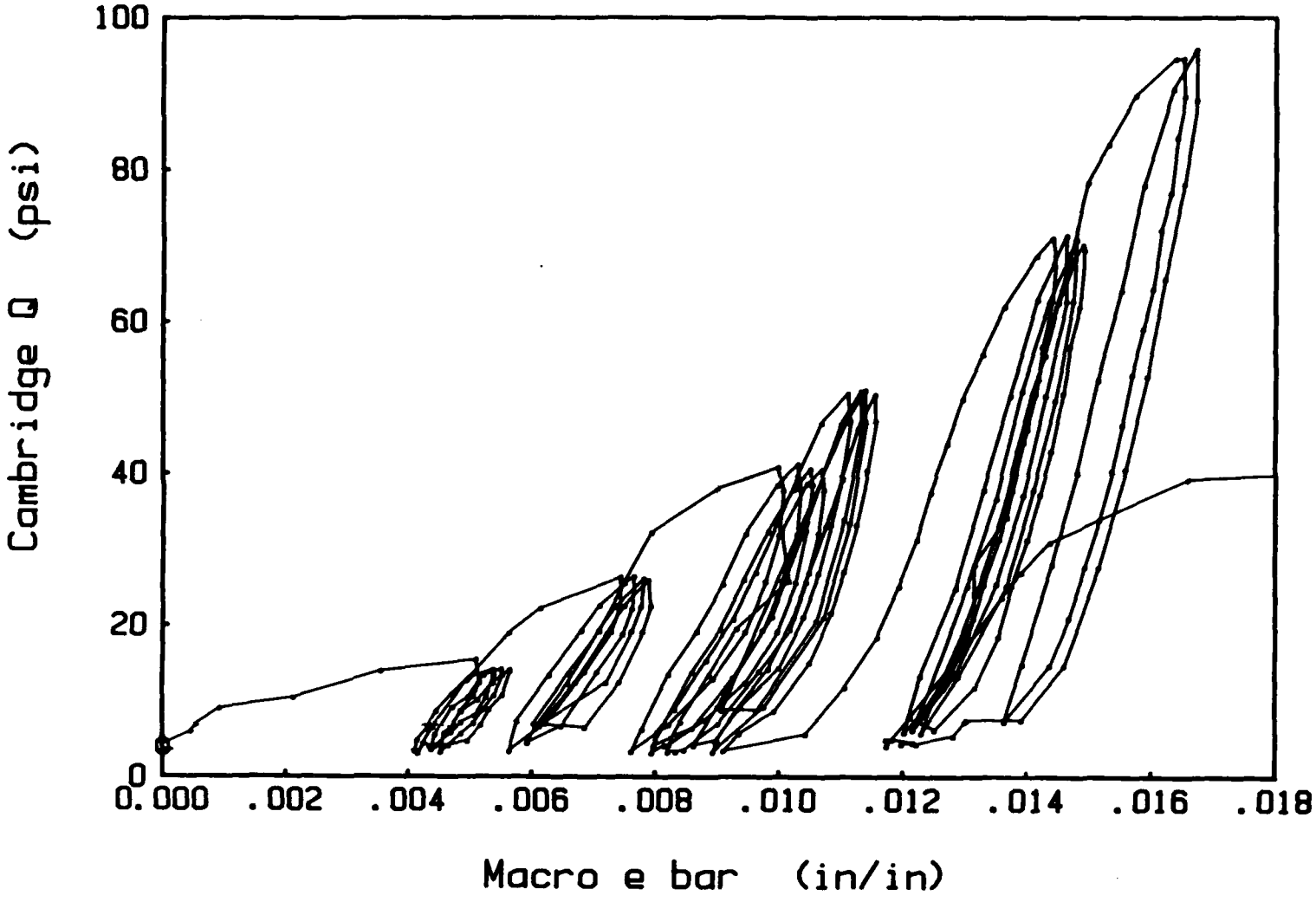

Figure 1.36 Test 6: Cyclic CTC at Different Initial Cell Pressures (Macro Reading)

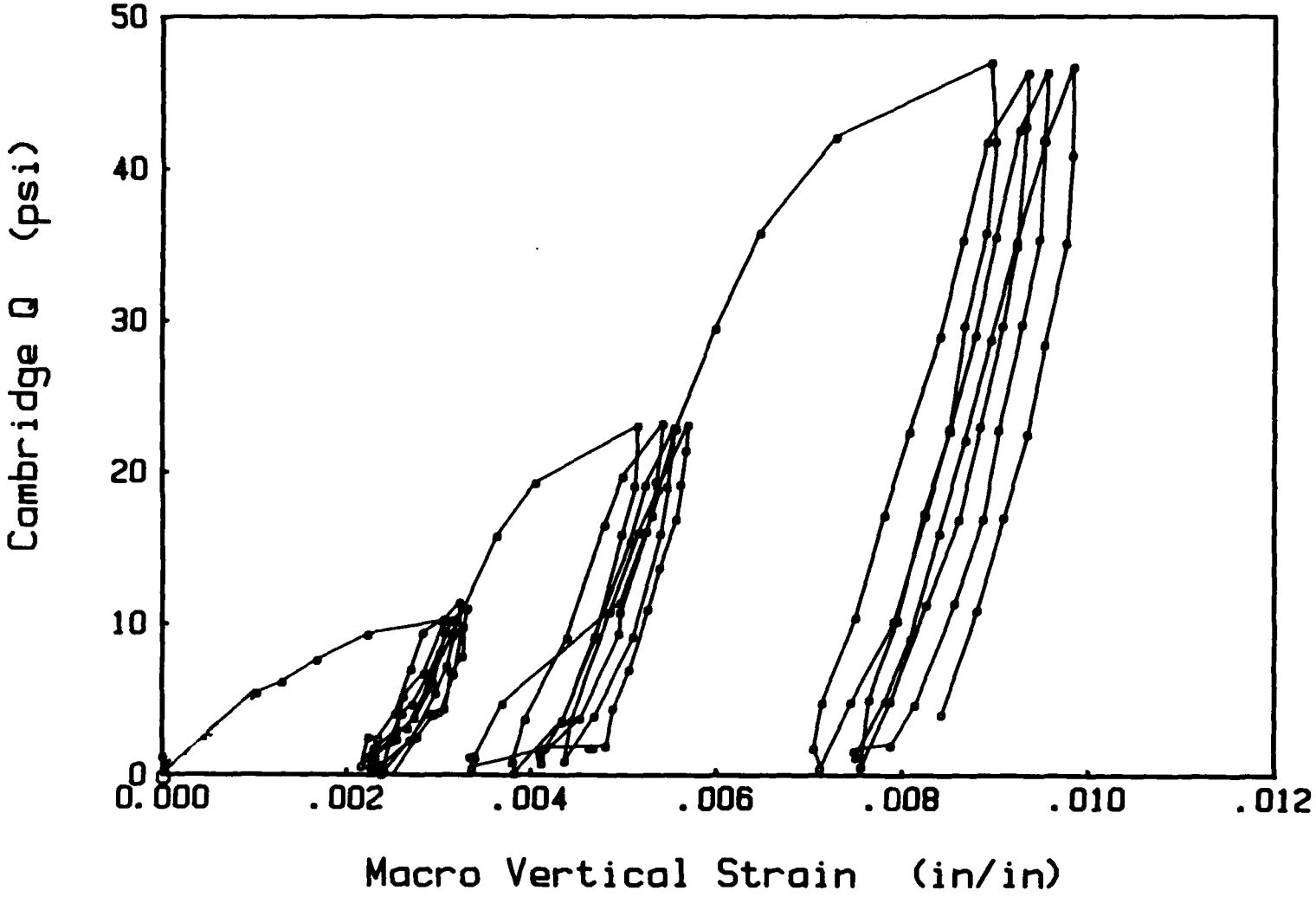

Figure 1.37 Test 7: Cyclic CTC at Different Initial Cell Pressures (Macro Reading)

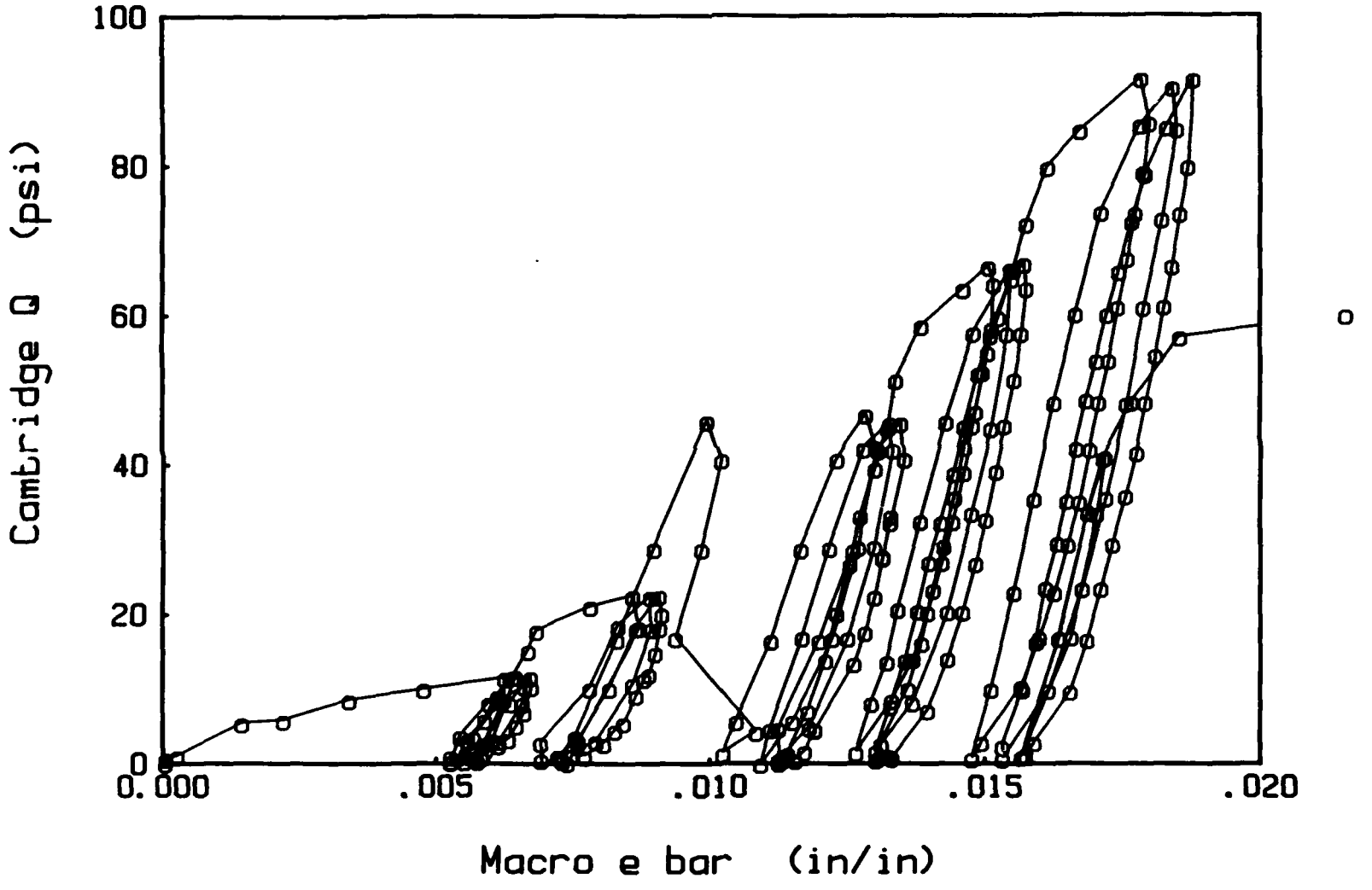

Figure 1.38 Test 8: Cyclic CTC at Different Initial Cell Pressures (Macro Reading)

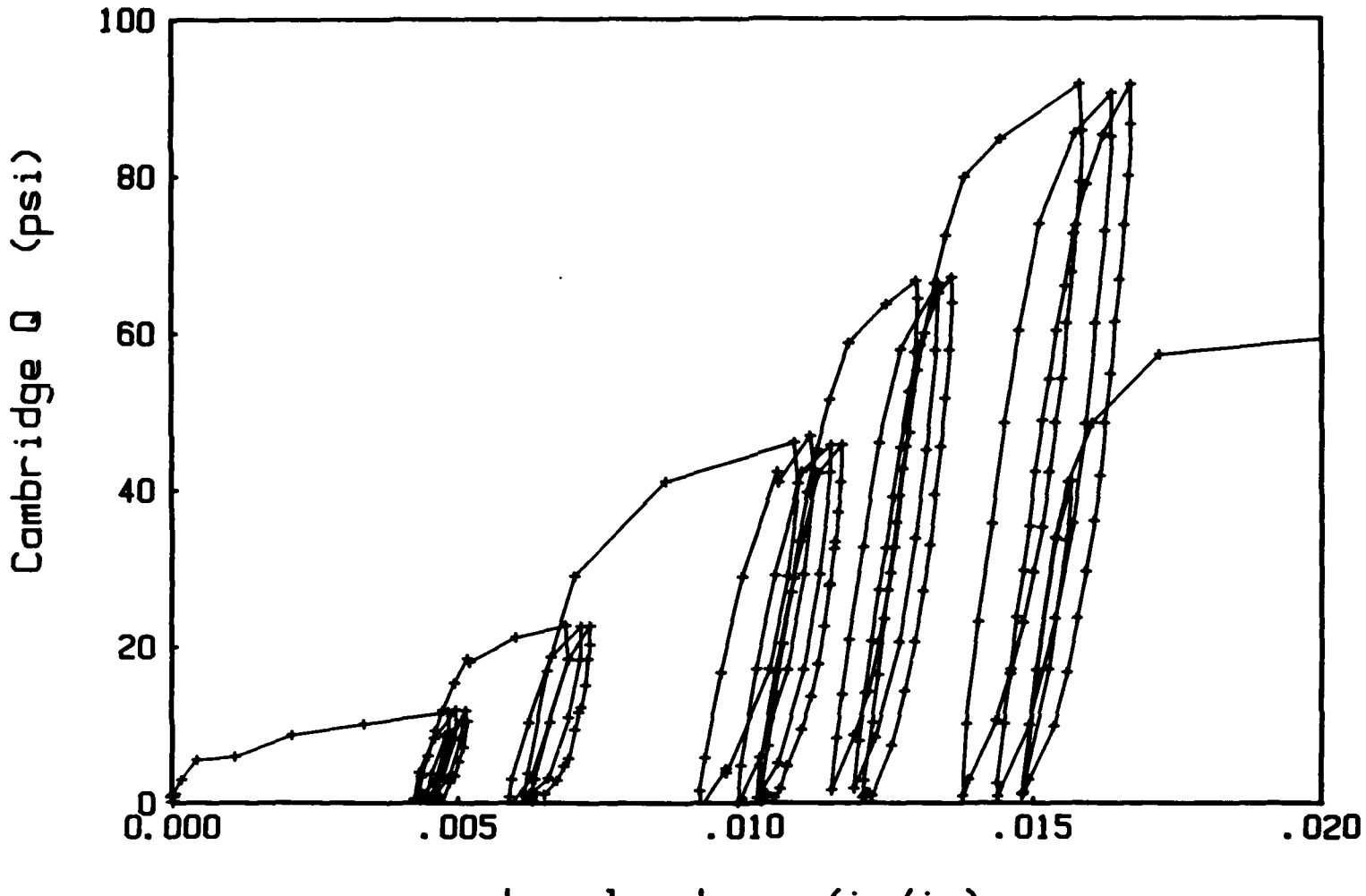

Figure 1.39 Test 8: Cyclic CTC at Different Initial Cell Pressures (Local Reading)

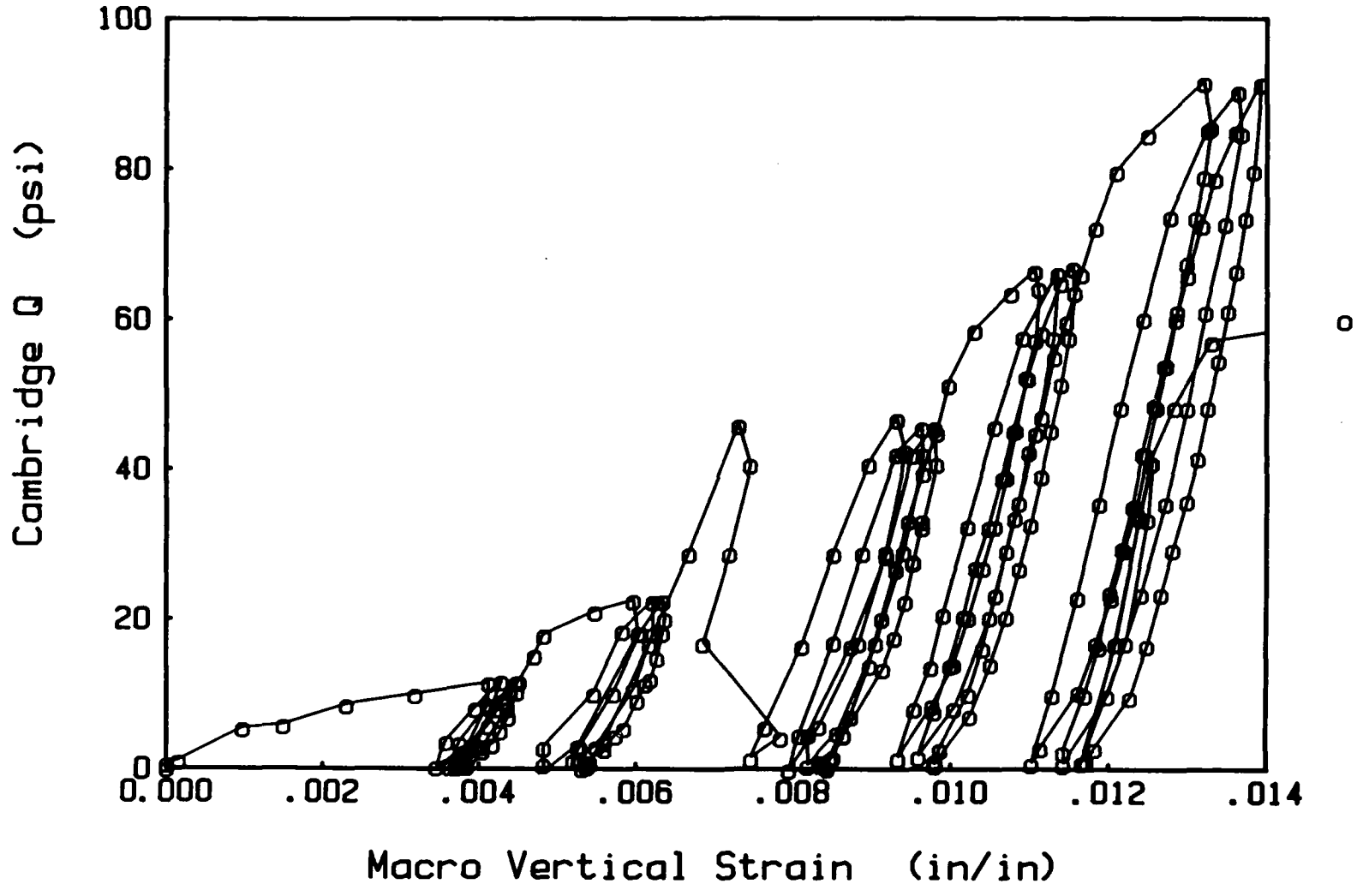

Figure 1.40 Test 8: Cyclic CTC at Different Initial Cell Pressures (Macro Reading)

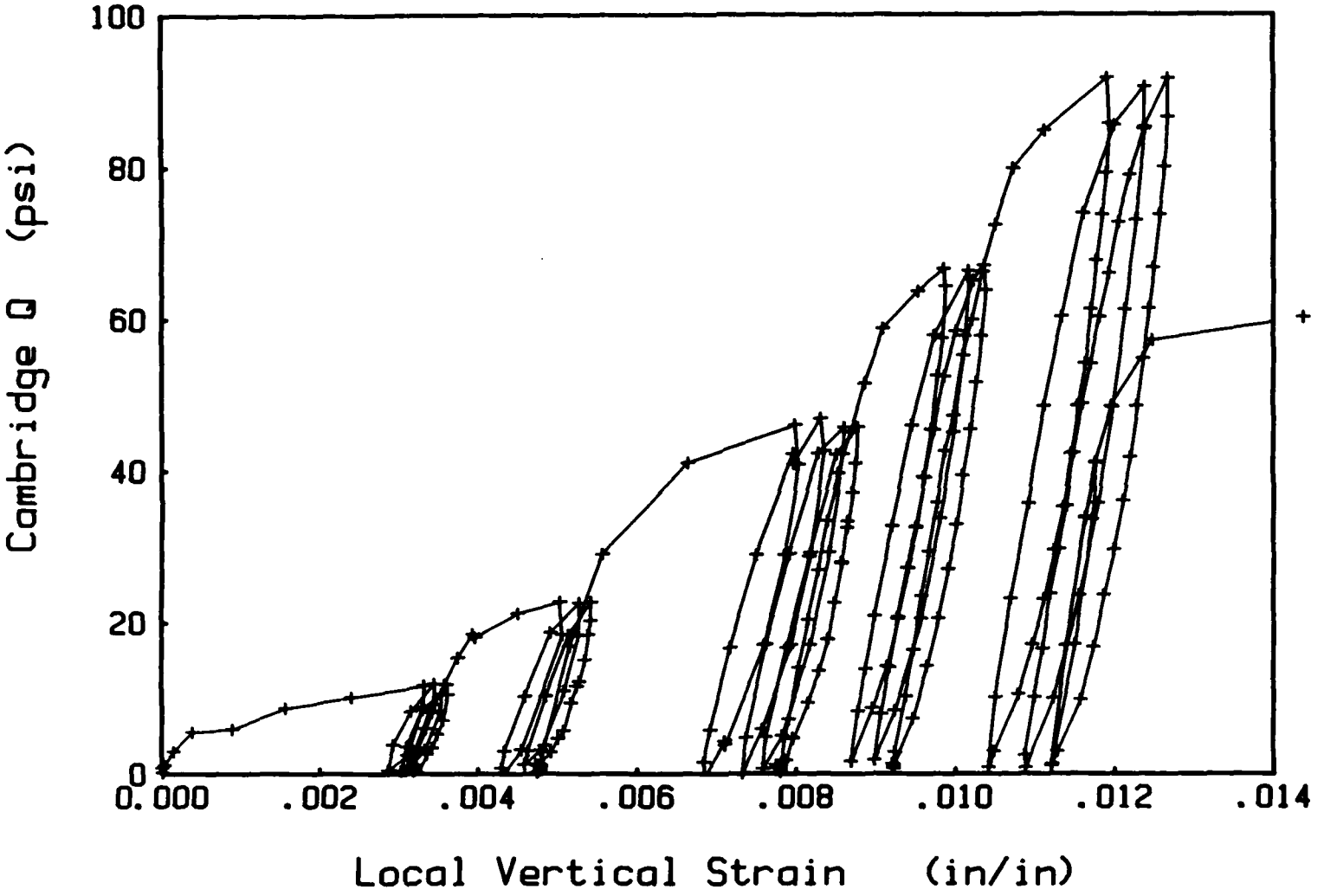

Figure 1.41 Test 8: Cyclic CTC at Different Initial Cell Pressures (Local Reading)

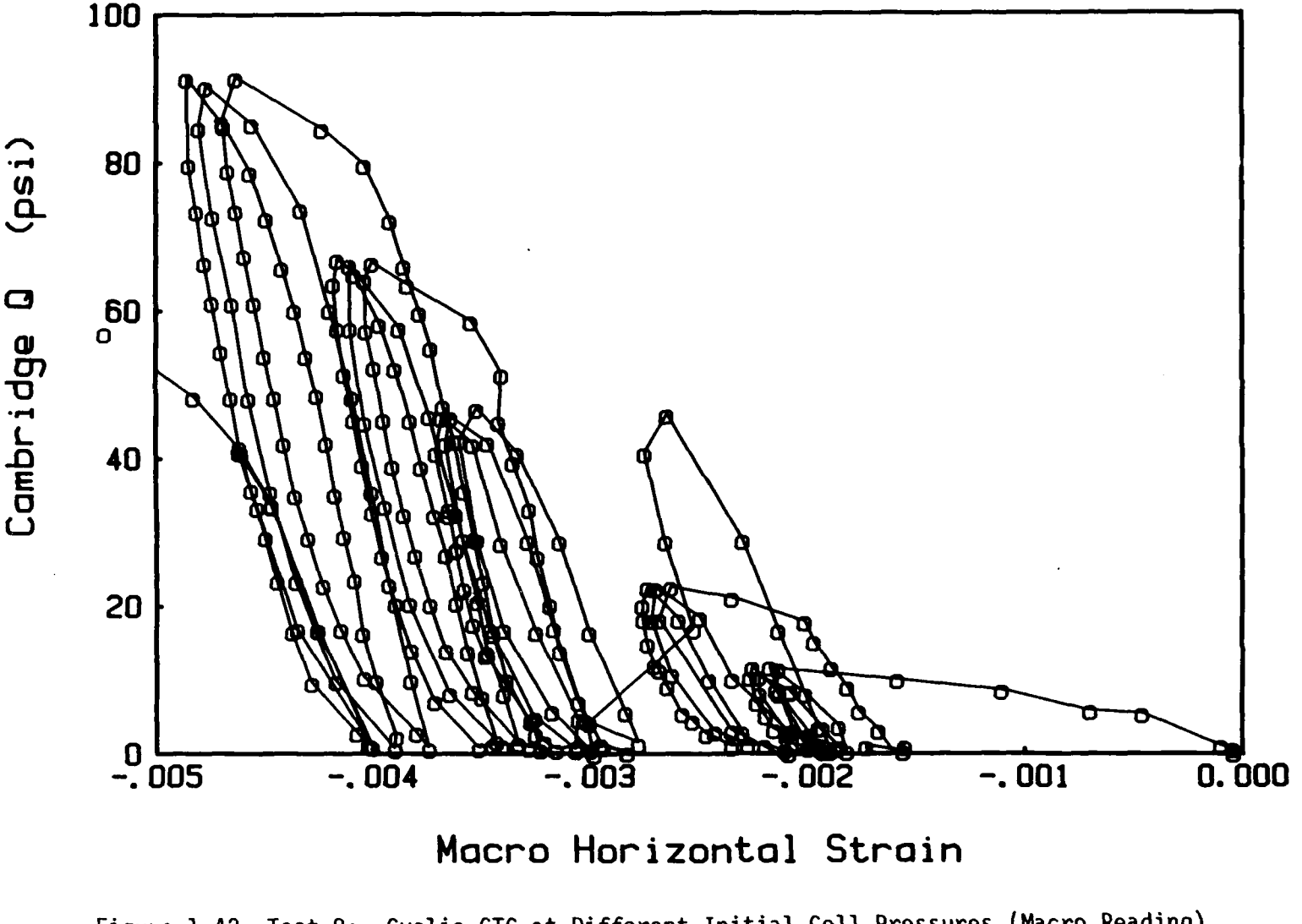

Figure 1.42 Test 8: Cyclic CTC at Different Initial Cell Pressures (Macro Reading)

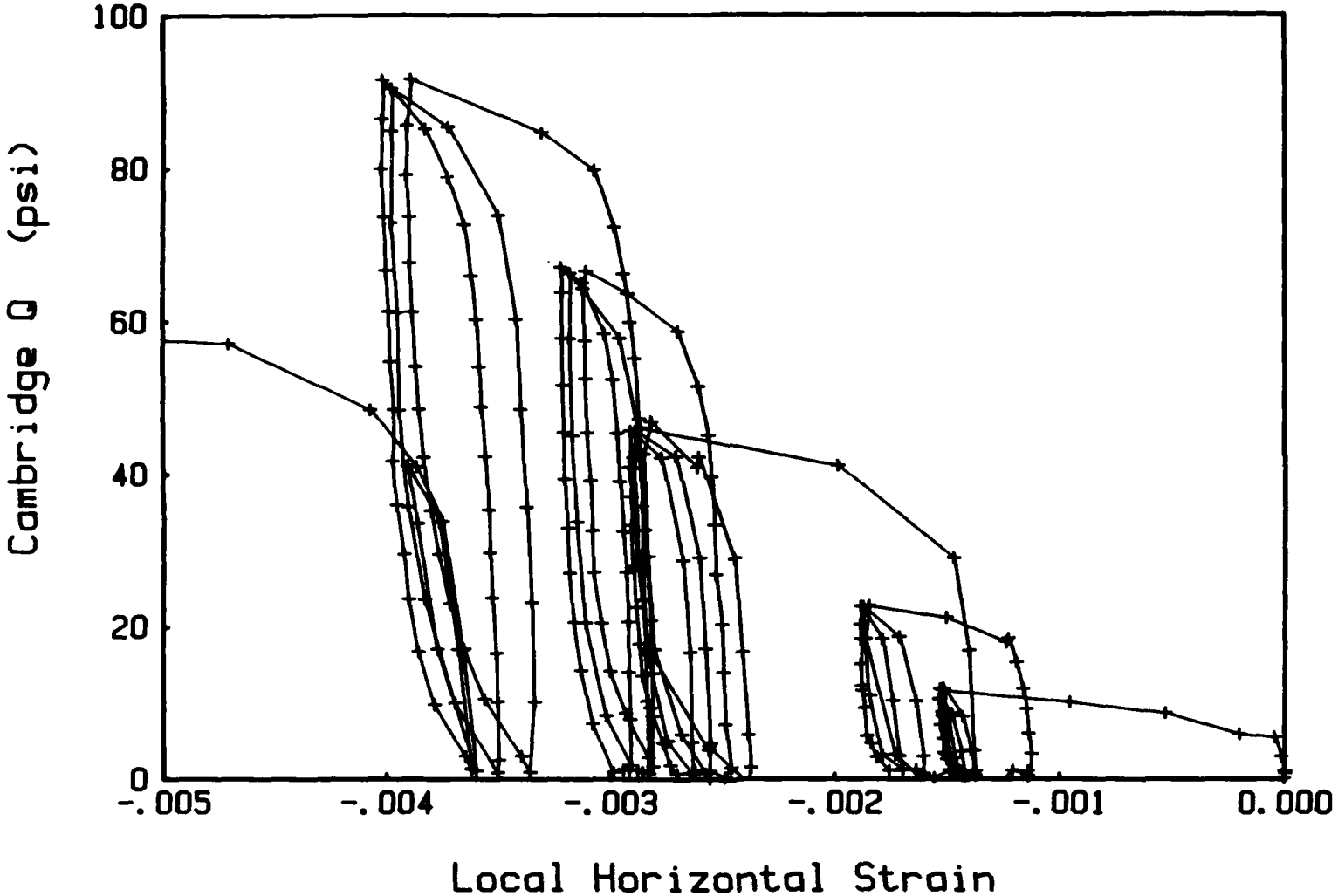

Figure 1.43 Test 8: Cyclic CTC at Different Initial Cell Pressures (Local Reading)

approach, burettes and a dial gauge attached to the piston. Evident from a comparison of Figures 1.38 with 1.39, and 1.41 with 1.42, is that the micro system, DCDTs, is a far superior system to the conventional approach. Unfortunately, in this series of tests the macro response could not be compared to the local behavior due to membrane effects discussed earlier (see 1.5.1)

Study of the stress-strain behavior for the different cell pressures reveals that if one were to normalize Q with respect to the initial mean stress then all results would be identical. From a plasticity viewpoint (see Chapter 3), the above suggests that the yield surface (separates elastic from plastic behavior) is contracting with the stress point and that the plastic modulus for virgin loading is independent of mean stress. An important finding, and one which will be expanded on in the model development of Chapter 3.

The final test reported on is the standard cyclic conventional triaxial compression test (CTC) which is used to predict permanent deformation from a passing moving wheel. The local (DCDTs) vertical strain versus deviatoric stress, Q (σ_v - σ_H) is presented in Figures 1.44 and 1.45 for one hundred replicate axial load applications. The latter figure is an expanded view of the former. Evident from the figures is the significant buildup of permanent axial strain due to cyclic loading.

1.5.3 Triaxial Moving Wheel Representation

As has been noted by previous research (Seereeram, McVay and Linton, 1985), the standard cyclic CTC stress path isn't the true representation of a passing moving wheel. For instance, it has been found that approximately one third of the maximum deviatoric stress occurs within extension stress space, i.e. principal stress direction aligned less than 45 degrees from the

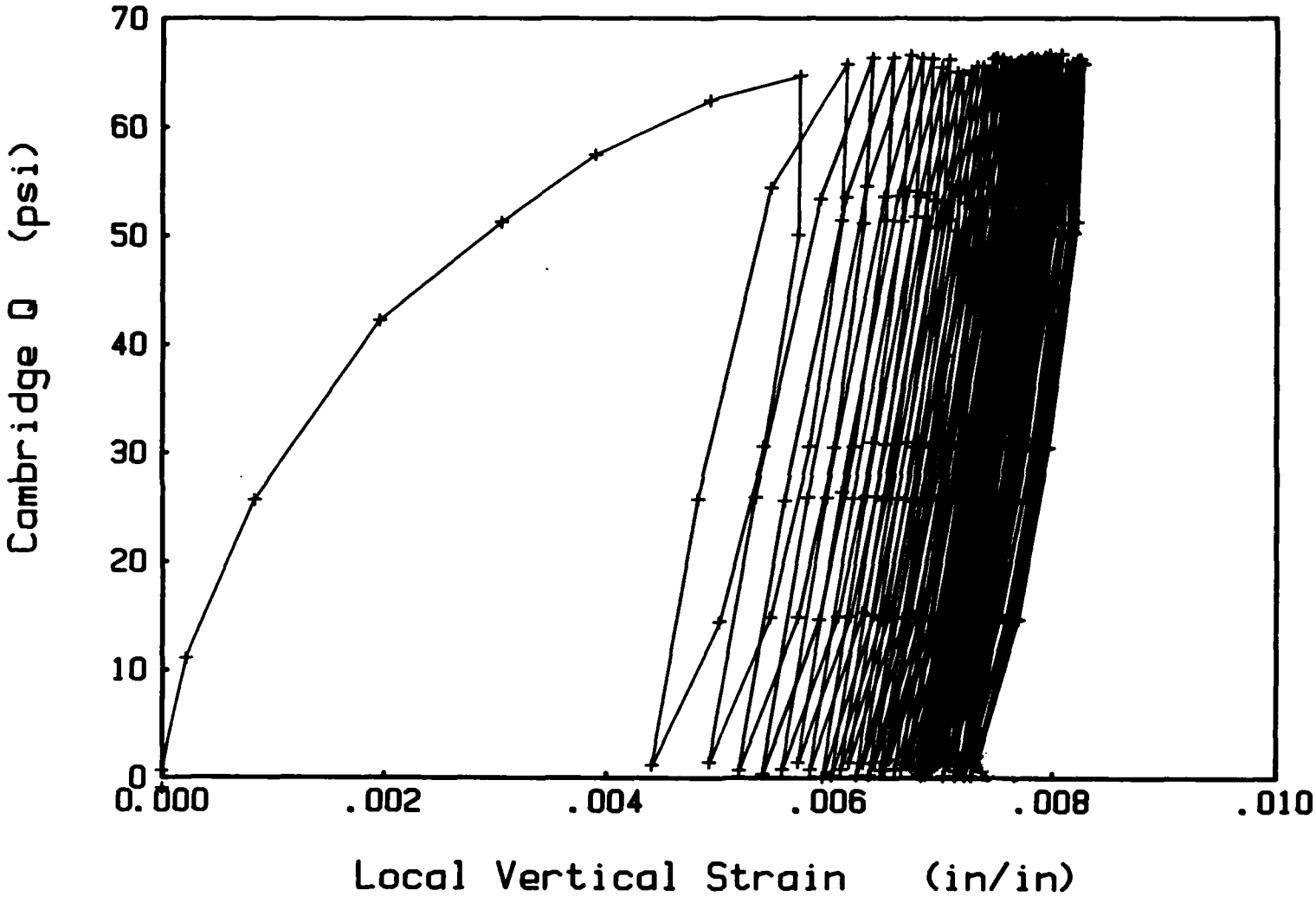

Figure 1.44 Test 9: Standard Cyclic CTC Representation of a Moving Wheel (Local Reading)

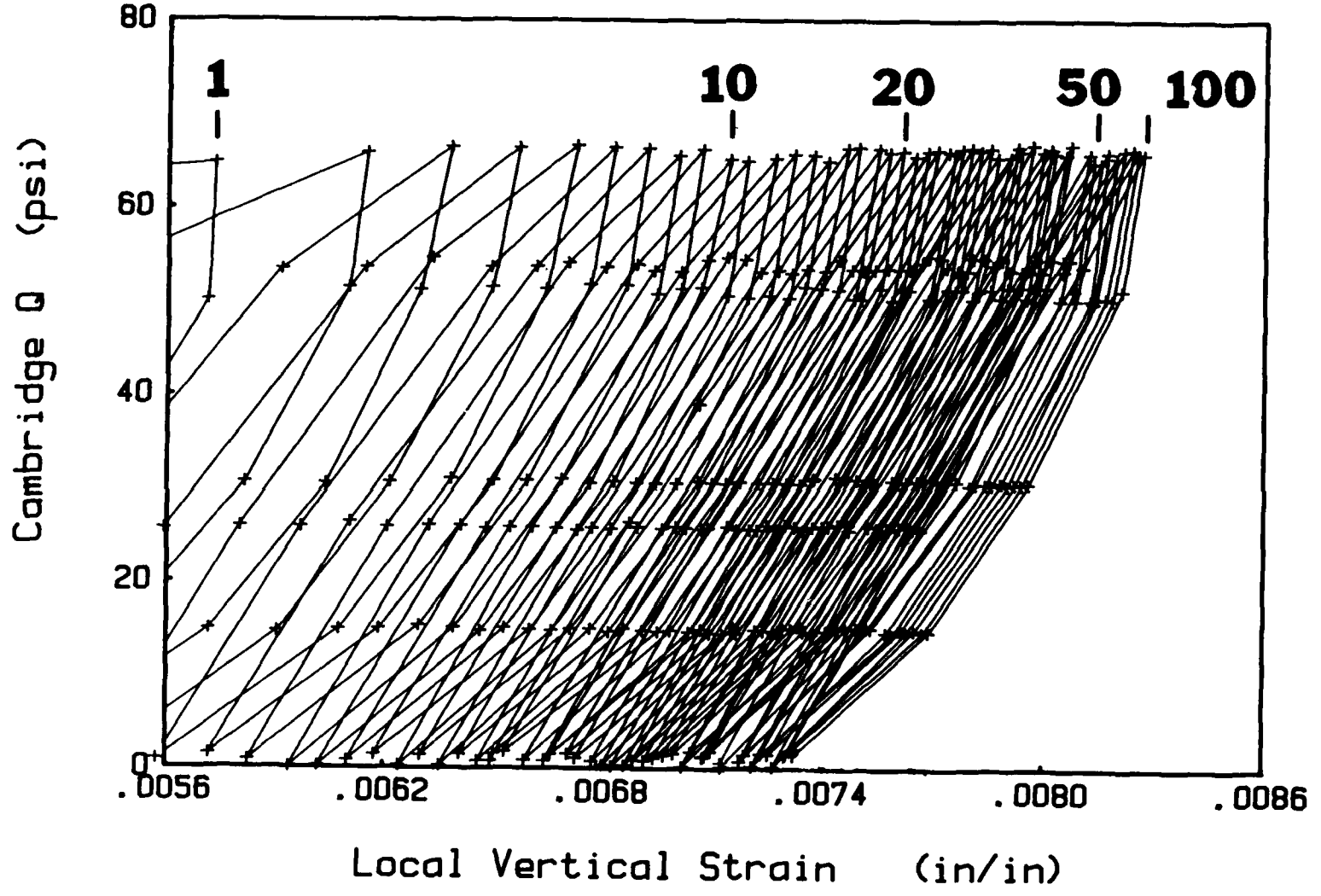

Figure 1.45 Test 9: Standard Cyclic CTC Representation of a Moving Wheel (Expanded View)

horizontal. Consequently, the tests reported herein were conducted to study the influence of entering the extension stress space on the maximum permanent strains, and to examine the suitability of the triaxial device in characterizing the moving wheel stress path.

Presented in Figure 1.46 is the P, mean stress $((\sigma_v + 2\sigma_H)/3)$, versus Q, deviatoric stress $(\sigma_v - \sigma_H)$, representation of a moving wheel. The path from points A to D represents the stress state within the base material as the wheel approaches approximately three radii from the point of interest. At this distance the major principal direction is aligned closer to the vertical than the horizontal, resulting in a jump to compression space, Path D-B. Path B-C represents the substantial increase in vertical stress as the wheel approaches the point with minimal change in the horizontal stress. It should be clearly understood that in an actual moving wheel, the point undergoes a continuous rotation of principal stress which can only occur if shear tractions are applied to the specimen. Unfortunately the triaxial device is incapable of supplying such stresses and as will be seen the results are extremely adverse.

Presented in Figure 1.47 is the deviatoric stress, Q, versus the axial strain for the triaxial stress path discussed above. Evident from the cyclic response is that there is little permanent strain buildup, and its magnitude is significantly less than that reported in Figure 1.44 (Path A-B-C in Figure 1.46) i.e. the standard (increase in only axial load) representation of a moving wheel. The permanent volumetric strain for Path A-D-B-C is however approximately 60% greater than Path A-B-C. Ishihara (1983) performed a moving wheel representation in a hollow cylinder device (allows the application of shear traction to specimen, see Chapter 3) and compared it to the standard conventional test, Path A-B-C. His correlation revealed that approximately

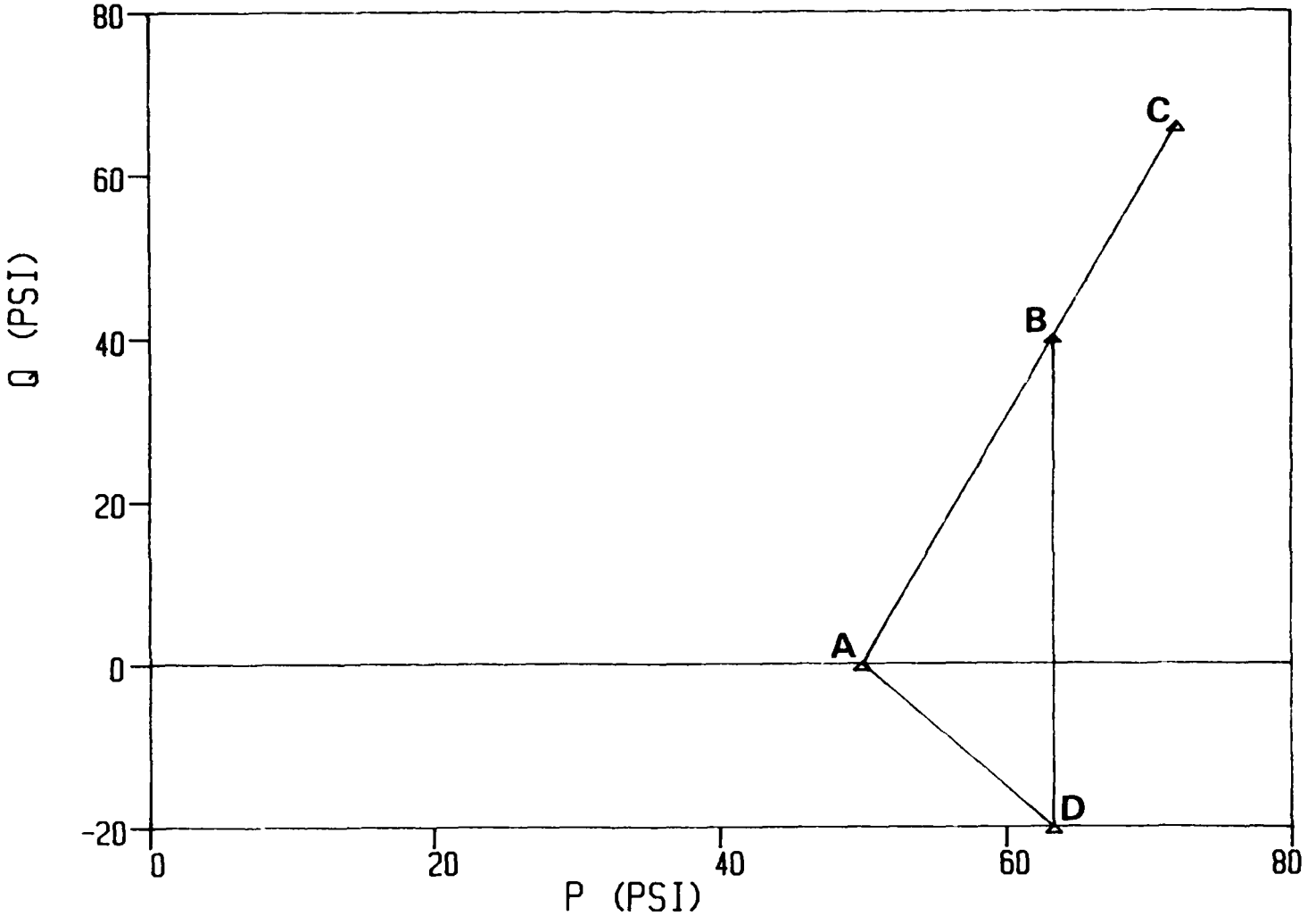

Figure 1.46 The Bounded Moving Wheel Representation in Triaxial Space

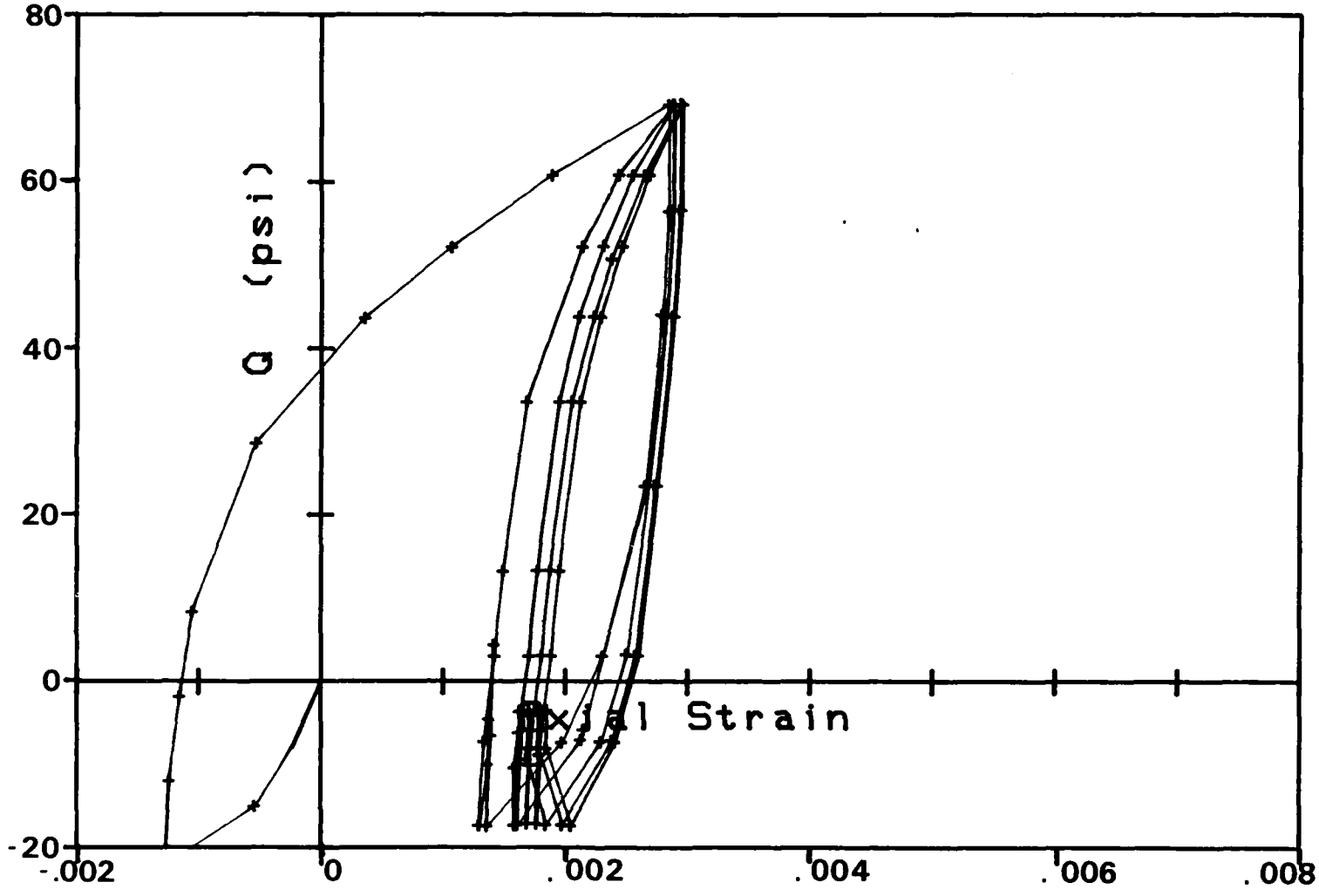

Figure 1.47 Test 10: Cyclic Representation of a Moving Wheel in Triaxial Space (local Reading)

three times as much volumetric and axial strain was developed in the hollow cylinder characterization as from the Standard CTC Path A-B-C. Consequently, it was recognized that excursions into the extension space as in Path A-D-B-C reoriented the soil's fabric from a volumetric standpoint, (similar to the hollow cylinder results) but the permanent axial stain was not increasing due to the fact that when most of the volumetric alterations were occurring, the axial stress wasn't increasing.

This was further verified in the triaxial device through the test Path A-D-A-B-C reported in Figure 1.48. Scrutiny of the figure reveals that there is a degradation (decrease) of permanent strain; however the permanent volumetric strain of the test was approximately 3 times that reported for stress Path A-B-C. This compares quite favorably with the hollow cylinder results of Ishihara (1983); unfortunately the axial response for this type of loading was quite adverse.

The results of Paths A-D-B-C and A-D-A-B-C are easily differentiable in terms of both the change in the soil's fabric and the applied stress paths. Along Paths A-D for both tests, the lateral stress increases, resulting the rearrangement of the major particle contact directions more towards the horizontal (requires particles to rotate and slide past one another, denser arrangement). However for Paths D-A-B and D-B, the major particle contact direction switches (this time from the horizontal to vertical); since the confining stress is decreasing mean pressure is also decreasing) for Paths D-A-B, the particles are free to rotate and slide (densify) into the necessary point contact alignment, whereas for Path D-B the mean pressure is constant and particle sliding (denser configuration) is limited.

This would also explain the soil's behavior under a moving wheel or a hollow cylinder test: applied shear tractions in combination with normal

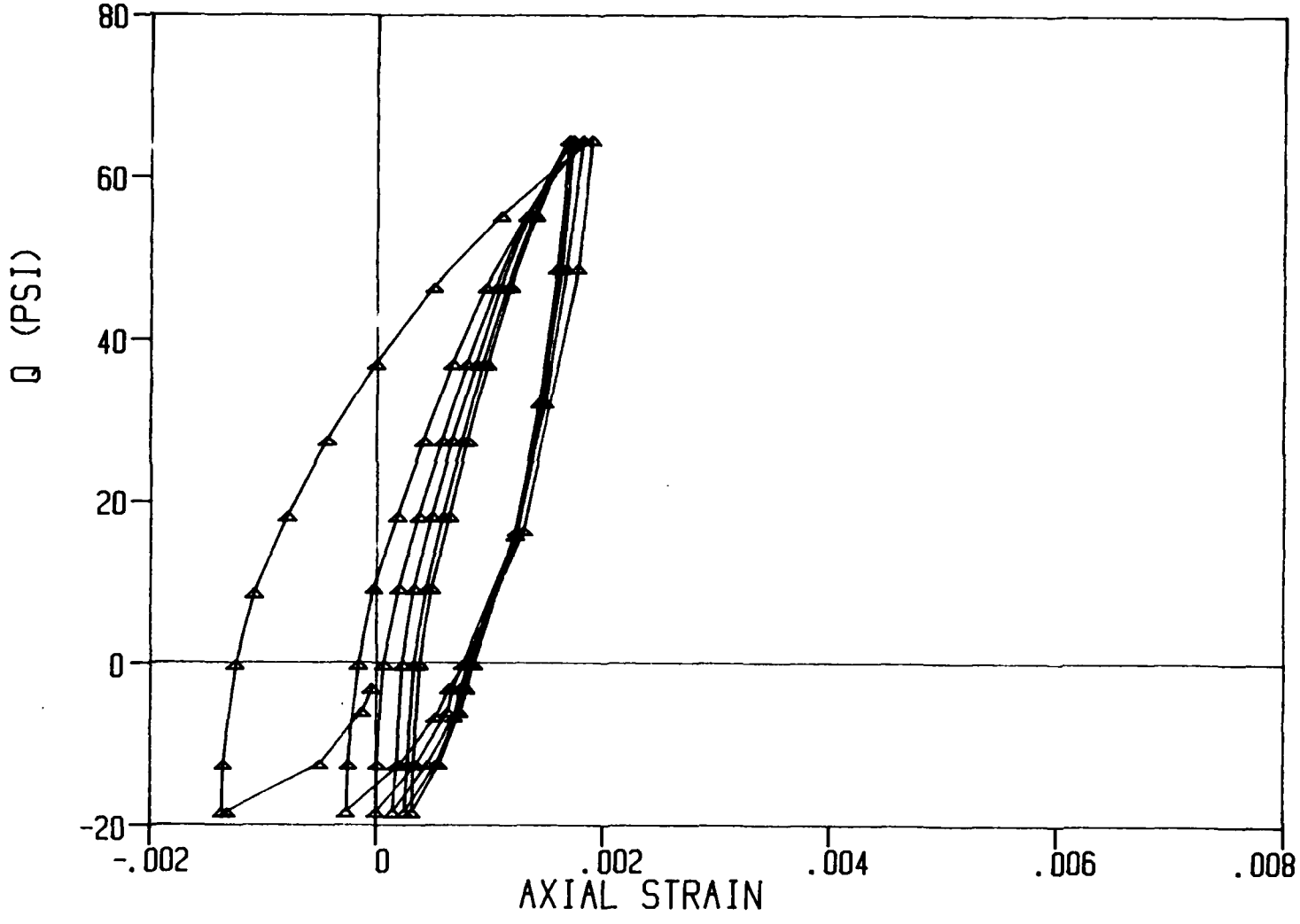

Figure 1.48 Test 11: Cyclic Excursions into Extension and Compression Triaxial Stress Space (Local Reading)

stresses, result in substantial particle sliding and realignment, leading to denser specimens (volumetric compression) as well as larger axial permanent strains (normal stresses are increasing). Consequently, the representation of a moving wheel in a triaxial device is not recommended, but further research into the study of the relationship between a soil's fabric and macro measurements (stress and strain) in the hollow cylinder device is warranted.

CHAPTER 2

FUNDAMENTALS OF CONTINUUM MODELLING

2.1 Stress-Strain Equations and Constitutive Theory

To solve statically indeterminate problems, the engineer utilizes the equations of equilibrium, the kinematic compatibility conditions, and a knowledge of the load-deformation response (or stress-strain constitution) of the engineering material under consideration. As an aside, it is useful to remind the soils engineer of two elementary definitions which are not part of the everyday soil mechanics vocabulary. Kinematics is the study of the motion of a system of material particles without reference to the forces which act on the system. Dynamics is that branch of mechanics which deals with the motion of a system of material particles under the influence of forces, especially those which originate outside the system under consideration.

For general applicability, the load-deformation characterization of the solid media is usually expressed in the form of a constitutive law relating the force-type measure (stress) to the measure of change in shape and/or volume (strain) of the medium. A constitutive law therefore expresses an exact correspondence between an action (force) and an effect (deformation). The correspondence functional--it is a mathematical representation of the physical processes which take place in a material as it passes from one state of equilibrium to another (Jain, 1980). This is an approriate point to interject and to briefly clarify the meaning of another word not commonly encountered by the soils engineer: functional.

Let us consider a sand mass which contains particle P and extend the discussion to include M discrete granules (P_i, i = 1,2,...,M). Say the body of sand was subjected to a system of boundary loads which induced a motion of

or conversely,

$$\dot{\varepsilon}_{kl} = D_{klij}\,\dot{\sigma}_{ij}\,, \tag{2.1.4}$$

where the superposed dot above the stress and strain tensors denote a differentiation with respect to time. In these equations, $\underset{\sim}{C}$ and $\underset{\sim}{D}$ are now tangent constitutive tensors. The terms $\dot{\underset{\sim}{\sigma}}$ and $\dot{\underset{\sim}{\varepsilon}}$ are the stress rate and strain rate respectively.

If the "step by step" stress-strain model is further idealized to be insensitive to the rate of loading, the incremental relationship may be written as:

$$d\sigma_{ij} = C_{ijkl}\,d\varepsilon_{kl}\,, \tag{2.1.5}$$

or inversely

$$d\varepsilon_{kl} = D_{klij}\,d\sigma_{ij}\,, \tag{2.1.6}$$

where $d\underset{\sim}{\sigma}$ and $d\underset{\sim}{\varepsilon}$ are the stress increment and strain increment respectively. Only rate-independent constitutive equations will be considered here in.

In the formulation of generalized, rate independent, incremental stress-strain models, the objective is one of the identifying the variables that influence the instantaneous magnitudes of the components of the stiffness ($\underset{\sim}{C}$) or compliance ($\underset{\sim}{D}$) tensors. Such a study bears resemblance to many others specialized disciplines of civil engineering. The econometrician, for instance, may determine by a selective process that the following variables influence the price of highway construction in a state for any given year: cost of labor, cost of equipment, material costs, business climate, and a host of other tangible and intangible factors. The soils engineer, perhaps using the econometrician's techniques of regression analysis and his personal

significant, but the econometrician uses variables which may frequently be intangible. Therefore, in the selection of constitutive variables (such as stress and strain) and in the actual formulation of the stress-strain equations, certain physical notions (leading to mathematical constraints) must be satisfied. These conditions are embodied in the so-called axioms or principles of constitutive theory. An axiom is well-established basis for theoretical development. Since geotechnical engineers are, for the most part, interested in isothermal processes, the principles linked to thermomechanical behavior are suppressed in the sequel.

The Axiom of Causality states that the motion of the material points of a body is to be considered a self-evident, observable effect in the mechanical behavior of the body. Any remaining quantities (such as the stress) that enter the entrophy production and the balance equations--i.e., the equations of conservation of mass, balance of momentum, and conservation of energy--are the causes or dependent variables. In other words, there can occur no deformation (effect) without an external force (cause).

The Principle of Determinism is that the stress in a body is determined by the history of the motion of that body. This axiom excludes the dependence of the stress at a point P on any point outside the body and on any future events. This phenomenon is sometimes referred to as the Principle of Heredity.

In the purely mechanical sense, the Axiom of Neighborhood or Local Action rules out any appreciable effects on the stress at P that may be caused by the motion of points distant from P; "actions at a distance" are excluded from constitutive equations.

During the discussion of stress and strain, it was made quite clear that the tensor measures should be independent of the perspective of the

sliding and rolling velocities between particles. These local strains are much larger than the overall (continuum) strain. The magnitude of the generated strain will, as mentioned before, depend on the composition, void ratio, anisotropic fabric, past stress history, and the stress increment. Composition is a term used in soil mechanics to refer to the average particle size, the surface texture and angularity of the typical grain, the grain size distribution, and the mineral type.

Figure 2.1 illustrates typical qualitative load-deformation response of loose and dense soil media subject to two conventional laboratory stress paths: hydrostatic compression, and conventional triaxial compression. Figure 2.2 shows these paths together with an assortment of other 'triaxial' stress paths used for research as well as routine purposes. In this context, note that the adjective 'triaxial' is somewhat ambiguous since this particular test scenario dictates that the circumferential stress always be equal to the radial stress. The stress state is therefore not truly triaxial, but biaxial. As we can gather from Figure 2.1, the stress-strain behavior of soil is quite complicated, and in order to approximately model real behavior, drastic idealizations and simplifications are necessary. More complex details of soil response are mentioned in Chapter 3.

The major assumptions in most present idealizations are that: a) soil response is independent of the rate of loading, b) behavior may be interpreted in terms of effective stresses, c) the interaction between the mechanical and thermal processes are negligible, and d) the strain tensor can be decomposed into an elastic part ($\underset{\sim}{\varepsilon}^e$) and a plastic conjugate ($\underset{\sim}{\varepsilon}^p$) without any interaction between the two simultaneously occuring strain types,

$$\underset{\sim}{\varepsilon} = \underset{\sim}{\varepsilon}^e + \underset{\sim}{\varepsilon}^p \ , \qquad (2.2.1)$$

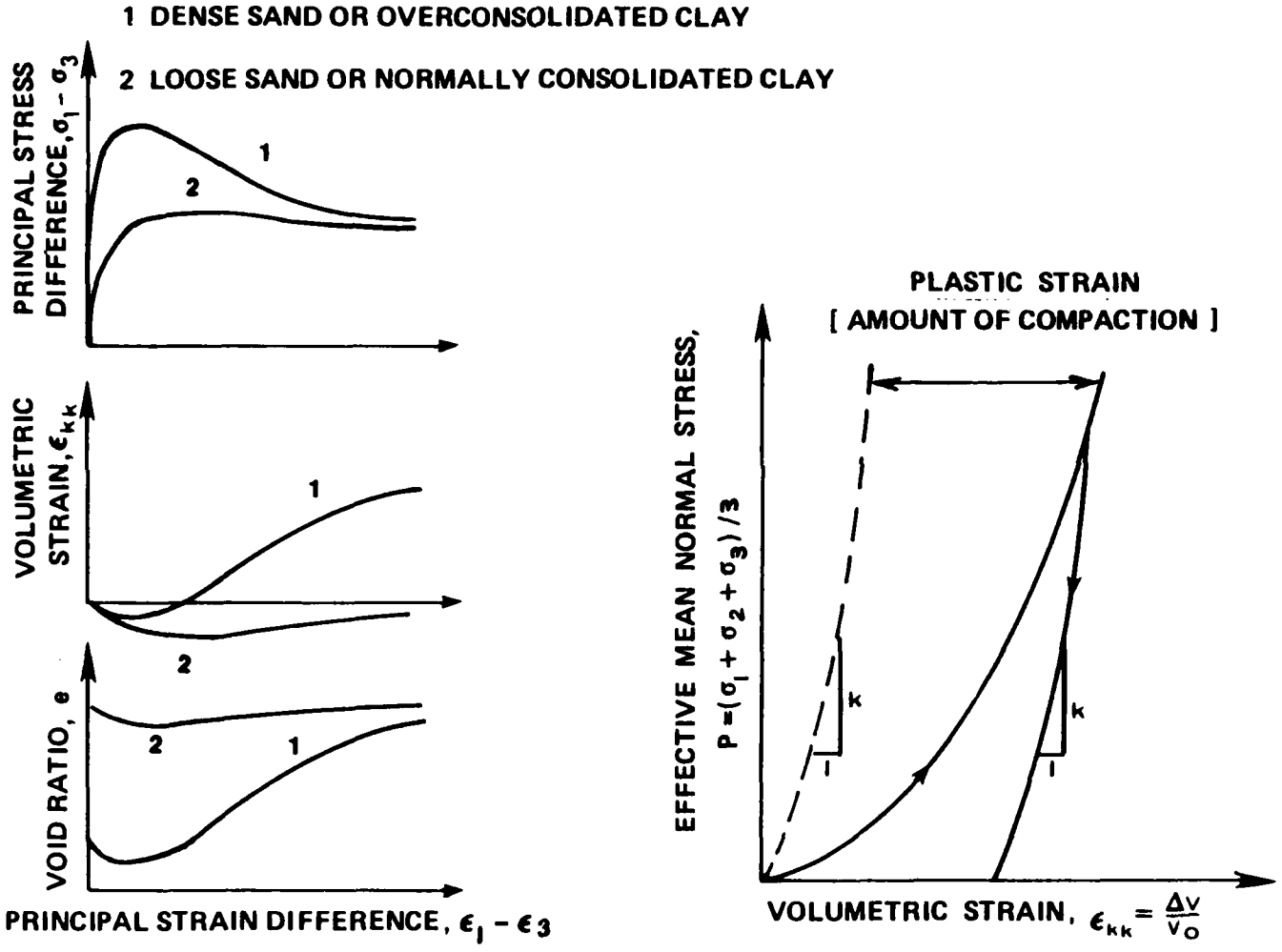

Figure 2.1 Typical stress-strain response of soil for a conventional 'triaxial' compression test (left) and a hydrostatic compression test (right)

NAME OF TEST	Standard Designation	DESCRIPTION
Conventional Triaxial Compression	CTC	$\Delta\sigma_x = \Delta\sigma_z = 0;\ \Delta\sigma_y > 0$
Hydrostatic Compression	H C	$\Delta\sigma_x = \Delta\sigma_z = \Delta\sigma_y > 0$
Conventional Triaxial Extension	CTE	$\Delta\sigma_x = \Delta\sigma_z > 0;\ \Delta\sigma_y = 0$
Mean Normal Pressure Triaxial Compression	TC	$\Delta\sigma_x + \Delta\sigma_z + \Delta\sigma_y = 0;$ $\Delta\sigma_y > \Delta\sigma_x\ (= \Delta\sigma_z)$
Mean Normal Pressure Triaxial Extension	TE	$\Delta\sigma_x + \Delta\sigma_z + \Delta\sigma_y = 0;$ $\Delta\sigma_x = \Delta\sigma_z > \Delta\sigma_y$
Reduced Triaxial Compression	RTC	$\Delta\sigma_x = \Delta\sigma_z < 0;\ \Delta\sigma_y = 0$
Reduced Triaxial Extension	RTE	$\Delta\sigma_y < 0;\ \Delta\sigma_x = \Delta\sigma_z = 0$

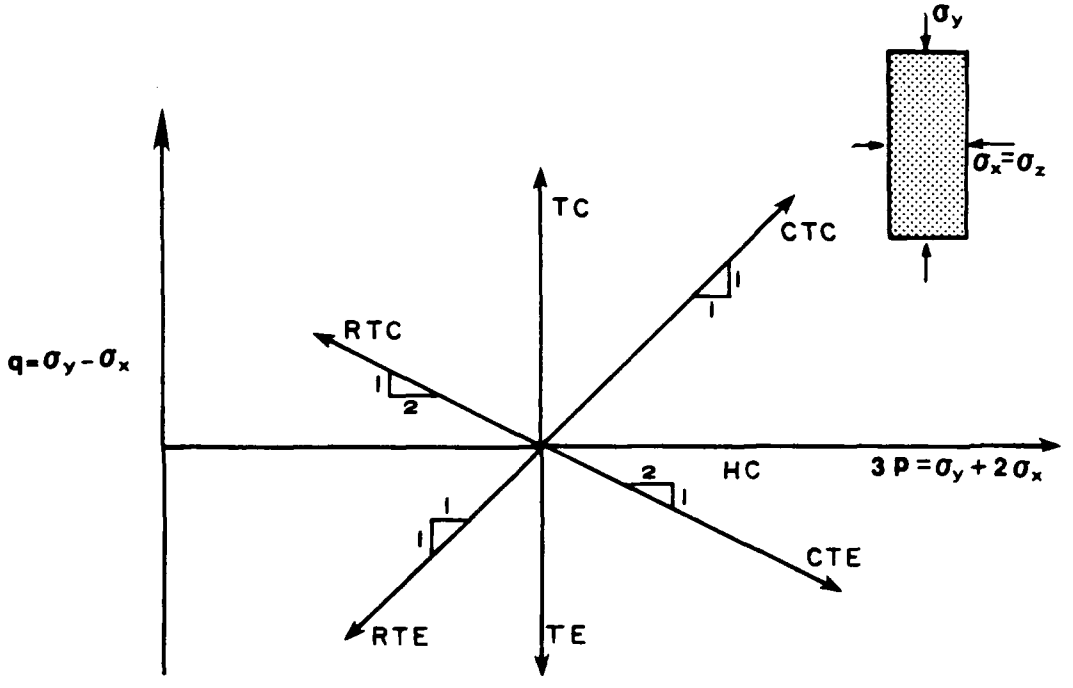

Figure 2.2 Typical stress paths used to investigate the stress-strain behavior of soil specimens in the triaxial environment

or in incremental form,

$$d\underset{\sim}{\varepsilon} = d\underset{\sim}{\varepsilon}^e + d\underset{\sim}{\varepsilon}^p \ . \qquad (2.2.2]$$

The elastic behavior ($\underset{\sim}{\varepsilon}^e$ or $d\underset{\sim}{\varepsilon}^e$) is modeled within the broad framework of elasticity theory, while the plastic part ($\underset{\sim}{\varepsilon}^p$ or $d\underset{\sim}{\varepsilon}^p$) is computed from plasticity theory. Both these theories will be elaborated later in this chapter.

With the introduction of the strain decomposition into elastic and plastic components, it is now important to emphasize the difference between irreversible strains and plastic strains for cyclic loading on soils. Consider a uniaxial cyclic test consisting of a virgin loading, an unloading back to the initial hydrostatic state of stress, and a final reloading to the previous maximum deviatoric stress level. During the first virgin loading both elastic and plastic strains are generated, and these components may be calculated using an elastic and a plastic theory respectively. If at the end of this segment of the stress path we terminate the simulation and output the total, elastic, and plastic axial strains, one may be tempted to think that the plastic component represents the irrecoverable portion of the strain. However, when the stress path returns to the hydrostatic state, the hysteresis loop in Figure 2.3 indicates that reverse plastic strains are actually generated on the unload and a (small) portion of the plastic strain at the end of the virgin loading cycle is, in fact, recovered. This is an illustration of the Bauschinger effect (Bauschinger, 1887). Therefore, for such a closed stress cycle, the total strain can more generally be broken down into the three components:

$$\underset{\sim}{\varepsilon} = \underset{\sim}{\varepsilon}^p_{irrev} + \underset{\sim}{\varepsilon}^p_{rev} + \underset{\sim}{\varepsilon}^e \ ,$$

where $\underset{\sim}{\varepsilon}^p_{irrev}$ is the irreversible plastic strain, $\underset{\sim}{\varepsilon}^p_{rev}$ is the reverse plastic strain, and as before $\underset{\sim}{\varepsilon}^e$ denotes the elastic strain, which is by definition

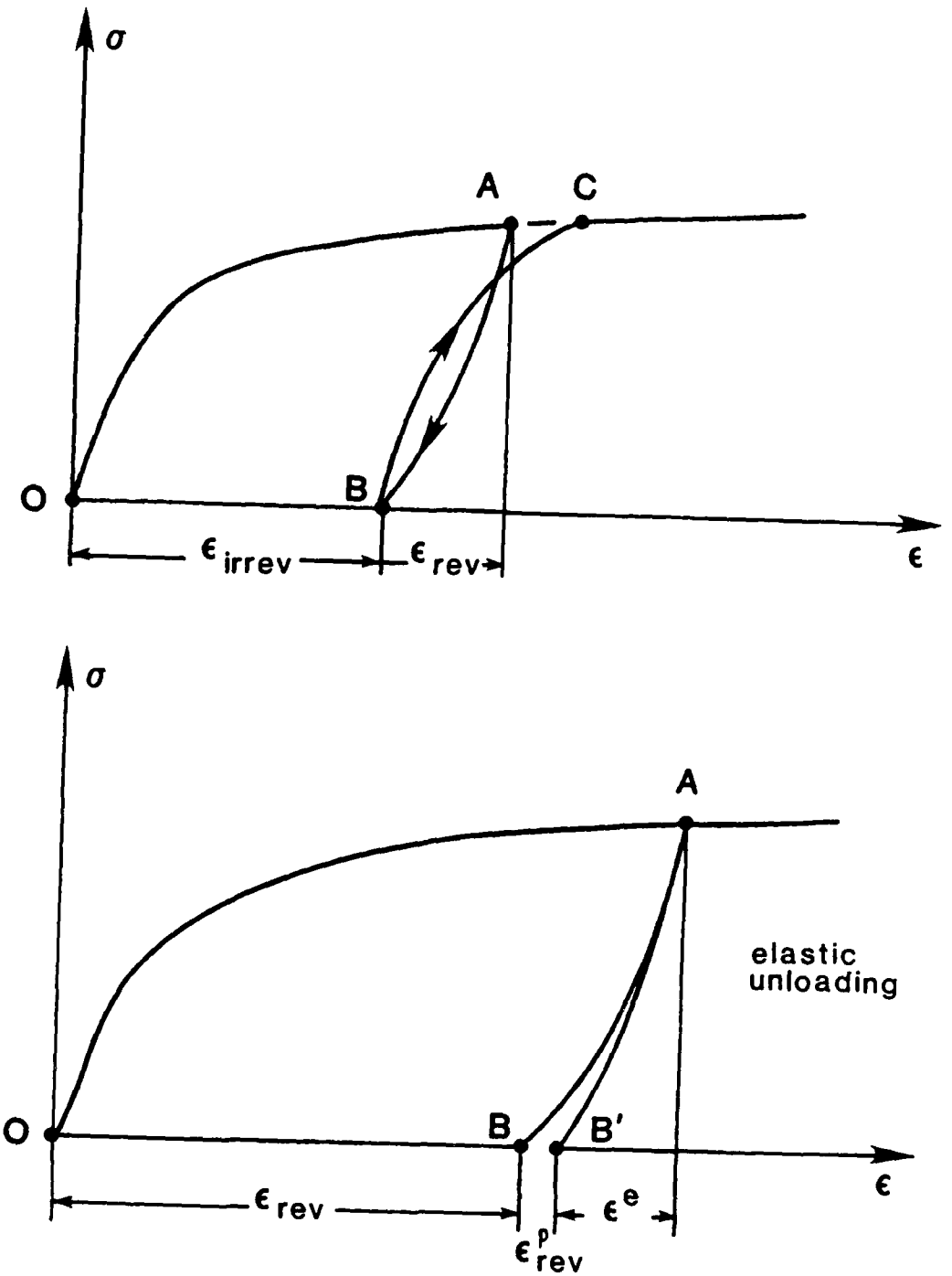

Figure 2.3 Components of strain: elastic, irreversible plastic, and reversible plastic

AD-A173 976 GENERALIZED PHENOMENOLOGICAL CYCLIC STRESS-STRAIN-STRENGTH CHARACTERIZATI (U) FLORIDA UNIV GAINESVILLE DEPT OF CIVIL ENGINEERING M C MCVAY ET AL 2/4

UNCLASSIFIED 02 SEP 84 AFOSR-TR-86-0918 AFOSR-84-0108 F/G 8/13 NL

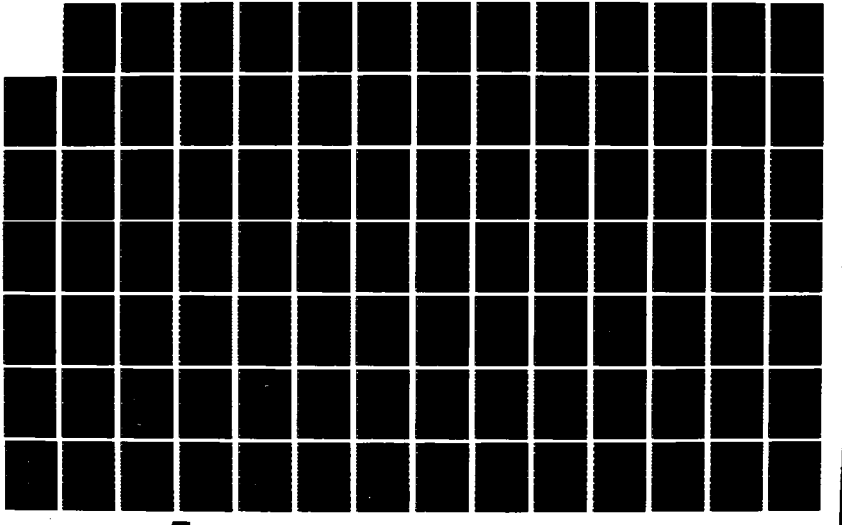

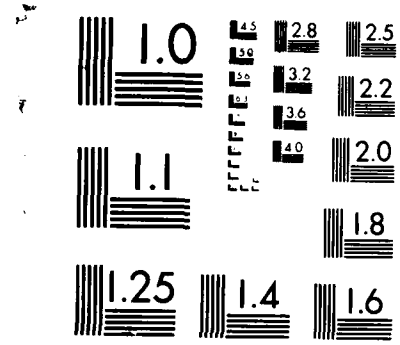

MICROCOPY RESOLUTION TEST CHART
NATIONAL BUREAU OF STANDARDS-1963-A

recoverable. Some complicated models of soil behavior, such as the Prevost model (Prevost, 1975), allow for reverse plastic strains on such "unloading" paths. However, ignoring this aspect of reality, as is done in Chapter Three, can lead to very rewarding simplificatons.

Three broad classes of continuum theories have evolved in the development and advancement of soil stress-strain models (Cowin, 1978): 1) the kinematically ambiguous theories, 2) the phenomenological theories, and 3) the microstructural the . ies.

The kinematically ambiguous hypotheses employ the stress equations of equilibrium in conjunction with a failure criterion to form a system of equations relating the components of the stress tensor. This category is referred to as kinematically ambiguous because displacements and strains do not appear in and are therefore not computed from the basic equations of the theory. They assume the entire medium to be at a state of incipient yielding. A modern example of this type of formulation can be found in Cambou (1982).

A phenomenological continuum theory endeavors to devise constitutive relations based on experimentally observed stress-strain curves. It is presently the most popular class of the theories and it concentrates on the macroscopically discernable stress and strain measures. This theory does not inquire very deeply into the mechanisms which control the process of deformation. A controversial assumption of these phenomenological continuum theories, as applied to granular media, is that the laboratory tests, such as the standard triaxial test, achieve homogenous states of strain and stress. Many researchers are now seeking the answer to the question of when bifurcation of the deformation mode becomes acute enough to render

interpretation of the supposedly "homogenous state" data troublesome (see, for example, Lade, 1982, and Hettler et al., 1984).

Microstructural theories attempt to incorporate geometric measures of local granular structure into the continuum theory. Local granular structure is also called fabric, which is defined as the spatial arrangement and contact areas of the solid granular particles and associated voids. For clarity, fabric is subdivided into isotropic fabric measures (such as porosity, density, etc.) and anisotropic fabric measures (which are mentioned in the next section). In this report, unless otherwise stated, the word fabric refers to anisotropic fabric. Perhaps the best known microstructural formulation is that proposed by Nemat-Nasser and Mehrabadi (1984).

2.3 Anisotropic Fabric in Granular Materials

2.3.1 Introduction

The fabric of earthen materials is intimately related to the mechanical processes occuring during natural formation (or test sample preparation) and the subsequent application of boundary forces and/or displacements. Fabric evolution can be examined in terms of the deformations that occur as a result of applied tractions (strain-induced anisotropy), or the stresses which cause rearrangement of the microstructure (stress-induced anisotropy). Strains are influenced to some extent by the relative symmetry of the applied stress with respect to the anisotropic fabric symmetry (or directional stiffness). If straining continues to a relatively high level, it seems logical to expect that the initial fabric will be wiped out and the intensity and pattern of the induced fabric will align itself with the symmetry (or principal) axes of stress. Before introducing and discussing a select group of microscopic fabric measures, some of the commonly encountered symmetry patterns, caused by combined kinematic/dynamic boundary conditions, will be reviewed.

2.3.2 Common Symmetry Patterns

Triclinic symmetry implies that the media possesses no plane or axis of symmetry. This fabric pattern is produced by complex deformations. Gerrard (1977) presents a simple example of how this most general and least symmetric system may arise: consider the sketch in the upper left hand corner of Figure 2.4, triclinic symmetry develops as a result of the simultaneous application of compression in direction 1, differential restraint in directions 2 and 3, and shear stress components acting in directions 2 and 3 on the plane having axis 1 as its normal.

Monoclinic symmetry is characterized by a single plane of symmetry. Any two directions symmetric with respect to this plane are equivalent. An example of this symmetry group is shown in the lower left of Figure 2.4. The concurrent events leading to it are compression in direction 1, no deformation in the 2 and 3 directions, and a shear stress component acting in the 2-direction and on the plane with axis 1 as its normal.

A slight modification of the previous example permits a demonstration of a case of n-fold axis symmetry or cross-anisotropy. Exclusion of the shear stress component causes an axis of fabric symmetry to develop such that all directions normal to this axis are equivalent, bottom right of Figure 2.4.

The orthorhombic symmetry group can best be described by bringing to mind the true triaxial device. Here for example (top right of Figure 2.4), three mutually perpendicular planes of symmetry are produced by normal stresses of different magnitudes on the faces of the cubical sand specimen.

Lastly, the rarest natural case is spherical symmetry or material isotropy which implies that all directions in the material are equivalent. However, because of its simplicity, isotropy is a major and a very common

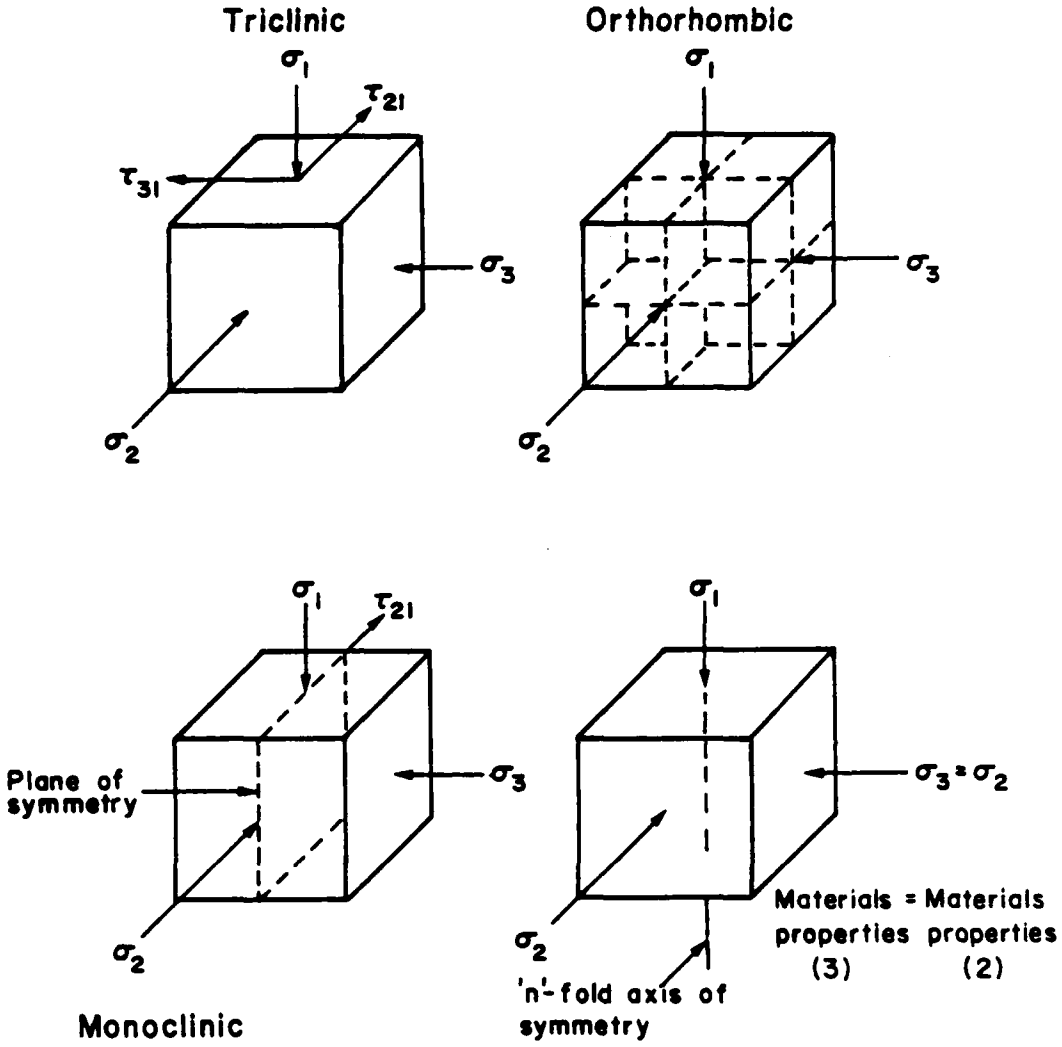

Figure 2.4 Common fabric symmetry types (after Gerrard, 1977)

simplifying assumption in many of the current representations of soil behavior.

2.3.3 Fabric Measures

The selection of the internal variables, $\underset{\sim}{q}_n$, to characterize the mechanical state of a sand medium (see Equation 2.1.7) has been a provocative subject in recent times (Cowin and Satake, 1978; and Vermeer and Luger, 1982). There is no doubt that the initial void ratio is the most dominant geometric measure, but as Cowin (1978) poses: "Given that porosity is the first measure of local granular structure or [isotropic] fabric, what is the best second measure of local granular structure or [anisotropic] fabric?" Trends suggest that the next generation of constitutive models will include this second measure. It is therefore worthwhile to review some of these variables.

An anthropomorphic approach is perhaps most congenial for introducing the reader to the concept of anisotropic fabric in granular material. Let us assume for illustrative purposes that, through a detailed experimental investigation, we have identified a microscopic geometric or physical measure (say variable X), which serves as the secondary controlling factor to the void ratio in interpreting the stress-strain response of sand. Some of the suggestions offered for the variable X are: 1) the spatial gradient of the void ratio $\frac{\partial e}{\partial \underset{\sim}{x}}$ (Goodman and Cowin, 1972); 2) the orientation of the long axes of the grains (Parkin et al., 1968); 3) the distribution of the magnitude and orientation of the inter-particle contact forces (Cambou, 1982); 4) the distribution of the inter-particle contact normals (see, for example, Oda, 1982); 5) the distribution of branches [note: a <u>branch</u> is defined as the vector connecting the centroids of neighboring particles, and it is thus

possible to replace a granular mass by a systems of lines or branches (Satake, 1978)]; 6) the mean projected solid path (Horne, 1964); and 7) mathematical representations in the form of second order tensor (Gudehus, 1968).

A commander (mother nature) of an army (the set representing the internal variable of the sand medium) stations her troops (variable X) in a configuration which provides maximum repulsive effort to an invading force (boundary tractions). The highest concentration of variable X will therefore tend to point in the direction of the imposed major principal stress. If the invading army (boundary tractions) withdraws (unloading), we should expect the general (mother nature) to keep her distribution of soldiers (X) practically unaltered. It is an experimental fact that there is always some strain recovery upon unloading, and this rebound is caused partly by elastic energy stored within individual particles as the soil was loaded and partly by inelastic reverse sliding between particles, Figure 2.3. Traditionally, it has been convenient to regard this unloading strain as purely elastic, but in reality, it stems from microstructural changes due to changes of the fabric and should be considered a dissipative thermodynamically irreversible process (Nemat-Nasser, 1982). Returning to our anthropomorphic description, we can therefore say that the general (mother nature) has a intrinsic command to slightly modify the arrangement of her troops (X) once the offensive army (boundary tractions) decamps. The configuration of the defensive forces (distribution of X) after complete or partial withdrawal of the aggressor (complete or partial removal of the boundary loads) still, however, reflects the intensity and direction of the earlier attack (prior application of the system of boundary loads). This represents an induced fabric or stress induced anisotropy in the granular material.

We can create additional scenarios with our anthropomorphic model to illustrate other features of fabric anisotropy. During the initial placement of the forces (initial distribution of the variable X during sample preparation or during natural formation of the soil deposit) under the general's command, there is a bias in this arrangement which is directly related to the general's personality (gravity as a law of nature). This is the so-called inherent anisotropy (Casagrande and Carillo, 1944) of soil which differs from the stress-induced anisotropy mentioned previously. Say the invading army (boundary tractions) attacks the defensive fortress (sand mass) with a uniform distribution of troops (uniform distribution of stress vectors), we will expect maximum penetration (strain) at the weakest defensive locations (smallest concentration of X), but our rational general (mother nature) should take corrective measures to prevent intrusion by the enemy forces (boundary tractions) through the inherently vulnerable sites (points of initially low X concentration). We can relate this situation to the effect of increasing hydrostatic pressure on an inherently cross-anisotropic sand specimen; the results of such a test carried out by Parkin et al. (1968) indicate that the ratio of the incremental horizontal strain to incremental vertical strain decreases from about 6 to 2.5. Increasing the hydrostatic pressure decreases the degree of anisotropy, but it does not completely wipe out the inherent fabric. We may infer that the general (mother nature) cannot reorient her forces at will since he is faced by the annoying internal constraints (particles obstructing each other) which plague most large and complex organizations (the microscopic world of particles sliding and rolling over each other).

It may seem logical to assume that if the demise of anisotropy is inhibited in some way, then so is its induction, but experimental evidence

reported by Oda et al. (1980) indicates that the principal directions of fabric (i.e., principal directions of the distribution of X or the second order tensor representation) match the principal directions of the applied stress tensor during a virgin or prime loading, even with continuous rotation of the principal stress axes. There appears to be no lag effect. Data presented by Oda (1972) describing the evolution of the contact normal distribution suggests that fabric induction practically ceases once the material starts to dilate. However, no firm conclusions can be drawn until many tests have been repeated and verified by the soil mechanics community as a whole.

2.4 Elasticity

We now turn our attention to the mathematical models used to simulate the stress-strain response of soil. In this section, the essential features of the three types of elasticity-based stress-strain relations are summarized (Eringen, 1962): 1) the Cauchy type, 2) the Hyperelastic (or Green) type, and 3) the incremental (or Hypoelastic) type. Although, in the strict sense, elastic implies fully recoverable response, it is sometimes convenient to pretend that total deformations are "elastic" and to disregard the elastic-plastic decomposition set forth in Equations 2.2.1 and 2.2.2. This approach has some practical applications to generally monotonic outward loading paths. For cases of unloading and reloading, however, this type of formulation will fail to predict the irrecoverable component of strain. One should not be mislead into believing that elasticity theory should be used exclusively for predicting one-way loading paths. Even in its most complicated forms, elasticity theory may fail to predict critical aspects of stress-strain behavior, many of which can be captured elegantly in plasticity theory.

2.4.1 Cauchy Type Elasticity

A Cauchy elastic material is one in which the current state of stress depends only on the current state of strain. Each stress component is a single-valued function of the strain tensor,

$$\sigma_{ij} = f_{ij} (\varepsilon_{kl}) \quad , \tag{2.4.1.1}$$

where f_{ij} are nine elastic response functions of the material. Since the stress tensor is symmetric, $f_{kl} = f_{lk}$ and the number of these independent functions reduce from nine to six. The choice of the functions f_{ij} must also satisfy the Principle of Material Frame Indifference previously mentioned in section 2.1; such functions are called hemitropic functions of their arguments. The stress $\underset{\sim}{\sigma}$ is an analytic isotropic function of $\underset{\sim}{\varepsilon}$ if and only if it can be expressed as (see, for example, Eringen, 1962; p. 158):

$$\sigma_{ij} = \phi_0 \delta_{ij} + \phi_1 \varepsilon_{ij} + \phi_2 \varepsilon_{im} \varepsilon_{mj} \quad , \tag{2.4.1.2}$$

where ϕ_0, ϕ_1, and ϕ_2 are functions only of the three strain invariants.

For a first order Cauchy elastic model, the second order strain termas vanish ($\phi_2 = 0$) and ϕ_0 is a linear function of the first strain invariant ε_{mm},

$$\sigma_{ij} = (\alpha_0 + \alpha_1 \varepsilon_{mm}) \delta_{ij} + \alpha_2 \varepsilon_{ij} \quad , \tag{2.4.1.3}$$

where α_0, α_1, α_2 are response coefficients. At zero strain, $\alpha_0 \delta_{ij}$ is the initial spherical stress. Higher order Cauchy elastic models can be formulated by letting the response functions ϕ_0, ϕ_1, and ϕ_2 depend on strain invariant polynomials of corresponding order. For example, the second order Cauchy elastic material is constructed by selecting as the response functions

$$\phi_0 = a_1 \varepsilon_{mm} + a_2 (\varepsilon_{mm})^2 + a_3 (\tfrac{1}{2} \varepsilon_{ij} \varepsilon_{ij}) \quad ,$$

$$\phi_1 = a_4 + a_5 \varepsilon_{mm} \quad ,$$

and

$$\phi_2 = a_6 \quad ,$$

where a_1, a_2,..., a_6 are material constants (Desai and Siriwardane, 1984).

An alternative interpretation of the first order Cauchy model is presented in order to show the link between the elastic bulk and shear moduli (K and G respectively) and Lame's constants (Γ and μ).For this material classification,

$$\sigma_{ij} = C_{ijkl}\ \varepsilon_{kl} \quad ,$$

where the components of C_{ijkl} are each a function of the strain components, or if isotropy is assumed, the strain invariants. Since both σ_{ij} and ε_{kl} are symmetric, the matric C_{ijkl} is also symmetric. A generalization of the second order tensor transformation formula to its fourth order analogue produces

$$C'_{ijkl} = Q_{ip}\ Q_{jq}\ Q_{kr}\ Q_{ls}\ C_{pqrs} \qquad (2.4.1.4)$$

as the transformation rule for the "elastic" stiffness tensor $\underset{\sim}{C}$. With the isotropy assumption, the material response must be indifferent to the orientation of the observer, and hence we must also insist that $\underset{\sim}{C}$ be equal to $\underset{\sim}{C}'$. A fourth order istropic tensor which obeys this transformation rule can be constructed from Kronecker deltas $\underset{\sim}{\delta}$ (see, for example, Synge and Schild, 1949, p. 211); the most general of these is

$$C_{ijkl} = \Gamma\ \delta_{ij}\ \delta_{kl} + \mu\ \delta_{ik}\ \delta_{jl} + \nu\ \delta_{il}\ \delta_{jk} \quad , \qquad (2.4.1.5)$$

where Γ, μ, and ν are invariants. From the symmetry requirement,

$$C_{ijkl} = C_{ijlk}, \qquad (2.4.1.6)$$

or

$$\Gamma\ \delta_{ij}\ \delta_{kl} + \mu\ \delta_{ik}\ \delta_{jl} + \nu\ \delta_{il}\ \delta_{jk} =$$

$$\Gamma\ \delta_{ij}\ \delta_{lk} + \mu\ \delta_{il}\ \delta_{jk} + \nu\ \delta_{ik}\ \delta_{jl}, \qquad (2.4.1.7)$$

and collecting terms,

$$(\mu - \nu)\ (\delta_{ik}\ \delta_{jl} - \delta_{il}\ \delta_{jk}) = 0 \quad , \qquad (2.4.1.8)$$

which implies that $\mu = \nu$. With this equality, Equation 2.4.1.5 simplifies to

$$C_{ijkl} = \Gamma\, \delta_{ij}\, \delta_{kl} + \mu\, (\delta_{ik}\, \delta_{jl} + \delta_{il}\, \delta_{jk}), \qquad (2.4.1.9)$$

where Γ and μ are Lame's elastic constants.

The incremental form of the first-order, istropic, elastic stress-strain relation is therefore

$$d\sigma_{ij} = [\, \Gamma\, \delta_{ij}\, \delta_{kl} + \mu\, (\delta_{ik}\, \delta_{jl} + \delta_{il}\, \delta_{jk})\,]\, d\varepsilon_{kl}$$

$$= \Gamma\, \delta_{ij}\, d\varepsilon_{mm} + 2\, \mu\, d\varepsilon_{ij}\ . \qquad (2.4.1.10)$$

Multiplication of both sides of this equation by the Kronecker delta δ_{ij} results in

$$d\sigma_{kk} = 3\, \Gamma\, d\varepsilon_{mm} + 2\, \mu\, d\varepsilon_{mm}, \qquad (2.4.1.11)$$

or

$$d\sigma_{kk}/3\, d\varepsilon_{mm} = K = \Gamma + \frac{2}{3}\, \mu\ ,$$

where K is the elastic bulk modulus.

Substituting the identities

$$d\sigma_{ij} = ds_{ij} + \frac{1}{3}\, d\sigma_{kk}\, \delta_{ij}$$

and

$$d\varepsilon_{ij} = de_{ij} + \frac{1}{3}\, d\varepsilon_{kk}\, \delta_{ij}$$

into Equation 2.4.1.10 results in

$$ds_{ij} + \frac{1}{3}\, d\sigma_{kk}\, \delta_{ij} = \Gamma\, \delta_{ij}\, d\varepsilon_{mm} + 2\, \mu\, (de_{ij} + \frac{1}{3}\, d\varepsilon_{kk}\, \delta_{ij})\ ,$$

and using Equation 2.4.1.11 in this expression shows that

$$ds_{ij}/2\, de_{ij} = G = \mu\ , \qquad (2.4.1.13)$$

where G is the elastic shear modulus.

Combining Equations 2.4.1.12 and 2.4.1.13 gives a more familiar form of the isotropic, elastic stiffness tensor, namely

$$C_{ijkl} = (K - \frac{2}{3} G)\, \delta_{ij}\, \delta_{kl} + G\, (\delta_{ik}\, \delta_{jl} + \delta_{il}\, \delta_{jk}) \quad . \qquad (2.4.1.14)$$

Many researchers have adapted this equation to simulate, on an incremental basis the non-linear response of soil; they have all essentially made K and G functions of the stress or strain level. Some of the better known applications can be found in Clough and Woodward, 1967; Girijavallabhan and Reese, 1968; Kulhawy et al., 1969; and Duncan and Chang, 1970.

2.4.2 Hyperelasticity or Green Type Elasticity

Green defined an elastic material as one for which a strain energy function, W, (or a complementary energy function, Ω) exists (quoted from Malvern, 1969, p. 282). The development of this theory was motivated by a need to satisfy thermodynamic admissibility, a major drawback of the Cauchy elastic formulation. Stresses or strains are computed from the energy functions as follows:

$$\sigma_{ij} = \frac{\partial W}{\partial \varepsilon_{ij}} \quad , \qquad (2.4.2.1)$$

and conversely,

$$\varepsilon_{ij} = \frac{\partial \Omega}{\partial \sigma_{ij}} \quad . \qquad (2.6.2.2)$$

For an initially isotropic material, the strain energy function, W, can be written out in the form (see, for example, Eringen, 1962)

$$W = W\,(\bar{I}_1, \bar{I}_2, \bar{I}_3) = A_0 + A_1\, \bar{I}_1 + A_2\, \bar{I}_2 + A_3\, \bar{I}_1^2 + A_4\, \bar{I}_1^3 +$$

$$A_5 \bar{I}_1 \bar{I}_2 + A_6 \bar{I}_3 + A_7 \bar{I}_1^4 + A_8 \bar{I}_1^2 I_2 +$$

$$A_9 \bar{I}_1 \bar{I}_3 + A_{10} \bar{I}_2^2 \quad , \qquad (2.4.2.3)$$

where $\bar{I}_1$, $\bar{I}_2$, and $\bar{I}_3$ are invariants of $\underset{\sim}{\varepsilon}$

$$\bar{I}_1 = \varepsilon_{kk}, \quad \bar{I}_2 = \frac{1}{2} \varepsilon_{ij} \varepsilon_{ij}, \quad \bar{I}_3 = \frac{1}{3} \varepsilon_{km} \varepsilon_{kn} \varepsilon_{mn} \quad ,$$

and A_k (k = 0,2..,10) are material constants determined from curve fitting. The stress components are obtained by partial differentiation,

$$\sigma_{ij} = \frac{\partial W}{\partial \bar{I}_1} \frac{\partial \bar{I}_1}{\partial \varepsilon_{ij}} + \frac{\partial W}{\partial \bar{I}_2} \frac{\partial \bar{I}_2}{\partial \varepsilon_{ij}} + \frac{\partial W}{\partial \bar{I}_3} \frac{\partial \bar{I}_3}{\partial \varepsilon_{ij}} \qquad (2.4.2.4)$$

$$= \phi_1 \delta_{ij} + \phi_2 \varepsilon_{ij} + \phi_3 \varepsilon_{im} \varepsilon_{mj} \quad , \qquad (2.4.2.5)$$

where ϕ_i (i = 1,2,3) are the response functions which must satisfy the condition $\partial \phi_i / \partial \bar{I}_j = \partial \phi_j / \partial \bar{I}_i$ in order to guarantee symmetry of the predicted stress tensor.

Different orders of hyperelastic models can be devised based on the powers of the independent variables retained in Equation 2.4.2.3. If, for instance, we keep terms up to the third power, we obtain a second-order hyperelastic law. These different orders can account for various aspects of soil behavior; dilatancy, for instance, can be realistically simulated by including the third term of Equation 2.4.2.3. Green's method and Cauchy's method lead to the same form of the stress-strain relationship if the material is assumed to be isotropic and the strains are small, but the existence of the

strain energy function in hyperelasticity imposes certain restrictions on the choice of the constitutive parameters. These are not pursued here, but the interested reader can find an in-depth discussion of these constraints in Eringen (1962). Also, detailed descriptions--including initialization procedures--for various orders of hyperelastic models can be found in Saleeb and Chen (1980), and Desai and Siriwardane (1984).

2.4.3 Hyperelasticity or Incremental Type Elasticity

This constitutive relation was introduced by Truesdell (1955) to describe a class of materials for which the current state of stress depends on the current state of strain and the history of the stress $\underset{\sim}{\sigma}^t$ (or the stress path). The incremental stress-strain relationship is usually written in the form

$$d\underset{\sim}{\sigma} = \underset{\sim}{f}(\underset{\sim}{\sigma}\ ,\ d\underset{\sim}{\varepsilon}) \quad , \tag{2.4.3.1}$$

where $\underset{\sim}{f}$ is a tensor valued function of the current stress $\underset{\sim}{\sigma}$, and the strain increment $d\underset{\sim}{\varepsilon}$. The principle of material frame indifference (or objectivity) imposes a restriction on $\underset{\sim}{f}$: it must obey the transformation

$$\underset{\sim}{Q}\ \underset{\sim}{f}(\underset{\sim}{\sigma},\ d\underset{\sim}{\varepsilon})\ \ \underset{\sim}{Q}^T = \underset{\sim}{f}(\underset{\sim}{Q}\ d\underset{\sim}{\varepsilon}\ \underset{\sim}{Q}^T,\ \underset{\sim}{Q}\ \underset{\sim}{\sigma}\ \underset{\sim}{Q}^T) \tag{2.4.3.2}$$

for any rotation $\underset{\sim}{Q}$ of the spatial reference frame. When $\underset{\sim}{f}$ satisfies this stipulation, it is, as mentioned in the previous section, a hemitropic function of $\underset{\sim}{\sigma}$ and $d\underset{\sim}{\varepsilon}$. A hemitropic polynomial representation of $\underset{\sim}{f}$ is (see, for example, Eringen, 1962, p. 256)

$$d\underset{\sim}{\sigma}' = \underset{\sim}{f}(\underset{\sim}{\sigma},\ d\underset{\sim}{\varepsilon}) = \alpha_0\ \mathrm{tr}(d\underset{\sim}{\varepsilon})\ \underset{\sim}{\delta} + \alpha_1\ d\underset{\sim}{\varepsilon} + \alpha_2\ \mathrm{tr}(d\underset{\sim}{\varepsilon})\ \underset{\sim}{\sigma}' +$$

$$\alpha_3\ \mathrm{tr}(\underset{\sim}{\sigma}'\ d\underset{\sim}{\varepsilon})\ \underset{\sim}{\delta} + \frac{1}{2}\ \alpha_4\ (d\underset{\sim}{\varepsilon}\ \underset{\sim}{\sigma}' + \underset{\sim}{\sigma}'\ d\underset{\sim}{\varepsilon}) + \alpha_5\ \mathrm{tr}(d\underset{\sim}{\varepsilon})\ \underset{\sim}{\sigma}'^2 +$$

$$\alpha_6\ \mathrm{tr}(\underset{\sim}{\sigma}'\ d\underset{\sim}{\varepsilon})\ \underset{\sim}{\sigma}' + \alpha_7\ \mathrm{tr}(\underset{\sim}{\sigma}'^2\ d\underset{\sim}{\varepsilon})\ \underset{\sim}{\delta} +$$

$$\frac{1}{2}\alpha_8 (d\underset{\sim}{\varepsilon}\,\underset{\sim}{\sigma}'^2 + \underset{\sim}{\sigma}'^2\, d\underset{\sim}{\varepsilon}) + \alpha_9\, tr(\underset{\sim}{\sigma}'\, d\underset{\sim}{\varepsilon})\,\underset{\sim}{\sigma}'^2 +$$

$$\alpha_{10}\, tr(\underset{\sim}{\sigma}'^2\, d\underset{\sim}{\varepsilon})\,\underset{\sim}{\sigma}' + \alpha_{11}\, tr(\underset{\sim}{\sigma}'^2\, d\underset{\sim}{\varepsilon})\,\underset{\sim}{\sigma}'^2 \quad , \qquad (2.4.3.3)$$

where $\underset{\sim}{\sigma}'$ is the nondimensional stress $\underset{\sim}{\sigma}/2\mu$ (μ being the Lame shear modulus of Equation 2.6.1.10), a_k ($k = 0,2,..,11$) are the constitutive constants and "tr" denotes the <u>trace</u> operator of a matrix (i.e., the sum of the diagonal terms). The constants a_k are usually dimensionless analytic functions of the three invariants of $\underset{\sim}{\sigma}'$, and these are determined by fitting curves to experimental results.

Various grades of hypoelastic idealizations can be extracted from Equation 2.4.3.3. This is accomplished by retaining up to and including certain powers of the dimensionless stress tensor $\underset{\sim}{\sigma}'$. A hypoelastic body of <u>grade zero</u> is independent of $\underset{\sim}{\sigma}'$, and in this case, the general form simplifies to

$$d\underset{\sim}{\sigma}' = \underset{\sim}{f}(\underset{\sim}{\sigma}, d\underset{\sim}{\varepsilon}) = \alpha_0\, tr(d\underset{\sim}{\varepsilon})\,\underset{\sim}{\delta} + \alpha_1\, d\underset{\sim}{\varepsilon} \quad . \qquad (2.4.3.4)$$

Comparing this equation with the first order Cauchy elastic model (Equation 2.4.1.10) shows that

$$\alpha_0 = \frac{\Gamma}{2\mu} \qquad \text{and} \qquad \alpha_1 = 1 \quad .$$

Similarly, a hypoelastic constitutive equation of <u>grade one</u> can be elicited from the general equation by keeping only the terms up to and including the first power of $\underset{\sim}{\sigma}'$,

$$d\underset{\sim}{\sigma}' = \underset{\sim}{f}(\underset{\sim}{\sigma}, d\underset{\sim}{\varepsilon}) = \alpha_0\, tr(d\underset{\sim}{\varepsilon})\,\underset{\sim}{\delta} + \alpha_1\, d\underset{\sim}{\varepsilon} + \alpha_2\, tr(d\underset{\sim}{\varepsilon})\,\underset{\sim}{\sigma}' +$$
$$\alpha_3\, tr(\underset{\sim}{\sigma}'\, d\underset{\sim}{\varepsilon})\,\underset{\sim}{\delta} + \frac{1}{2}\alpha_4 (d\underset{\sim}{\varepsilon}\,\underset{\sim}{\sigma}' + \underset{\sim}{\sigma}'\, d\underset{\sim}{\varepsilon}) \quad .$$

By a similar procedure, the description can be extended up to <u>grade two</u>, with the penalty being the task of fitting a larger number of parameters to the experimental data. These parameters must be determined from representative

laboratory tests using curve fitting and optimization techniques, and it often leads to uniqueness questions since it may be possible to fit more than one set of parameters to a given data set.

Romano (1974) proposed the following special form of the general hypoelastic equation to model the behavior of granular media:

$$d\sigma_{ij} = [\alpha_o \, d\varepsilon_{mm} + \alpha_3 \, \sigma_{pq} \, d\varepsilon_{pq}] \, \delta_{ij} + \alpha_1 \, d\varepsilon_{ij} + [\alpha_2 \, d\varepsilon_{mm} + \alpha_6 \, \sigma_{rs} \, d\varepsilon_{rs}]\sigma_{ij} \quad . \tag{2.4.3.5}$$

This particular choice ensures that the predicted stress increment is a linear function of the strain increment; in other words, if the input strain increment is doubled, then so is the output stress increment. Imposing linearity of the incremental stress-strain relation is one way of compelling the stress-strain relation to be rate-independent; a more general procedure for specifying rate indepedence will be described in the section on plasticity theory.

Davis and Mullenger (1978), working from Romano's equation, have developed a model which can simulate many aspects of real soil behavior. Essentially, they have used well-established empirical stress-strain relations and merged them with concepts from plasticity to arrive at restrictions on the interdependency of the constitutive parameters.

2.5 Plasticity

Having outlined the theories used to compute the elastic, or sometimes pseudo-elastic component $d\underset{\sim}{\varepsilon}^e$ of the total strain increment $d\underset{\sim}{\varepsilon}$, the next topic deals with the computation of its plastic conjugate $d\underset{\sim}{\varepsilon}^p$. This section prefaces the mathematical theory of plasticity, a framework for constitutive laws, which until 1952 (Drucker and Prager, 1952) remained strictly in the domain of metals. Over the past three decades, the role of elastic-plastic constitutive equations in soil mechanics has grown in importance with the development of sophisticated computers and computer--based numerical

techniques. These tools have significantly increased the geotechnical engineer's capacity to solve complicated boundary value problems. The three main ingredients for these modern solution techniques are computer hardware, numerical schemes, and stress-strain equations, and, of these, the development of constitutive laws for soils has lagged frustratingly behind.

The fundamentals of plasticity theory still remain a mystery to many geotechnical engineers. It is very likely that a newcomer to this field will find considerable difficulty in understanding the literature, usually written in highly abstruse language. The chief objective of this section is to provide some insight into plasticity theory by highlighting the basic postulates, with special emphasis on their applicability and applications to soil mechanics.

In brief, plasticity theory answers these questions:

a) When does a material plastically flow or yield? Or more directly, how do we specify all possible stress states where plastic deformation starts? The answer to this question lies in the representation of these stress states by yield surfaces. Also underlying this discussion are the definitions of and the possible interpretations of yield.

b) Once the material reaches a yield stress state, how are the plastic strains computed? And, if the stress path goes beyond the initial yield surface (if an initial one is postulated), what happens to the original yield surface (if anything)? The first question is addressed in the discussion on the flow rule (or the incremental plastic stress-strain relation), while the second is treated in the discussion on hardening rules.

2.5.1 Yield Surface

Perhaps the best starting point for a discussion of plasticity is to introduce, or rather draw attention to, the concept of a yield surface in stress space. At the outset, it should be noted that yield is a matter of definition, and only the conventional interpretations will be mentioned in this chapter. The reader is, however, urged to keep an open mind on this subject since a different perspective, within the framework of a new theory for sands, will be proposed in Chapter 3.

Since strength of materials is a concept that is familiar to geotechnical engineers, it is used here as the stimulus for the introduction to yield surfaces. Figure 2.5 shows a variety of uniaxial rate-insensitive stress-strain idealizations. In particular, Figures 2.5 (d) and (e) show examples of perfectly plastic response, and one may infer from this that yield and failure are equivalent concepts for this simplest idealization of plastic response.

In the calculation of the stability of earth structures, the Mohr-Coulomb failure criterion is typically used to estimate the maximum loads a structure can support. That is, when this load is reached, the shear stress to normal stress ratio is assumed to be at its peak value at all points within certain zones of failure. This method of analysis is known as the limit equilibrium method. Using the classification set forth in section 2.2, it is a kinematically ambiguous theory in that no strains are predicted. Another common method of analysis is the wedge analysis method. This is a trial and error procedure to find the critical failure plane, a failure plane being a plane on which the full strength of the material is mobilized and the critical plane being the one that minimizes the magnitude of the imposed load.

A feature common to both the limiting equilibrium and the wedge analysis methods is the need to provide a link between the shear and normal stress at

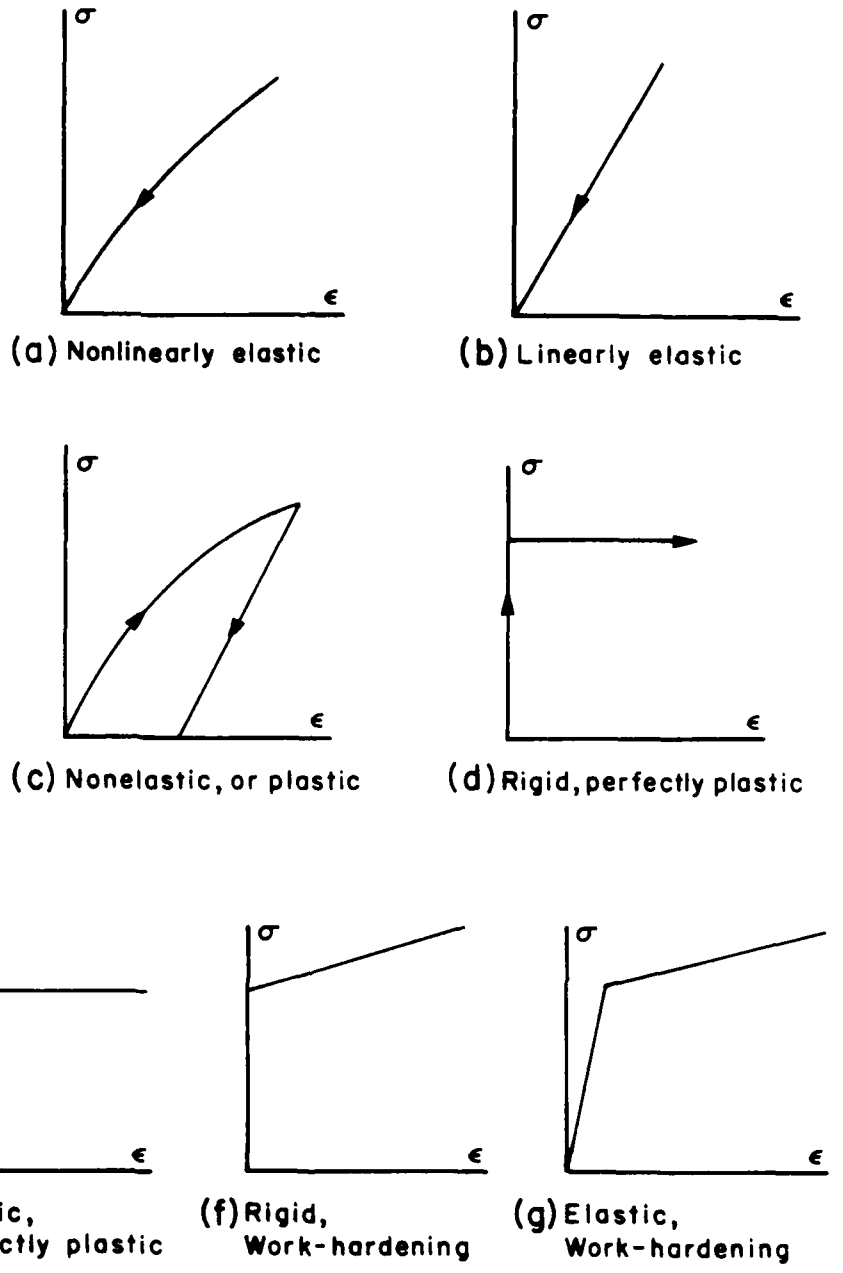

Figure 2.5 Rate-independent idealizations of stress-strain response

failure. A constitutive law, which is a manifestation of the internal constitution of the material, provides this information. More generally, the kinematically ambiguous theories for a perfectly plastic solid must specify the coordinates of all possible failure points in a nine dimensional stress space. Mathematically, this is accomplished by writing a failure function or criterion in the form $F(\sigma_{ij}) = 0$; many well-established forms of the yield function are previewed in the following.

The Mohr-Coulomb frictional failure criterion states that shear strength increases linearly with increasing normal stress, Figure 2.6. For states of stress below the failure or limit or yield line, the material may be considered rigid [Fig. 2.5 (d)] or elastic [Fig. 2.5 (e)]. For a more general description, it is necessary to extend the two-dimensional yield curve of Figure 2.6 to a nine-dimensional stress space. Although such a space need not be regarded as having an actual physical existence, it is an extremely valuable concept because the language of geometry may be applied with reference to it (Synge and Schild, 1949). The set of values σ_{11}, σ_{12}, σ_{13}, σ_{21}, σ_{22}, σ_{23}, σ_{31}, σ_{32}, and σ_{33} is called a point, and the variables σ_{ij} are the coordinates. The totality of points corresponding to all values of say N coordinates within certain ranges constitute a space of N dimensions denoted by V_N. Other terms commonly used for V_N are hyperspace, manifold, or variety.

Inspection of, say, the equation of a sphere in rectangular cartesian coordinates (x,y,z),

$$F(x,y,z) = (x - a)^2 + (y - b)^2 + (z - c)^2 - K^2 = 0$$

where a, b, and c are the center coordinates and k is the radius, is a simple way of showing that the nine-dimensional equivalent of a stationary surface in

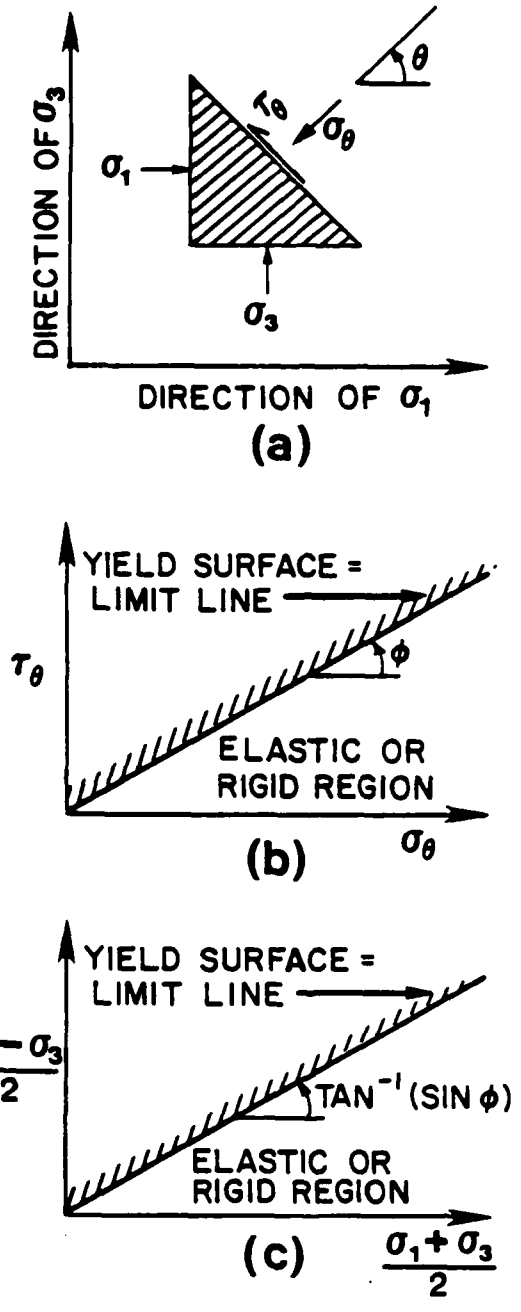

Figure 2.6 Two dimensional picture of Mohr-Coulomb failure criterion

stress space may be expressed as:

$$F(\sigma_{ij}) = 0 \quad . \tag{2.5.1.1}$$

A surface in four or more dimensions is called a hypersurface. The theoretician must therefore postulate a mechanism of yield which leads directly to the formulation of a yield surface in stress space or he must fit a surface through observed yield points.

Rigorously speaking, a yield stress (or point) is a stress state which marks the onset of plastic or irrecoverable strain and which may lie within the failure surface. Yield surfaces specify the coordinates of the entirety of yield stress states. These (not necessarily closed) surfaces bound a region in stress space where the material behavior is elastic. But an all-important practical question still looms: How can we tell exactly where plastic deformation begins? Is the transition from elastic to elastic-plastic response distinct? At least for soils, it is not that simple a task. The stress-strain curves continuously turn, and plastic deformation probably occurs to some extent at all stress states for outward loading paths. However, for the perfectly plastic idealization, there should be no major difficulty since the limit states are usually easy to identify.

Among the techniques used to locate the inception of yield are:

a) for materials like steel with a sharp yield point, the yield stress is usually taken as the plateau in stress that occurs just after the yield point;

b) for soft metals like aluminium, the yield stress is defined as the stress corresponding to a small value of permanent strain (usually 0.2%);

c) a large offset definition may be chosen which more or less gives the failure stress;

d) a tangent modulus definition may be used, but it must be normalized if mean stress influences response; and

e) for materials like sand which apparently yield even at low stress levels, a Taylor-Quinney (1931) definition is used. This and some of the alternative definitions are illustrated in Figure 2.7.

Soil mechanicians will identify the Taylor-Quinney definition with the Casagrande procedure (Casagrande, 1936) for estimating the preconsolidation pressure of clays.

Defining a yield surface using the methods outlined above usually leads to one with a shape similar to that of the failure or limit surface. However, in Chapter 3, an alternative approach will be suggested for determining the shape of the yield surface based on the observed trajectory of the plastic strain increment--for sands, these surfaces have shapes much different from the typical failure or yield surfaces.

2.5.2 Failure Criteria

If an existing testing device had the capability to simultaneously apply the six independent components of stress to a specimen, the yield function $F(\sigma_{ij}) = 0$ could be fitted to a comprehensive data set. Unfortunately, such equipment is not available at present, and most researchers still rely on the standard triaxial test (Bishop and Henkel, 1962). However, if the material is assumed to be isotropic, as is usually done, then the number of independent variables in the yield functions reduces from six to three; i.e., the three stress invariants or three principal stresses replace the six independent components of $\underset{\sim}{\sigma}$. In other words, material directions are not important, only the intensity of the stress is. Therefore, by ignoring anisotropy, all that the theoretician needs is a device, like the cubical triaxial device, which can vary

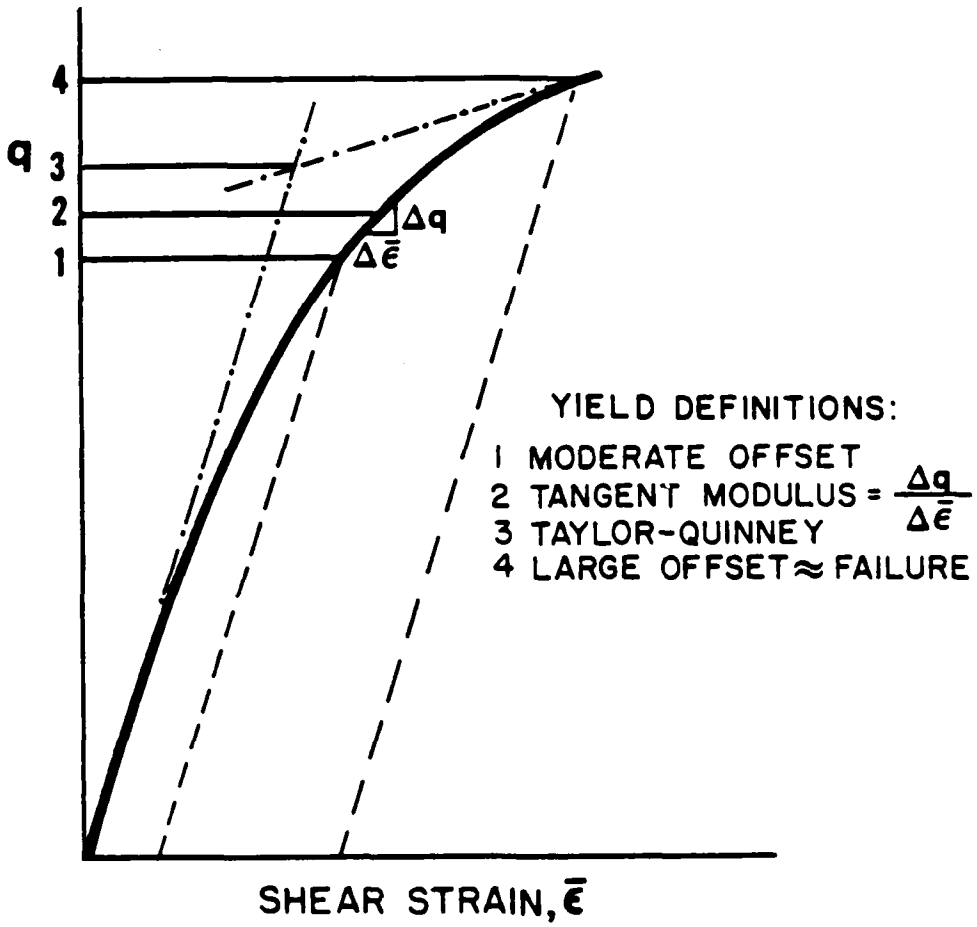

Figure 2.7 Commonly adopted techniques for locating the yield stress

σ_1, σ_2, and σ_3 independently.

Another implication of the isotropy assumption is that stress data can be plotted in a three dimensional stress space with the principal stresses as axes. This stress space is known as the Haigh-Westergaard stress space (Hill, 1950). Working in this stress space has the pleasant consequence of an intuitive geometric interpretation for a special set of three independent stress invariants. In order to see them, the rectangular coordinate reference system (σ_1, σ_2, σ_3) must be transformed to an equivalent cylindrical coordinate system (r, θ, z) as described in the following.

Figure 2.8 depicts a yield surface in Haigh-Westergaard (or principal) stress space. The hydrostatic axis is defined by the line

$$\sigma_1 = \sigma_2 = \sigma_3 ,$$

which is identified with the axis of revolution (z) perpendicular to the plane at the origin of a polar system. For cohesionless soils (no tensile strenth), the origin of stress space is also the origin of this axis. The perpendicular plane is called the deviatoric or octahedral plane and is given by

$$\sigma_1 + \sigma_2 + \sigma_3 = \text{constant} .$$

When this constant is equal to zero, the octahedral plane passes through the orgin of stress space and is then known as a π plane.

If we perform a constant pressure test (paths TC or TE of Figure 2.3), the stress point follows a curve on a fixed deviatoric plane for the entire loading. Such stress paths provide a useful method for probing the shape and/or size of the yield surface's π-plane projection for different levels of mean stress. Polar coordinates (r, θ) are used to locate stress points on a given deviatoric plane.

By elementary vector operations, the polar coordinates r, θ, and z can be correlated to each of the stress invariants $\sqrt{J_2}$, θ and I_1, which are defined

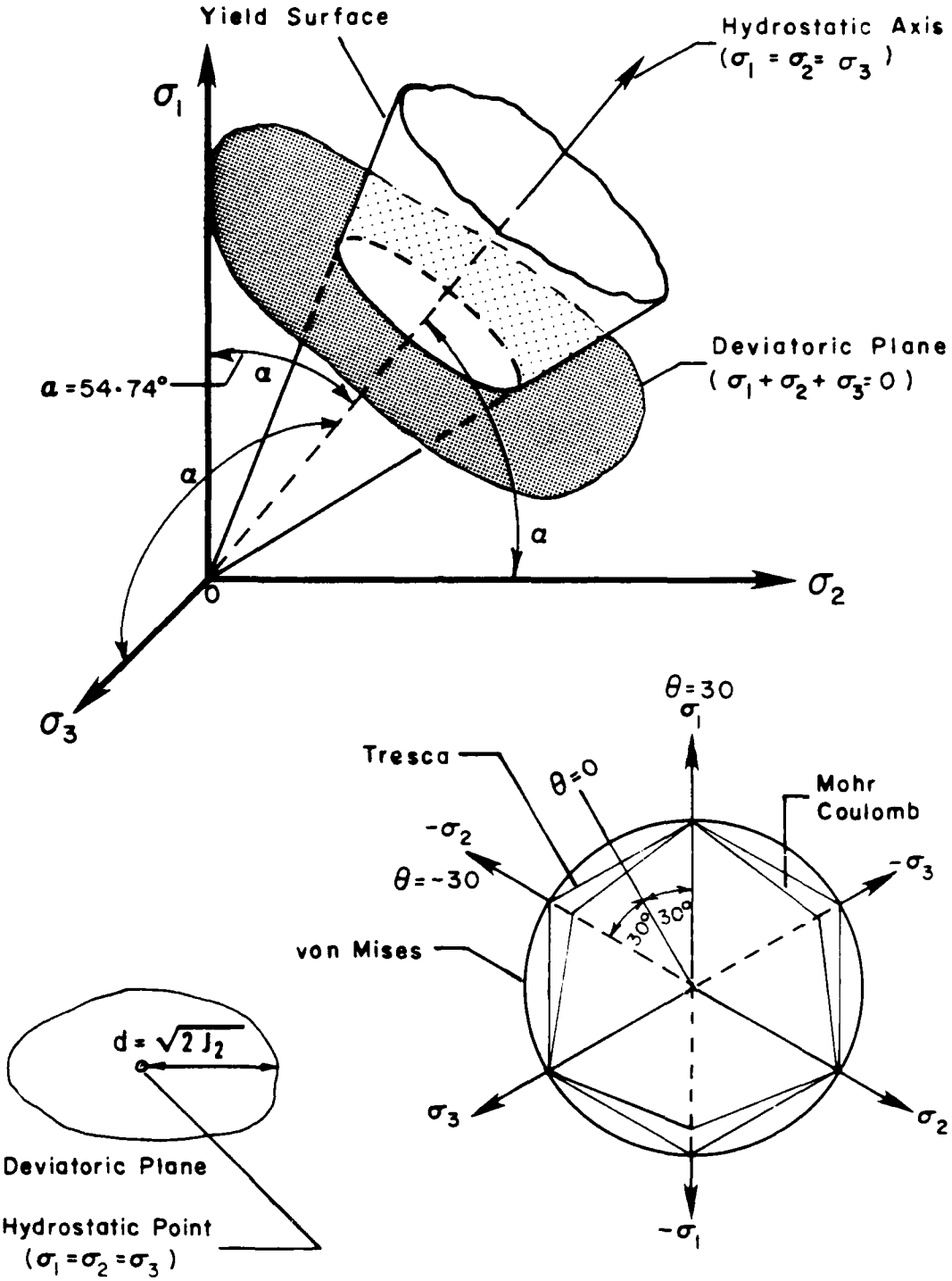

Figure 2.8 Yield surface representation in Haigh-Westergaard stress space

as:

$$I_1 = \sigma_{11} + \sigma_{22} + \sigma_{33}$$

$$J_2 = \frac{1}{2} S_{ij} S_{ij} \qquad (2.5.2.1)$$

$$J_3 = \frac{1}{3} S_{ij} S_{jk} S_{ki}$$

$$\theta = \frac{1}{3} \sin^{-1} \left[\frac{3\sqrt{3}}{2} \left(\frac{J_3}{J_2^{3/2}}\right)\right]$$

where

$$S_{ij} = \sigma_{ij} - \frac{1}{3} I_1 \delta_{ij} \ .$$

Other stress invariants of interest used in describing the Haigh-Westergaard stress space are

$$I_2 = -(\sigma_{11} \sigma_{22} + \sigma_{22} \sigma_{33} + \sigma_{11}) + \sigma_{23}^2 + \sigma_{31}^2 + \sigma_{12}^2 \qquad (2.5.2.2)$$

and the determinant of the stress tensor

$$I_3 = \begin{vmatrix} \sigma_{11} & \sigma_{12} & \sigma_{13} \\ \sigma_{21} & \sigma_{22} & \sigma_{23} \\ \sigma_{31} & \sigma_{32} & \sigma_{33} \end{vmatrix} \qquad (2.5.2.3)$$

A measure of the shear stress intensity is given by the radius

$$r = \sqrt{(2J_2)} \qquad 2.5.2.4)$$

from the hydrostatic point on the octahedral plane to the stress point.

The polar angle shown in Figure 2.8 is the same as the Lode angle θ . It provides a quantitative measure of the relative magnitude of the intermediate principal stress (σ_2) . For example,

$\sigma_2 = \sigma_3$ (compression test) $\rightarrow \theta = +30^0$

$$\sigma_1 = \sigma_2 \qquad \text{(extension tests)} \qquad \rightarrow \quad \theta = -30^0$$

and

$$\sigma_1 + \sigma_3 = 2\,\sigma_2 \qquad \text{(torsion tests)} \qquad \rightarrow \quad \theta = 0^0 \ .$$

Lastly, the average pressure, an important consideration for frictional materials, is proportional to the perpendicular distance "d" from the origin of stress space to the deviatoric plane;

$$d = I_1/\sqrt{3} \ , \tag{2.5.2.5}$$

where I_1 is the first invariant of $\underset{\sim}{\sigma}$.

For isotropic materials, the yield function (Equation 2.5.1.1) may therefore be recast in an easily visualized form (Figure 2.8)

$$F(I_1, \sqrt{J_2}, \theta) = 0 \ . \tag{2.5.2.6}$$

Some of the more popular failure/yield criterion for istropic soils and metals are reviewed in the following.

The much used Mohr-Coulomb failure criteria (Coulomb, 1773) for soils is usually encountered in practice as:

$$(\sigma_1 - \sigma_3) \div (\sigma_1 + \sigma_3) = \sin \phi = k \ , \tag{2.5.2.7}$$

where ϕ is a constant termed the angle of internal friction. The symbol "k" is used as a generic parameter in this section to represent the size of yield surfaces. This criteria asserts that plastic flow occurs when the shear stress to normal stress ratio on a plane reaches a critical maximum. If the equations which express the principal stresses in terms of the stress invariants (Equation 2.5.2.1) are substituted into Equation 2.5.2.7, the Mohr-Coulomb criteria can be generalized to (Shield, 1955)

$$F = \frac{I_1}{3} \sin \phi + \sqrt{J_2}\left\{ \frac{\sin \theta \ \sin \phi}{\sqrt{3}} - \cos \theta \right\} = 0 \tag{2.5.2.8}$$

A trace of this locus on the π plane is shown in Figure 2.8. The surface plots as in irregular hexagonal pyramid with its apex at the origin of stress space for non-cohesive soils.

Also depicted in this figure are the well-known Tresca and Mises yield surfaces used in metal plasticity, Mises (1928) postulated a yield representation of the form

$$F = \sqrt{J_2} - k = 0 \quad , \tag{2.5.2.9}$$

and physically, this criteria can be interpreted to mean that plastic flow commences when the load-deformation process produces a critical strain energy of distortion (i.e., strain energy neglecting the effects of hydrostatic pressure and volume change).

Tresca (1868), on the other hand, hypothesized that a metal will flow plastically when the shear stress on any plane through the point reaches a peak value. By calling to mind the Mohr's circle stress representation, the radius of the largest circle $[(\sigma_1 - \sigma_3)/2]$ is the maximum shear stress. Replacing the principal stresses with the stress invariants gives the following alternate form for the Tresca criterion:

$$F = \frac{-1}{\sqrt{3}} \sqrt{J_2} \left[\sin\left(\theta + \frac{4}{3}\pi\right) - \sin\left(\theta + \frac{2}{3}\pi\right) \right] - k = 0 \quad .$$

which, upon expanding the trigonometric terms, simplifies to

$$F = \sqrt{J_2} \cos\theta - k = 0 \quad . \tag{2.5.2.10}$$

A noticeable difference between the Mises or Tresca criterion and the Mohr-Coulomb criterion is the absence of the variable I_1 in the former. This reminds us that yielding of metals is usually not considered to be dependent on hydrostatic pressure, as the experiments of Bridgman (1945) have demonstrated.

Drucker and Prager (1952) modified the Mises criteria to account for pressure-sensitivity and proposed the form

$$F = \frac{\sqrt{J_2}}{I_1} - k = 0 \quad . \tag{2.5.2.11}$$

To match the Drucker-Prager and Mohr-Coulomb yield points in compression space ($\sigma_2 = \sigma_3$), one must use

$$k = \frac{2 \sin \phi}{\sqrt{3}\,(3 - \sin \phi)} \quad , \tag{2.5.2.12}$$

but, to obtain coincidence in extension space ($\sigma_1 = \sigma_2$) ,

$$k = \frac{2 \sin \phi}{\sqrt{3}\,(3 + \sin \phi)} \tag{2.5.2.13}$$

must be specified. Although the development of the Drucker-Prager yield function was motivated mainly by mathematical convenience, it has been widely applied to soil and rock mechanics. However, there is considerable evidence to indicate that the Mohr-Coulomb law provides a better fit to experimental results (see, for example, Bishop, 1966).

Scrutiny of sketches of the previously defined yield surfaces in principal stress space (see Figure 2.8) reveals that they are all "open" along the hydrostatic stress axis. Therefore, for an isotropic compression path, no plastic strains will be predicted. This contradicts the typical behavior observed along such paths, Figure 2.1. Recognizing this dificiency, Drucker et al. (1957) capped the Drucker-Prager cone with a sphere to allow for plastic yielding for generally outward but non-failure loading paths. The equation for the spherical cap (of radius k) centered on the origin of stress space can be derived by rearranging Equation 2.5.2.2,

$$F(\sigma_{ij}) = \sigma_{ij}\sigma_{ij} - k^2 = I_1^2 - 2\, I_2 - k^2 = 0 \quad . \tag{2.5.2.14}$$

As a result of the development of more sophisticated testing devices, sensing equipment, and data capture units, more reliable and reproducible stress-strain data is becoming available. This has quite naturally led to the development of many new mathematical representations of yielding in soils. Most notably, Lade and Duncan (1975), using a comprehensive series of test data obtained from a true triaxial device (Lade, 1973), have suggested that failure is most accurately modeled by the function

$$F = (I_1^3/I_3)\ (I_1/p_a)^m - k = 0 \quad , \tag{2.5.2.15}$$

where I_3 is the third stress invariant defined in Equation 2.5.2.3, p_a is the atmospheric pressure in consistent units, and m is a constant to model deviation from purely frictional response. A spherical cap was subsequently added by Lade (1977) to "close"this "open-ended" function along the hydrostatic axis.

Another recent proposal, based on a sliding model, was put forward by Matsuoka and Nakai (1974). They defined the spatial mobilized plane as the plane on which soil particles are most mobilized on the average in three dimensional stress space. Only for special cases when any two of the three principal stresses are equal does this criterion coincide with the Mohr-Coulomb criterion. Based on the postulate that the shear/normal stress ratio on the spatial mobilized plan governs failure, Matsuoka and Nakai have derived the following failure criterion:

$$F = \sqrt{\left[\frac{I_1\ I_2 - 9\ I_3}{9\ I_3}\right]} - k = 0 \quad . \tag{2.5.2.16}$$

The mobilized plane concept is essentially a three-demmensional extension of the Mohr-Coulomb criteria that takes into account the relative weight of the intermediate principal stress.

Even more recently, Desai (1980) has shown that the Mises, Drucker-Prager, Lade, and Matsuoka surfaces are all special cases of a general third-order tensor invariant polynomial he proposed. Using statistical analyses, he found that the failure criterion

$$F = [I_2 + (I_1 I_3^{1/3})] - k = 0 \qquad (2.5.2.17)$$

gave the best fit to experimental data sets on Ottawa sand and an artificial soil. Research in this field in presently very active, and as more high quality data becomes available, it is anticipated that even more proposals for failure/yield functions will emerge in the near future.

2.5.3 Incremental Plastic Stress-Strain Relation, and Prager's Theory

A material at yield signals the onset of plastic strain, and this section describes the computation of the resulting plastic strain increment. By definition, plasticity theory excludes any influence of the rate of application of the stress increment on the predicted plastic strain increment, and as will be shown later, this leads to restrictions on the possible forms of the stress-strain relation.

In analogy to the flow lines and equipotential lines used in seepage analysis, the existence of a plastic potential, G, in stress space can be postulated such that (Mises, 1928)

$$d\varepsilon^p_{ij} = \Lambda \frac{\partial G}{\partial \sigma_{ij}} \quad , \Lambda > 0 \qquad (2.5.3.1)$$

where Λ is a scalar factor which controls the magnitude of the generated plastic strain increment, and G is a surface in stress space (like the yield surface) that dictates the direction of the plastic strain increment. More specifically, the plastic strain increment is perpendicular to the level surface $G(\sigma_{ij}) = 0$ at the stress point.

To get a better grasp of Equation 2.5.3.1, the soils engineer may think of the function G as a fixed equipotential line in a flow net problem. The partial derivatives $\partial G/\partial \sigma_{ij}$ specify the coordinate components of a vector pointing in the direction perpendicular to the equipotential. This direction is, in fact, the direction of flow (along a flow line) of a particle of water instantaneously at the spatial point. Supplanting now the spatial coordinates (x,y,z) of the seepage problem with stress axes (σ_x, σ_y σ_z), while keeping the potential and flow lines in place, illustrates the mathematical connection between the movement of a particle of water and the plastic deformation of a soil element. The plastic geometrical change of a soil element is in a direction perpendicular to the equipotential surface $G(\sigma_{ij}) = 0$. At different points in the flow problem, the particles of water move at speeds governed by Darcy's law; therefore, it is possible to construct a scalar point function which gives the speed at each location. In an equivalent manner, the scalar multiplier Λ in Equation 2.5.3.1 determines the speed (or equivalently, the magnitude of the incremental deformation) of the soil particle at different locations in stress space. For example, the closer the stress point is to the failure line, a larger magnitude of Λ (with a corresponding larger magnitude of $d\underset{\sim}{\varepsilon}^p$) is expected. Therefore, in the crudest sense, the two elements of plasticity theory which immediately confront us are: a) the specification of the <u>direction</u> of the plastic strain increment through a choice of the function $G(\sigma_{ij})$, and b) the computation of the <u>magnitude</u> of $d\underset{\sim}{\varepsilon}^p$. There are, of course, other important questions to be answered, such as "What does the subsequent yield surface look like?", and these will be treated in later sections and the next chapter.

Mises (1928) made the assumption that the yield surface and the plastic potential coincide and proposed the stress-strain relation

$$d\varepsilon^p_{ij} = \Lambda \frac{\partial F}{\partial \sigma_{ij}} \quad . \tag{2.5.3.2}$$

This suggests a strong connection between the flow law and the yield criterion. When this assumption is made, the flow rule (Equation 2.5.3.1) is said to be associated and Equation 2.5.3.2 is called the normality rule. However, if we do not insist upon associating the plastic potential with the yield function (as suggested by Melan, 1938), the flow rule is termed non-associated. The implications of the normality rule, it turns out, are far reaching, and as a first step to an incisive understanding of them, Prager's (1949) treatment of the incremental plastic stress-strain relation will be summarized.

The first assumption is designed to preclude the effects of rate of loading, and it requires the constitutive equation

$$d\underset{\sim}{\varepsilon}^p = \hat{d\underset{\sim}{\varepsilon}^p} \; (\underset{\sim}{\sigma}, d\underset{\sim}{\sigma}, \underset{\sim}{q}_\eta)$$

to be homogenous of degree one in the stress increment $d\underset{\sim}{\sigma}$. Recall that homogeneity of order n ensures that

$$d\underset{\sim}{\varepsilon}^p = \hat{d\underset{\sim}{\varepsilon}^p} \; (\underset{\sim}{\sigma}^t, \Lambda \, d\underset{\sim}{\sigma} \, \underset{\sim}{q}_\eta) = \Lambda^n \, \hat{d\underset{\sim}{\varepsilon}^p} \; (\underset{\sim}{\sigma}^t, d\underset{\sim}{\sigma}, \underset{\sim}{q}_\eta) \; , \tag{2.5.3.3}$$

where Λ is a positive constant.

A simple example will help clarify this seemingly complex mathematical statement. Suppose an axial stress increment of 1 psi produced an axial plastic strain increment of .01%; this means that if Λ is equal to 2, the stress increment of 2 psi (Λ x 1 psi) will predict a plastic strain increment of .02% (Λ x .01%) . Ideally then, the solution should be independent of the stress increment, provided the stiffness change is negligible over the range of stress spanned by the stress increment.

The simplest option, which ensures homogeneity of order one, is the linear form

$$d\varepsilon^{p}_{ij} = D_{ijkl}\, d\sigma_{kl} \quad , \qquad (2.5.3.4)$$

where $\underset{\sim}{D}$ is a fourth order plastic compliance tensor, the components of which may depend on the stress history $\underset{\sim}{\sigma}^{t}$, the strain history $\underset{\sim}{\varepsilon}^{t}$, the fabric parameter, etc., but not on the stress increment $d\underset{\sim}{\sigma}$. This is referred to as the linearity assumption.

The second assumption, the condition of continuity, is intended to eliminate the possibility of jump discontinuities in the stress-strain curve as the stress state either penetrates the elastic domain (i.e., the yield hypersurface) from within or is unloaded from a plastic state back into the elastic regime. To guarantee a smooth transition from elastic to elastic-plastic response and vice-versa, a limiting stress increment vector, $d\underset{\sim}{\sigma}^{t}$, tangential to the exterior of the yield surface must produce no plastic strain. As a consequence, an infinitesimal change of stress, $d\underset{\sim}{\sigma}$, added to a body at yield [i.e., $F(\underset{\sim}{\sigma}) - k = 0$ is satisfied] gives rise to three possibilities:

$$\text{a)}\ \frac{\partial F}{\partial \underset{\sim}{\sigma}} : d\underset{\sim}{\sigma} < 0 \rightarrow \text{pure elastic response (unloading)} \qquad (2.5.3.5)$$

$$\text{b)}\ \frac{\partial F}{\partial \underset{\sim}{\sigma}} : d\underset{\sim}{\sigma} = 0 \rightarrow \text{pure elastic response (neutral loading)} \qquad (2.5.3.6)$$

or

$$\text{c)}\ \frac{\partial F}{\partial \underset{\sim}{\sigma}} : d\underset{\sim}{\sigma} > 0 \rightarrow \text{elastic \& plastic response (loading).} \qquad (2.5.3.7)$$

The notation ":" is the double contraction operator used here to compactly denote the scalar produce $\frac{\partial F}{\partial \sigma_{ij}} d\sigma_{ij}$ (see, for instance, Malvern, 1969).

A further implication of the continuity condition can be deduced by decomposing an arbitrary stress increment $d\underset{\sim}{\sigma}$ into its components normal ($d\underset{\sim}{\sigma}^n$) and tangential ($d\underset{\sim}{\sigma}^t$) to the yield surface,

$$d\underset{\sim}{\sigma} = d\underset{\sim}{\sigma}^t + d\underset{\sim}{\sigma}^n \quad .$$

Since the incremental stress-strain relation is linear, we can superpose the individual effects of $d\underset{\sim}{\sigma}^t$ and $d\underset{\sim}{\sigma}^n$ to obtain the combined effect of $d\underset{\sim}{\sigma}$. But we know that $d\underset{\sim}{\sigma}^t$ constitutes a neutral loading and generates no plastic strain. Therefore, plastic loading is attributed only to the normal component ($d\underset{\sim}{\sigma}^n$) of $d\underset{\sim}{\sigma}$.

$$d\underset{\sim}{\varepsilon}^p \propto \left| d\underset{\sim}{\sigma}^n \right| = d\underset{\sim}{\sigma} : \underset{\sim}{n} = d\underset{\sim}{\sigma} : \nabla \underset{\sim}{F} / \left| \nabla \underset{\sim}{F} \right| \quad , \qquad (2.5.3.8)$$

where $\underset{\sim}{n}$ is the unit tensor normal to the yield surface, ∇ is a vector differential operator which means, for example, that for the scalar function $F(x,y,z) = 0$,

$$\nabla \underset{\sim}{F} = \frac{\partial F}{\partial x} \underset{\sim}{i} + \frac{\partial F}{\partial y} \underset{\sim}{j} + \frac{\partial F}{\partial z} \underset{\sim}{k} \quad .$$

In his presentation of the restrictions imposed by the uniqueness condition, Prager (1949) made use of the following boundary value problem: given the instantaneous mechanical state in a body together with a system of infinitesimal added surface tractions, find the corresponding stress increments throughout the body. A reasonable demand is that plasticity theory predict a unique solution to the problem. But let us assume that the boundary value problem admits two solutions. Say these two solutions resulted in a difference between the predicted stress increments at a given point of the body equal to $\nabla(d\underset{\sim}{\sigma})$, and similarly, differences in elastic and plastic strain

increments equal to $\Delta(d\underset{\sim}{\varepsilon}^e)$ and $\Delta(d\underset{\sim}{\varepsilon}^p)$ respectively. Now, since the two solutions correspond to the same increment of surface tractions on a body of volume V, the principle of virtual work requires that

$$\int_V [\ \Delta(d\underset{\sim}{\sigma}) \ : \ \{\Delta(d\underset{\sim}{\varepsilon}^e) + \Delta(d\underset{\sim}{\varepsilon}^p)\}\ ]\, dV = 0, \qquad (2.5.3.9)$$

with the integrand being positive definite. By virtue of Hooke's law the quanity

$$\Delta(d\underset{\sim}{\sigma}):\Delta(d\underset{\sim}{\varepsilon}^e)$$

will always be positive definite so proof of the uniqueness condition is actually a proof that the quantity

$$\Delta(d\underset{\sim}{\sigma}) : \Delta(d\underset{\sim}{\varepsilon}^p) \qquad (2.7.3.10)$$

is positive definite.

In considering Equation 2.5.3.10, three cases must be examined: a) both solutions result in unloading, b) both solutions involve loading, and c) one solution is an unloading event while the other is a plastic loading process. For the first case, $d\underset{\sim}{\varepsilon}^p$ is zero for both instances and Equation 2.5.3.10 vanishes trivially. To investigate the second case, we label the two "loading" solutions as $d\underset{\sim}{\sigma}^{(1)}$ and $d\underset{\sim}{\sigma}^{(2)}$ and require that the plastic strain increment be directed such that Equation 2.5.3.10 is always positive. The limiting scenario occurs when $d\underset{\sim}{\sigma}^{(1)}$ and $d\underset{\sim}{\sigma}^{(2)}$ are both tangential to the yield surface but directed in an opposite sense. Therefore, the only provision which will ensure this is a plastic strain increment directed along the outward normal to the yield surface--i.e., the normality condition. The arguments for case 3 parallel those for case 2, and we can conclude that a sufficient condition for uniqueness of a boundary value problem is that the

flow rule be associated and that normality of the plastic strain increment apply,

$$d\varepsilon^p_{ij} \propto \frac{\nabla \underset{\sim}{F}}{|\nabla \underset{\sim}{F}|} \quad . \tag{2.5.3.11}$$

By merging the linearity, the continuity, and the uniqueness conditions--Equations 2.5.3.4, 2.5.3.8, and 2.5.3.11 respectively--, the flow rule takes the form

$$d\underset{\sim}{\varepsilon}^p = \frac{1}{K_p} \frac{\nabla \underset{\sim}{F}}{|\nabla \underset{\sim}{F}|} \{ \frac{\nabla \underset{\sim}{F}}{|\nabla \underset{\sim}{F}|} : d\underset{\sim}{\sigma} \} \quad , K_p > 0 \tag{2.5.3.12}$$

where, for reasons which will become apparent later, the scalar K_p (the generalized plastic modulus) is used instead of its inverse. Equation 2.5.3.12 is valid only if the stress state resides on a yield surface [i.e., $F(\sigma) = 0$] and a plastic loading event is taking place ($\underset{\sim}{n}:d\underset{\sim}{\sigma} > 0$] . For non-associative flow, Equation 2.5.3.12 is modified to

$$d\underset{\sim}{\varepsilon}^p = \frac{1}{K_p} \frac{\nabla \underset{\sim}{G}}{|\nabla \underset{\sim}{G}|} \{ \frac{\nabla \underset{\sim}{F}}{|\nabla \underset{\sim}{F}|} : d\sigma \} \quad , \quad K_p > 0 \tag{2.5.3.13}$$

where G is the plastic potential, a surface distinct from the yield surface F.

Frequently in the literature on plasticity, the quantity

$$L = \frac{1}{K_p} \{ \frac{\nabla \underset{\sim}{F}}{|\nabla \underset{\sim}{F}|} : d\sigma \} \tag{2.5.3.14}$$

is synthesized as a single term and designated the loading function or loading index "L". With this terminology, the flow rule is then encountered as:

$$d\varepsilon^p_{ij} = L\, m_{ij} \quad , \tag{2.5.3.15}$$

where m_{ij} are the components of the unit gradient tensor to the plastic potential G.

If incremental plastic deformation takes place, the stress point, which was initially on a yield surface, must move to another plastic state. This means that the updated stress point must reside on another yield surface or a transformed version of the initial one. In this chapter, discussion is restricted to subsequent yield surfaces which evolve from the initial one. The other option--the multiple yield surface concept--is described in Seereeram, McVay, and Linton (1985).

During plastic loading, the material remains at yield as it moves from one plastic state $F(\sigma) = 0$ to another, $F(\underset{\sim}{\sigma} + d\underset{\sim}{\sigma}) = 0$. When this requirement is met, the consistency condition is said to be satisfied. To stay with the stress point, the yield surface may undergo a size change, or a shape change, or translate, or rotate, or undergo any combination of these processes. No change in the initial yield surface is the perfectly plastic idealization: the yield surface is also the limit surface. In conventional plasticity, changes in the yield surface occur only when the material undergoes plastic deformation ($\underset{\sim}{n}:d\underset{\sim}{\sigma} > 0$) , however in Chapter 3 a new concept is proposed whereby the yield surface also changes during unloading ($\underset{\sim}{n}:d\sigma < 0$) .

Remembering that the yield surface encloses the elastic (or "stiffer") region, we may interpret these yield surface transmogrifications as a specification of how the "hard" region in stress space evolves during loading. These are the hardening rules of plasticity. Anyone who has ever bent a wire hanger or a paper clip and then tried to bend it back to its original shape can attest to the phenomeno· of hardening. Hardening of a material can also mean that more work per unit volume is required to alter the plastic state. The implications of this particular interpretation are profound, and they are treated in the next section.

2.5.4 Drucker's Stability Postulates

It is now approriate to introduce one of the cornerstones of modern plasticity theory: Drucker's stability postulates (Drucker, 1950a, 1950b, 1951, 1956, 1958, and 1966). Emanating from these basic postulates is a classification of material behavior which results in normality of $d\underset{\sim}{\varepsilon}^p$ at a smooth point on and convexity of the yield surface.

The meaning of work hardening in the case of an axial compression test is simply that the stress is a monotonically increasing function of strain. This is considered stable response. Drucker (1950a) observed, however, that the definition of work hardening is not such a simple picture for more general states of stress and paths of loading where some components of stress may increase, while others may decrease. There, working from the notion of the stability of simple rigid bodies, he advanced a definition of intrinsic material stability using the sign of the work done by the addition of and the addition and removal of a small stress increment. This is commonly referred to as "stability in the small" to distinguish it from a later postulate he called "stability in the large", wherein a finite disturbance was considered.

Imagine a material element with a homogenous state of stress $\underset{\sim}{\sigma}$ and strain $\underset{\sim}{\varepsilon}$. Let an external agency, entirely separate and distinct from the agency which caused the existing state of stress and strain, apply small surface tractions which alter the stress state at each point by $d\underset{\sim}{\sigma}$ and produce correspondingly small strain increments $d\underset{\sim}{\varepsilon}$ Next, assume this external agency slowly removes the added surface tractions, and in the process recovers the elastic strain increment $d\underset{\sim}{\varepsilon}^e$. In layman terms, a small external load is used to probe the stability of an existing "system"; if the body "runs away" with any small probe, or if upon removal of the probe the material rebounds past its original position, the system is said to be unstable. Stability therefore

implies that positive work is done by the external agency during the application of the set of stresses,

$$d\sigma : d\varepsilon > 0 \ , \tag{2.5.4.1}$$

and that the net work performed by it over the cycle of application and removal is zero or postive,

$$d\underset{\sim}{\sigma} : (d\underset{\sim}{\varepsilon} - d\underset{\sim}{\varepsilon}^{e}) = d\underset{\sim}{\sigma} : d\underset{\sim}{\varepsilon}^{p} \geq 0 \ . \tag{2.5.4.2}$$

It is emphasized that the work referred to is not the total work done by all the forces acting, but only the work done by the added set on the displacements which result. The latter postulate (Equation 2.5.4.2) can be rephrased: work hardening means that useful energy over and above the elastic energy cannot be extracted from the material and the system of forces acting upon it. If Equation 2.5.4.2 is to hold for any outward $d\underset{\sim}{\sigma}$, then it is obvious that $d\underset{\sim}{\varepsilon}^{p}$ must be normal to the yield surface.

Drucker (1951) extended his postulates by considering the external agency to apply a finite set of surface tractions to the body with its initial stress state $\underset{\sim}{\sigma}^{*}$ residing within the yield surface at a reference time t = 0. The external agency first causes the stress state to move to a point $\underset{\sim}{\sigma}$ (at time t) exactly on the yield surface. Then, it gives rise to an infinitesimal loading increment $d\underset{\sim}{\sigma}$ (with a corresponding $d\underset{\sim}{\varepsilon}^{p}$), over an arbitrarily short interval Δt, which now moves the point to a neighboring point outside of or on the yield surface. Finally, the external agency removes the stress increment $d\underset{\sim}{\sigma}$ and returns $\underset{\sim}{\sigma}^{*}$ (at time t^{*}) along an elastic path. The new work done (dW_{net}) by the external agency over the cycle is assumed to be positive, and it is equal to the total work during the cycle (dW_t) minus the work (dW_o) that would have been done during the cycle by the initial stress $\underset{\sim}{\sigma}^{*}$,

$$dW_t = \int_0^t (\underset{\sim}{\sigma} : d\underset{\sim}{\varepsilon}^e)\, dt + \int_t^{t+\Delta t} [\underset{\sim}{\sigma} : (d\underset{\sim}{\varepsilon}^e + d\underset{\sim}{\varepsilon}^p)]\, dt +$$

$$\int_{t+\Delta t}^{t^*} (\underset{\sim}{\sigma} : d\underset{\sim}{\varepsilon}^e)\, dt \quad . \tag{2.5.4.3}$$

However, the net elastic work during the cycle is zero so this equation simplifies to

$$dW_t = \int_t^{t+\Delta t} (\underset{\sim}{\sigma} : d\underset{\sim}{\varepsilon}^p)\, dt \quad , \tag{2.5.4.4}$$

and similarly, we can show that

$$dW_o = \int_t^{t+\Delta t} (\underset{\sim}{\sigma}^* : d\underset{\sim}{\varepsilon}^p)\, dt \quad . \tag{2.5.4.5}$$

Therefore,

$$dW_{net} = dW_t - dW_o \int_t^{t+\Delta t} [(\underset{\sim}{\sigma} - \underset{\sim}{\sigma}^*) : d\underset{\sim}{\varepsilon}^p]\, dt > 0 \quad , \tag{2.5.4.6}$$

and so by Drucker's definition, the following must hold:

$$(\underset{\sim}{\sigma} - \underset{\sim}{\sigma}^*) : d\underset{\sim}{\varepsilon}^p > 0 \quad . \tag{2.5.4.7}$$

With this "stability in the large" restriction, convexity of the yield surface can be demonstrated from simple geometric considerations: all vectors $\underset{\sim}{\sigma} - \underset{\sim}{\sigma}^*$ must lie to one side of the hyperplane which is normal to the strain increment vector $d\underset{\sim}{\varepsilon}^p$, and this must hold for all points on the yield hypersurface, thus proving convexity. Drucker (1956) has also shown that stability is a necessary condition for uniqueness.

2.5.5 Applicability of the Normality Rule to Soil Mechanics

The essential difference between a plastic material and an assemblage of two bodies with a sliding friction contact is the necessary volume expansion which accompanies the latter in shear (Drucker, 1954). This volume explansion

will be predicted by a pressure sensitive yield surface using the normality assmption. Experimental studies on sand response all generally agree that normality of the shear strain component is almost satisfied on the octahedral plane. However, the observed volumteric component of the plastic strain increment, $d\varepsilon^p_{kk}$,has been found to be inconsistent with that specified by normality to a conventionally defined yield surface--i.e., one using a moderate or Taylor-Quinney definition of yield (see, for example, the study by Lade and Duncan, 1975).

Two options are usually suggested to correct for this discrepancy: the first and more complicated approach is to determine a plastic potential function G, which is entirely distinct from and unrelated to the yield surface. The second and perhaps more appealing approach is to modify the normal vector $\partial F/\partial \underset{\sim}{\sigma}$ to bring it into agreement with the direction of $d\underset{\sim}{\varepsilon}^p$. As a first step to explaining the second alternative, observe from Equation 2.5.3.2 that

$$de^p_{kk} = \Lambda \frac{\partial F}{\partial \sigma_{kk}} \tag{2.5.5.1}$$

and

$$de^p_{ij} = \Lambda \frac{\partial F}{\partial s_{ij}} \tag{2.5.5.2}$$

respectively.

In order to bring the gradient $\partial F/\partial \underset{\sim}{\sigma}$ in line with the observed trajectory of $d\underset{\sim}{\varepsilon}^p$, the volumetric component $d\varepsilon^p_{kk}$ and the deviatoric components are modified by the scalar factors A_1 and A_2,

$$d\varepsilon^p_{kk} = \Lambda A_1 \frac{\partial F}{\partial \sigma_{kk}} \tag{2.5.5.3}$$

and

$$de_{ij}^{p} = \Lambda A_2 \frac{\partial F}{\partial s_{ij}} \quad . \tag{2.5.5.4}$$

To clarify the influence of these factors, these equations are restated in terms of 'triaxial' stress parameters

$$\frac{dv^{p}}{v} = \Lambda A_1 \frac{\partial F}{\partial p} \quad , \tag{2.5.5.5}$$

and

$$d\bar{\varepsilon}^{p} = \frac{2}{3} (d\varepsilon_1^{p} - d\varepsilon_3^{p}) = \Lambda A_2 \frac{\partial F}{\partial q} \quad , \tag{2.5.7.6}$$

where dv^{p}/v is the plastic volume strain and $d\bar{\varepsilon}^{p}$ is the plastic equivalent shear strain. Figure 2.9 is a geometric interpretation of these equations. Figure 2.9 (a) corresponds to the normality rule (i.e., $A_1 = A_2 = 1$) and Figure 2.9 (b) shows how the volumetric and deviatoric components are modified to change both the magnitude and direction of the resulting plastic strain increment vector. Lastly, Figure 2.9 (c) illustrates how the magnitude of the plastic strain increment vector may be changed without altering its direction.

Restrictions on the selection of the two factors A_1 and A_2 imposed by stability considerations have been discussed by Jain (1980). Stability in the small (Equation 2.5.4.2),

$$d\underset{\sim}{\sigma}:d\underset{\sim}{\varepsilon}^{p} = dp\, de_{kk}^{p} + d\underset{\sim}{s}:d\underset{\sim}{\varepsilon}^{p} > 0 \quad ,$$

or for this special case,

$$d\sigma_{mn} d\varepsilon_{mn}^{p} = \Lambda \left[dp\, A_1 \frac{\partial F}{\partial \sigma_{kk}} + ds_{ij}\, A_2 \frac{\partial F}{\partial s_{ij}}\right] > 0 \quad , \tag{2.5.5.7}$$

requires a frictional system to dissipate energy regardless of whether it expands or contracts. Since shear distortions are considered to be the result

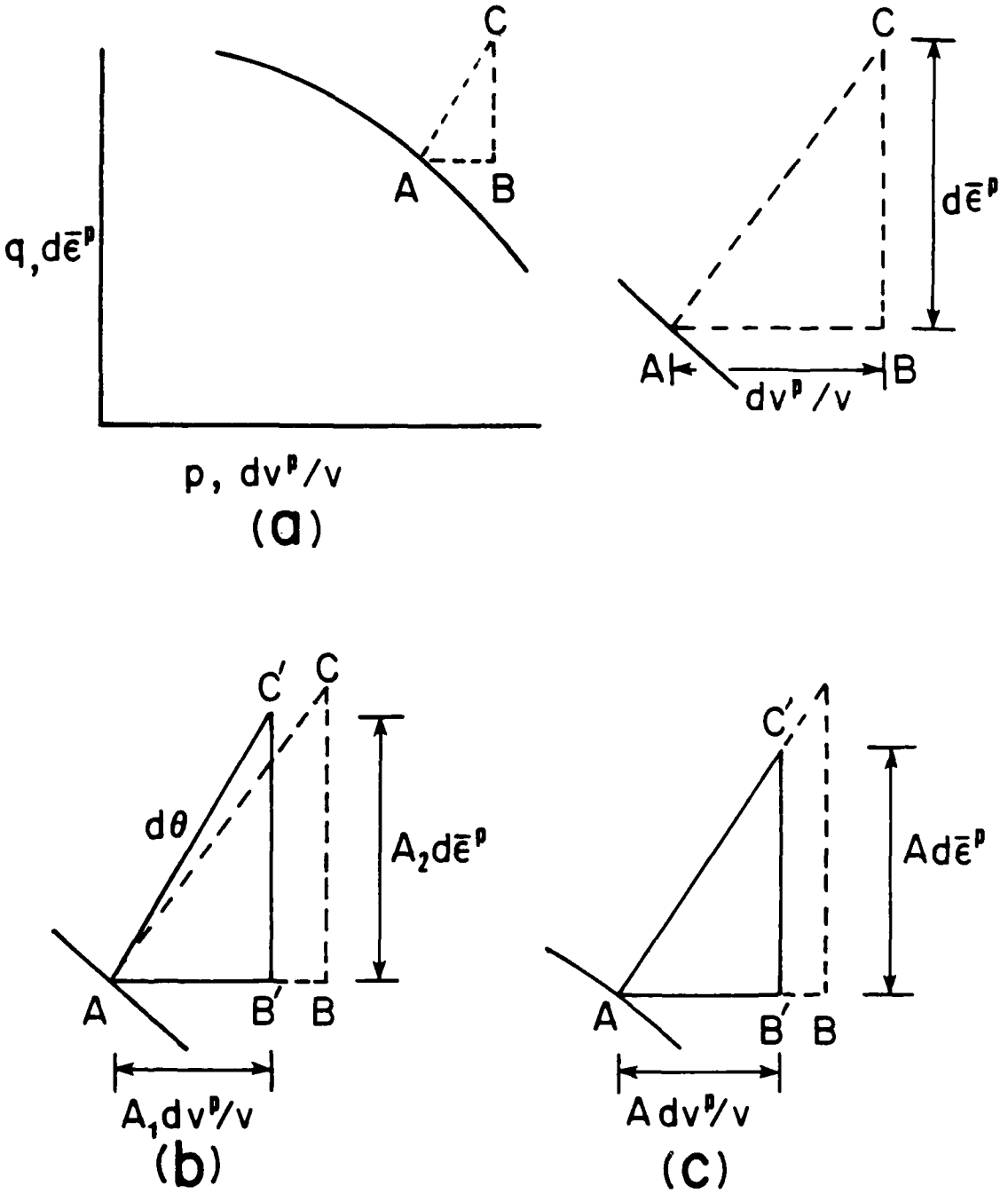

Figure 2.9 Diagrams illustrating the modifying effects of the coefficients A1 and A2: (a) A1 = A2 = 1; (b) A1 ≠ A2; (c) A1 = A2 = A (after Jain, 1980)

of frictional sliding and therefore dissipative, A_2 must always be positive. On the other hand, the modifying fact A_1 is permitted to take on a negative value. This means that the spherical stress can extract energy from the system, but the choice of A_1 must still ensure that total energy is dissipated (i.e., Equation 2.5.5.7 must still hold). Examples of models which incorporate these parameters can be found in the papers by Prevost (1978), Desai and Siriwardane (1980), and Sture et al. (1984).

2.5.6 Isotropic Hardening

Based on physical postulates and experimental stress probes, various rules have been suggested to describe the metamorphosis (or hardening) of the yield surface. Of these, the simplest idealization is that of isotropic hardening (Hill, 1950). To illustrate this concept, consider a hypothetical isotropic material with a circular initial yield curve (or surface) centered at the origin of principal stress space and of some initial radius k_0, Figure 2.10. Also assume the existence of an outer concentric failure or limiting or bounding surface of fixed radius k_f. Although this is an inapproriate representation of yielding in engineering materials, its visual and mathematical features are ideal for demonstration. It is used almost exclusively in this section as a vehicle for introducing other related concepts.

For a uniaxial compression stress path, Figure 2.10, the stress point moves up the σ_1 axis and meets the initial yield surface where $\sigma_1 = k_0$, point A. As the stress point continues up this axis, the initial surface expands uniformly about the origin to stay with the stress point; the current radius of the circle k is equal to σ_1 . Note also that, from the geometry of this yield surface, the only non-zero component of plastic strain is ε_1^p . If loading continues until $\sigma_1 = k_f$, the material fails (i.e., $K_p \to 0$), but if the

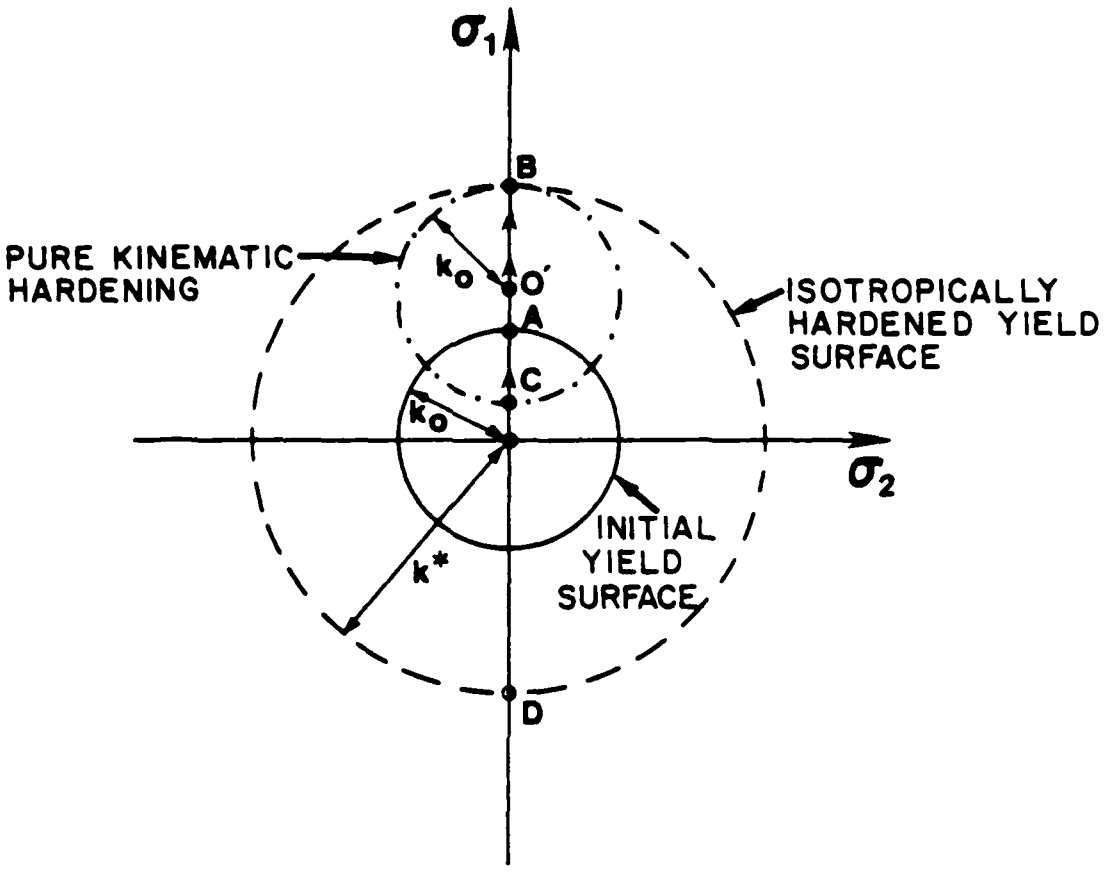

Figure 2.10 Schematic illustration of isotropic and kinematic hardening

path terminates at some pre-failure stress $\sigma_1 = k^*$, point B in Figure 2.10, and is followed by an (elastic) unloading back to the origin 0, the expanded yield surface of radius k^* remains as memory of the prior loading. Now, if σ_2 is increased while maintaining σ_1 at zero stress, the material yields or flows plastically only if σ_2 reaches and then exceeds a magnitude of k^*. Expansion of the yield surface takes place as before when $\sigma_2 > k^*$. Thus, in effect, isotropic hardening means that the material hardens equally well in all directions--it remains istropic despite the hardening.

How might isotropic hardening correspond to reality? If the material under investigation is a soil, we may assume that hardening takes place primarily as a result of compaction, and that the anisotropic realignment of the microstructure is insignificant. Reduction in the porosity represents an all around (or isotropic) hardening (or strengthening) of the material. However, if the hardening is not due to an all around effect like porosity changes or if the anisotropic fabric induction is consequential, then we must keep track of the material directions and account for anisotropy within the framework of plasticity theory. Because of the important role isotropic hardening rules play in soil mechanics today, these are discussed in some detail before introducing the specific rules designed for anisotropic (or kinematic) hardening.

If the stress tensor appears as the only independent variable in the equation for the yield surface, the configuration of the current yield surface, as given by say the size of the isotropically expanding or expanded circle, is determined solely by the stress history. This particular choice is the basis for the stress hardening theories. Prager (1949) proposed, however, that the mechanical state of a material, as manifested by its yield surface, should, in addition to $\underset{\sim}{\sigma}$,also depend on the components of the plastic strain

$\underset{\sim}{\varepsilon}^p$, $F(\underset{\sim}{\sigma}, \underset{\sim}{\varepsilon}^p) = 0$. Applying this postulate to the illustrative isotropic hardening model implies that the radius k, should depend on $\underset{\sim}{\varepsilon}^p$, $F[\underset{\sim}{\sigma}, k(\underset{\sim}{\varepsilon}^p)] = 0$. With this additional constraint. the consistency condition takes on added importance since the differential

$$dF = \frac{\partial F}{\partial \sigma_{ij}} \, d\sigma_{ij} + \frac{\partial F}{\partial \varepsilon^p_{rs}} \, d\varepsilon^p_{rs} = 0 \qquad (2.5.6.1)$$

must be satisfied during plactic loading. Substituting the flow rule (Equation 2.5.3.12) into this equation makes the consequence of the restriction more transparent,

$$\frac{\partial F}{\partial \sigma_{ij}} \, d\sigma_{ij} + \frac{\partial F}{\partial \varepsilon^p_{mn}} \, \frac{1}{K_p} \, \frac{\partial F}{\partial \sigma_{mn}} \, \frac{1}{\left|\underset{\sim}{\Delta F}\right|^2} \left\{ \frac{\partial F}{\partial \sigma_{pq}} \, d\sigma_{pq} \right\} = 0 \ ,$$

from which the scalar term $(\partial F/\partial \sigma_{ij})d\sigma_{ij}$ may then be factored out to show that

$$K_p = - \frac{\partial F}{\partial \varepsilon^p_{mn}} \, \frac{\partial F}{\partial \sigma_{mn}} \, \frac{1}{\left|\underset{\sim}{\nabla F}\right|^2} \ , \qquad (2.5.6.1)$$

or for the illustrative example,

$$K_p = - \frac{\partial F}{\partial k} \, \frac{\partial k}{\partial \varepsilon^p_{mn}} \, \frac{\partial F}{\partial \sigma_{mn}} \, \frac{1}{\left|\underset{\sim}{\nabla F}\right|^2} \ . \qquad (2.5.6.3)$$

Therefore, the plastic modulus can be computed directly from Equation 2.5.6.3 if one can postulate an equation linking the size of the yield surface (k) with the plastic strain $\underset{\sim}{\varepsilon}^p$,or its invariants if material isotropy is assumed. Even more generally, any number of identifiable plastic internal variables q_n (including $\underset{\sim}{\varepsilon}^p$) may be used to characterize the state of the material, $F(\underset{\sim}{\sigma}, q_n) = 0$. The name plastic internal variable (PIV) is selected in order to emphasize its association with plasticity in particular, while the

name internal variables is associated with inelasticity in general (Dafalias, 1984). Examples of PIVs include the plastic strain tensor, the plastic work, and a scalar measure of cumulative plastic strain; many authors prefer to identify the (non-plastic) internal variables of soil as the porosity, and the numerous fabric measures such as the orientation of the particles and their contact planes. The evolution of $\underset{\sim}{q}_n$ is given by

$$d\underset{\sim}{q}_n = L\, \underset{\sim}{r}_n \ ,$$

where L is the loading index defined in Equation 2.5.3.14, and $\underset{\sim}{r}_n$ are functions of the state variables (Lubliner, 1974). If, for example, $\underset{\sim}{q}_1$ represents $\underset{\sim}{\varepsilon}^p$, then $\underset{\sim}{r}_1$ is the unit normal to the yield surface $\underset{\sim}{n}$ in associative plasticity. The generalization of Equation 2.9.6.2 is therefore

$$K_p = - \frac{\partial F}{\partial \underset{\sim}{q}_n} \underset{\sim}{r}_n \frac{1}{\left| \nabla \underset{\sim}{F} \right|} \ .$$

Perhaps the three most popular plastic internal variables used in soil plasticity are the plastics volumetric strain ε^p_{kk} , the plastic work

$$W_p = \int (\sigma_{ij}\, d\varepsilon^p_{ij})\, dt \ . \qquad (2.5.6.4)$$

and the arc length of the deviatoric plastic strain $\underset{\sim}{\varepsilon}p$

$$\eta = \int \sqrt{(de^p_{ij} de^p_{ij})}\, dt \ . \qquad (2.5.6.5)$$

When plastic work appears as the state variable, the formulation is classified as a work-hardening theory. Similarly, if one or a combination of the invariants or arc lengths of $\underset{\sim}{\varepsilon}^p$ or its deviation $\underset{\sim}{e}^p$ are employed, the material is said to be strain-hardening. Concepts similar to that of work hardening were employed as early as the 1930's by Taylor and Quinney (1931) and Schmidt (1932). The arc length was used as a state variable by Odqvist (1933).

However, in these earlier works, the total strain $\underset{\sim}{\varepsilon}$ was used instead of the plastic strain $\underset{\sim}{\varepsilon}^p$. This was clearly inapproriate because elastic strains occuring within the yield surface could alter it. With regards to modern soil plasticity, the reader is referred to Lade's work (Lade and Duncan, 1975) to find an application of a work-hardening theory and to Nova and Wood's (1979) for a strain-hardening description. Mroz (1982) has surveyed the many specialized forms of these plastic internal variables or hardening parameters, with emphasis on their applications to soil mechanics.

Models based on the concept of density or volumetric hardening utilize the irreversible plastic volumetric strain as the state variable, $F(\underset{\sim}{\sigma}, \varepsilon^p_{kk}) = 0$; examples of this approach can be found in Drucker, Gibson, and Henkel (1957); Schofield and Wroth (1968); Roscoe and Burland (1968); DiMaggio and Sandler (1971); and Sandler, DiMaggio, and Baladi (1976). With this choice of state variable, Equation 2.5.6.3 specializes to

$$K_p = - \frac{\partial F}{\partial k} \frac{dk}{d\varepsilon^p_{mm}} \frac{1}{3} \frac{\partial F}{\partial p} \frac{1}{\left| \nabla \underset{\sim}{F} \right|^2} \qquad (2.5.6.6)$$

where p is the mean stress.

One may wonder how the size of the yield surface k may be analytically linked to the plastic volumetric strain ε^p_{mm} . This is illustrated by alluding to an isotropically hardening spherical yield surface. Consider the typical stress-strain response of soil in hydrostatic compression, Figure 2.1, and observe from Figure 2.11 that the radius of the yield surface (k) is equal to $\sqrt{3}$ p for this stress path. The latter information could have also been retrieved directly from Equation 2.5.2.5. It is well known in soil mechanics that the pressure-volume response along this path can be reasonably approximated by the equation

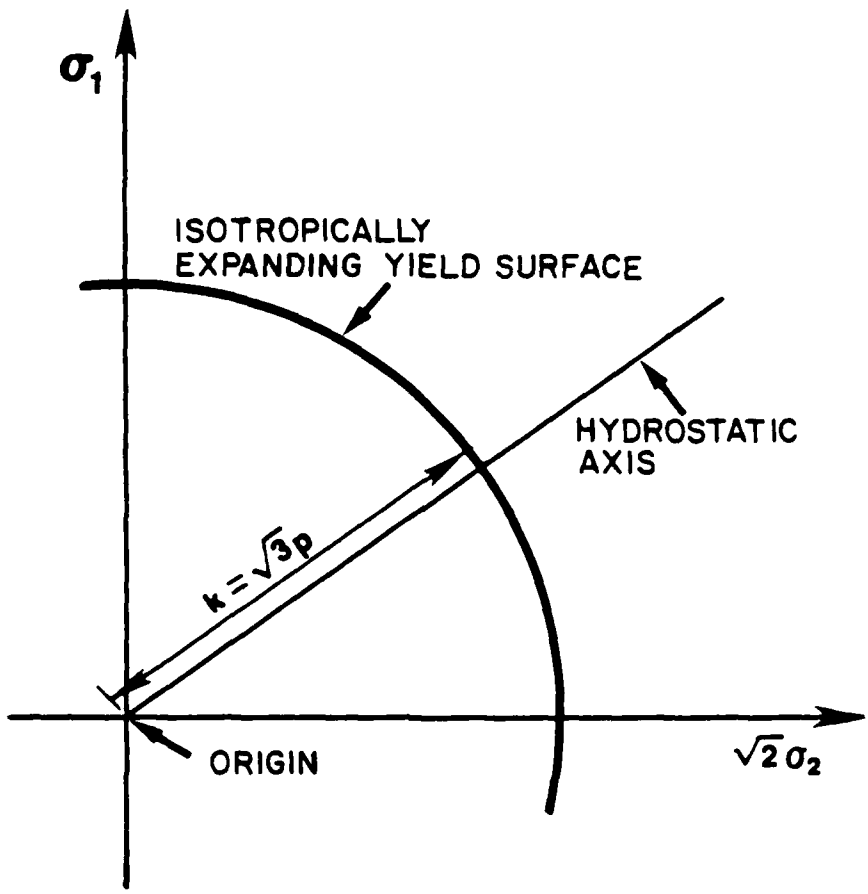

Figure 2.11 Two dimensional view of an isotropically hardening yield sphere for hydrostatic loading

$$p = p_o \exp(\lambda \varepsilon^p_{kk}), \tag{2.5.6.7}$$

or alternatively,

$$k = k_o \exp(\lambda \varepsilon^p_{kk}) \quad , \tag{2.5.6.8}$$

where p (or k) and p_o (or k_o) are the current and the initial sizes respectively, and λ is a constant which characterizes the plastic compressibility of the material. Higher magnitudes of λ imply a stiffer (or denser) sand. Soils engineers will perhaps recognize this equation as being an alternative expression for the linear voids ration vs. log mean stress plot.

From Equation 2.5.6.7, we find that

$$\frac{dp}{d\varepsilon^p_{kk}} = \lambda p_o \exp(\lambda \varepsilon^p_{kk}) = \lambda p \quad , \tag{2.5.6.9}$$

and for this particular empirical stress-strain relation, the plastic modulus (derived from Equation 2.5.6.6) is

$$K_p = -\frac{1}{|\nabla F|^2} 3 \frac{(\partial F)^2}{\partial p} \lambda p \quad . \tag{2.5.6.10}$$

Notice that $K_p \to 0$ as $\partial F/\partial p \to 0$, which means that plastic flow is isochoric (volume preserving) at failure. Normally consolidated clays and loose sands generally exhibit this phenomenon.

Three types of hardening rules have been described: stress-hardening, work-hardening, and strain-hardening. With work- and strain-hardening, the plastic modulus is computed from the consistency condition, but nothing has yet been said about the stress-hardening theory. Because of its applicability to the proposed formulation in Chapter 3, it is embedded in the ideas presented there.

Recently, Drucker and Palgen (1981) reminded us that "the temptation to think of the special form $F(\underset{\sim}{\sigma}, \underset{\sim}{\varepsilon}^p) = 0$ as good first approximation to reality must be resisted. Writing

$$dF = 0 = \frac{\partial F}{\partial \sigma_{ij}} d\sigma_{ij} + \frac{\partial F}{\partial \varepsilon^p_{mn}} d\varepsilon^p_{mn}$$

and replacing

$$\frac{\partial F}{\partial \sigma_{ij}} d\sigma_{ij} \text{ by } - \frac{\partial F}{\partial \varepsilon^p_{mn}} d\varepsilon^p_{mn}$$

generally leads to an undesirable and misleading constraint." They proposed that the plastic modulus may be entirely stress dependent--that is, the state of the material (i.e., the yield surface and the plastic modulus) is given soley by the state of stress. In Chapter 3, it will be shown that "freeing" the plastic modulus from the consistency condition does, in fact, lead to a simpler and more elegant approach.

2.5.7 Anisotropic Hardening

Kinematic hardening is a term introduced by Prager (1955) to describe his proposition that the yield surface rigidly translates in stress space. It is easy to visualize this movement and its connotation by considering again the hypothetical elastic-plastic material with the circular yield surface, Figure 2.10. If after the unloading from $\sigma_1 = k^*$ to zero stress was followed by a complete reversal of σ_1, the isotropic hardening idealization would not predict any plastic strains until σ_1 reaches and then goes beyond $-K^*$. Experimental evidence suggests that this is not true: Bauschinger (1887) found that if a metal specimen is compressed beyond its elastic limit, then its yield stress in tension is lowered. This mode of response was anticipated

earlier by Wiedmann (1860) and has been confirmed more recently by many experimental investigations. See, for example, Naghdi, Essenburg, and Koff (1958); Ivey (1961); and Phillips and Weng (1975).

To capture the essence of the Bauschinger effect, Prager (1955) assumed that the yield surface translates without deforming to follow the stress point, the direction of translation being the direction of $d\underset{\sim}{\varepsilon}^p$. With such an idealization, yielding would be predicted at point C in Figure 2.10 on an unload following a loading from 0 to B. This is in striking contrast to point D, which would have been predicted for the isotropic hardening theory. Therefore, in order to more generally characterize a yield surface, not only should its size k be monitored, but also its center coordinate $\underset{\sim}{\varepsilon}$, $F(\underset{\sim}{\sigma}, \underset{\sim}{\varepsilon}, k) = 0$. The consistency condition is now more generally written as:

$$dF = \frac{\partial F}{\partial \underset{\sim}{\sigma}} : d\underset{\sim}{\sigma} + \frac{\partial F}{\partial \underset{\sim}{\varepsilon}} : d\underset{\sim}{\varepsilon} + \frac{\partial F}{\partial k}\, dk = 0, \qquad (2.5.7.1)$$

or $F(\underset{\sim}{\sigma} + d\underset{\sim}{\sigma}, \underset{\sim}{\varepsilon} + d\underset{\sim}{\varepsilon}\ k + dk) = 0$ must be satisfied during plastic loading.

Yield surfaces may simultaneously change their size and center coordinate, and these are said to follow in isotropic/kinematic hardening rule. If the center coordinate $\underset{\sim}{\varepsilon}$ is some scalar magnitude multiplied by the Kronecker delta $\underset{\sim}{\delta}$, the material remains isotropic, but in general, the translation of the yield surface takes induced anisotropy into account and reflects the history of loading.

As mentioned before, Prager (1955) assumed that the yield surface's center translates in a direction parallel to the plastic strain increment vector $d\underset{\sim}{\varepsilon}^p$. However, in the application of this hardening rule, a problem

arises: although the yield surface remains rigid in nine-dimensional stress space, it may not appear rigid in subspaces. To overcome this difficulty, Ziegler (1959) proposed that the surface translates in the direction of a radius connecting its center with the stress point [i.e., $d\underset{\sim}{\varepsilon} \propto (\underset{\sim}{\sigma} - \underset{\sim}{\varepsilon})$]. Based on experimental observations, Phillips (Phillips and Weng, 1975) has postulated that the yield surface translates in the direction of the stress increment (i.e., $d\underset{\sim}{\varepsilon} \propto d\underset{\sim}{\sigma}$), while simultaneously changing its shape to manifest the cross effect. He accomplished this by pulling in the "rear" of the yield surface as it moved along the trajectory of the stress path. Baltov and Sawczuk (1965) described an analytical hardening rule in which the yield surface rotates in addition to translating and isotropically hardening.

Virtually all of these anisotropic hardening rules have been employed in soil plasticity. Prevost (1978), in describing an early version of his pressure-sensitive model, gives options for using all but the rotation and shape transformation hardening. Anandarajah et al. (1984) describes a special application wherein the yield surface is permitted to rotate about the origin as well as isotropically expand. A similar approach was also adopted by Ghaboussi and Momen (1982). Poorooshasb, Yong, and Lelievre (1982) describe a graphical procedure for obtaining the shape of the deviatoric section of the yield surface for complicated paths of loading. The possible variations on the hardening law are endless, and for additional discussion of research on hardening, the reader is referred to Naghdi (1960).

A second option for specifying the plastic modulus as a function of stress history is to assume that there are a field of nesting (i.e., non-intersecting) yield surfaces in stress space, each of which has a plastic modulus associated with it (Mroz, 1967, and Iwan, 1967). Depending upon the loading, a yield surface will translate and/or change its size such that its

resulting motion may engage an interior or exterior member of the family of yield surfaces. To avoid intersecting adjacent members, the active yield surface must follow a Mroz kinematic hardening rule; this has been implemented and was described in Seereeram, McVay and Linton (1985). The plastic modulus in the nested surface models vary in a piecewise linear manner, and has memory of the loading history built into the current configuration of the yield surfaces.

2.5.8 Incremental Elasto-Plastic Stress-Strain Relation

When elastic and plastic strain increments are occurring simultaneously, the constitutive equations must be organized in a compact but general form for computational purposes. The equation for the total strain increment (Equation 2.1.2) is

$$d\underset{\sim}{\varepsilon} = d\underset{\sim}{\varepsilon}^{e} + d\underset{\sim}{\varepsilon}^{p} ,$$

and if the test simulation is stress controlled (i.e., $d\underset{\sim}{\sigma}$ is input), both these components can be computed explicitly. Elastic increments are computed by combining equatons 2.4.1.12 and 2.4.1.13,

$$d\varepsilon_{ij}^{e} = de_{ij}^{e} + \frac{1}{3}\, d\varepsilon_{mm}^{e}\, \delta_{ij}$$

$$= (ds_{ij} + 2G) + \frac{1}{3}\,(d\sigma_{kk} + 3K)\,\delta_{ij}, \qquad (2.5.8.1)$$

which may then be put in the alternative form:

$$d\underset{\sim}{\varepsilon}^{e} = \underset{\sim}{D}^{e}\, d\underset{\sim}{\sigma} , \qquad (2.5.8.2)$$

where $\underset{\sim}{D}^{e}$ is the fourth order, incremental, elastic compliance tensor,

$$D^{e}_{ijkl} = \frac{2G - 3K}{18\,KG}\,\delta_{ij}\,\delta_{kl} + \frac{1}{4\,G}\,(\delta_{ik}\,\delta_{jl} + \delta_{il}\,\delta_{jk}) \quad .$$

(2.5.8.3)

Plastic strain increments are computed from the flow rule (Equation 2.5.3.13), and when combined with Equation 2.5.8.2, the total strain increment is

$$d\underset{\sim}{\varepsilon} = \underset{\sim}{D}^{e}\, d\underset{\sim}{\sigma} + \frac{1}{K_p}\,\frac{\nabla\underset{\sim}{G}}{|\nabla\underset{\sim}{G}|}\,\frac{\{\partial F : d\underset{\sim}{\sigma}\}}{\partial\underset{\sim}{\sigma}} \quad . \tag{2.5.8.4}$$

If, however, a strain increment was specified, as in a finite element routine, the inverse of this incremental stress-strain relation will be needed. The algebraic operations involved in this inversion are carried out in the following. First multiply both sides of Equation 2.5.8.4 by the inverse of the $\underset{\sim}{D}^{e}$ matrix or $\underset{\sim}{C}^{e}$,

$$\underset{\sim}{C}^{e}\, d\underset{\sim}{\varepsilon} = d\underset{\sim}{\sigma} + \underset{\sim}{C}^{e}\,\frac{1}{K_p}\,\frac{\nabla\underset{\sim}{G}}{|\nabla\underset{\sim}{G}|}\,\frac{1}{|\nabla\underset{\sim}{F}|}\,\frac{\{\partial F : d\underset{\sim}{\sigma}\}}{\partial\underset{\sim}{\sigma}} \quad , \tag{2.5.8.5}$$

and if we replace $(\nabla\underset{\sim}{G} \;/\; |\nabla\underset{\sim}{G}|)$ and $(\nabla\underset{\sim}{F} \;/\; |\nabla\underset{\sim}{F}|)$ by their unit tensor notation $\underset{\sim}{m}$ and $\underset{\sim}{n}$ respectively,

$$\underset{\sim}{C}\, d\underset{\sim}{\varepsilon} = d\underset{\sim}{\sigma} + \underset{\sim}{C}^{e}\,\frac{1}{K_p}\,\underset{\sim}{m}\,\{\underset{\sim}{n} : d\underset{\sim}{\sigma}\} \quad . \tag{2.5.8.6}$$

The next step is to multiply both sides of this equation by the tensor $\underset{\sim}{n}$,

$$\underset{\sim}{n} : \underset{\sim}{C}^{e}\, d\underset{\sim}{\varepsilon} = \underset{\sim}{n} : d\underset{\sim}{\sigma} + \underset{\sim}{n} : \underset{\sim}{C}^{e}\,\frac{1}{K_p}\,\underset{\sim}{m}\,\{\underset{\sim}{n} : d\underset{\sim}{\sigma}\} \quad ,$$

and from this result, we find that

$$\frac{1}{K_p}\,\underset{\sim}{n} : d\underset{\sim}{\sigma} = \frac{\underset{\sim}{n} : \underset{\sim}{C}^{e}\, d\underset{\sim}{\varepsilon}}{K_p + \underset{\sim}{n} : \underset{\sim}{C}^{e} : \underset{\sim}{m}}$$

which when substituted into Equation 2.5.8.6 gives

$$\underset{\sim}{C}^e \; d\underset{\sim}{\varepsilon} = d\underset{\sim}{\sigma} + \frac{(\underset{\sim}{C}^e:\underset{\sim}{m})\;(\underset{\sim}{n}:\underset{\sim}{C}^e)}{K_p + (\underset{\sim}{n}:\underset{\sim}{C}^e:\underset{\sim}{m})}\; d\underset{\sim}{\varepsilon} \quad , \tag{2.5.8.7}$$

or

$$d\underset{\sim}{\sigma} = \left[\underset{\sim}{C}^e + \frac{(\underset{\sim}{C}^e:\underset{\sim}{m})\;(\underset{\sim}{n}:\underset{\sim}{C}^e)}{K_p + (\underset{\sim}{n}:\underset{\sim}{C}^e:\underset{\sim}{m})}\right] d\underset{\sim}{\varepsilon} = \underset{\sim}{C}\; d\underset{\sim}{\varepsilon} \quad . \tag{2.5.8.8}$$

If the flow rule is associated (i.e., $\underset{\sim}{m} = \underset{\sim}{n}$), the elastic-plastic stiffness matrix $\underset{\sim}{C}$ is symmetric, but if $\underset{\sim}{m}$ is not equal to $\underset{\sim}{n}$(i.e., non-associative flow) the matrix loses its major symmetry and leads to increased computation costs in numerical applications. For completeness, the independent components of the symmetric elastic-plastic stiffness tensor $\underset{\sim}{C}$ of the incremental stress-strain relation

$$\begin{Bmatrix} d\sigma_{11} \\ d\sigma_{22} \\ d\sigma_{33} \\ d\sigma_{23} \\ d\sigma_{31} \\ d\sigma_{12} \end{Bmatrix} = \begin{bmatrix} C_{11} & C_{12} & C_{13} & C_{14} & C_{15} & C_{16} \\ C_{21} & C_{22} & C_{23} & C_{24} & C_{25} & C_{26} \\ C_{31} & C_{32} & C_{33} & C_{34} & C_{35} & C_{36} \\ C_{41} & C_{42} & C_{43} & C_{44} & C_{45} & C_{46} \\ C_{51} & C_{52} & C_{53} & C_{54} & C_{55} & C_{56} \\ C_{61} & C_{62} & C_{63} & C_{64} & C_{65} & C_{66} \end{bmatrix} \begin{Bmatrix} d\varepsilon_{11} \\ d\varepsilon_{22} \\ d\varepsilon_{33} \\ d\varepsilon_{23} \\ d\varepsilon_{31} \\ d\varepsilon_{12} \end{Bmatrix}$$

are written out in long form:

$$C_{11} = \Gamma + 2\mu + F\,[\Gamma\, n_{kk} + 2\,\mu\, n_{11})^2]$$

$$C_{12} = \Gamma + F[(\Gamma\, n_{kk} + 2\,\mu\, n_{11})(\Gamma\, n_{kk} + 2\,\mu\, n_{22})]$$

$$C_{13} = \Gamma + F[(\Gamma n_{kk} + 2\,\mu\, n_{11})(\Gamma\, n_{kk} + 2\,\mu\, n_{33})]$$

$$C_{14} = F\,[(\Gamma\, n_{kk} + 2\,\mu\, n_{11})(2\,\mu\, n_{23})]$$

$$C_{15} = F\,[(\Gamma\, n_{kk} + 2\,\mu\, n_{11})(2\,\mu\, n_{13})]$$

$$C_{16} = F\,[(\Gamma\, n_{nn} + 2\,\mu\, n_{11})(2\,\mu\, n_{12})]$$

$$C_{22} = \Gamma + 2\,\mu + F\,[(\Gamma\, n_{kk} + 2\,\mu\, n_{22})^2]$$

$$C_{23} = \Gamma + F\,[(\Gamma\, n_{kk} = 2\,\mu\, n_{22})(\Gamma\, n_{kk} + 2\,\mu\, n_{23})]$$

$$C_{24} = F\,[(\Gamma\, n_{kk} + 2\,\mu\, n_{22})(2\,\mu\, n_{23})]$$

$$C_{25} = F\,[(\Gamma\, n_{kk} + 2\,\mu\, n_{22})(2\,\mu\, n_{13})]$$

$$C_{26} = F[(\Gamma\, n_{kk} + 2\,\mu\, n_{22})(2\,\mu\, n_{12})]$$

$$C_{33} = \Gamma + 2\,\mu + F\,[(\Gamma\, n_{kk} + 2\,\mu\, n_{33})^2]$$

$$C_{34} = F\,[(\Gamma\, n_{kk} + 2\,\mu\, n_{33})(2\,\mu\, n_{23})]$$

$$C_{35} = F\,[(\Gamma\, n_{kk} + 2\,\mu\, n_{33})(2\,\mu\, n_{13})]$$

$$C_{36} = F\,[(\Gamma\, n_{kk} + 2\,\mu\, n_{33})(2\,\mu\, n_{12})]$$

$$C_{44} = \mu + F\,[4\,(\mu\, n_{23})^2]$$

$$C_{45} = F\,[(2\,\mu\, n_{23})(2\,\mu\, n_{13})]$$

$$C_{46} = F\,[(2\,\mu\, n_{23})(2\,\mu\, n_{12})]$$

$$C_{55} = \mu + F\,[f\,(\mu\, n_{13})^2]$$

$$C_{56} = F\,[(2\,\mu\, n_{13})(2\,\mu\, n_{12})]$$

$$C_{66} = \mu + F\,[4\,(\mu\, n_{12})^2]$$

where

$$F = -\frac{1}{K_p + \Gamma\,(n_{kk})^2 + 2\,\mu}\ .$$

CHAPTER 3

PROPOSED PLASTICITY THEORY FOR GRANULAR MEDIA

3.1 Introduction

A constitutive model for sand is proposed within the framework of a rather special time-independent or elastic-plastic theory. In its simplest form, the material model exhibits no memory of prior plastics deformation, although modifications can be easily devised to account for more complicated aspects of real behavior. This elementary form, with no account of hardening, lies at the extreme end of a spectrum of idealizations where the conventional work-hardening theories are at the other extreme and the "bounding surface" type formulations are intermediate.

The key features of the theory as applied to sand are:

1. The material remains at yield during unloading as well as loading, Figure 3.1.
2. Yielding is defined as any plastic deformation, no matter how small, and not by the traditional moderate offset or Taylor-Quinney (1931) definition, Figure 3.2.
3. Material behavior at each state of stress is assumed to be stable in the small for any direction of motion of the stress point. This implies that the plastic strain increment $(d\underset{\sim}{\varepsilon}^p)$ is normal to the yield surface (Figure 3.2) and is calculated as (cf. Equation 2.5.3.12):

$$d\underset{\sim}{\varepsilon}^p = \frac{1}{K_p} \underset{\sim}{n} (\underset{\sim}{n}:d\underset{\sim}{\sigma}), \tag{3.1.1}$$

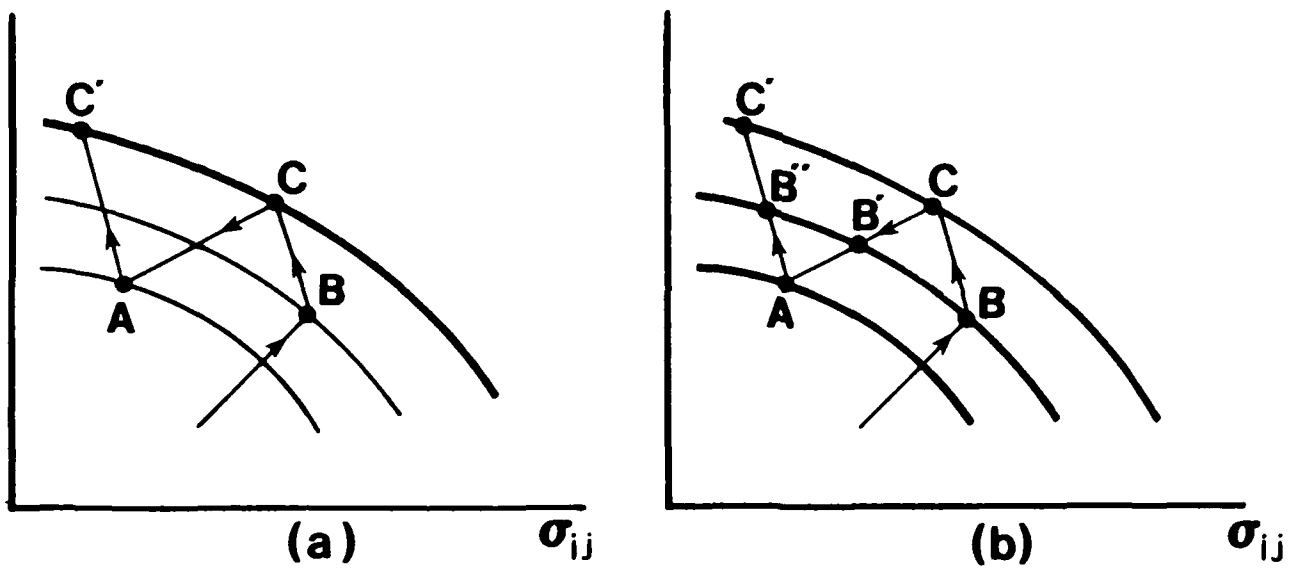

Figure 3.1 In conventional plasticity (a) path CAC' is purely elastic; in the proposed formulation (b) path CB'A is elastic but AB"C' is elastic-plastic

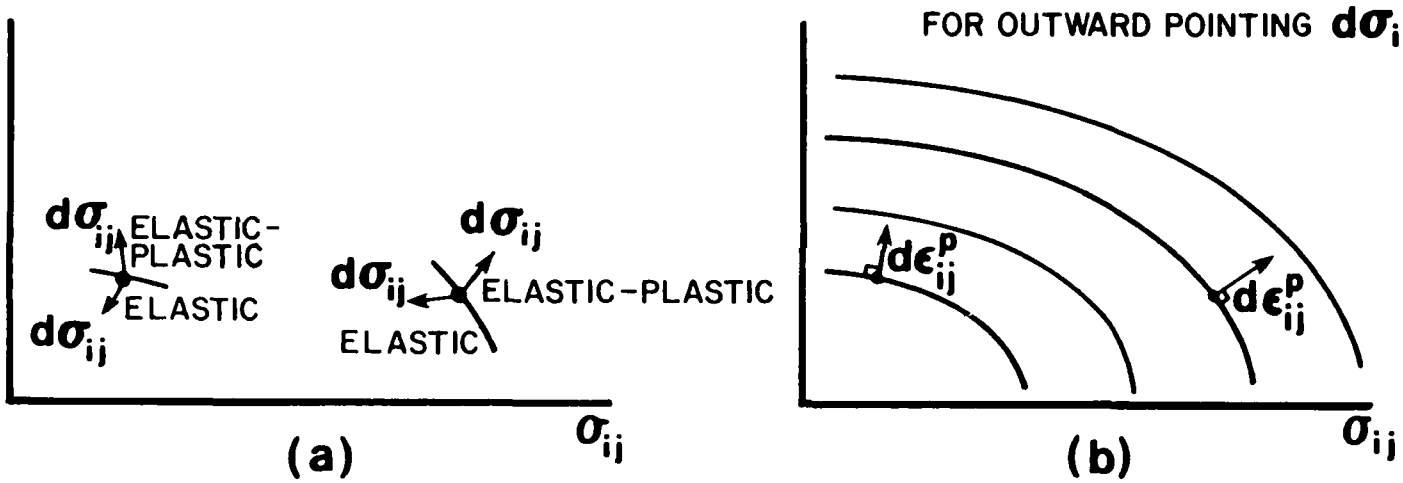

Figure 3.2 The current yield surface passes through the current stress point and locally seperates the domain of purely elastic response from the domain of elastic-plastic response

where K_p is the plastic modulus $\underset{\sim}{n}$ is the unit normal to the yield surface, and $d\underset{\sim}{\sigma}$ is the stress increment.

4. Unlike many formulations, the consistency condition is automatically satisfied, and plays no role in the determination of the plastic modulus K_p. For the non-hardening version proposed here, K_p depends solely on the current stress state, whereas with the hardening modification, stress history effects are manifested by the evolution of an independent hardening control surface. This surface is generally not coincident with a yield surface.
5. In the simplest version, with no history dependence, the nested family of yield surfaces and scalar field of plastic moduli do not change; i.e., there is no hardening and cyclic response is immediately stable.
6. The yield surfaces are chosen so that the normal to each is constant in direction along a radial line from the origin, Figure 3.3.
7. The scalar field of plastic moduli in stress space varies from a continually increasing maximum plastic stiffness in pure hydrostatic loading to zero as the stress point approaches a stationary failure or limit surface, Figure 3.3.
8. The limit or failure surface is also <u>not</u> a member of the family of yield surfaces; it intersects them at an appreciable angle, Figure 3.3.
9. No purely elastic domain of stress exists.

The first part of this chapter describes those aspects of sand behavior that suggest the use of such an unorthodox theory. Then, working from well-established experimental observations on sand, detailed analytical forms are tendered for the set of yield surfaces, the scalar field of plastic moduli

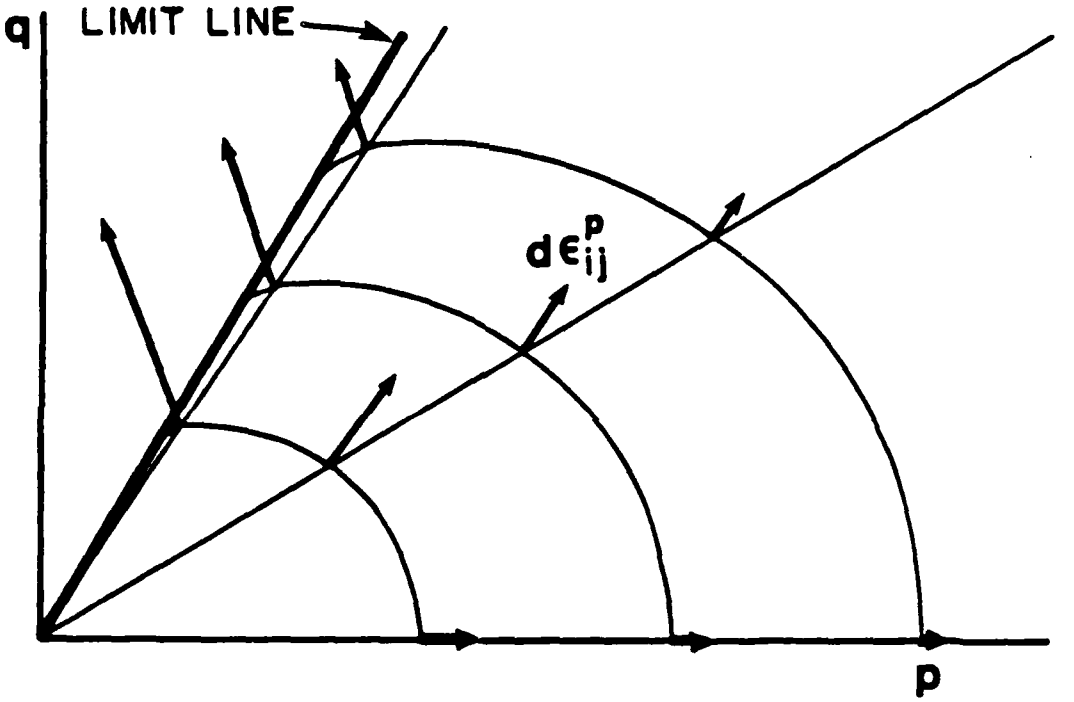

Figure 3.3 Pictorial representation for sand of the nested set of yield surfaces, the limit line, and the field of plastic moduli, shown by the $d\underset{\sim}{\varepsilon}^{p}$ associated with a constant value of $n_{pq} d\sigma_{pq}$

(which implicity defines a limit surface), and the rule to ensure that the yield surface follows the stress point.

At the outset, it must be emphasized that these selections were not instituted after a systematic rejection of other alternatives, but they evolved during the course of development as certain features were incorporated and others, deemed less important, were deleted. It is therefore quite possible for a potential user to match data equally well or even better with an alternative set of choices. The structure of the theory does not hinge on these details.

After presenting the analytical forms for the yield surface and the field of plastic moduli, a description of the initialization procedure follows, with emphasis on the physical significance of each parameter and its expected variation with initial porosity. All models constants are then identified with a corresponding stress-strain or strength parameter (or concept) in common use by geotechnical engineers. The slope of the zero dilation line (or the friction angle at constant volume) is taken as independent of initial void ratio as found experimentally. Each of the other parameters each parameter depends only on the initial density. Two standard laboratory tests specify the material parameters: a hydrostatic compression test and uniaxial compression test with a small unload-reload loop to assess the elastic properties. Calculation of each of the eight constants--two elastic and six plastic--of the simple model is straightforward and can be carried out expeditiously with the aid of only a hand calculator; the procedure involves no heuristic, or curve fitting, or optimization techniques. In fact, if the elastic and plastic strains are already separated and if typical values for two less critical plastic parameters are chosen in advance, the procedure will take as little as ten minutes.

A comparison of calculated results and experiments, for a series of hollow cylinder and triaxial tests over a range of confining pressures and on materials of different origin and initial density, demonstrates the realism of the simple idealization for a wide variety of stress paths.

Two hardening modifications to the simple theory also are presented. The first is an adaptation of Dafalias and Hermann's (1980) bounding surface theory for clays, the key characteristics of which are: i) the largest yield surface established by the prior loading history acts as a boundary of "virgin" plastic moduli, and ii) a radial mapping rule is used to locate conjugate points on the boundary surface for interior stress states. These constitutive equations are implemented in a finite element routine to solve a boundary value problem of growing interest in soil mechanics, especially in the field of insitu testing, and one for which measured data was available: the expansion of a vertically embedded cylindrical cavity.

Based on the documented behavior of sand, a second more realistic hardening option is then proposed. It differs from the previous one in that: i) the hardening control surface does not resemble the yield surface, and ii) a new interpolation function for the reload modulus is implemented. The versatility of this novel formulation is explored by simulating: a) the influence of isotropic preloading on an axial compression test, and b) the buildup of axial strain in a cyclic stress controlled uniaxial test.

Finally, advantages and limitations of the model are indicated; a difficulty does arise for somewhat unusual inward loading paths which start near the failure surface.

3.2 Material Behavior Perceived as Most Essential and Relevant

Those aspects of the behavior of sand (or of any material) that are identified as key aspects will vary greatly with the problems of prime

interest. Furthermore, any representation of the actual complex inelastic behavior of a material is a matter of background and taste. Drastic idealization is necessary and so tends to be controversial even in those rare instances when ample experimental data are available.

For example, in the consideration of geomaterials, just as for metal polymers and composites, the simplest model suitable for generally increasing load will differ radically from the simplest model suitable for cyclic loading between fixed limits of stress or strain. The simplest model that covers both types of loading will not match some aspects of each very closely.

Adequacy of representation clearly is a matter of viewpoint and judgement. The aspects selected here as the key aspects of the inelastic behavior of sands are:

1. The existence of an essentially path-independent (stationary) limit or failure surface that bounds the reachable states of stress, Figure 3.4. This surface more or less resembles the Mohr-Coulomb criterion on the octahedral plane, but it may exhibit some degree of curvature (or deviation from a pure friction criterion) on meridional (or q-p) sections. Studies by Wu, Loh, and Malvern (1963), Bishop (1966), and more recently, by Matsuoka and Nakai (1974), Lade and Duncan (1975), Desai (1980), and Podgorski (1985) are among the many on which this assumption is based.
2. A generally outward path of loading from a state of hydrostatic pressure to the limit or failure surface will induce inelastic volume contraction to start. The incremental inelastic volume change will go to zero at a stress point fairly close to but clearly below failure. Then as the stress increases toward failure (peak stress) in a stable manner, there will be appreciable continuing dilation.

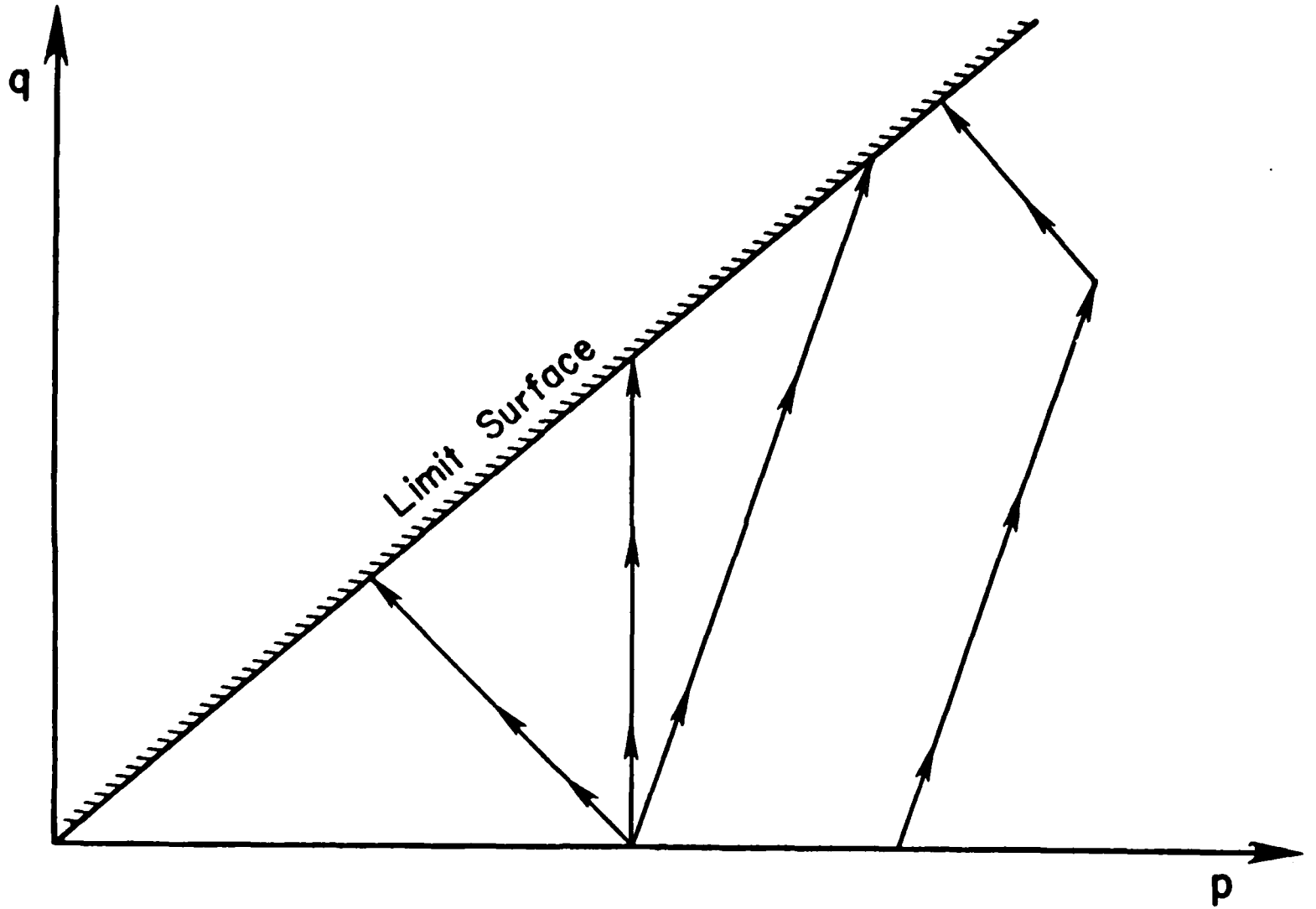

Figure 3.4 Path independent limit surface as seen in q-p stress space

The stress-strain data of Figure 3.5, taken a recent conference paper by Hettler et al. (1984), illustrates this phenomenon for axial compression tests on sand specimens over a range of initial densities.

3. The response to partial unloading is dominantly elastic, while the response to reloading is dominantly inelastic as well as elastic (Figure 3.6). It is this inelastic response on reloading at stress levels (defined by q/p) below those reached on the prior loading that led many years ago to proposals of nested set of yield surfaces with an innermost surface of small diameter and more recently to bounding surface models.
4. The inelastic response in subsequent extension testing is not altered much by moderate prior inelastic deformation in the compression test regime, as the data of Tatsuoka and Ishihara (1974b) in Figure 3.7 suggests.
5. The ratios of the components of the increments of inelastic strain remain fairly constant along each radial or proportional (q/p = constant) loading path in stress space. Data presented by Poorooshasb et al. (1966), Figure 3.8, and Tatsuoka (1972) substantiate this contention. Implicit in this premise is the existence of a radial, path-independent zero dilation line, and experimental studies by Kirkpatrick (1962) and Habib and Luong (1978) have confirmed the existence of such a line.
6. At a given stress point, the ratios of the components of the inelastic strain increments are the same for all outward loading paths through the point (Poorooshasb et al., 1966), Figure 3.9. This aspect of sand behavior has not always been found. For example, in

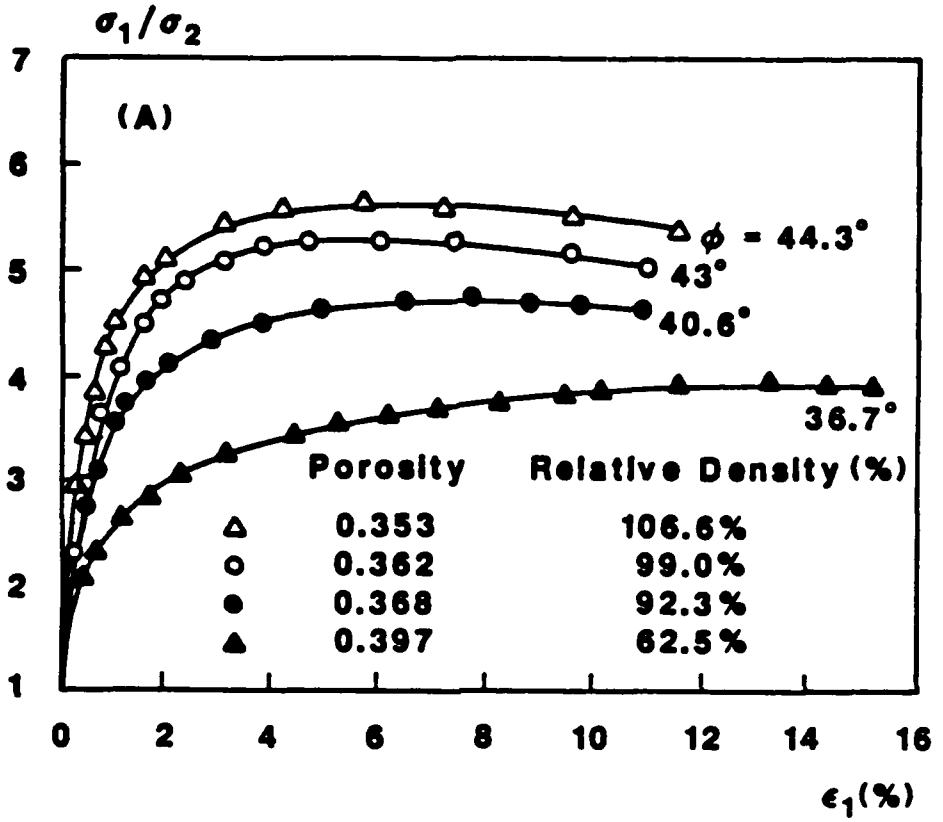

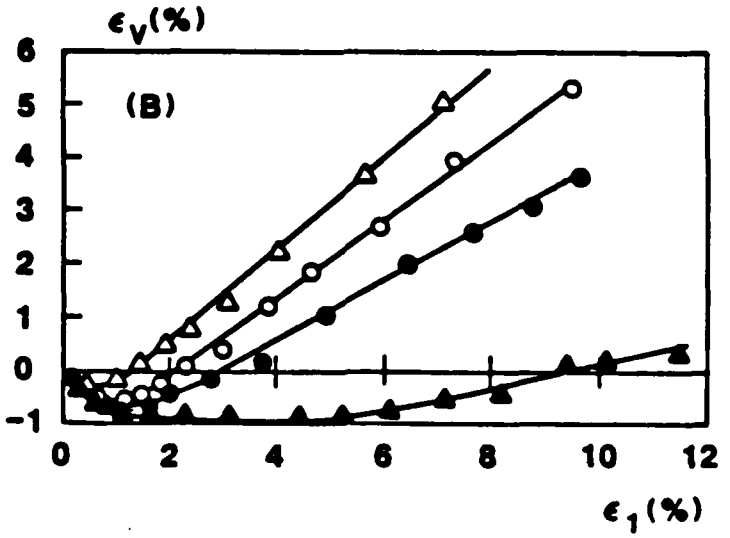

Figure 3.5 Axial compression stress-strain data for Karlsruhe sand over a range of porosities and at a constant confinement pressure of 50 kN/m^2 (after Hettler et al., 1984)

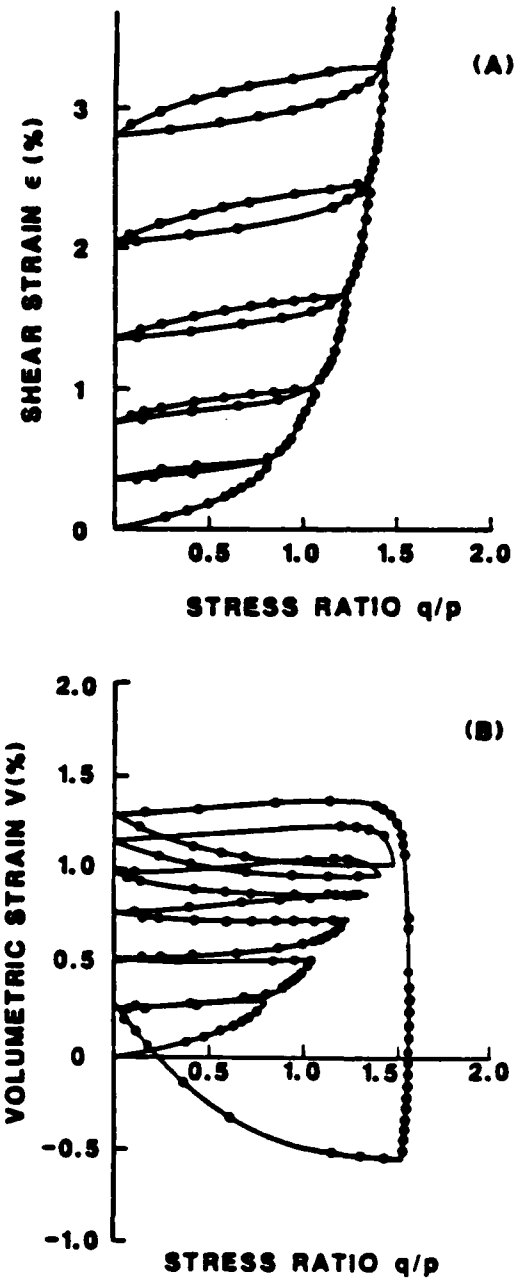

Figure 3.6 Stress-strain response for a cyclic axial compression test on loose Fuji River sand (after Tatsuoka, 1972)

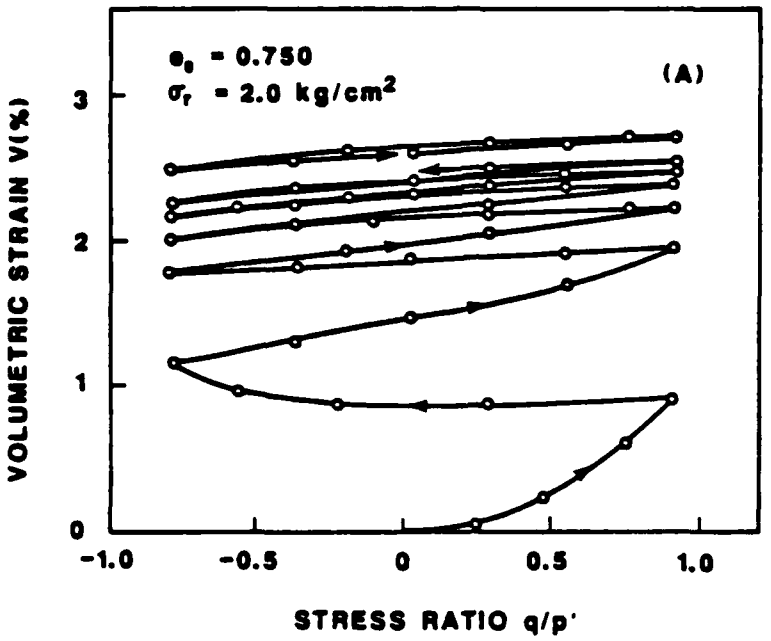

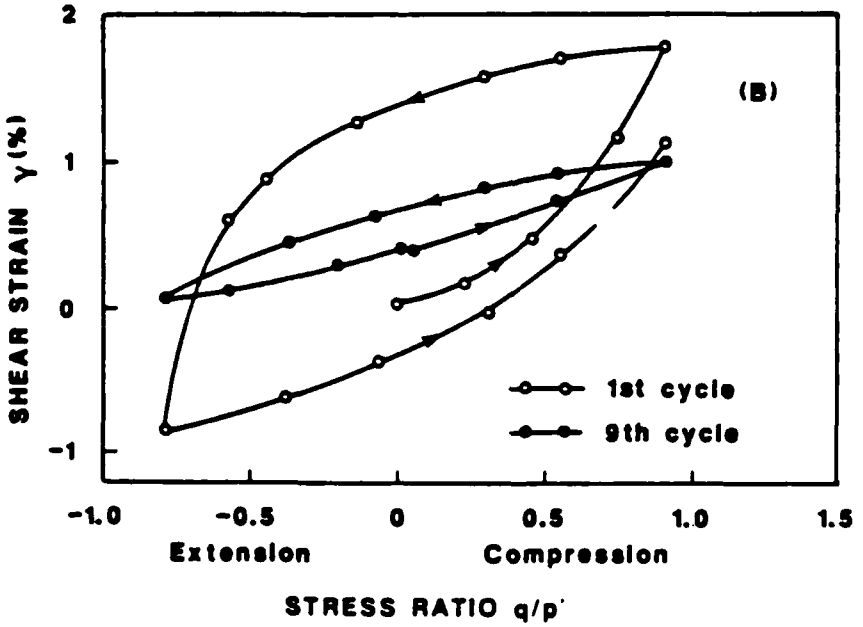

Figure 3.7 Medium amplitude axial compression-extension test on loose Fuji River sand (after Tatsuoka and Ishihara, 1974b)

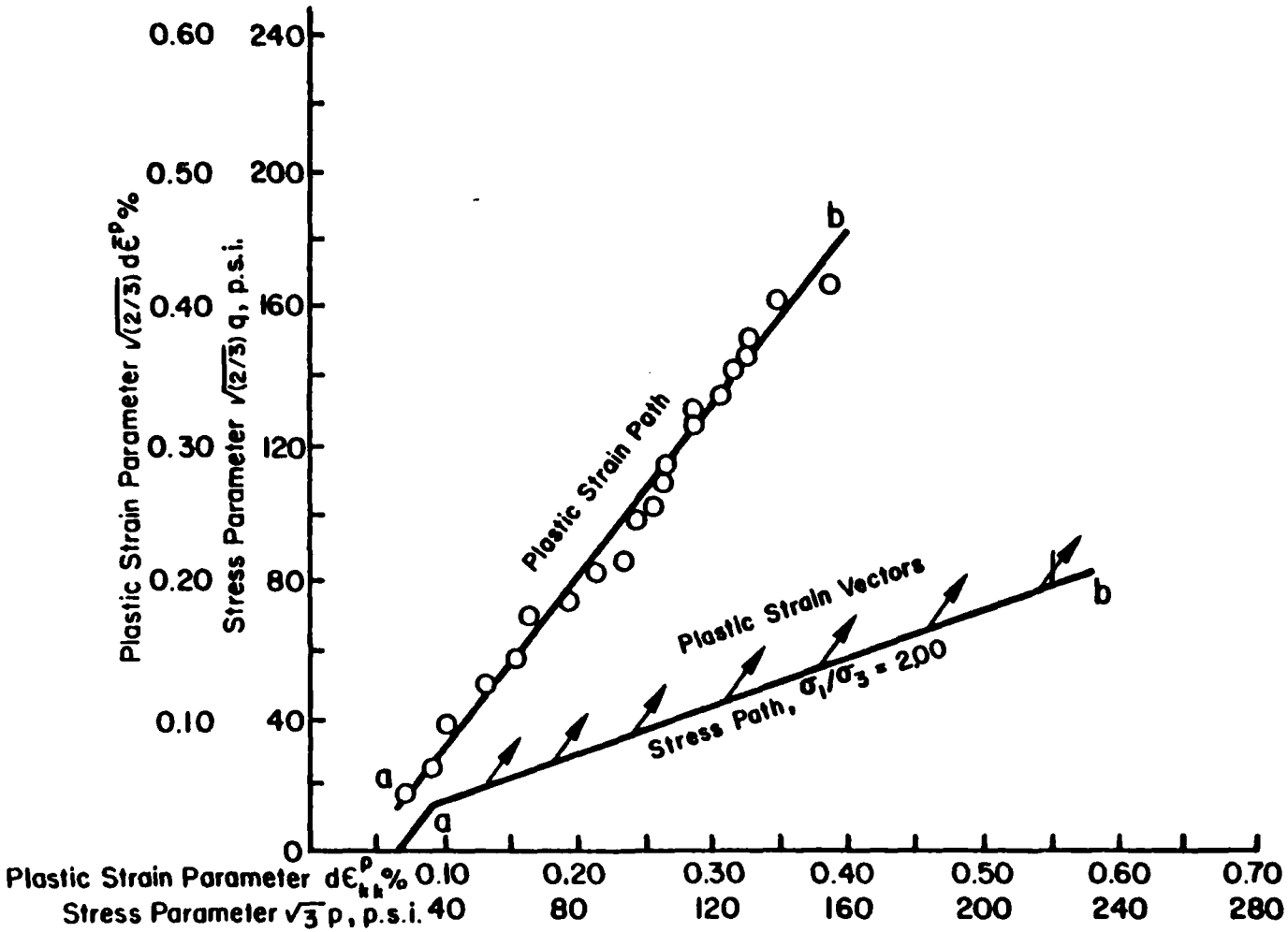

Figure 3.8 Plastic strain path obtained from an anisotropic consolidation test (after Poorooshasb et al., 1966)

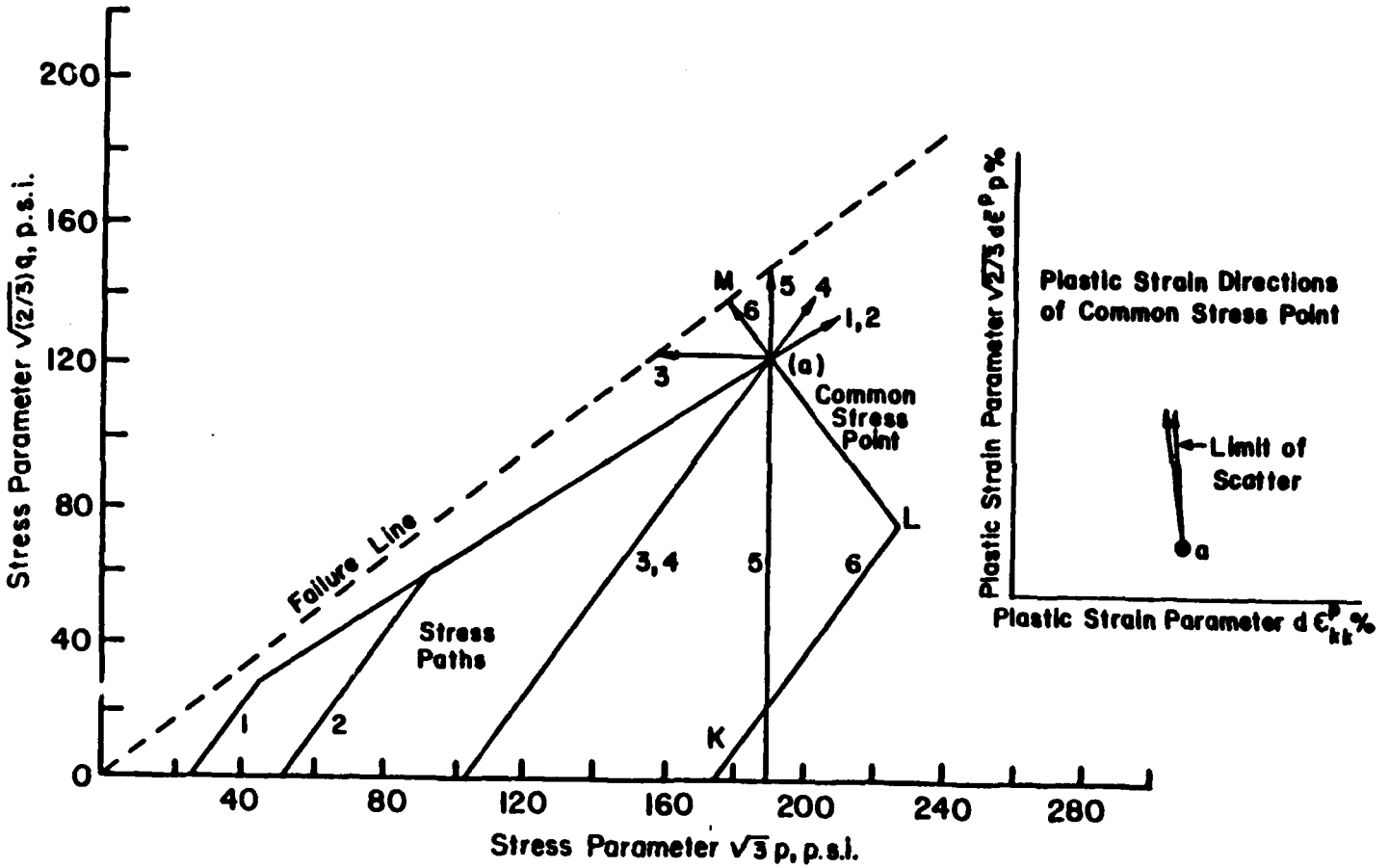

Figure 3.9 Plastic strain direction at common stress point (after Poorooshasb et al., 1966)

comparing constant pressure shear paths and radial loading paths, Tatsuoka (1972) noticed some degree of stress path influence on the direction of the plastic strain increment. But this divergence he found was more pronounced at lower (and thus less critical) stress levels.

7. Except at very high magnitudes of stress where particle crushing becomes important, the stress-strain response of sand in hydrostatic compression is of the "locking" type: the incremental pressure-volume response becomes stiffer with increasing levels of bulk stress.
8. At a constant all-around pressure, the overall stiffness of the sand decreases as the intensity of the shear stress increases.

Much of the recent literature on constitutive relations for granular media, quite approriately, is devoted to the proper characterization of the state of the material and the change in state. However, as a first approximation, the simple form of the proposal implemented here postulates that the state of the material is unchanged by the inelastic deformation. This hypothesis is a special case of what Cherian et al. (1949) in their study of commercially pure aluminum, termed orthorecovery: the reloading curve, for the uniaxial case, is finitely displaced from and parrellel to the original curve, Figure 3.10.

In the application to sands, such a formulation does automatically give those key aspects of the inelastic behavior labelled 3, 4, and 6. Simple and approriate choices of the scalar field of plastic moduli and the field of yield surfaces permit matching the failure surface (aspect 1) and produce the type of inelastic behavior labeled 2, 5, 7 and 8.

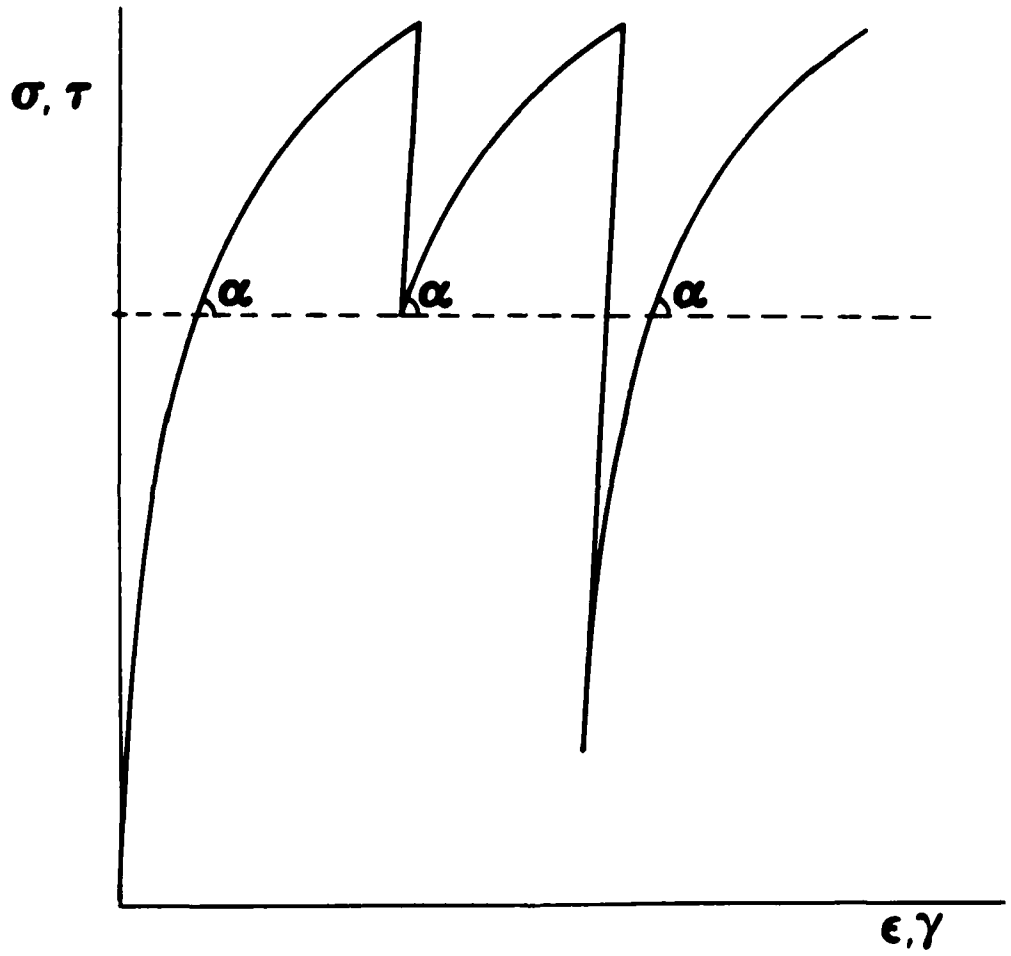

Figure 3.10 Successive stress-strain curves for uniaxial stress or shear are the initial curve translated along the strain axis in simplest model

3.3 Details of the Yield Function and Its Evolution

The analytical representation of the yield surface is guided strongly by experimental observation, and to a lesser extent by some certain very helpful mathematical simplifications. But before going into these details, it is instructive to remind the reader that yielding, in this context, is the existence of a plastic strain increment vector (Figure 3.2) no matter how small and is not defined by the traditional offset or Taylor-Quinney (1931) methods.

3.3.1 Isotropy

The soil is assumed to be isotropic, and thus the yield function may be expressed solely in terms of the stress invariants. A cylindrical coordinate system in Haigh-Westergaard (or principal) stress space is particularly attractive because a simple geometrical interpretation can be attached to each of the following invariants:

$$I_1 = \sigma_{kk} = 3\,p, \tag{3.3.1.1}$$

$$\sqrt{J_2} = \sqrt{\left(\frac{1}{2}\, s_{ij}\, s_{ij}\right)} = q/\sqrt{3}\ , \text{ and} \tag{3.3.1.2}$$

$$\theta = \sin^{-1} \frac{[\sigma_1 + \sigma_3 - 2\,\sigma_2]}{2\sqrt{(3\,J_2)}}\ , \qquad -30^0 \leq \theta \leq 30^0\ . \tag{3.3.1.3}$$

With such an isotropic representation, the general six dimensional form of the yield surface simplifies to (cf. Equation 2.5.2.6)

$$F(I_1,\ \sqrt{J_2},\ \theta) = 0\ . \tag{3.3.1.4}$$

This depiction is reduced further to two dimensions by normalizing $\sqrt{J_2}$ with a function of θ, say $g(\theta)$ to obtain a modified octahedral shear stress,

$$\sqrt{J_2}^{*} = \sqrt{J_2} \,/\, g(\theta) = q^{*}/\sqrt{3}\ . \tag{3.3.1.5}$$

The function $g(\theta)$ is such that $g(30°) = 1$ and it determines the shape of the π-section. For instance the Mohr-Coulomb relation, Equation 2.7.2.5, gives

$$g(\theta) = \frac{\cos(30^0) - \{[\sin(30^0) \sin \phi]/\sqrt{3}\}}{\cos \theta - [(\sin \theta \sin \phi)/\sqrt{3}]}$$

which defines a straight line with corners occuring at $\theta = \pm 30^0$ as shown in Figure 2.9. To avoid these corners, continuous functions are chosen such that

$$\frac{dg(\theta)}{d\theta} = 0 \quad \text{at} \quad \theta = \pm 30^0 \ .$$

Such functions can be written in polynomial or trigonometric form. Taking $g(30°) = 1$ and $g(-30°) = R$, William and Warnke (1974) suggest an elliptic expression of the form

$$g(\theta) = \frac{(1-R^2)\, A + (2R-1)\sqrt{[(2+B)\,(1-R^2) + 5R^2 - 4R]}}{(2+B)\,(1-R^2) + (1-2R)^2} \qquad (3.3.1.6)$$

where

$$A = \sqrt{3} \cos \theta - \sin \theta \ ,$$

$$B = \cos 2\theta - \sqrt{3} \sin 2\theta \ ,$$

and R specifies the ratio of the radius $[\sqrt{(2J_2)}]$ in extension to that in compression. For convexity, R must like in the range

$$0.5 \leq R \leq 2 \ .$$

By selecting

$$R = \frac{3 - \sin \theta}{3 + \sin \theta} \qquad (3.3.1.7)$$

the function $g(\theta)$ ensures that the smooth deviatoric locus matches the Mohr-Coulomb criterion in compression and extension. Although this choice is made here for convenience, other magnitudes of R may generally be determined from experiment. Furthermore, observe that by setting R = 1, the yield surface becomes a Drucker-Prager (1952) or extended von Mises criterion.

A simpler alternative to Equation 3.3.1.6 was proposed by Gudehus (1973),

$$g(\theta) = \frac{2R}{(1+R) - (1-R) \sin 3\theta} \ , \qquad (3.3.1.8)$$

but this function suffers from the unrealistic constraint that R must be greater than 0.77 or ($\phi < 23^0$) to ensure convexity.

With the introduction of this modified octahedral shear stress, the form of the isotropic yield surface is now written as:

$$F(I_1, \sqrt{J_2^*}) = 0 \quad . \tag{3.3.1.9}$$

3.3.2 Zero Dilation Line

An important aspect of the theory is the existence of a zero dilation radial line in $\sqrt{J_2^*}$-I_1 (or q^*-p) space, say slope of N in $\sqrt{J_2^*}$-I_1 space

$$\frac{\sqrt{J_2^*}}{I_1} = N \quad . \tag{3.3.2.1}$$

Ascribing special significance to this locus is not without merit because many laboratory investigations on the behavior of sand have confirmed its existence. Perhaps most noteworthy, Habib and Luong (1978) and Luong (1980), using a number of careful experiments, have studied this phenomenon which they termed the "characteristic state." It is similar and probably identical to the "phase transformation line" observed by Ishihara et al. (1975) in saturated undrained experiments.

From their extensive tests, Habib and Luong (1978) concluded that the characteristic state of a soil is associated with:

1. a zero volumetric strain rage ($\dot{\varepsilon}_{kk} = 0$),
2. a unique stress level (q/p) where net interlocking ceases and effective disruption of interlocking starts,
3. a relatively low distortion deformation ($\bar{\varepsilon}$) ,
4. an independence of the initial porosity and the grain size distribution, and
5. an absence of the influence of fabric anisotropy and stress history.

In addition, their data shown in Figure 3.11 suggests that the projection of the characteristic state curve on the q-p plane is practically a straight line passing through the origin of stress space, even though the limit envelope may be highly non-linear along the pressure axis. However, their data does not agree with the deviatoric variation of the zero dilation line mathematically built into Equation 3.3.2.1. This equation suggests that the mobilized friction angles at the point of zero dilatancy in compression and extension are the same, or that the deviatoric traces of the zero dilation and the failure loci are concentric. Figure 3.12 presents data from Habib and Luong's (1978) paper which indicates this is not strictly true: $\phi = 24.6^0$ in extension vs. 32.5° in compression. If in later applications this turns out to be a serious limitation of the model, it may be very easily remedied by selecting an experimentally determined magnitude of R to normalize the zero dilation line in $\sqrt{J_2^*} - I_1$ stress space and another magnitude to normalize the failure locus. Such an improvement will require at least one additional material parameter.

For comparison, the differences between the concept of characteristic state and the more familiar critical state concept (Schofield and Wroth, 1968) are highlighted in Table 3.1.

Two analytic functions are used to describe the yield surface: one for the region below the zero dilation line, in the sub-characteristic domain, and another for the region between the zero dilation line and the limit line, in the super-characteristic domain. These two portions of the yield surface are chosen to be continuous and differentiable at the zero dilation locus.

3.3.3 Consolidation Portion of Yield Surface

From the istropy assumption, pure plastic volumetric strain must be predicted for an isotropic compression path. Therefore, a smooth yield

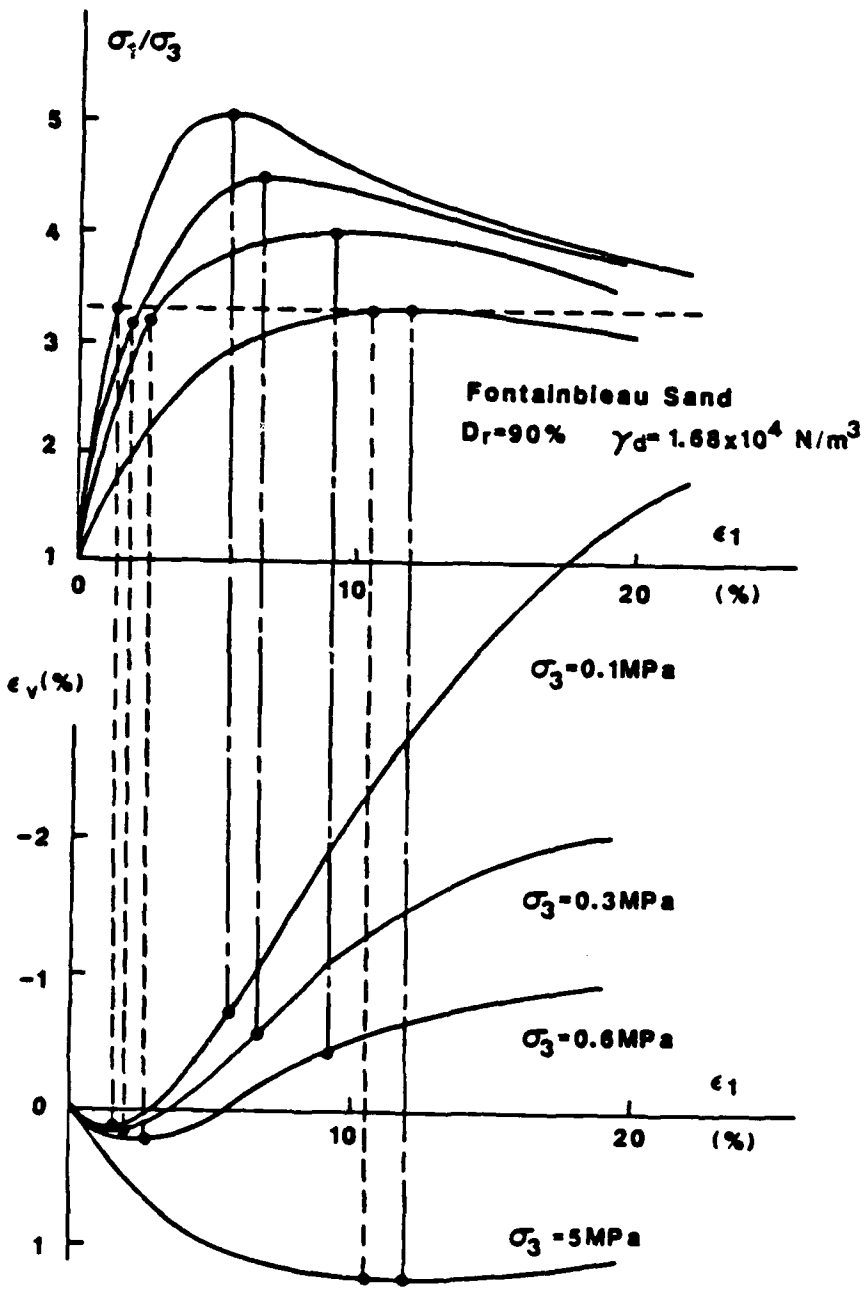

Figure 3.11 Constant q/p ratio (as given by constant σ_1/σ_3 ratio) at zero dilation as observed from axial compression stress-strain curves on dense Fountainbleau sand. Note that the peak stress ratio decreases with increasing pressure (after Habib and Luong, 1978)

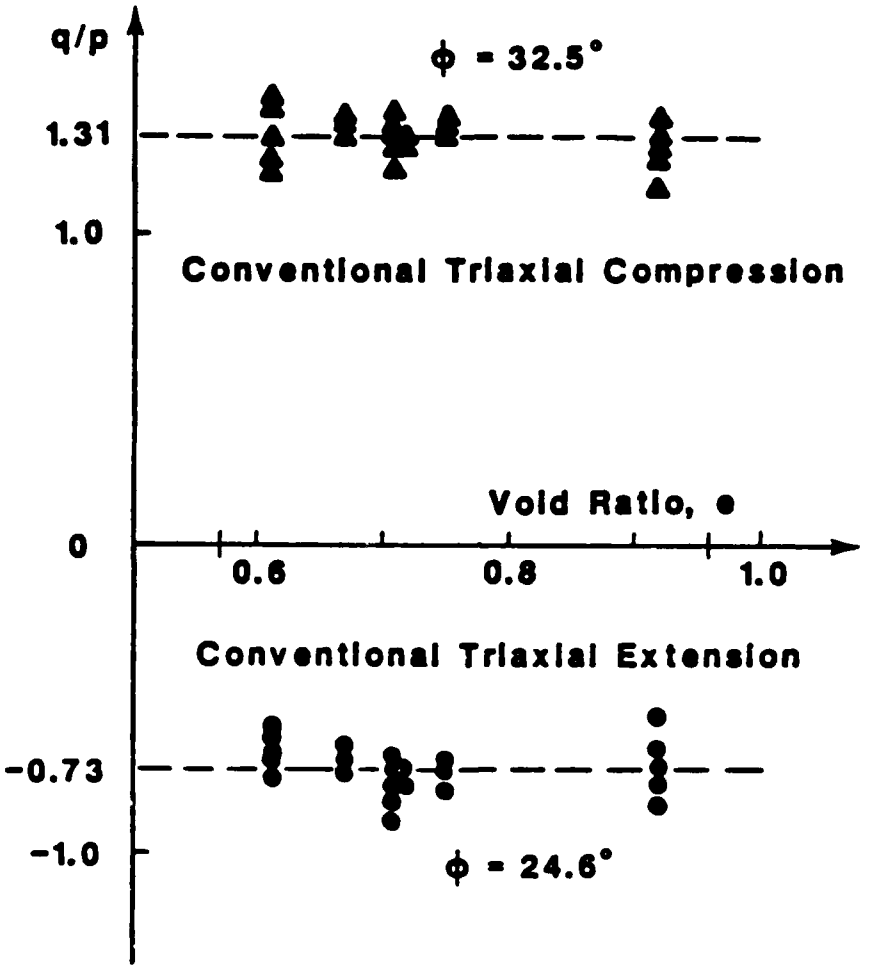

Figure 3.12 Characteristic state friction angles in compression and extension are different, suggesting that the Mohr-Coulomb criterion is an inappropriate choice to model the zero dilation locus (after Habib and Luong, 1978)

Table 3.1 Comparison of the Characteristic State and Critical State Concepts.

	PROPERTY	CHARACTERISTIC STATE	CRITICAL STATE
1.	Volume Variation	$\dot{\varepsilon}_v = 0$ at any $\dot{q}$	$\dot{\varepsilon}_v = 0$ at $\dot{q} = 0$
2.	Shear Strain, $\bar{\varepsilon}$	low (prior to failure)	indeterminate (at failure)
3.	Deformation	small	large
4.	Void Ratio (e)	any e	$e_{critical}$
5.	Grain Structure	maximum "locking" effect	uncertain
6	Loading	monotonic or cyclic	monotonic, asymptotic
7.	Behavior	transitionary	asymptotic
8.	Definition	threshold demarcating contractancy and dilatancy domains	idealized concept of soil
9.	Experimental Determination	direct therefore easy	by extrapolation therefore delicate

Source: Habib and Luong, 1978

surface must intersect the hydrostatic axis perpendicularly, and by a similar reasoning, it must also be parrellel to the hydrostatic axis at the zero dilation line.

Figure 3.13 shows plots of smooth yield surfaces back-fitted from the trajectory of plastic strain increments observed from a series of axial compression tests on Ottawa sand (Poorooshasb et al., 1966). Guided by these pictures, the meridional section of the yield surface below the zero dilation line ($\sqrt{J_2^*}/I_1 < N$) was chosen to be an ellipse

$$F = I_1^2 - 2\,(I_0/Q)\,I_1 + [(Q-1)/N]^2\,J_2^* + I_0^2\,[(2/Q)-1] = 0\,, \qquad (3.3.3.1)$$

where I_0 is its point of intersection with the I_1 axis, and Q is a parameter which controls the major to minor axis ratio of the ellipse. Figure 3.14 shows a plot of this yield surface in q^*-p space; note the mathematical interpretation of the parameter Q in this figure. Figure 3.15 gives an alternate view of the yield surface on the triaxial plane with material reference coordinates. This choice of the yield function is by no means original. Roscoe and Burland (1968) derived a particular form of this equation for their modified Cam-Clay theory in which the parameter Q was fixed at a magnitude of two such that

$$F = I_1^2 - I_0\,I_1 + (1/N^2)\,J_2^* = 0. \qquad (3.3.3.2)$$

However, in this work, Q is retained as a material parameter to enhance the simple model's ability to predict the compaction phenomenon. Magnitudes of Q reckoned from Poorooshasb's plots (Figure 3.13) are 1.75, 1.77, and 2.06 for Ottawa sand at 39%, 70%, and 94% relative density respectively, so if only a crude estimate is desired, it is not unrealistic to assume Q = 2. Theoretically and in general, however,

$$1 < Q < \infty\,. \qquad (3.3.3.3)$$

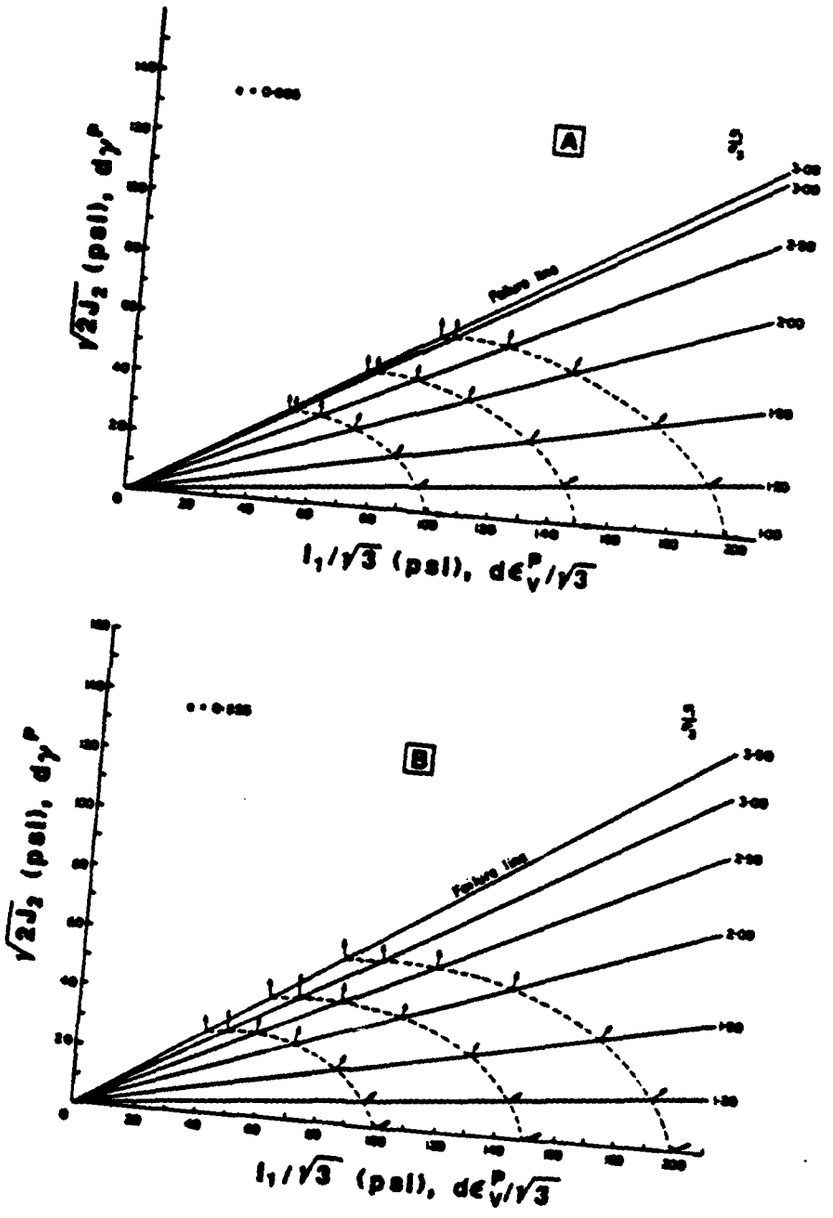

Figure 3.13 Establishment of the yield surfaces from the inclination of the plastic strain increment observed along axial compression paths on Ottawa sand at relative densities of (a) 39% (e=0.665), (b) 70% (e=0.555), and (c) 94% (e=0.465) (after Poorooshasb et al., 1966)

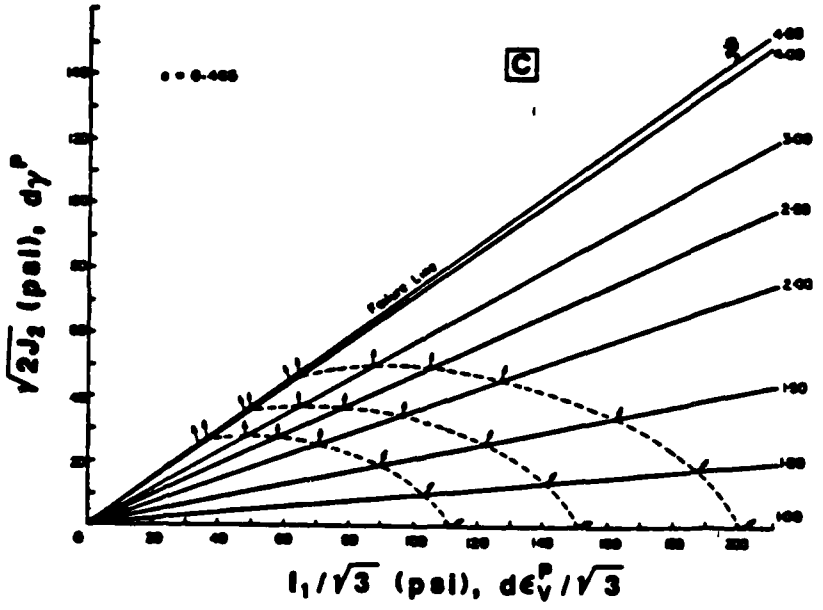

Figure 3.13 (continued)

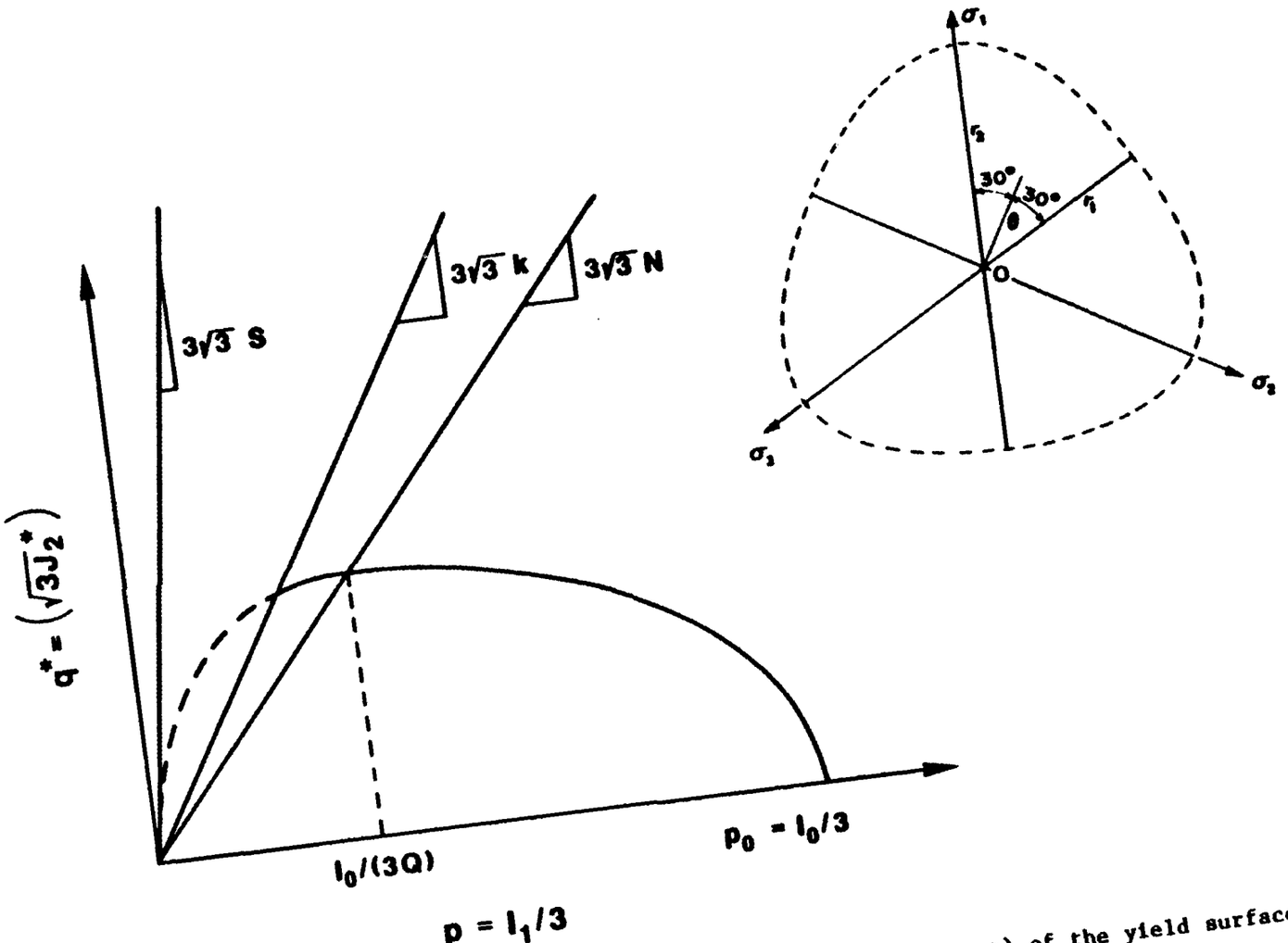

Figure 3.14 A typical meridional (q*-p) and octahedral projection (inset) of the yield surface

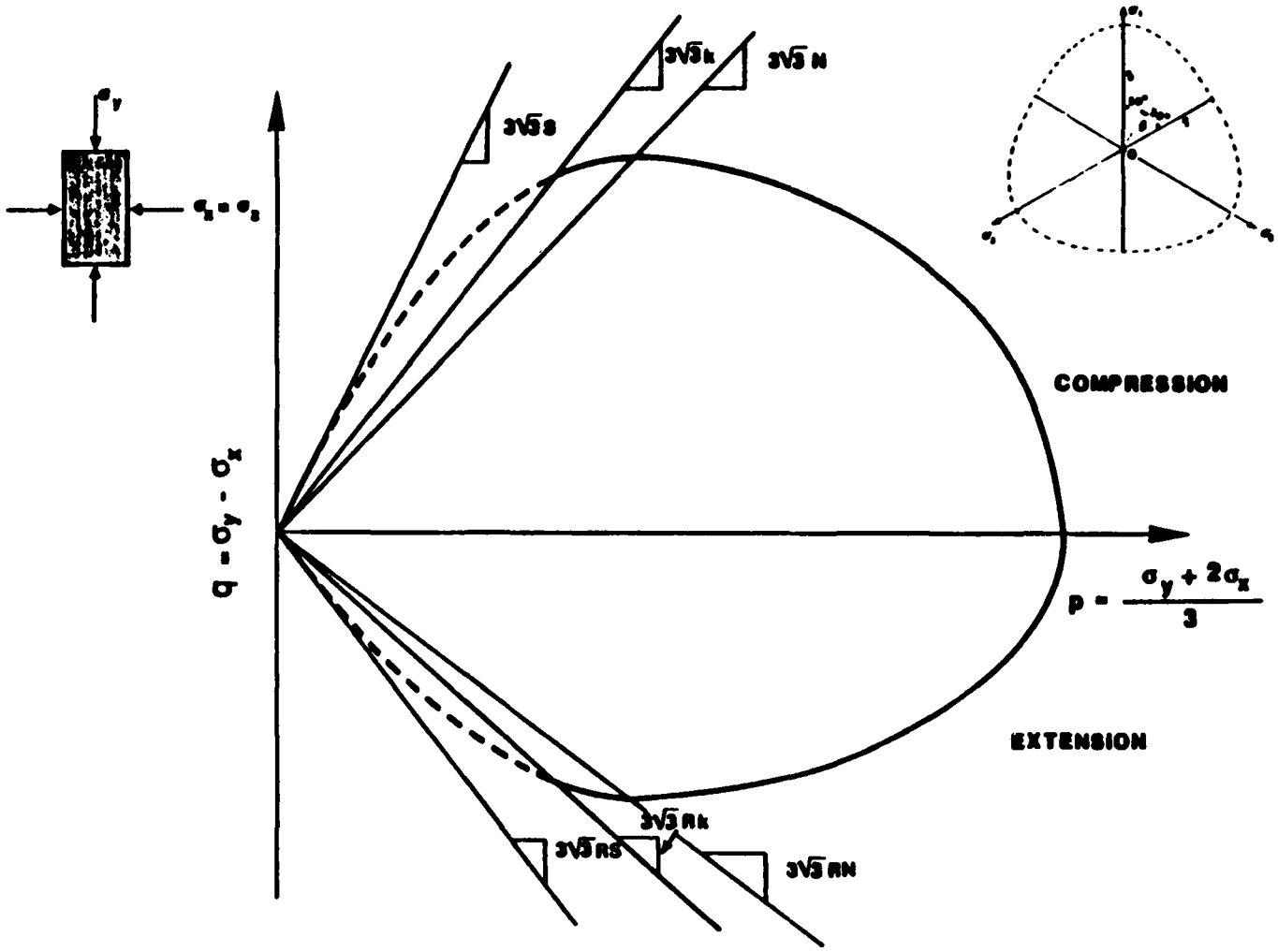

Figure 3.15 Projection of the yield surface on the triaxial q-p plane

3.3.4 Dilation Portion of Yield Surface

The yield surface's meridional segment above the zero dilation line intersects the limit or failure curve at an angle which has no obvious physical basis (Figure 3.3) This angle plays no role in theory and therefore offers no useful mathematical link between the yield surface and the limit surface. Nevertheless, the limit line does serve to delineate the real from the unreachable part of the dilation portion of the yield surface since the analytical form of the yield surface does not terminate abruptly at the limit line. In Figure 3.14, the real part of the dilation portion of the yield surface is the solid curve bounded by the zero dilation and limit lines, while the unreachable part is the dashed portion beyond the limit line.

A second order polynomial in $\sqrt{J_2^*}$-I_1 stress space was developed specifically for this portion of the surface. Constraints were imposed to ensure that: i) the surface passes through the origin of $\sqrt{J_2^*}$ - I_1 stress space at a specified slopes, and ii) its first partial derivatives merge continuously with the half-ellipse at the zero dilation line. The first requirement is an artifact of an earlier phase in the study (Seereeram et al., 1985) when it was thought that the slopes of the limit line and the yield surface should coincide at points on the limit line. However, in the version here, the slope S is fixed at a slope much steeper than the limit line to give more leverage in choosing the dilation portion of the yield surface to model plastic flow.

The proposed yield surface for the dilation domain $(\sqrt{J_2^*}/I_1 > N)$ is

$$F = I_1^2 + b\, J_2^* + \left[\frac{S}{N^2} - \frac{2}{N} - S\, b\right] I_1 \sqrt{J_2^*} + \left(I_0/Q\right)\left[\frac{1}{N} - bN\right]\left[\sqrt{J_2^*} - S\, I_1\right] = 0 , \qquad (3.3.4.1)$$

where b is a dimensionless material parameter. A detailed derivation of this equation and the restriction on the parameter "b" are presented in Appendix A.

From limited experience with this new yield surface, a preselected magnitude of S equal to 1.5 appears to work well. For reference, note that the slope of the limit line ($\sqrt{J_2^*}/I_1$ at failure) is typically in the range 0.20 to 0.35.

The constant b is constrained to be less than $\frac{1}{N^2}$, and the discriminant of Equation 3.3.4.1,

$$\left[\frac{S}{N^2} - \frac{2}{N} - Sb\right]^2 - 4b, \qquad (3.3.4.2)$$

identifies the canonical form of the surface. With S = 1.5, the back-computed dilation portion of the yield surface usually turns out to be elliptical.

For completeness, the yield surface gradient tensor equations are included in Appendix B.

3.3.5 Evolutionary Rule for the Yield Surface

To remain at yield during loading and unloading, the yield surface is assumed to contract and expand isotropically to stay with the stress point. This rule was selected because it produces many desirable features, among which are:

1. successive yield surfaces remain similar, as the data of Figure 3.13 suggest;
2. a unique zero dilation line is preserved for all loading paths, and more generally, the ratio of the components of the plastic strain increment vector remain constant for radial lines;

3. mathematical tractability; and

4. it can be readily modified to give "bounding surface" type hardening rules.

Since, in this theory, no elastic domain is postulated, plastic strains can occur at any stress level, and there are no restricted (or elastic) zones to impede the movement of the yield surface. The size of the yield surface is given by its intersection I_0 with the hydrostatic axis (Figure 3.14). Once the current state of stress is known, I_0 can be solved for directly from Equation 3.3.3.1 if the stress point is below the zero dilation line, or from Equation 3.3.4.1 if it is above. Thus, in effect, the consistency condition is automatically satisfied. If it is postulated that the yield surface does not follow the stress point on unloading, this evolutionary rule degenerates to that of a conventional stress-hardening theory of plasticity.

The equations for updating I_0 are presented in Appendix C.

3.4 Choice of the Field of Plastic Moduli

The expected magnitude and variation of the plastic modulus along three lines in $\sqrt{J_2^*}$-I_1 stress space dictated the choice of the field of plastic moduli:

1. the hydrostatic axis,

2. the zero dilation line, and

3. the failure or limit line.

Each of these three loading paths are now explored in sequence.

Consider a pure hydrostatic or spherical loading on an isotropic material with a yield function $F(\sqrt{J_2}, I_1) = 0$. Since such a path must produce only volumetric strain, $\partial F/\partial I_1$ is the only non-zero gradient component, and the

flow rule (Equation 3.1.1) therefore specializes to

$$d\varepsilon^p_{kk} = \frac{1}{K_p} \frac{\partial F/\partial I_1 \ (\partial F/\partial I_1 \ dI_1)}{\partial F/\partial I_1)^2} = \frac{1}{K_p} \ dI_1 \ . \qquad (3.4.1)$$

A comparison of this equation with its elastic analogue,

$$d\varepsilon^e_{kk} = \frac{1}{3K} \ d\sigma_{kk},$$

shows that the plastic modulus K_p is analogous to three times the elastic bulk modulus (K) for hydrostatic compression.

Following a similar development, we find that at a point of zero dilaton,

$$\partial F/\partial I_1 = 0,$$

$$\partial F/\partial \sqrt{J_2} \neq 0.$$

and therefore

$$de^p_{ij} = \frac{1}{K_p} \frac{\partial F/\partial \sqrt{J_2} \ s_{ij} \ (\partial F/\partial \sqrt{J_2}) \ (s_{mn} \ ds_{mn})}{4 \ J_2 \ (\partial F/\partial \sqrt{J_2})^2} = \frac{1}{K_p} \frac{s_{ij} \ s_{mn} ds_{mn}}{2 \ J_2}$$

from which we then see that

$$\sqrt{(\frac{1}{2} \ de^p_{ij} de^p_{ij})} = \frac{1}{K_p} \frac{s_{mn} \ ds_{mn}}{2\sqrt{J_2}} = \frac{1}{K_p} \ d(\sqrt{J_2}) \ ,$$

$$\text{or} \quad d\bar{\varepsilon}^p = \sqrt{(\frac{3}{2} \ de^p_{ij} de^p_{ij})} = \frac{1}{K_p} \ dq \ . \qquad (3.4.2)$$

Comparing this equation with its elastic analog shows that K_p is comparable to twice the elastic shear modulus (G) at the zero dilation line.

Mathematically, this means that at the point of zero dilatancy

$$\frac{1}{K_p} = \frac{1}{dq/d\bar{\varepsilon}} - \frac{1}{2 \ G} \ , \qquad (3.4.3)$$

where $dq/d\bar{\varepsilon}$ is the tangent modulus. Note that this is a general result not contingent on any particular choice of the yield surface.

The final case considers the magnitude of the plastic modulus at the failure line. At this locus, the material fails in the sense that the incremental plastic strains are supposedly "infinite". Therefore, in order to asymptotically approach this response at the limit state, the plastic modulus must approach zero at all points on this line (see Equation 3.1.1).

The plastic modulus functions as a bulk modulus for hydrostatic loading, a shear modulus at the zero dilation line for shear loading, and a "failure" modulus (zero) on the limit surface.

With this background, a specific form is now derived for the plastic moduli on the hydrostatic axis, and an interpolation rule is then adopted to model its approach to zero at the limit surface.

The plastic modulus on the hydrostatic axis increases with mean pressure. A familiar pressure-volume relationship along this axis is assumed

$$I_1 = (I_1)_i \exp(\lambda \varepsilon^p_{kk}) \quad , \tag{3.4.4}$$

where $(I_1)_i$ is the magnitude of I_1 at the start of a virgin hydrostatic loading, and λ is a plastic stiffness constant. Soils engineers will recognize this equation as an alternative statement of the typical linear voids ratio vs. log mean pressure relationship. In incremental form

$$dI_1 = (I_1)_i \lambda \, d\varepsilon^p_{kk} \exp(\lambda \varepsilon^p_{kk}) = \lambda I_1 \, d\varepsilon^p_{kk} \quad , \tag{3.4.5}$$

which, by comparison with Equation 3.4.1, shows that the plastic modulus K_p is equal to λI_1, a linear stress-dependent function.

It is reasonable to expect the plastic stiffness to decrease monotonically from its bulk modulus magnitude (λI_1) on the hydrostatic axis to zero on the fixed limit surface

$$f(\underset{\sim}{\sigma}) = k \quad . \tag{3.4.6}$$

A simple and not unreasonable rule for this decrease is

$$K_p = \lambda\, I_1 \{1 - [f(\underset{\sim}{\sigma})/k]\}^n \,, \qquad (3.4.7)$$

in which the exponent "n" is regarded as a material constant. Geometrically, this interpolation function forces the equi-plastic modulus loci on the octahedral plane in principal stress space to resemble the π-section of the selected failure criterion $f(\underset{\sim}{\sigma})$. As will be described later in the initialization procedure, the observed plastic (shear) modulus at the zero dilation line provides the necessary information for computing the exponent "n" directly.

Any desired frictional failure criterion $f(\underset{\sim}{\sigma})$ may be inserted in Equation 3.4.7. The form chosen here is

$$\frac{\sqrt{J_2^*}}{I_1} = k \,. \qquad (3.4.8)$$

Because one of the sands used in the evaluation had a significantly curved (along the pressure axis) failure envelope, the straight line representation was modified to

$$\frac{\sqrt{J_2^*}}{I_1} \left(I_1/p_a\right)^m = k \,, \qquad (3.4.9)$$

to allow for non-linear pressure dependence. The exponent "m" in this equation is material parameter that describes the degree of curvature, and p_a is atmospheric pressure in consistent units. The modifying factor $(I_1/p_a)^m$ was proposed by Lade (1977). So, in general, two parameters "k" and "m", characterize the strength of the material, but as discussed earlier, the parameter "R" in Equation 3.3.1.6 may also be considered a model constant if no a priori assumptions are made about matching the compression and extension radii with a Mohr-Coulomb or any other criterion.

3.5 Elastic Characterization

Two elastic stress-strain relations are employed. The simpler idealization is used for simulations within a limited range of mean stress, while the more complicated option is used for stress paths which cover a wider range.

In the first alternative, the elasticity of the material is assumed to be isotropic and linear, while anisotropy and nonlinear effects are attributed to plastic deformation. The incremental elastic stress-strain relation is

$$d\varepsilon^e_{kk} = d\sigma_{kk} / (3\,K) \quad , \text{ and} \tag{3.5.1}$$

$$d\underset{\sim}{e}^e = d\underset{\sim}{s} / (2\,G) \quad , \tag{3.5.2}$$

where K and G are the elastic bulk and shear moduli respectively, and $d\varepsilon^e_{kk}$ and $d\underset{\sim}{e}^e$ are the trace and deviatoric components respectively of the elastic strain increment $d\underset{\sim}{\varepsilon}^e$.

For the second more complicated option, it is assumed that: i) the material is elastically isotropic, and ii) the Young's modulus E depends on the minor principal stress σ_3 as proposed by Janbu (1963). That is,

$$E = K_u\, p_a\, (\sigma_3/p_a)^r \tag{3.5.3}$$

where K_u is a dimensionless modulus number, and r is an exponent to regulate the influence of σ_3 on E. As suggested by Lade (1977), Poisson's ratio ν for sands is assumed equal to 0.2.

It is recognized that these elastic stress-strain relations are the simplest of choices, and if a more complete elastic characterization of sand is desired, degradation effects and shear stress dependency must also be

AD-A173 976 GENERALIZED PHENOMENOLOGICAL CYCLIC STRESS-STRAIN-STRENGTH CHARACTERIZATI (U) FLORIDA UNIV GAINESVILLE DEPT OF CIVIL ENGINEERING M C MCVAY ET AL. 3/4

UNCLASSIFIED 02 SEP 84 AFOSR-TR-86-0918 AFOSR-84-0108 F/G 8/13 NL

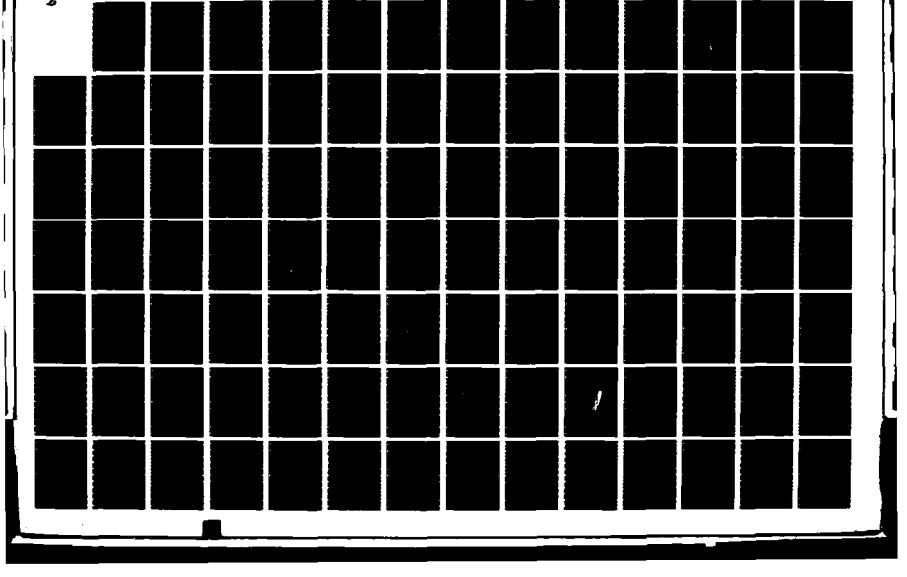

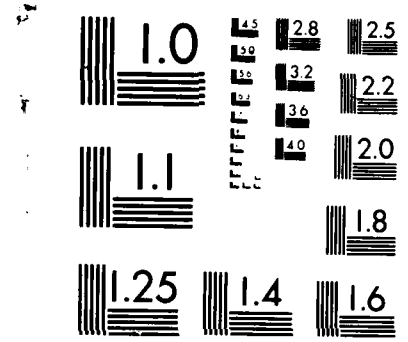

MICROCOPY RESOLUTION TEST CHART
NATIONAL BUREAU OF STANDARDS-1963-A

included. Examples of these more sophisticated elastic idealizations have been presented by Ghaboussi and Momen (1982) and Loret (1985).

3.6 Parameter Evaluation Scheme

A hydrostatic compression test and an axial compression test furnish the data to initialize the simple model. But, since it is customary to hydrostatically consolidate a specimen prior to axial compression, one such set of experiments can provide the necessary calibration data. Quite naturally, the initialization procedure will require more tests if certain aspects of the simple model are to be improved. For example, if the stress-dependent elastic characterization or the curved failure envelope options are included, data must be obtained from a series of, say, three axial compression tests over an appropriate range of confining pressures. Furthermore, if precise matching of the failure or the zero dilation locus on the deviatoric plane is warranted, an axial extension test or equivalent will also be needed.

Before going into the details of the parameter evaluation scheme, this is an ideal juncture to emphasize an important innate aspect of the simple theory: if the failure envelope is a straight line, the representation predicts exactly the same plastic strains for parallel stress paths which all emanate from points on the hydrostatic axis. Therefore, for instance, the theory will predict identical q/p vs. $\bar{\varepsilon}^p$(or q/p vs ε^p_{kk}) curves for a series of conventional axial compression paths covering a range of confining pressures. Data will be presented later which demonstrates this intrinsic trait of the simple theory.

Material parameters are divided into three conceptually distinct groups:

1. The elastic constants: K_u and r, or K and G.
2. The plastic stiffness/strength parameters which serve to define the scalar field of plastic moduli: λ, n, and k.

3. The parameters governing the shape of the yield surface, or alternatively, the parameters governing the direction of the plastic strain increment vector (n_{ij}) and the extent of plastic loading ($n_{ij}d\sigma_{ij}$) : Q and b.

3.6.1 Elastic Constants

The elastic Young's modulus is determined from an unloading segment in the axial compression test,

$$E = (1 + \nu) \frac{\Delta q}{\Delta \bar{\varepsilon}^e} \quad , \qquad (3.6.1.1]$$

where Δq is the deviatoric load reduction, $\Delta \bar{\varepsilon}^e$ is the recoverable (or resilient) shear strain, and ν is Poisson's ratio assumed equal to 0.2. For the more complicated option in which E depends on the minor principal stress, the modulus exponent r and log (K_u) are the slope and intercept respectively of a straight line fit to a plot of log (E/p_a) vs. log (σ_3/p_a) . This data is most conveniently obtained from the unloading loops of a series of axial compression tests at different levels of confining stress (σ_3) .

3.6.2 Field of Plastic Moduli Parameters

The parameter λ is matched to the stiffness of the material in hydrostatic compression (Equation 3.4.4). It is simply the slope of a plot of log $[I_1/(I_1)_i]$ vs. ε^p_{kk} for an istropic consolidation test, or in terms of conventional geotechnical parameters,

$$\lambda = \log_e(10) \frac{1 + e_o}{C_c - C_s} \quad , \qquad (3.6.2.1)$$

where e_o is the initial voids ration and C_c and C_s are the compression and swell indices respectively. As an aid in separating the elastic and plastic volumetric strains, note that direct integration of Equation 3.5.3 gives

$$\varepsilon^{e}_{kk} = \frac{3\,(1 - 2\,\nu)\,(p_a)^{r-1}}{K_u\,(1-r)}\,[p^{1-r} - p^{1-r}_{initial}] \qquad (3.6.2.2)$$

for a hydrostatic compression path.

The strength parameter k is the peak stress ratio $\sqrt{J_2^*}/I_1$ determined from an axial compression or any other shear path to failure. In terms of more familiar strength constants,

$$3\sqrt{3}\,k = (q/p)_{peak} = 6 \sin \phi_c/(3 - \sin \phi_c) \quad , \qquad (3.6.2.3)$$

where ϕ_c is the friction angle computed from a compression test (cf. Equation 2.5.2.12).

If the curved failure surface option is used, the exponent m and log (k) are the slope and intercept respectively of a straight line fit to plot a log $(\sqrt{J_2^*}/I_1)_{peak}$ vs. log (p_a/I_1) for a number of tests.

At the point of zero dilatancy on the q/p vs. $\bar{\varepsilon}^p$ stress-strain curve, a) the mean stress p, b) the stress ratio q/p, and c) the tangent modulus $dq/d\bar{\varepsilon}$ are used to compute the slope of the zero dilation line,

$$N = \frac{(q/p)}{3\sqrt{3}} \quad (\text{at } d\varepsilon^p_{kk} = 0). \qquad (3.6.2.4)$$

The result is then combined with $^{p}\,d\varepsilon^p_{kk} = 0$ and $K_p\;d\varepsilon^p_{k\bar{k}} = 0$ (computed from Equation 3.4.3) to calculate the exponent n of the interpolation function as:

$$n = \log (K_p/3\lambda p) \div \log (1 - \frac{N}{k}) \quad . \qquad (3.6.2.5)$$

Choosing n exactly as given in this equation guarantees that the plastic stiffness at the zero dilation line will be matched. But in order to obtain a better overall fit to the data, it may be desirable to alter this constant somewhat. In Equation 3.6.2.5, $K_p/3\lambda p$ is the ratio of the plastic stiffness

at the zero dilation line to that on the hydrostatic axis. For a given N/k ratio, the exponent n may be interpreted as a measure of the stiffness of the stress-strain curve. Higher magnitudes of n produce a softer response.

3.6.3 Yield Surface or Plastic Flow Parameters

The constants Q and b (with a preselected slope of S = 1.5) govern the direction of the plastic strain increment. For a compression shear test [g(θ) = 1],

$$\chi = \sqrt{3}\, d\varepsilon^{p}_{kk}/d\bar{\varepsilon}^{p} = 6\, \frac{\partial F}{\partial I_1} \Big/ \frac{\partial F}{\partial \sqrt{J_2^*}} \quad . \tag{3.6.3.1}$$

Substituting the explicit forms of the partial derivatives for the consolidation surface (listed in Appendix B) into this identity gives

$$1 - 2\left[1 - \frac{z\,(Q-1)^2}{6\,\chi\,N^2}\right] + \frac{(Q-1)^2}{N^2}\, z^2 + \left[1 - \frac{(Q-1)^2\, z}{6\,\chi\,N^2}\right]^2 (2Q - Q^2) = 0 \quad , \tag{3.6.3.2}$$

where z is the mobilized stress ratio $\sqrt{J_2^*}/I_1$. Similarly, for the dilation surface, it can be shown that

$$b = \frac{1}{(z-S)^2}\left[6\,\chi\,(2z - S + C\,z^2) + C\,S + 1\right] \quad , \tag{3.6.3.3}$$

where

$$C = \left[\frac{S}{N^2} - \frac{2}{N}\right]$$

Therefore, by recording the pointwise incremental plastic

volumetric/shear strain ratio χ and the corresponding mobilized stress ratio z along an axial compression path, the parameter b can be solved for directly using Equation 3.6.3.3, while Q must be solved for iteratively from Equation 3.6.3.2. The back-computed magnitudes of Q and b have been found not to change much from point to point indicating that reasonable choices were made for both portions of the yield surface.

3.6.4 Interpretation of Model Parameters

An attempt is made in Table 3.2 to attach the simplest possible geotechnical interpretation to each model constant. Table 3.3 summarizes the likely trends in the magnitudes of these parameters with increasing relative density. Later, in the evaluation of the model, there will be an opportunity to compare these expected trends with calculated parameters for a range of densities.

3.7 Comparison of Measured and Calculated Results Using the Simple Model

Three data sets are used to demonstrate the range of applicability (in terms of the loading paths) of the simple model. First, a recent series of hollow cylinder tests reported by Saada et al. (1983) is used to assess the model performance along different linear monotonic paths. Each of these paths emanate from the same point on the hydrostatic axis (p= 30 psi) and move out in principal stress space at different Lode angles (θ), while the intermediate principal stress or the mean pressure is held constant.

The second test sequence was extracted from a recent paper by Hettler et al. (1984). It consists of a comprehensive series of axial compression tests on sands at different densities and all-around pressures. This data is considered very reliable because it has been reproduced by other researchers using alternative testing devices (see, for example, Goldscheider, 1984, and Lanier and Stutz, (1984). Since these tests covered a wide range of

Table 3.2 Simple Interpretation of Model Constants

MODEL PARAMETER	GEOTECHNICAL INTERPRETATION
K	Friction angle, ϕ
m	Degree of curvature of the Mohr-Coulomb failure envelope
N	Friction angle at constant volume, ϕ_{cv}
λ	Slope of voids ratio (e) vs. log mean stress (p) plot, or compression index
b	Magnitude of positive angle of dilation [see Rowe (1962) for a development of the theory of stress-dilatancy]
Q	Magnitude of negative angle of dilation
K_u and r	Elastic constants which vary with confining pressure
n	Stiffness of the shear stress-clear strain ((q vs. $\bar{\varepsilon}$) curve.

Table 3.3 Expected Trends in the Magnitude of Key Parameters With Relative Density

PARAMETER	EXPECTED TREND WITH INCREASING RELATIVE DENSITY
Q	increases, implying less compation per unit shear strain
b	increases, implying greater dilatancy per unit shear strain
N	unchanged, as implied by characteristic state theory
n	decreases slightly, modeling a less ductile response
k	increases, higher strength due to greater degree of interlocking
m	increases, deviation from pure frictional behavior becomes more pronounced as interlocking contribution to shear resistance increases
λ	increases, stiffer response in hydrostatic compression due to denser configuration of particles
K_u	increases, stiffer elastic response because denser packing results in lower inter-particle contact stresses
r	decreases, lower interparticle contract forces result in a smaller fraction of the granules being cushed

densities, it was also possible to compare the calculated material parameters with the trends suggested in Table 3.3.

Thirdly, a comparison of measured and simulated response for a special series of load-unload-reload stress paths (Tatsuoka and Ishihara, 1974a and 1974b) shows, at least in a qualitative sense, the realistic nature of the simple representation for much more complicated stress histories.

3.7.1 Simulation of Saada's Hollow Cylinder Tests

Figure 3.16 depicts the state of stress in a typical hollow cylinder device. All tests paths were stress controlled and were either constant intermediate principals stress (i.e., constant $\sigma_r=\sigma_\theta$) or constant mean pressure shear paths. Fifteen trajectories were considered in principal stress space. When dealing with such an assortment of stress paths, it is always convenient to introduce a compact but unmistakably clear notation, and Saada's (Saada et al., 1983) convention is adopted here. The letters "D" and "G" appear first in the test designation and they refer to loading conditions with constant intermediate principal stress or constant mean stress respectively. The letters "C" or "T" follow and they indicate whether the axial stress (σ_z)was in relative compression or tension respectively. If a shear stress ($\tau_{z\theta}$) was applied, the letter "R" is appended to "C" or "T". The number which comes after the letters is the fixed angle (in degrees) between the major principal stress (σ_1) and the vertical (or z) direction; this is shown as the angle β in Figure 3.17. These angles were nominally 0° [with Lode angle $\theta = 30^0$ (compression tests)], 15° ($\theta = 27^0$), 32^0 ($\theta = 15^0$), 45^0 [$\theta= 0^0$ (pure torsion)], 58^0 ($\theta = -15^0$) , 75^0 ($\theta = -27^0$) , and 90^0 [$\theta = -30^0$ (extension tests)]. So, for example, a GTR 58 test is one in which:

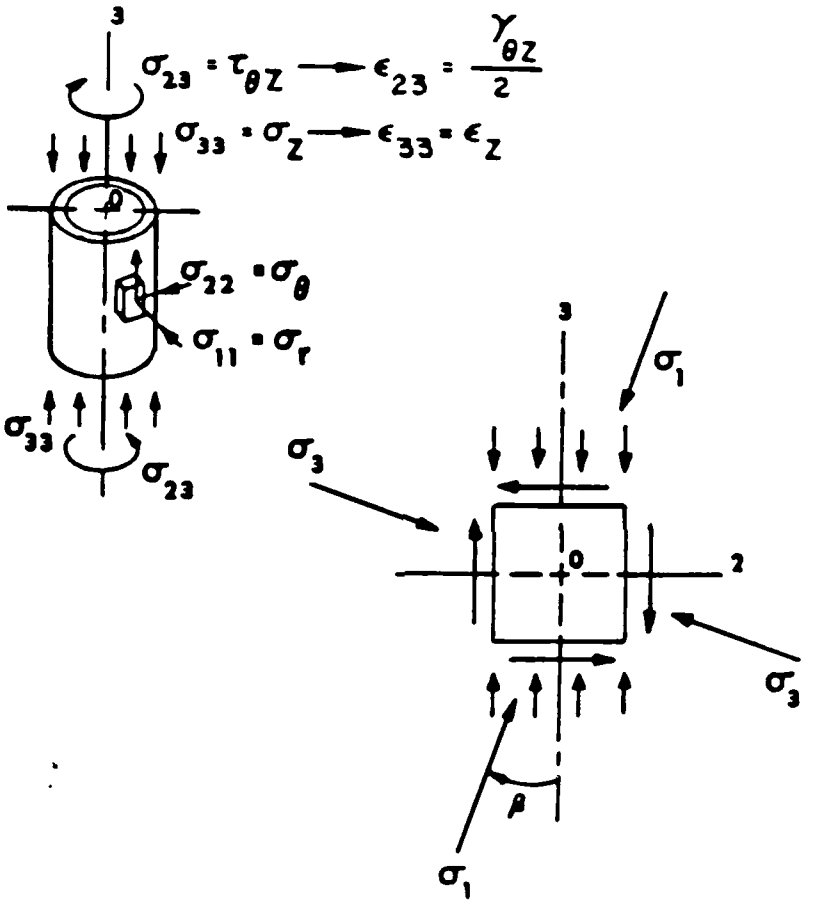

Figure 3.16 Stress state in "thin" hollow cylinder

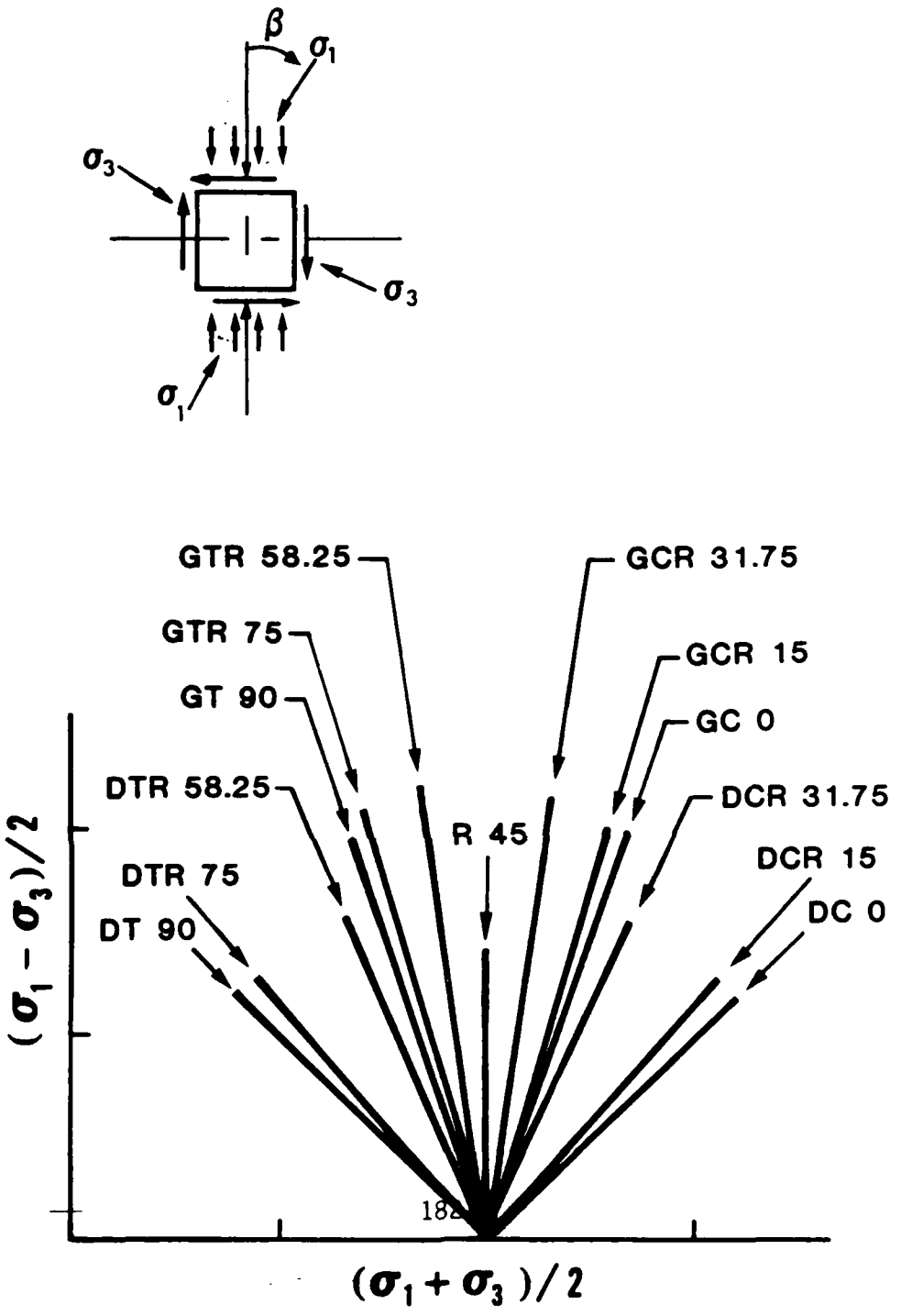

Figure 3.17 Saada's hollow cylinder stress paths in Mohr's stress space (after Saada et al., 1983)

a) the incremental application of the stress components ensures no change in mean stress (G), b) the axial stress is in tension relative to the initial hydrostatic state (T), c) a torque is applied (R), d) the angle between σ_1 and the vertical axis is constant and equal to 58 degrees (Lode's parameter θ = -15°). Wherever possible, the more familiar test path nomenclature of Figure 2.2 is juxtaposed with this specialized test designation. Figure 3.17 depicts the trajectories of these shear paths in Mohr's stress space, and with reference to Figure 2.2, all test paths are included except the CTE.

Reid-Bedford sand, at a relative density of 75%, was the material tested in all experiments. Its physical characteristics are given in Chapter 1.

Following the recommended initialization procedure, all but the elastic parameters were determined from the axial compression and hydrostatic compression paths of Saada's series of tests. The elastic constants had to be estimated from the unloading triaxial tests given in Chapter 1, because Saada monotonically sheared (to failure) all of his specimens. Two solid cylindrical axial compression tests, at confining pressures of 35 and 45 psi, were also extracted from Chapter 1 to supplement Saada's data.

Table 3.4 lists the computed parameters. Figures 3.18 and 3.19 show the measured and fitted response for the hydrostatic compression and axial compression paths respectively. Very close agreement is observed in both cases. Figures 3.20 and 3.21 show measured and predicted response for the axial compression paths on the solid cylindrical specimens at confining pressures of 35 and 45 psi respectively. Again the correspondence is good. However, it appears that the observed volumetric compression in the solid cylinder tests is slightly less than that recorded in the hollow cylinder test (see Figure 3.19)

Table 3.4 Model Constants for Reid-Bedford Sand at 75% Relative Density

PARAMETER	MAGNITUDE
Elastic Constants:	
Modulus number, k_u	2,400
Modulus exponent, r	0.50
Yield Surface Parameters:	
Slope of zero dilation line, N	0.128
Shape controlling parameter of consolidation portion of yield surface, Q	2.6
Shape controlling parameter of dilation portion of yield surface, b	15.0
Field of Plastic Moduli Parameters:	
Plastic compressibility parameter, λ	280
Strength parameter, k (note: no curvature in failure meridian assumed)	.300
Exponent to model decrease of plastic modulus, n	2

Note: these parameters were computed solely from the experiments of Saada et al. (1983)

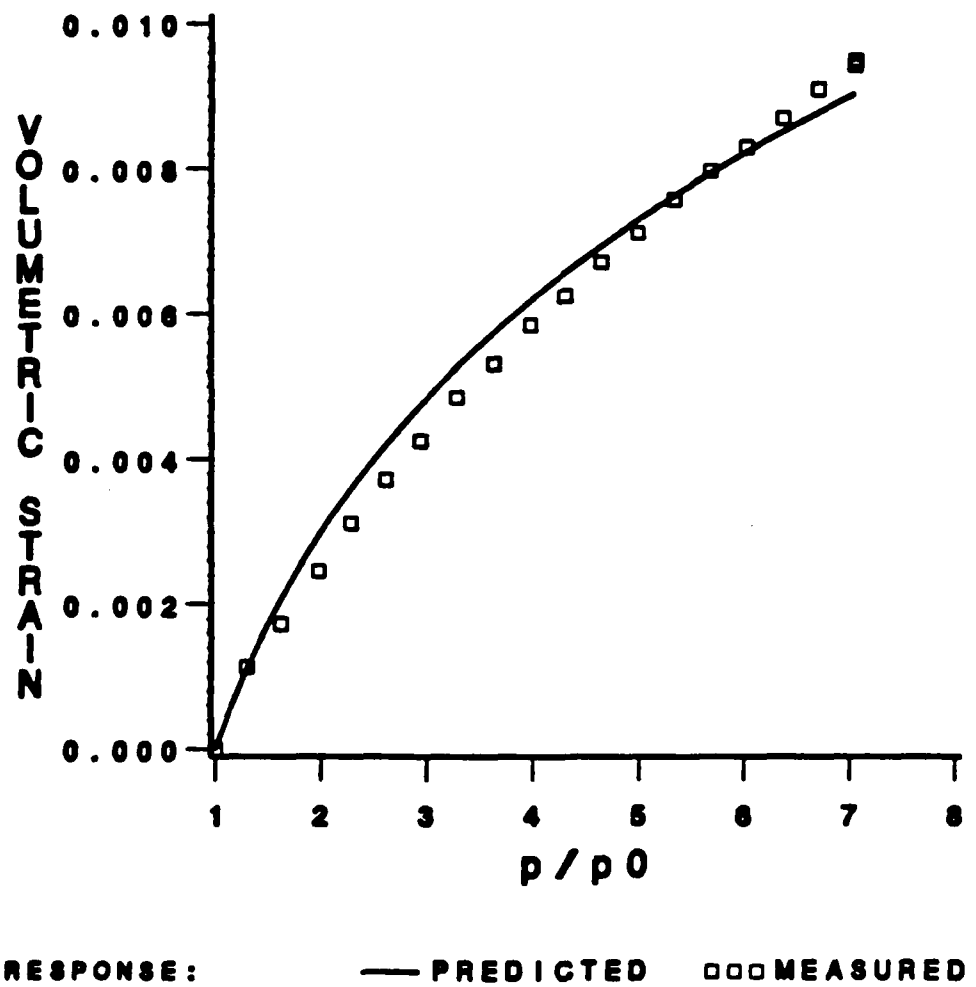

Figure 3.18 Measured vs. fitted response for hydrostatic compression (HC) test using proposed model (p_0 = 10 psi)

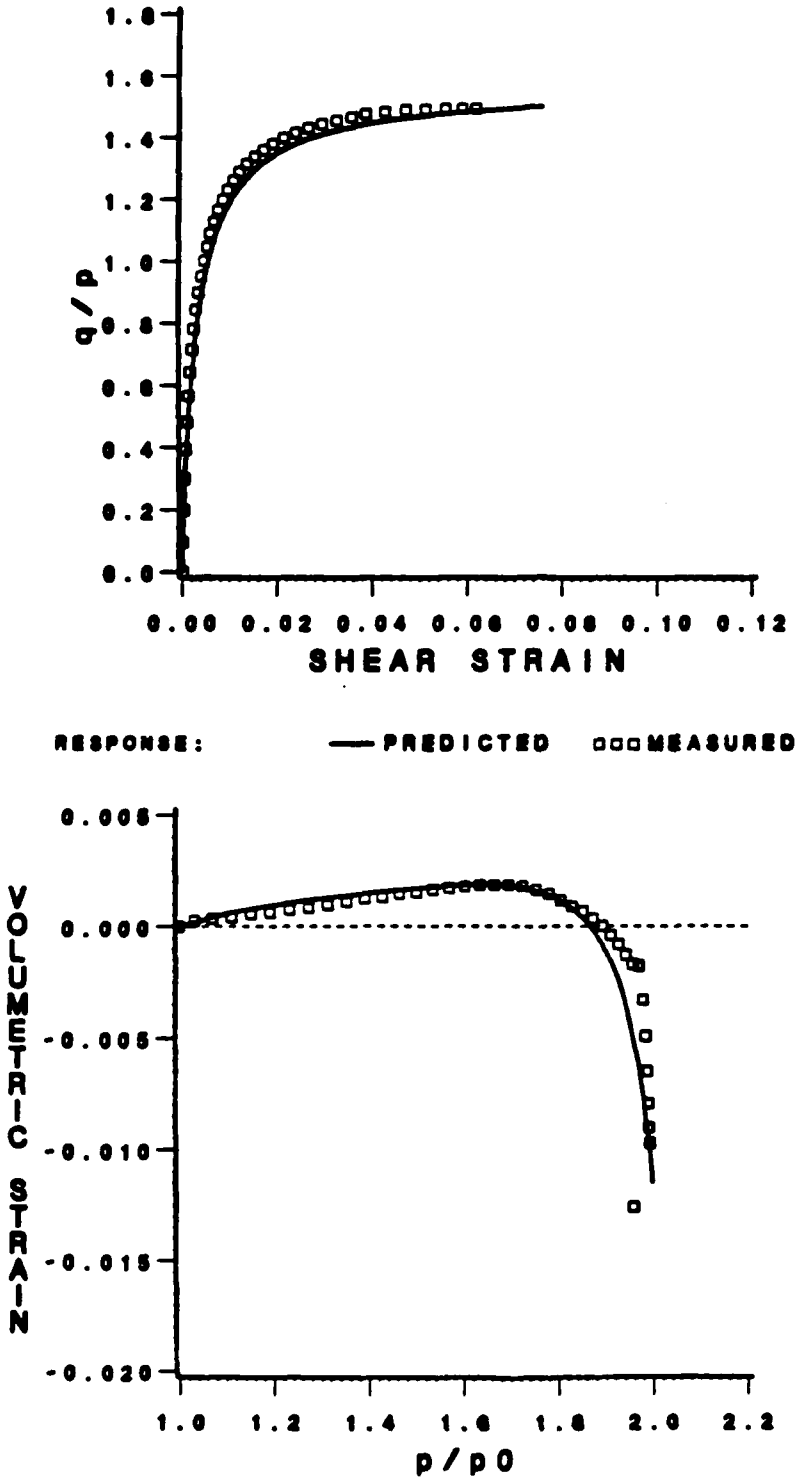

Figure 3.19 Measured vs. fitted response for axial compression test (DC 0 or CTC of Figure 2.3) @30 psi using proposed model

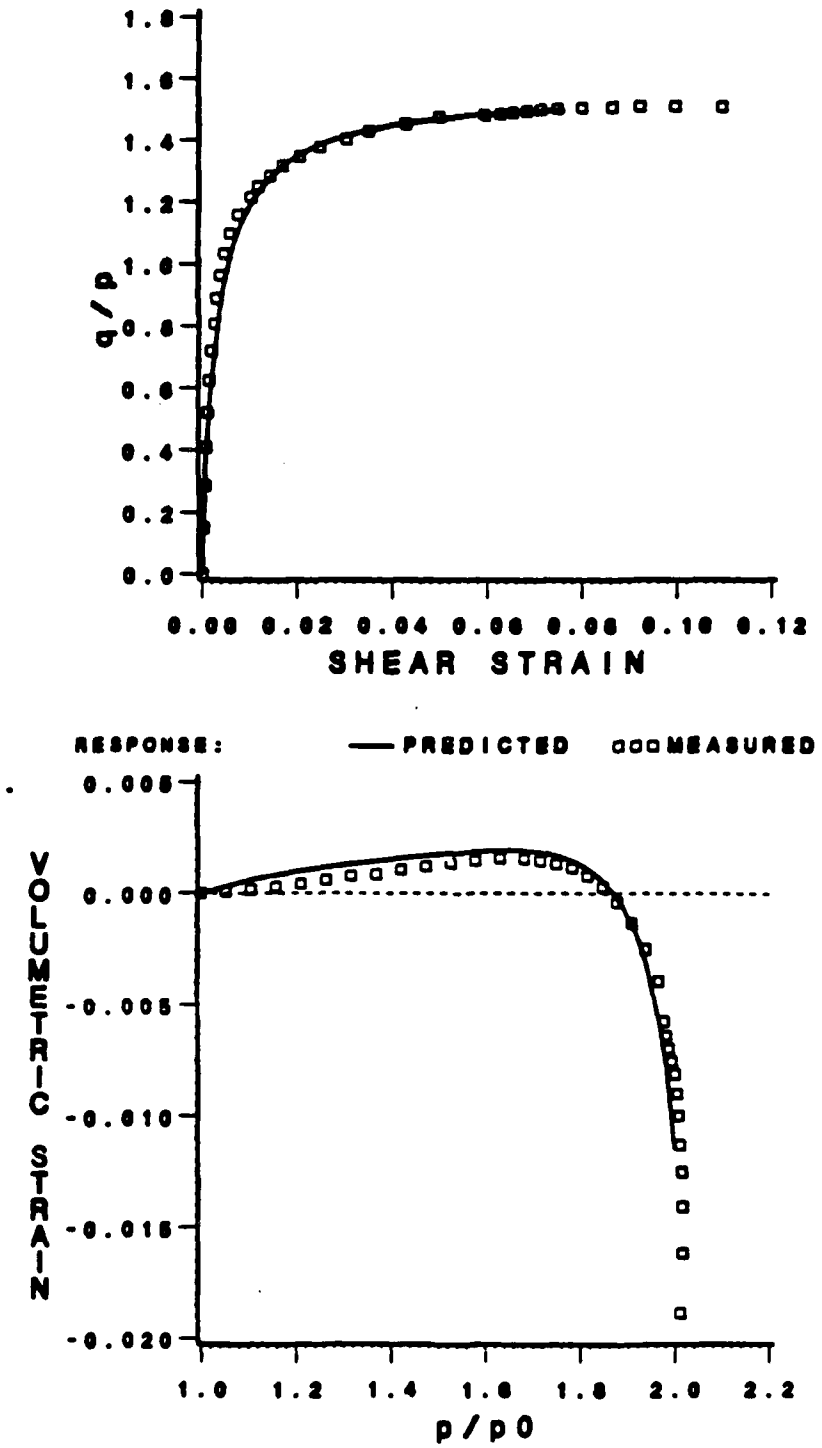

Figure 3.20 Measured vs. predicted response for axial compression test (NC 0 or CTC of Figure 2.3) @35 psi using proposed model

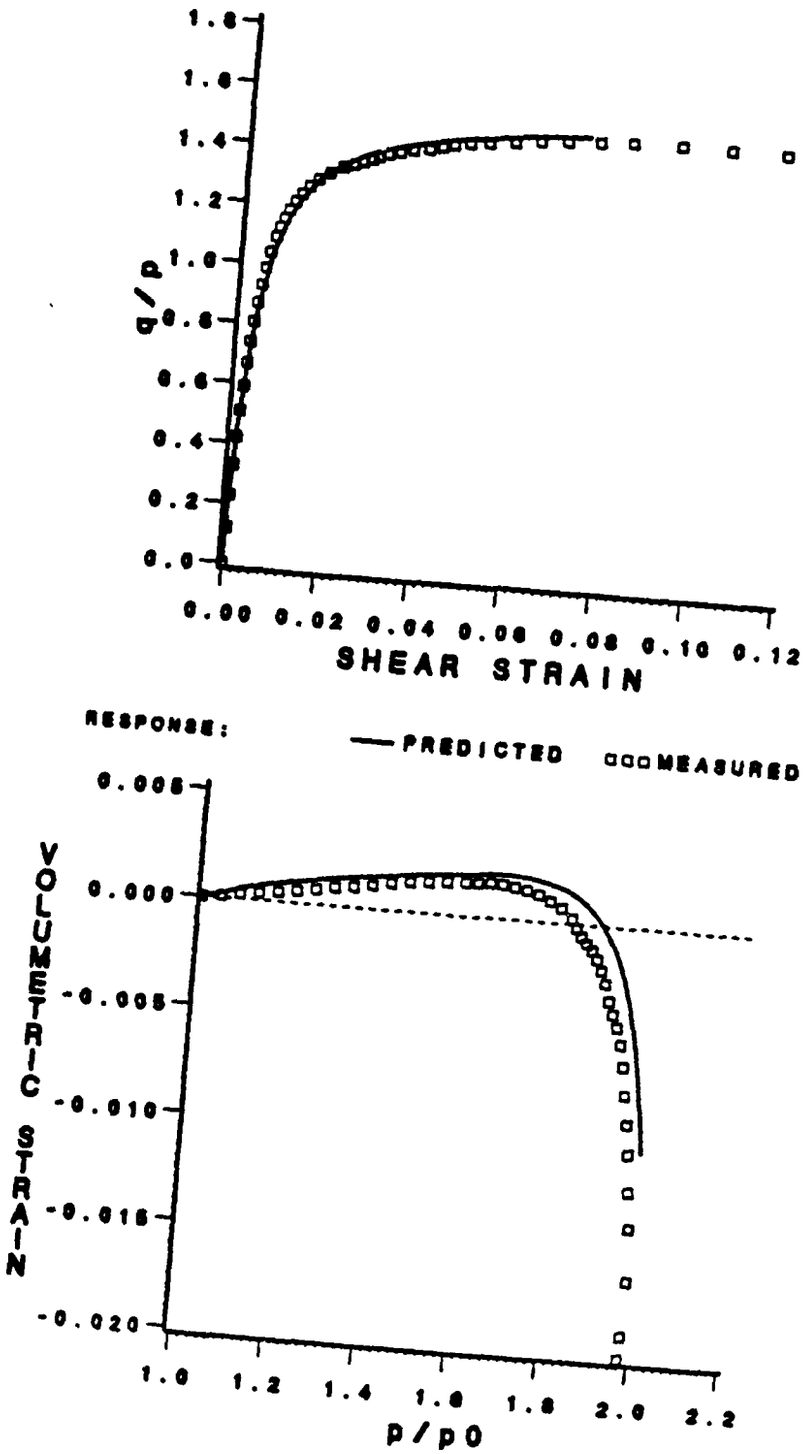

Figure 3.21 Measured vs. predicted response for axial compression test (DC 0 or CTC of Figure 2.3) @45 psi using proposed model

Predictions for the RTC and TC stress paths (of Figure 2.2) are given in Figures 3.22 and 3.23. Although the predictions here are not as precise as the previous axial compression paths, they are satisfactory considering the radical departure from the axial compression trajectory used in fitting the parameters.

Lode's parameter θ in all of the previous experiments were the same ($\theta = 30^0$). When the stress path moves on another meridional plane, as shown by the prediction of the axial extension test ($\theta = -30^0$) in Figure 3.24, the agreement is far less impressive. Even though the strength asymptote appears to be reasonably matched, the pre-peak model response is too stiff, and the large compression strains observed just prior to failure are not predicted. Close inspection of the remainder of the hollow cylinder predictions complied in Appendix D uncovers two distinct trends i) as the trajectory of the stress path moves away from compression toward extension, the simulations worsen in that the calculated shear stress-shear strain and volumetric compressive response become stiffer than the measured data, ii) the strength asymptote is underpredicted for the tests where the angle between the vertical direction and the major principal stress is close to 32°, while it is overpredicted near 75°. Seereeram, McVay and Linton (1985) have attempted to explain the second discrepancy by correlating (anisotropic) strength with the angle between the stress characteristics and those of the slip-line field. An important point to emphasize is that all the constant pressure shear paths, including the pure torsion test, trace identical curves in q^*-p stress space, and so generate exactly the same predicted response.

Because of the well-known experimental difficulties associated with extension tests (Jamal, 1971, and Lade, 1982), it is perhaps premature to conclude from this single series of tests that the formulation is unsuitable

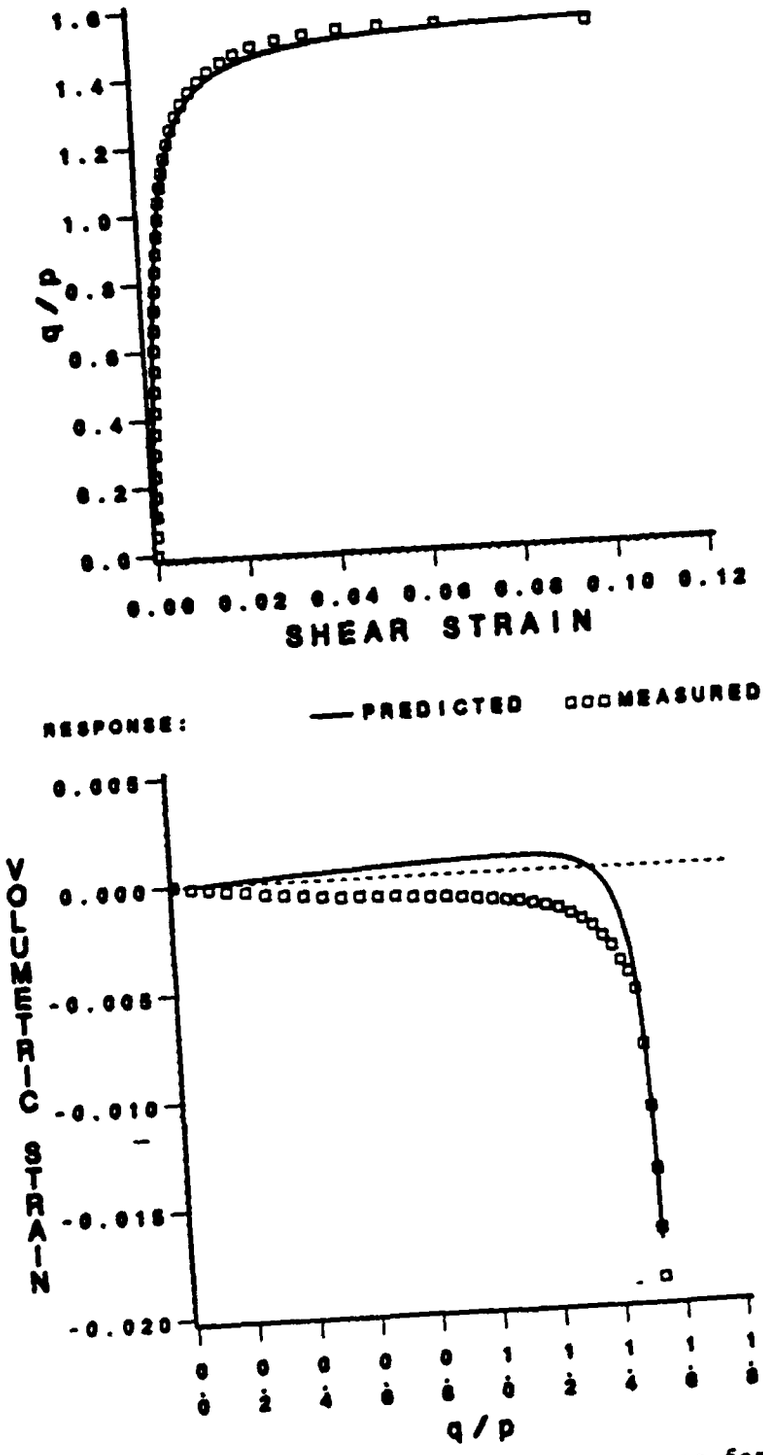

Figure 3.22 Measured vs. predicted response for constant mean pressure compression shear test (GC 0 or TC of Figure 2.3) using proposed model

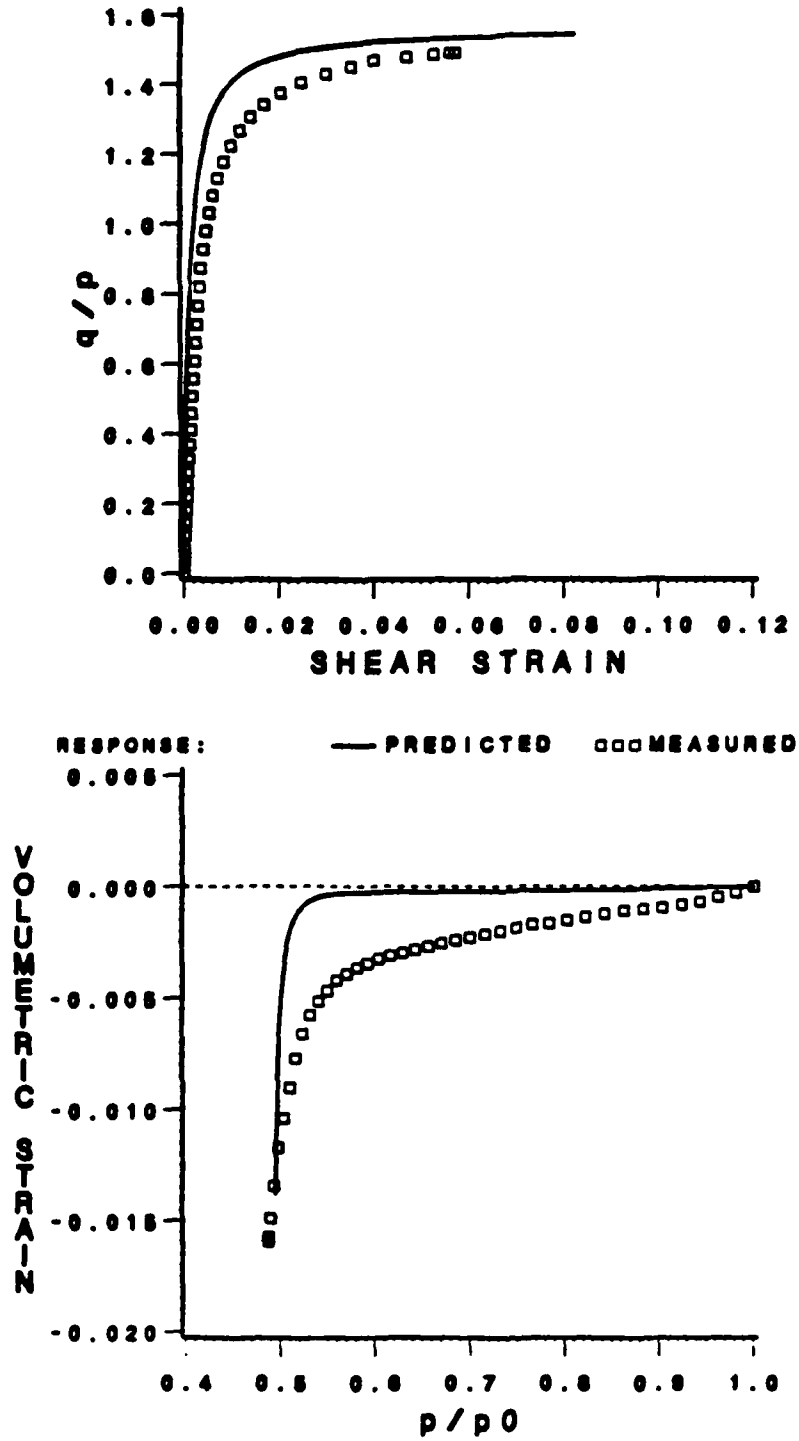

Figure 3.23 Measured vs. predicted response for reduced triaxial compression test (RTC of Figure 2.3) using proposed model

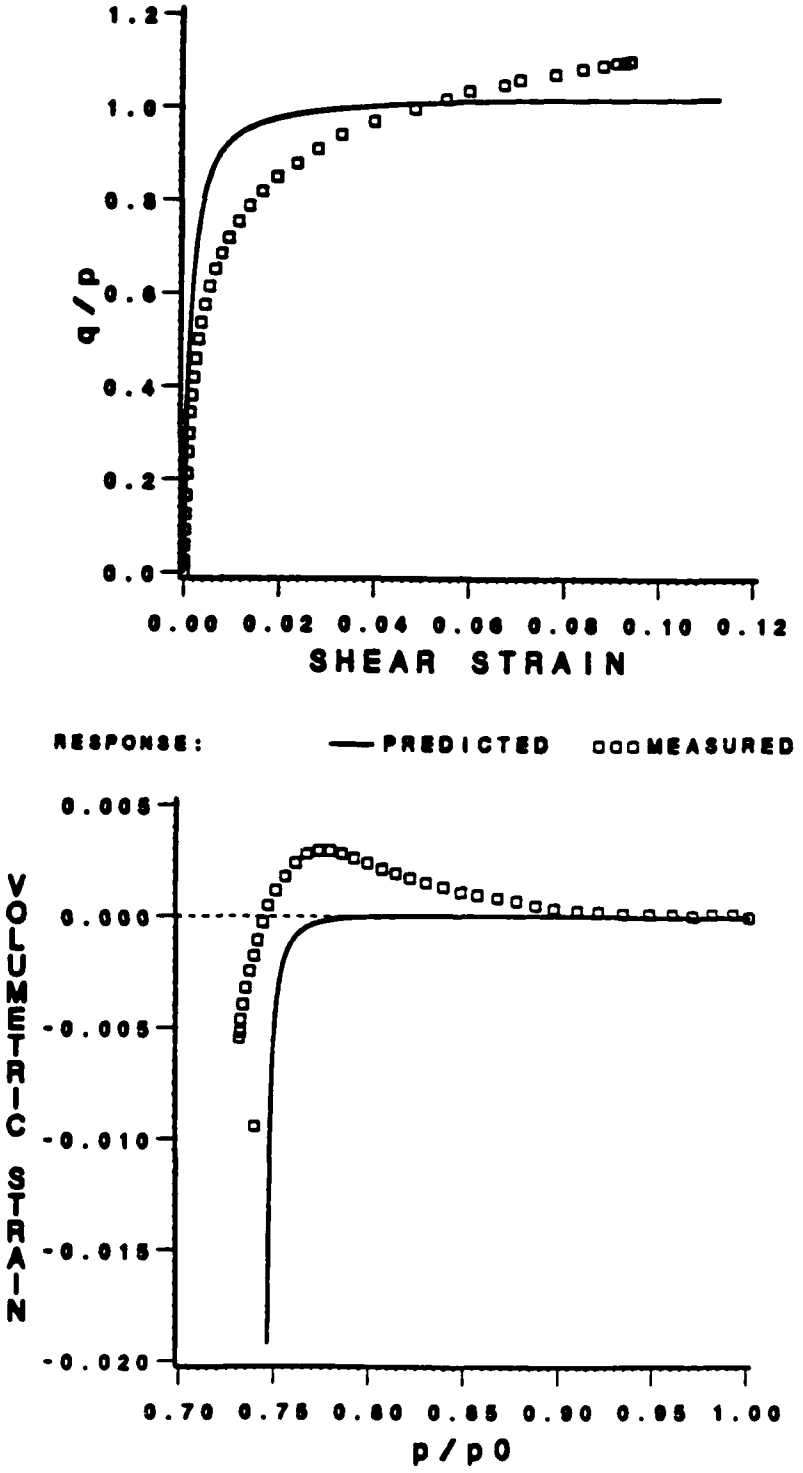

Figure 3.24 Measured vs. predicted response for axial extension test (DT 90 or RTE of Figure 2.3) using proposed model

for loading paths which are far removed from compression stress space. In fact, the axial extension tests and constant pressure extension tests reported by Tatsuoka and Ishihara (1974b) and Luong (1980), respectively, contradict Saada's data and seem to be consistent with the simple model will give.

As part of this research, an experiment was devised specifically to investigate the volume change phenomenon during an axial extension test. A solid cylindrical specimen, of height to diameter ratio of unity as suggested by Lade (1982), was equipped with LVDTs (Linear Variable Differential Transducers) at the center third of a water-saturated sample. During extension shear, volume changes were measured by the LVDTs and the conventional burette readings, and the results of this study are pictured in Figure 3.25. Superposed on this plot are: a) the observed volumetric response as recorded by the LVDTs and the burette, b) Saada's hollow cylinder extension test data, and c) the model prediction. Based on this graphic evidence, it does indeed seem premature to criticize the model's performance in simulating extension volume strains. The reader is therefore urged to withhold judgment on this aspect until the soil mechanics community can concur on what is real behavior for extension tests. This statement is in the spirit of Professor Scott's epilog in his recent Terzaghi lecture (Scott, 1985) where he called for the development of an international data bank of test results on soils.

If we do not withhold judgment and assume that the behavior recorded by Saada is real and that the material is reasonably isotropic, then the data suggests that both the shape of the consolidation portion of the yield surface and the plastic moduli interpolation rule in extension differ markedly from compression. There is evidence, however, to indicate that the sand specimens used in Saada's experiments were anisotropic. Many researchers have verified that, at least on the octahedral plane, the strength of nearly isotropic soil

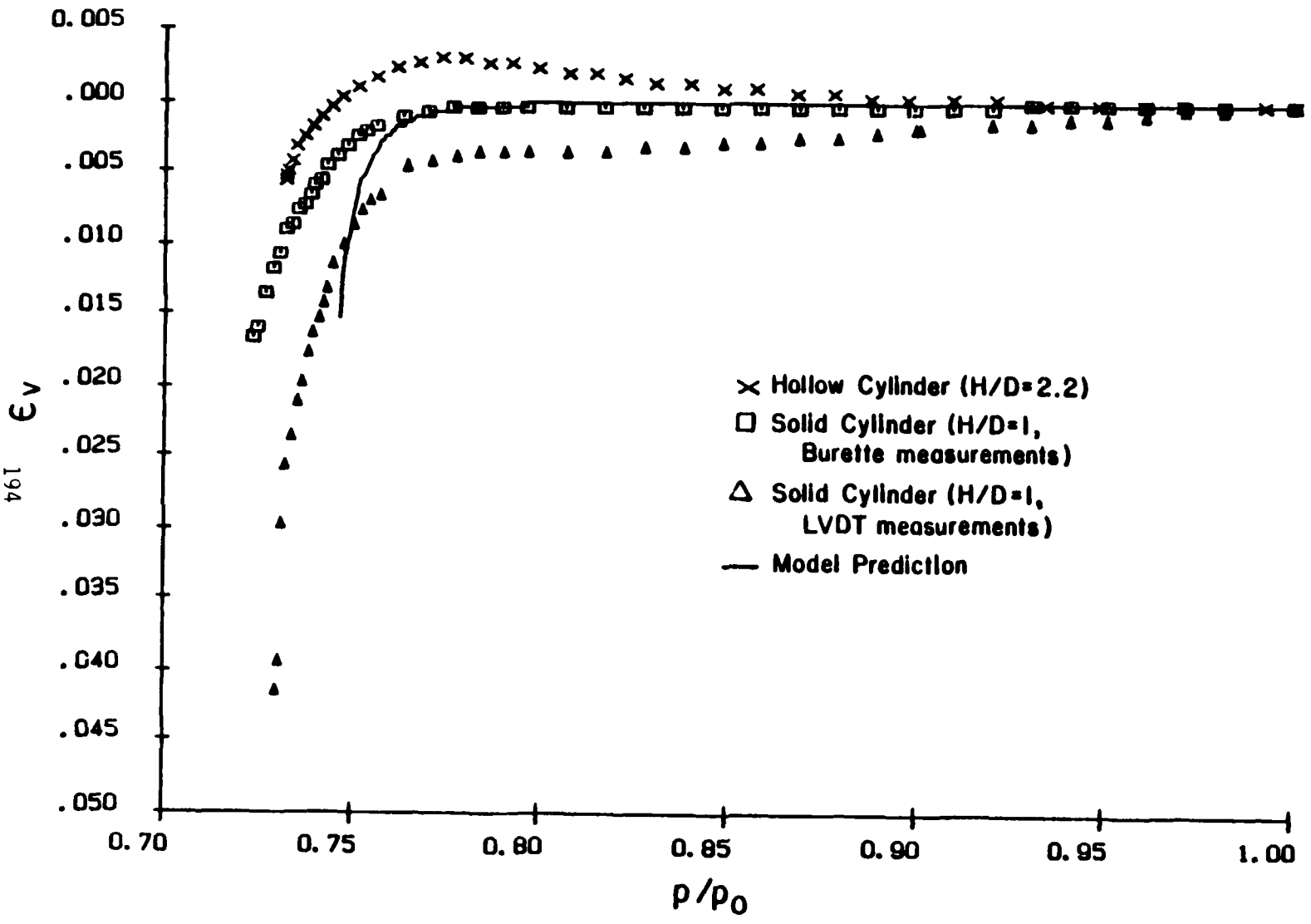

Figure 3.25 Volume change comparison for axial extension test (hollow cylinder data after Saada et al., 1983)

approximates a Mohr-Coulomb type failure criterion. Podgorski (1985) has recently surveyed these isotropic failure criteria. Therefore, if such a criterion is taken for granted, and if the soil is indeed isotropic, the computed strength parameter should be approximately constant and independent of the path of loading. To test this hypothesis, three well-known isotropic failure criteria were used to evaluate Saada's data, and the results are presented in Table 3.5. Clearly, looking for instance only at the "G" tests to rule out the possibility of nonlinear pressure effects, inherent anisotropy has a significant influence on the strength and there is no reason not to expect it to also have an effect on the stress-strain response. Anistropy could therefore be the cause of the discrepant axial extension prediction, and if this is true, it renders Saada's data an unsuitable proving ground for the proposed theory.

3.7.2 Simulation of Hettler's Triaxial Tests

The physical characteristics of the two sands used in this study--one a medium-grained sand from Karlsruhe, Germany, and the other a fine-grained dune sand from Holland--are described by Goldscheider (1984) and Hettler et al. (1984).

In the first series of tests, the medium grained Karlsruhe sand was used to prepare four specimens at a relative density (D_r) of 99.0%. These samples were sheared to failure in axial compression with constant confining pressures of 50, 80, 200, and 300 kN/m^2 respectively, and this data is given in Figure 3.26. Notice here that the failure envelope is straight (constant σ_1/σ_3 ratios) and the stress-strain curves are neatly normalized.

Table 3.5 Computed Isotropic Strength Constants for Saada's Series of Hollow Cylinder Tests

	$\left[\left(\frac{I_1^3}{I_3}\right) - 27\right] \left(\frac{I_1}{p_a}\right)^{.056}$	$\left[-\left(\frac{I_1 I_2}{I_3}\right) - 9\right]$	Friction Angle
Reference:	(Lade, 1977)	(Matsuoka, 1974)	(Shield, 1955)
Constant Intermediate Principal Stress Tests:			
DC 0 (or CTC of Fig. 2.2)	30.6	4.45	36.71
RTC (of Fig. 2.2)	28.2	4.43	36.67
DCR 15	34.7	5.00	40.39
DCR 32	45.9	7.74	49.69
DTR 58	26.7	5.81	42.74
DTR 75	23.9	5.34	39.49
DT 90 (or RTE of Fig. 2.2)	29.6	6.64	42.34
Constant Mean Normal Pressure Tests:			
GC 0 (or TC of Fig. 2.2	31.7	4.73	37.57
GCR 15	40.2	5.83	42.89
GCR 32	66.1	11.22	55.02
R 45 (or pure torsion)	40.4	8.22	49.32
GTR 58	23.9	5.15	41.00
GTR 75	17.9	3.91	35.49
GT 90 (or TE of Fig. 2.2)	25.6	5.63	40.00

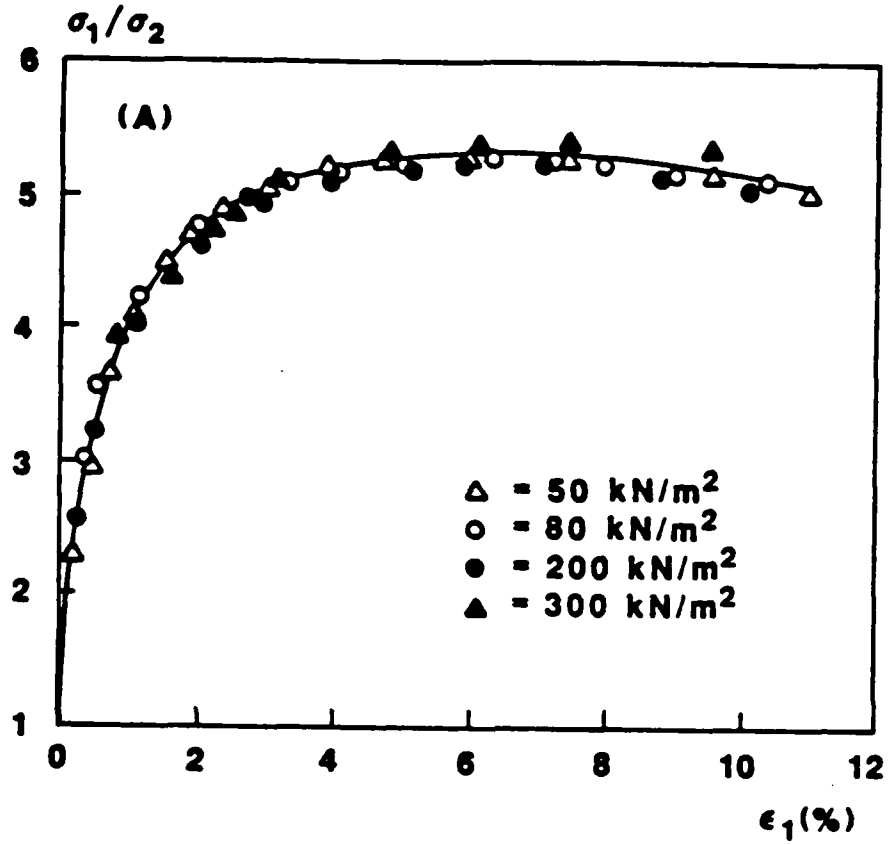

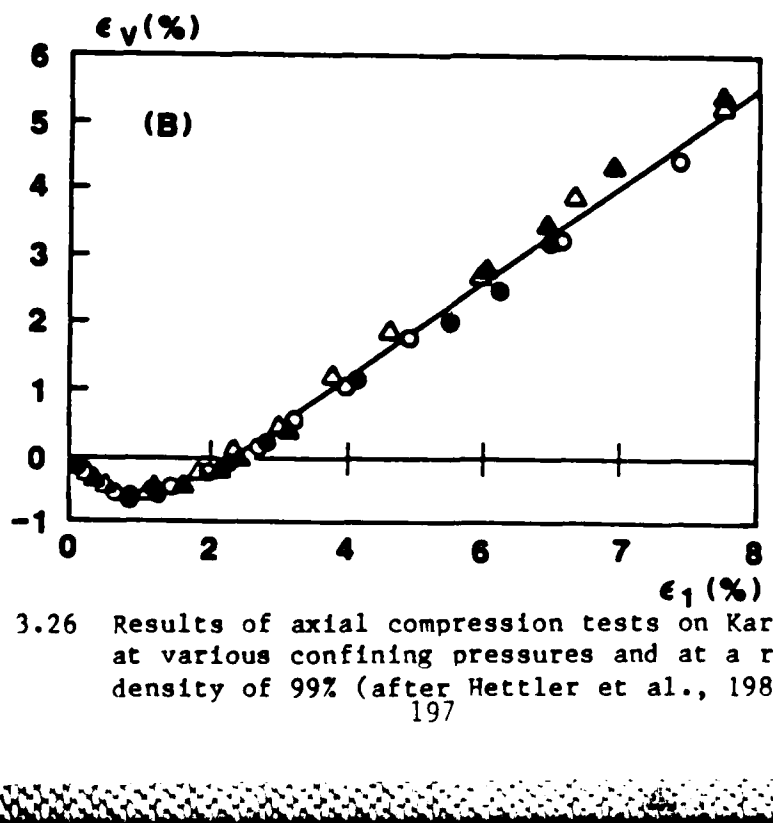

Figure 3.26 Results of axial compression tests on Karlsruhe sand at various confining pressures and at a relative density of 99% (after Hettler et al., 1984)

The second phase of the program consisted of tests in which the confining pressure was kept constant at 50 kN/m^2 while the relative density of the prepared specimens was varied. Stress-strain data for this test sequence was obtained at relative densities of 62.5%, 92.3%, 99.0%, and 106.6%; see Figure 3.5. Accompanying these data sets on Karlsruhe sand were the results of a hydrostatic consolidation test (at 99% relative density) and an axial compression test (at 92.3% relative density) with an all-around stress of 400 kN/m^2. Hettler took care to point out that the specimens were initially isotropic by noting the equality of the normal strain components during hydrostatic compression.

The final series of Hettler's experiments were carried out on three specimens of Dutch dune sand, each prepared at an initial relative density of 60.9%. These samples were sheared in axial compression under ambient pressures of 50, 200, and 400 kN/m^2 respectively. Unlike the medium-grained sand from Karlsruhe, the failure meridian of this fine-grained sand was curved as exhibited in Figure 3.27 by the unequal σ_1/σ_3 ratio at failure.

The model parameters for each sand were initialized and these are summarized in Table 3.6. Other than the parameters "Q" and "b" (which control the shape of the yield surface), this list of model constants reflects the general trends with increasing relative density suggested in Table 3.3. Since no unloading data was presented by Hettler et al. (1984), the elastic shear moduli were reckoned, using an ad-hoc procedure suggested by Lade and Oner (1984), to be twice that of the initial slopes of the shear stress vs. shear strain (q vs. $\bar{\varepsilon}$) data. And except for the Karlsruhe sand at a relative density of 99%, hydrostatic consolidation tests were also available, so it was necessary to estimate the density hardening parameters (λ) in all but this one case.

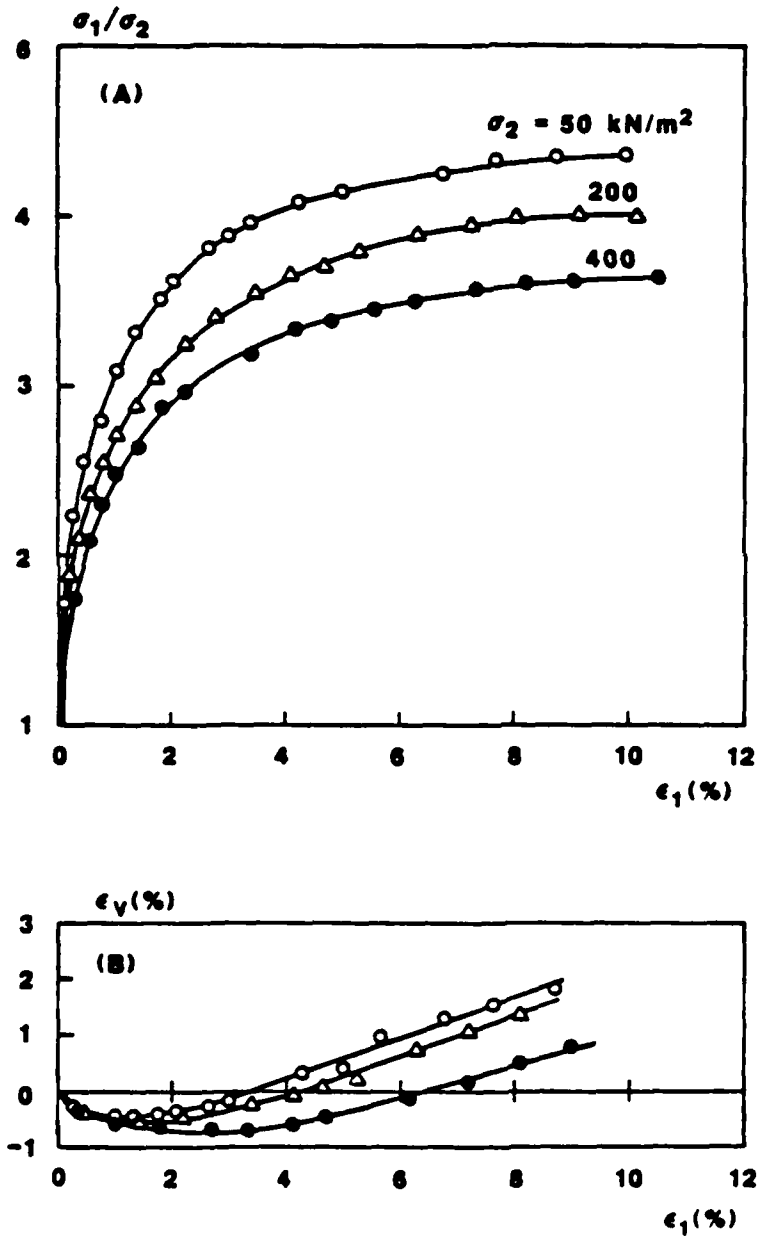

Figure 3.27 Results of axial compression tests on Dutch dune sand at various confining pressures and at a relative density of 60.9% (after Hettler et al., 1984)

Table 3.6 Model Parameters for Karlsruhe Sand and Dutch Dune Sand

	MEDIUM GRAINED KARLSRUHE SAND Relative Density				DUTCH DUNE SAND Relative Density
PARAMETER	62.5%	92.3%	99.0%	106.6%	60.9%
Field of Plastic Moduli Constants:					
k	.2868	.3195	.3390	.3503	.3400
m	-	-	-	-	.0601
n	2.2	2.0	2.0	1.9	2.6
λ	300	500	530	550	300
Plastic Flow or Yield Surface Parameters:					
N	.265	.265	.265	.265	.230
Q	1.8	1.4	1.3	1.5	1.8
b	12.9	11.4	11.1	11.6	14.8
Elastic Constants:					
k_u	1,070	1,810	2,100	2,200	1,332
r	.70	.65	.62	.57	.668

Note: The slope of the yield surface at the origin of $\sqrt{J_2^*}$-I_1 stress space, S, is assumed equal to 1.5 in all cases. Also note that these parameters were computed from the data of Hettler et al. (1984).

As mentioned previously in section 3.6, the representation gives the same plastic response for each of a series of parallel stress paths emanating from the hydrostatic axis if the failure envelope is straight. However, if the failure envelope is curved, of if the plastic bulk modulus increases non-linearly with hydrostatic pressure, this statement would not be true. Hettler's data indicate that in cases where the failure envelope is straight, see Figure 3.5 for example, the stress-strain curves can indeed be normalized. Therefore, in such cases, all verifications could just as well be placed on one plot. However, this was not taken advantage of in preparing the figures. But, for economy of presentation, the predictions given in the body of the report for Karlsruhe sand (i.e., the sand with the normalizable data) are only at one level of confining pressure, 50 kN/m^2, while the remainder have been included for reference in Appendix E.

Figures 3.28-3.32 are, in sequence, plots of the calculated results superposed with the experimental data points for the hydrostatic compression test at 99% relative density, and the axial compression paths on samples of relative densities 62.5%, 92.3%, 99.0%, and 106.6%. Correspondence between measured and predicted response is remarkably accurate in all cases. This is particularly encouraging because the data are known to be of high quality. The model's intrinsic ability to simulate this wide cross-section of densities over a range of confining pressures is testimony to its rationality.

Figures 3.33-3.35 are the predictions of the axial compression tests on the fine-grained dune sand with the curved failure envelope. These are also impressive considering the "non-normalizable" nature of the data.

3.7.3 Simulation of Tatsuoka and Ishihara's Stress Paths

Figure 3.36 shows the type "A" and type "B" triaxial stress paths of Tatsuoka and Ishihara (1974a), and Figures 3.37 and 3.38 are plots of the

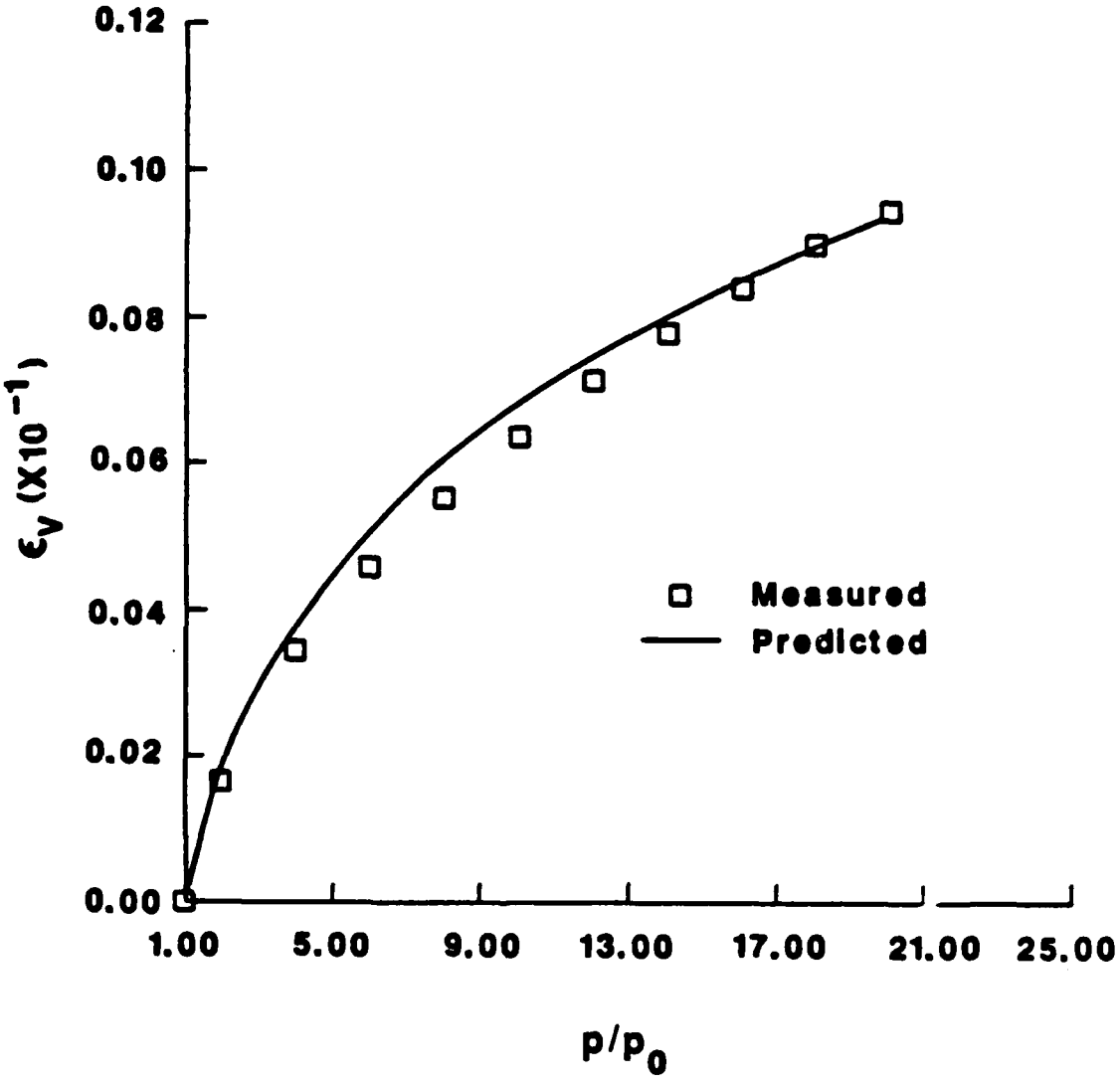

Figure 3.28 Measured and predicted response for hydrostatic compression test on Karlsruhe sand at 99% relative density (measured data after Hettler et al., 1984)

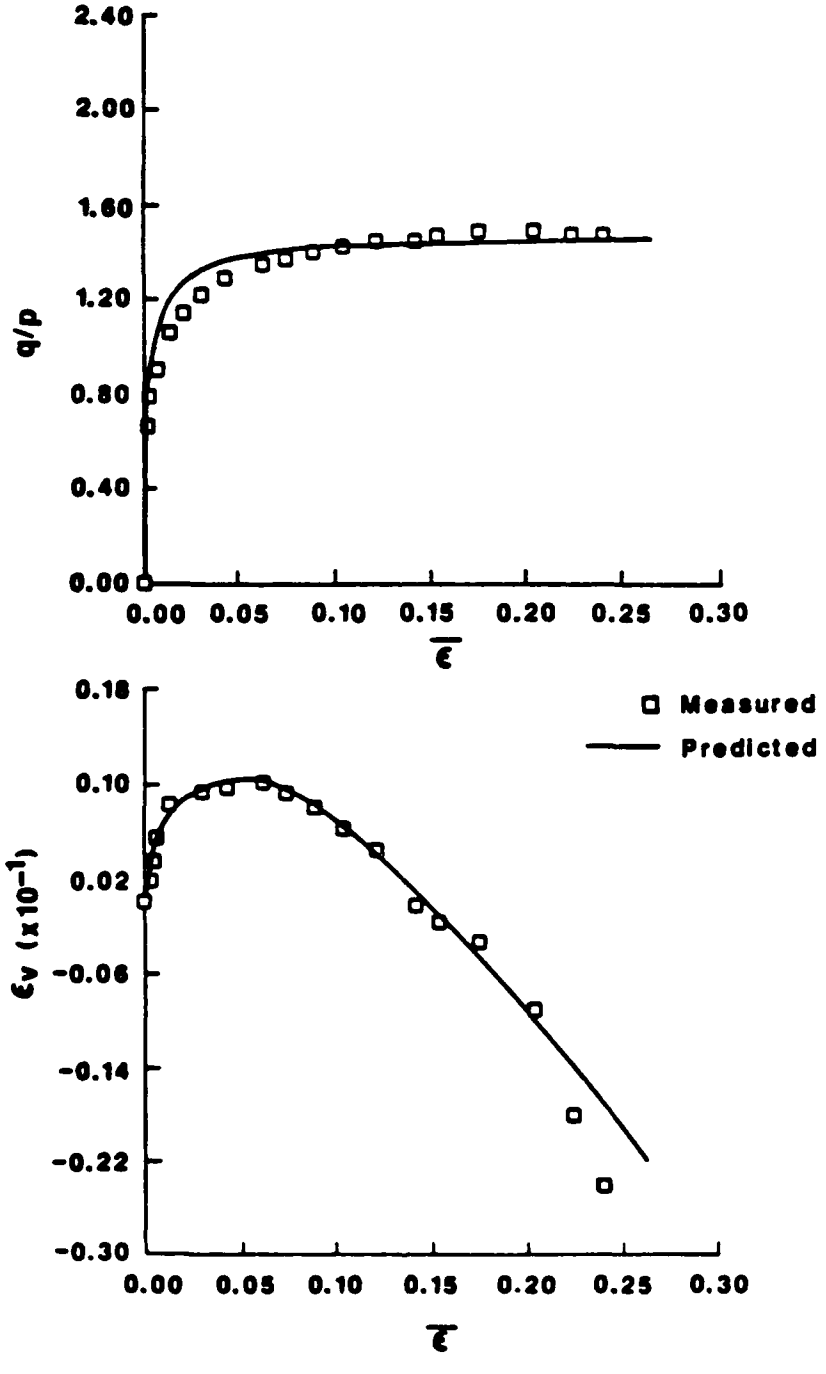

Figure 3.29 Measured and predicted response for axial compression test (σ_3 = 50 kN/m^2) on Karlsruhe sand at 62.5% relative density (measured data after Hettler et al., 1984)

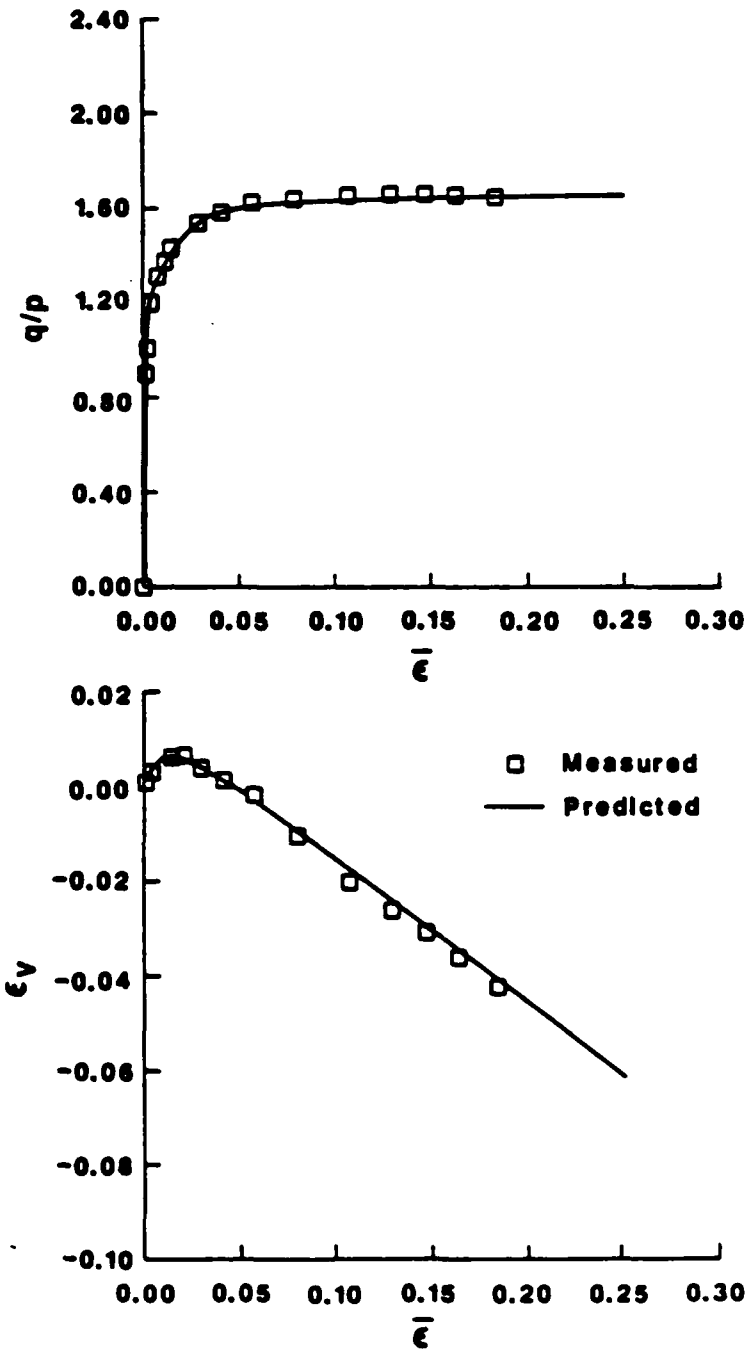

Figure 3.30 Measured and predicted response for axial compression (σ_3 = 50 kN/m^2) on Karlsruhe sand at 92.3% relative density (measured data after Hettler et al., 1984)

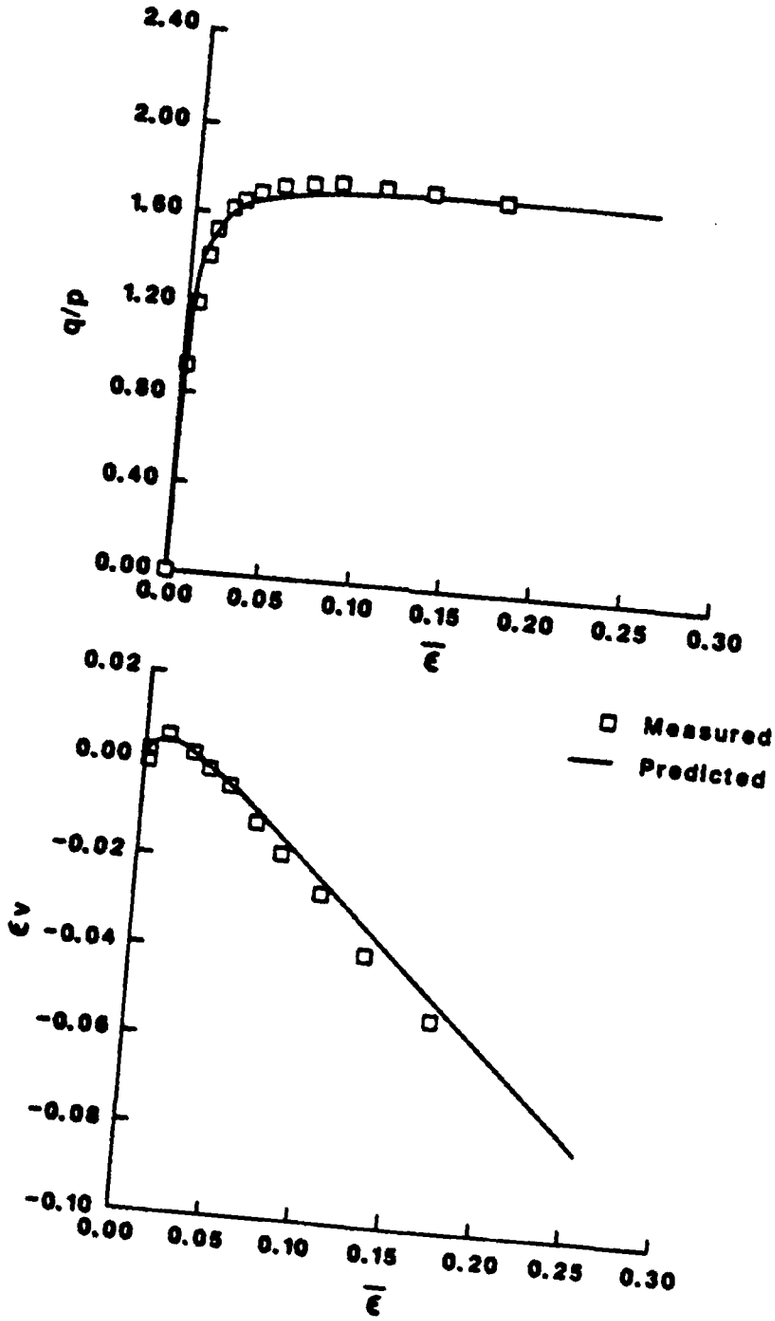

Figure 3.31 Measured and predicted response for axial compression test (σ_3 = 50 kN/m^2) on Karlsruhe sand at 99.0% relative density (measured data after Hettler et al., 1984)

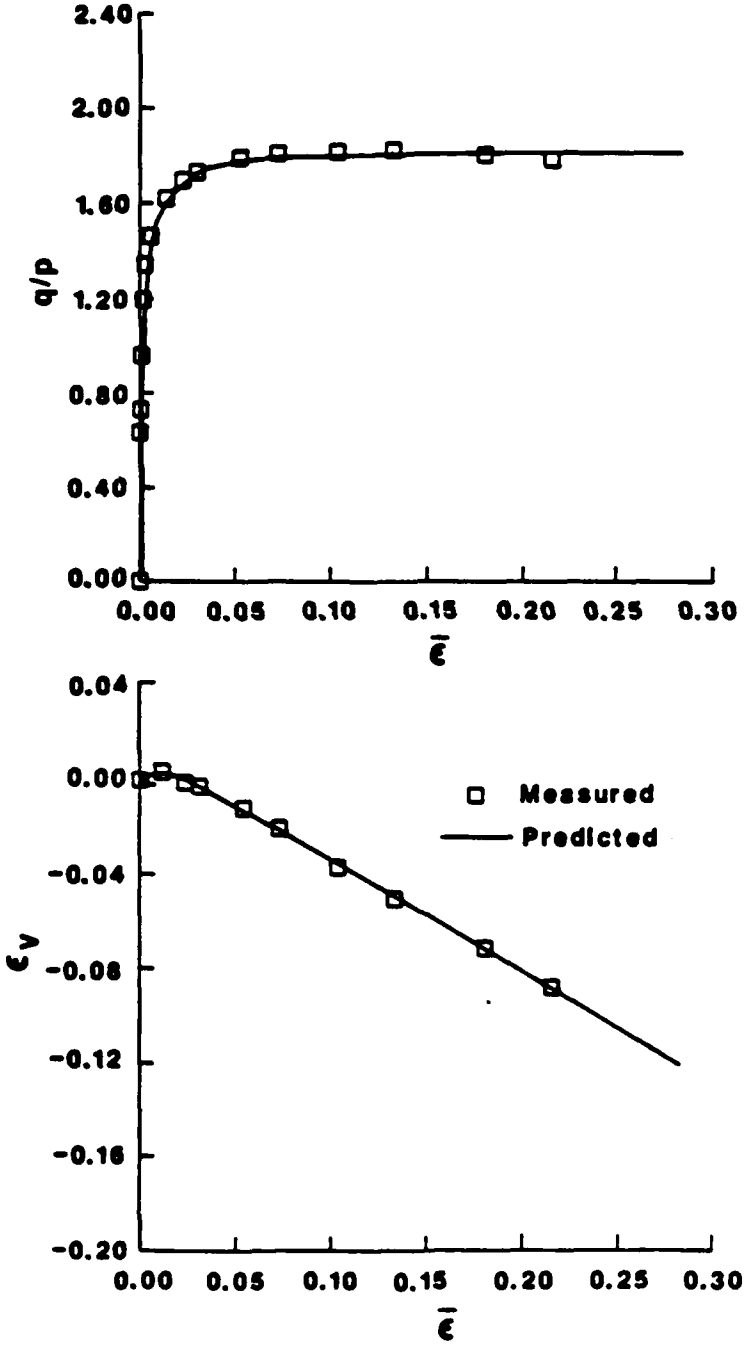

Figure 3.32 Measured and predicted response for axial compression test (σ_3 = 50 kN/m^2) on Karlsruhe sand at 106.6% relative density (measured data after Hettler et al., 1984)

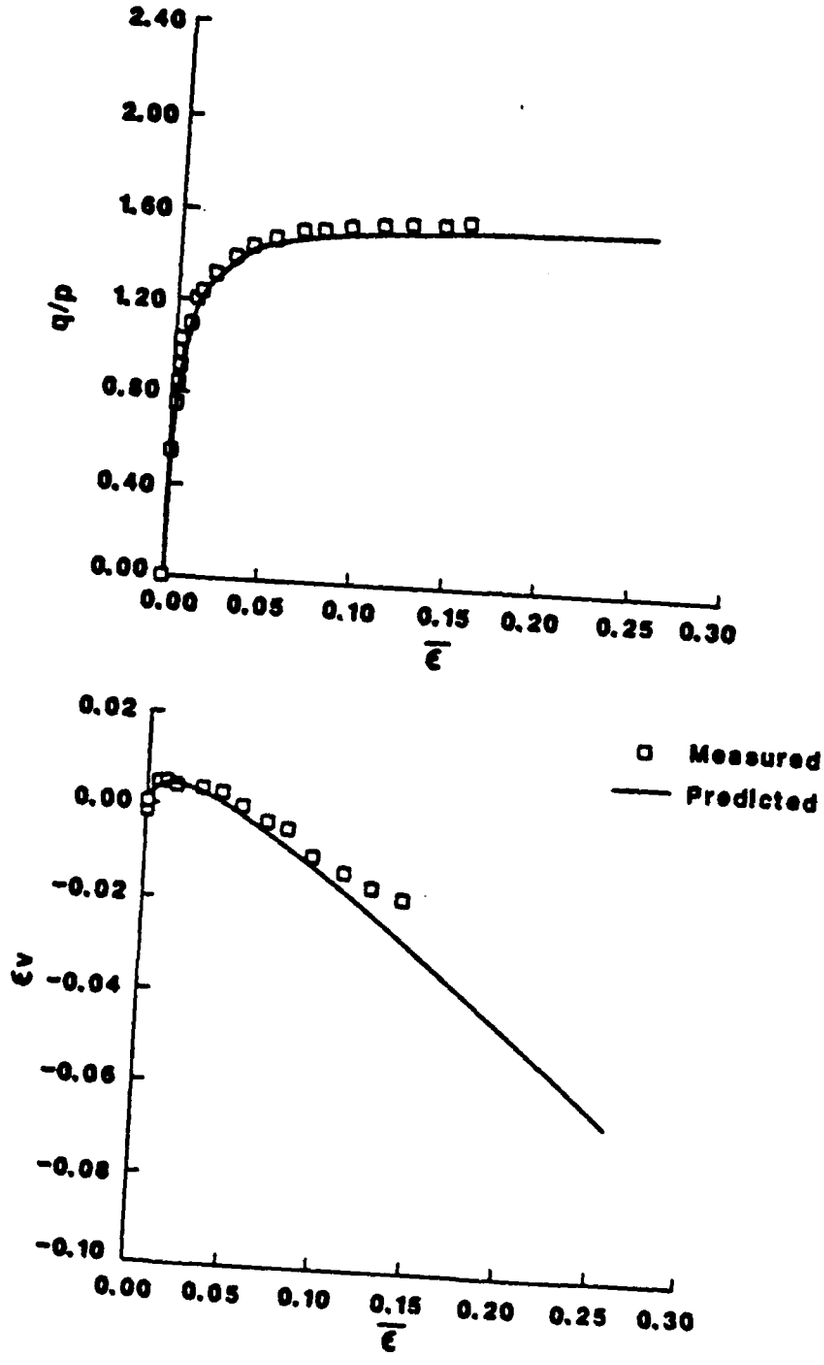

Figure 3.33 Measured and predicted response for axial compression test (σ_3 = 50 kN/m^2) on Dutch dune sand at 60.9% relative density (measured data after Hettler et al., 1984)

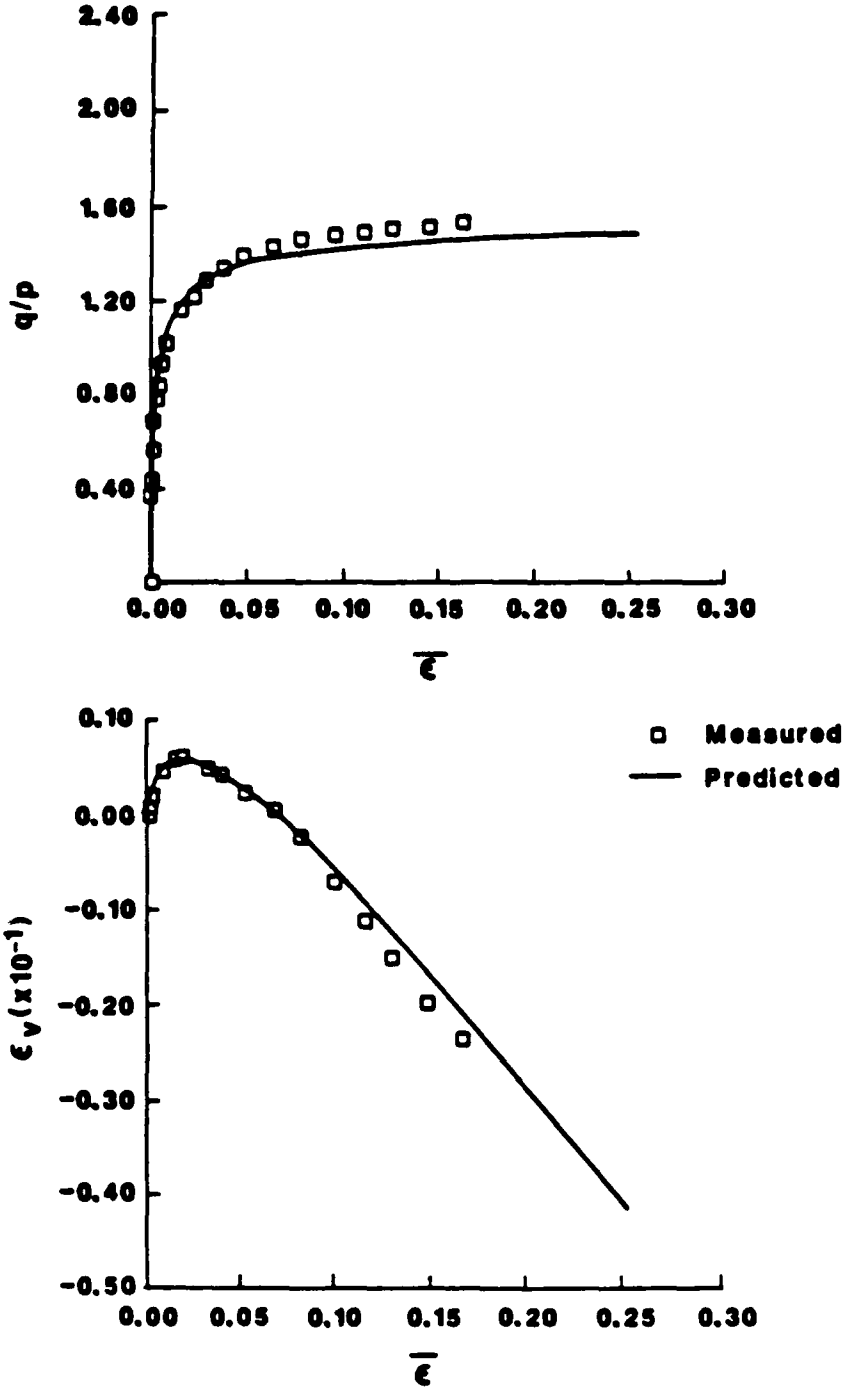

Figure 3.34 Measured and predicted response for axial compression test (σ_3 = 200 kN/m^2) on Dutch dune sand at 60.9% relative density (measured data after Hettler et al., 1984)

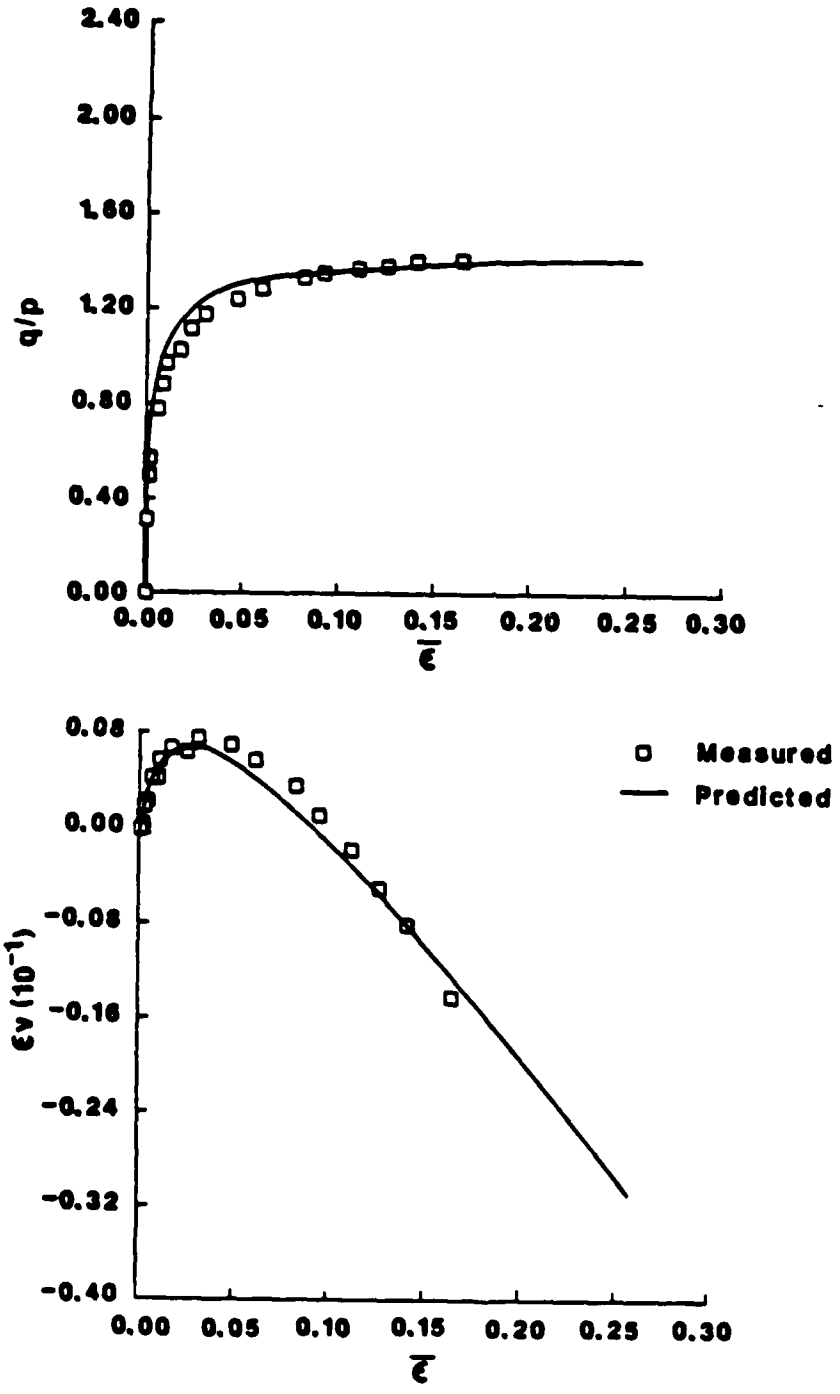

Figure 3.35 Measured and predicted response for axial compression test (σ_3 = 400 kN/m^2) on Dutch dune sand at 60.9% relative density (measured data after Hettler et al., 1984)

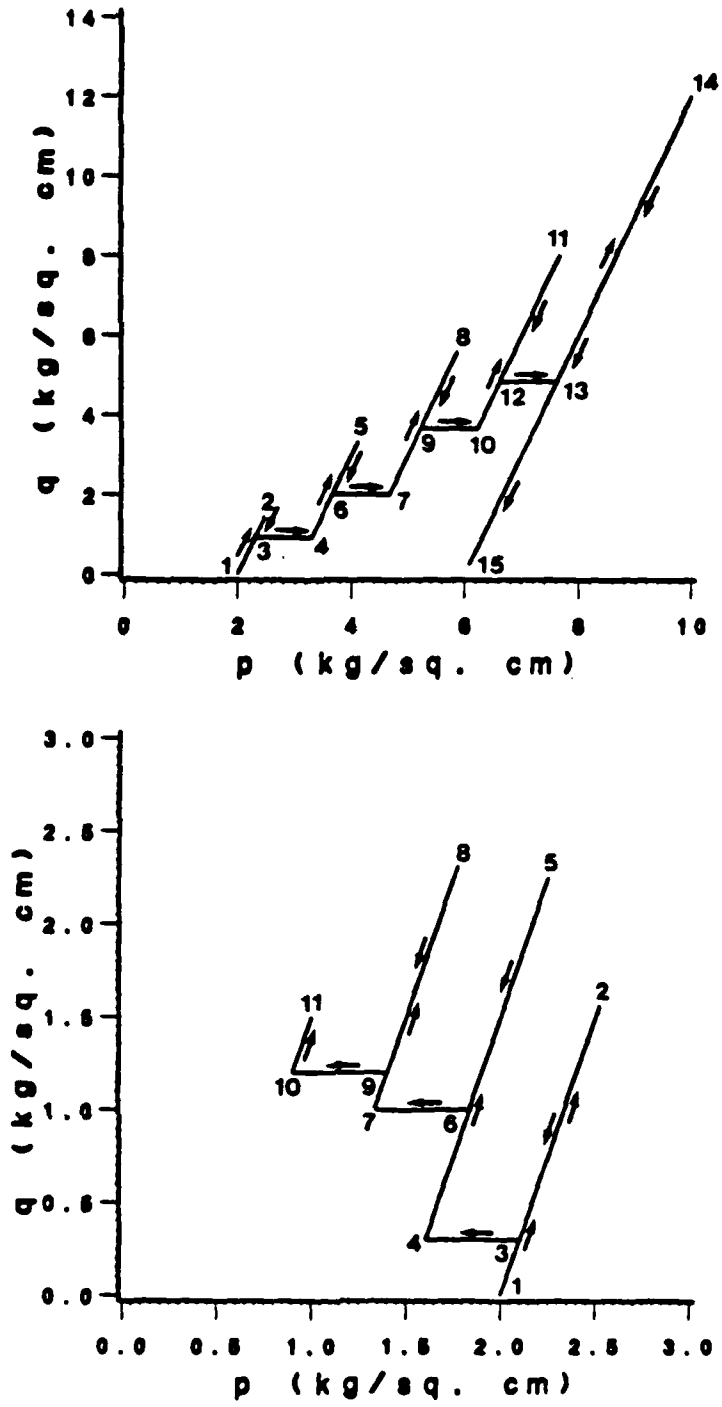

Figure 3.36 Type "A" (top) and type "B" (bottom) stress paths of Tatsuoka and Ishihara (1974a)

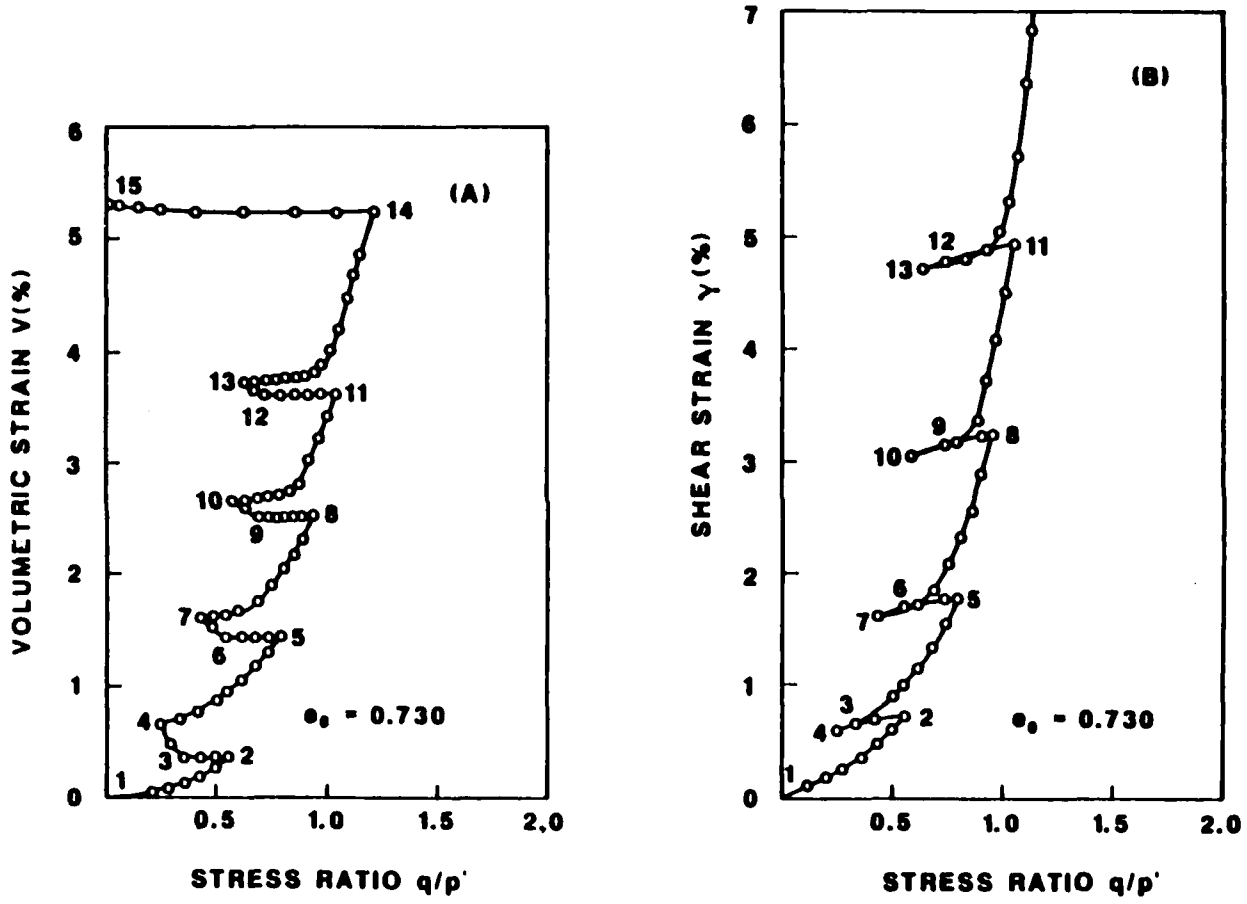

Figure 3.37 Observed stress-strain response for type "A" loading path on loose Fuji River sand (after Tatsuoka and Ishihara, 1974a)

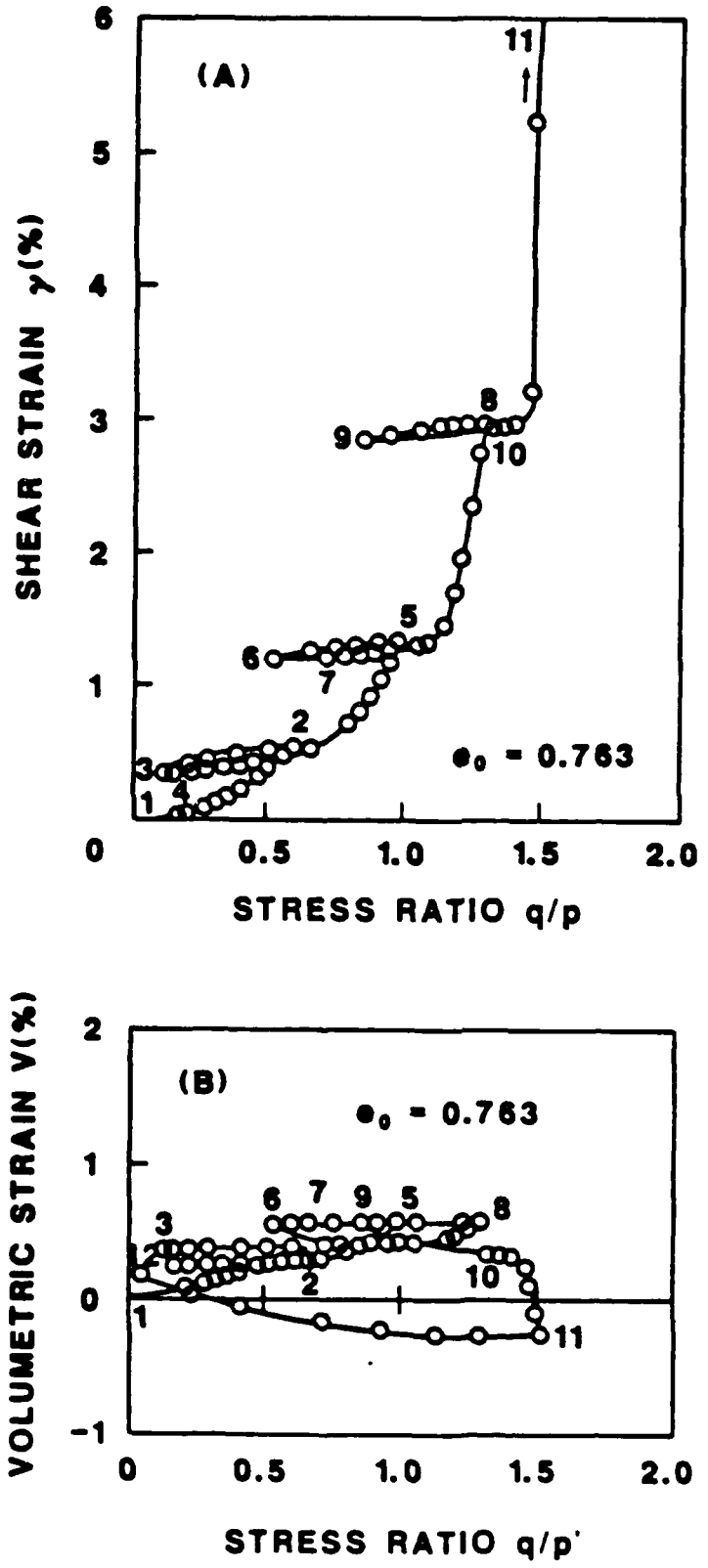

Figure 3.38 Observed stress-strain response for type "B" loading path on loose Fuji River sand (after Tatsuoka and Ishihara, 1974a)

corresponding stress-strain curves they recorded for these paths. The material tested was loose Fuji River sand, they physical characteristics of which has been described by Tatsuoka and Ishihara (1974a). Both these loading paths consist of a series of axial compression paths which are offset at increasing increments of confining stress for the type "A" case and at decreasing levels for the type "B".

To a fairly close approximation, all of the axial shear paths for the type "A" loading program appear to produce somewhat parallel stress-strain curves, Figure 3.37 (b). This observation lends credence to the idea that, at least along these paths and for this type and density of sand, hardening may be neglected without sacrificing too much modeling power. Using the data of this plot and the results of a hydrostatic compression test presented by Tatsuoka (1972), the model parameters for this loose sand were computed and are listed in Table 3.7.

The predicted curves for the type "A" loading path are shown in Figure 3.39, and except for the shear strain direction during the incremental hydrostatic loadings from points 3 to 4, 6 to 7, 9 to 10, and 12 to 13, this prediction agrees qualitatively with the measured data. Induced anisotropy is believed to be the cause of the wrong direction predicted by the isotropic model for the small hydrostatic segments.

Quantitatively, the model response is about 15 % stiffer than the measured data, and this problem stems from the choice of the interpolation rule that controls the field of plastic moduli. In its present form, it is not capable of precisely matching stress-strain curves in which the tangent modulus decreases significantly well below the zero dilation line. Furthermore, by looking at the shape of the stress-strain curve in Figure 3.37 (b), it is difficult to imagine that failure should occur at a q/p ratio of 1.55.

Table 3.7 Model Parameters for Loose Fuji River Sand

PARAME	MAGNITUDE
Elastic Constants:	
Modulus number, K_u	1,816
Modulus exponent r	.513
Yield Surface Parameters:	
Slope of zero dilation line, N	0.271
Shape controlling parameter of consolidation portion of yield surface, Q	2.50
Shape controlling parameter of dilation portion of yield surface, b	11.0
Field of Plastic Moduli Parameters:	
Plastic compressibility parameter, λ	150
Strength parameter, k (note: no curvature in failure meridian assumed)	0.288
Exponent to model decrease of plastic modulus, n	2

note: these parameters were computed from data reported by Tatsuoka (1972) and Tatsuoka and Ishihara (1974a)

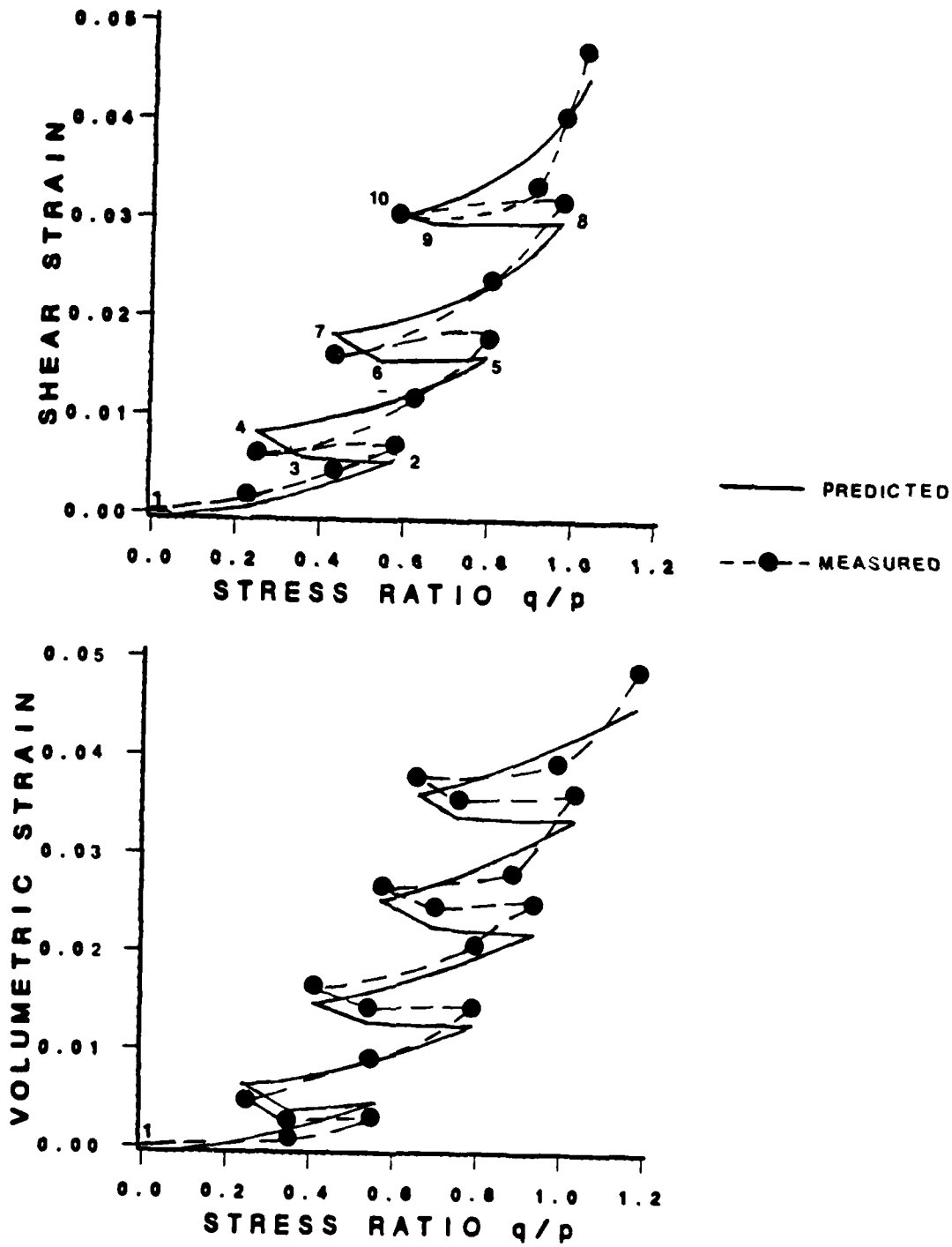

Figure 3.39 Simulation of type "A" loading path on loose Fuji River sand using the simple representation

To gain greater control over the rate at which K_p decreases, the interpolation rule may be improved as follows. The plastic modulus at each point on the zero dilation line can be taken as some fraction of its corresponding magnitude on the hydrostatic axis, and its reduction between these two radial lines may be governed by one exponent, while a different exponent may be used to control its approach to zero (at the failure line) beyond the zerio dilation line. But before doing all this work, it is important to verify that the observed response is indeed real because the simple form of the interpolation rule was quite adequate for matching Hettler's tests on sands of similar relative density (Hettler et al., 1984); see, for example, Figures 3.29, 3.33, 3.34, and 3.35.

For the type "B" loading path, Figure 3.36 (b), hardening appears to be more pronounced, but as the simulation depicted in Figure 3.40 suggests, the qualitative nature of the simple representation is again not a poor first approximation.

As shown earlier in Figure 3.7, Tatsuoka and Ishihara (1974b) also performed medium amplitude axial compression-extension cycles on this loose Fuji River sand. And as they concluded from their study,"...the memory of previous stress history experienced during the cycle in extension [compression] does not appear in the subsequent triaxial compression [extension], and therefore, the sample shows yielding from the outset as if it were in a virgin state." Figure 3.41 shows a simulation of this path using the parameters of Table 3.7, and for the first cycle, the "no-hardening" postulate does seem relevant. After many cycles, too much strain will be predicted if hardening is completely ignored. But, for materials subject to many cycles of loading, as in highway base courses, the parameters governing the stiffness of the fixed field of plastic moduli may be derived from the

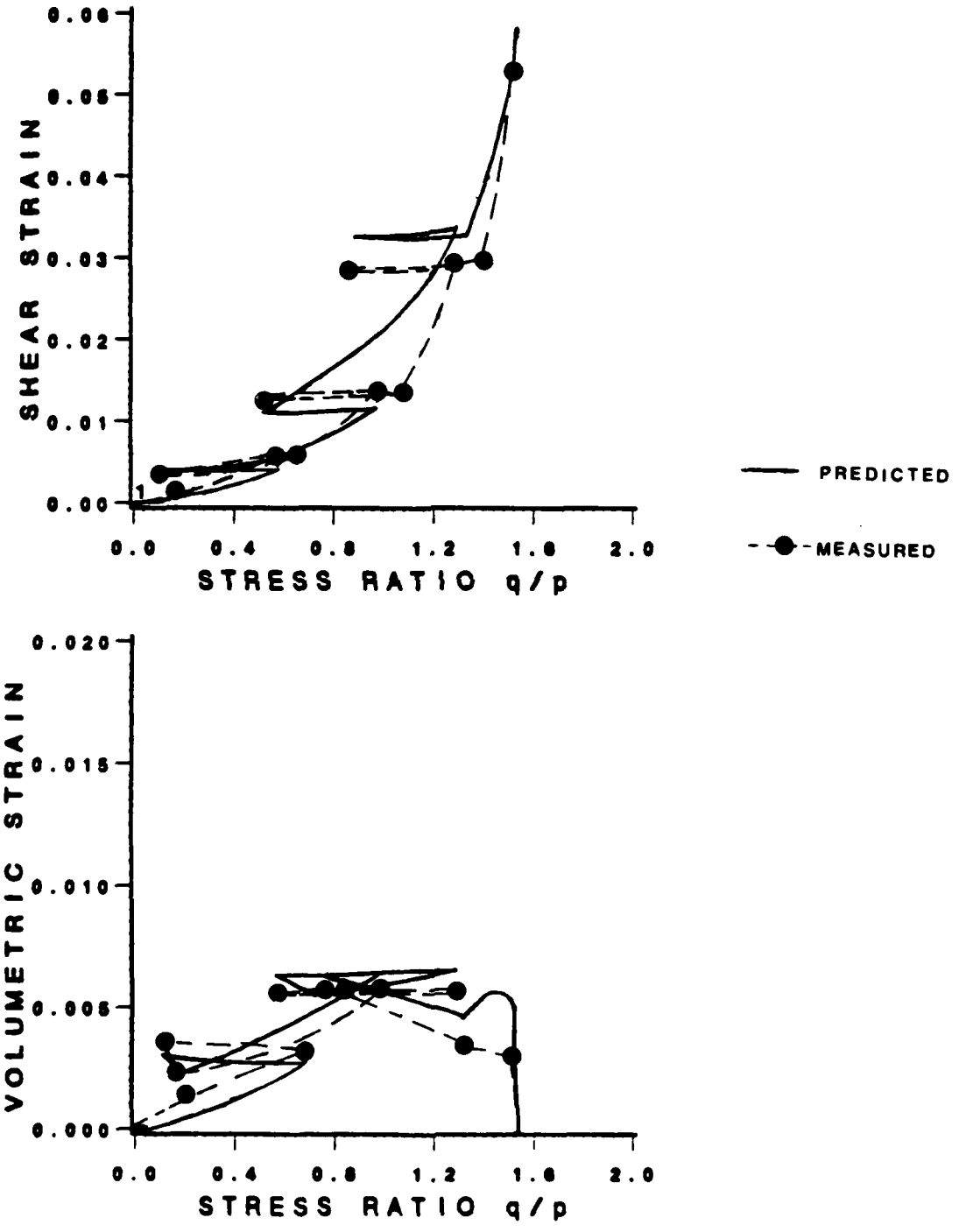

Figure 3.40 Simulation of type "B" loading path on loose Fuji River sand using the simple representation

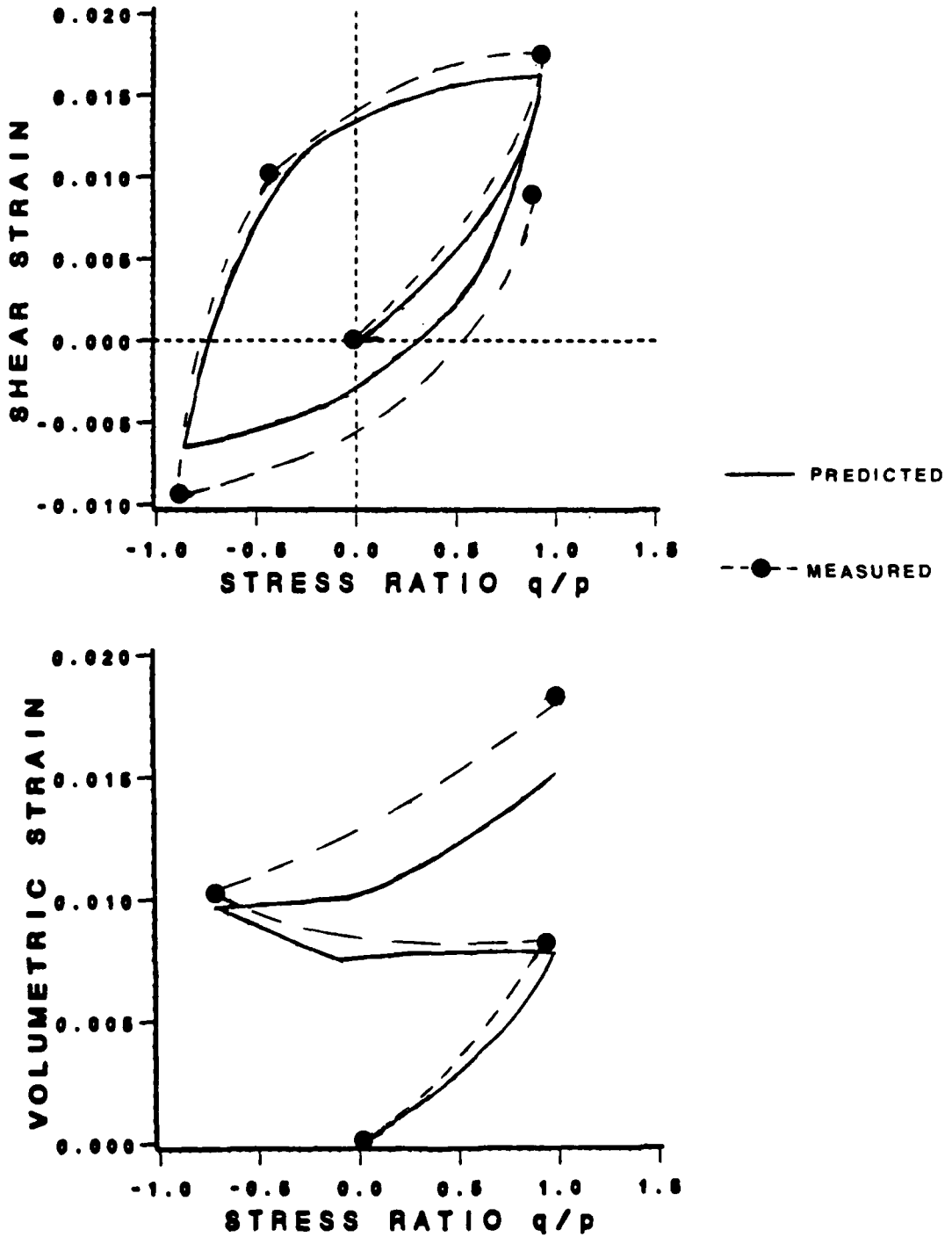

Figure 3.41 Simulation of compression-extension cycle on loose Fuji River sand using the simple representation

cyclically stabilized stress-strain curve to give more realistic predictions of the accumulation of permanent deformation.

3.8 Modifications to the Simple Theory to Include Hardening

Two hardening options are implemented. The first is similar in many respects to the bounding surface proposal of Dafalias and Hermann (1980). The key difference is that the plastic modulus here is given solely as a function of stress. This bounding surface adaptation is incorporated in a finite element computer program to predict a series of cyclic cavity expansion tests.

Although the first option could simulate inelastic reloading response for reloading paths which more or less retrace their unloading paths, the shape specified for the hardened region does not resemble the shapes intimated by the experimental stress probes of Pooroorshasb et. al., (1967) and Tatsuoka and Ishihara (1974a). A second option is then proposed to take these well-known observations into account. This new theory is used to predict the influence of isotropic preloading on an axial compression test and the build-up of permanent strain in a cyclic triaxial test.

Unfortunately, both hardening options sacrifice the ability to predict "virgin" response in extension after an excursion in compression stress space.

3.8.1 Conventional Bounding Surface Adaptation

In the cyclic context, the term hardening could refer to the increase in the size of the elastic region or to the increase in the plastic tangent modulus at a given stress or both (Drucker and Palgen, (1982). This first modification, which originates from the bounding surface concept of Dafalias and Popov (1975), involves only an increase in the plastic modulus. Given the loading history, the objective is therefore first to identify the shape and size of the hardened region in stress space, or the totality of points where the purely stress-dependent plastic moduli are higher than the magnitudes they

would assume for virgin loading, and then to specify the plastic moduli at each of these interior points. In general, the hardening control surface may not resemble the yield surface; if it does, it is a bounding surface as defined in the theory of Dafalias and Popov (1975).

For simplicity, the hardened region is assumed to have a shape similar to the yield surface (Figure 3.16) and a size equal to the largest yield surface established by the prior loading. Thus, the hardening control surface is really a conventional bounding surface ($F_p = 0$), within which the yield surface ($F = 0$) moves. For virgin loading, the bounding surface and yield surface coincide.

The essence of the bounding surface concept is that for any stress state $\underset{\sim}{\sigma}$ within the boundary surface or hardened domain $F_p = 0$, a corresponding image point $\bar{\underset{\sim}{\sigma}}$ on F_p can be specified using an appropriate mapping rule. Having established $\bar{\underset{\sim}{\sigma}}$, the plastic modulus is rendered an increasing function of: i) the Euclidean distance between the actual stress state ($\underset{\sim}{\sigma}$) and the image stress state ($\bar{\underset{\sim}{\sigma}}$), and ii) the plastic modulus $\bar{K}_p$ at $\bar{\underset{\sim}{\sigma}}$. Dafalias and Hermann (1980) employed the radial mapping rule illustrated in Figure 3.42 such that

$$K_p = \hat{K}_p \left[\bar{K}_p, \delta, \delta_o, (K_p)_o\right] , \tag{3.8.1.1}$$

where $(K_p)_o$ is the plastic modulus at $\delta = \delta_o$. To ensure a smooth transition from reloading to virgin or prime loading, the function $\hat{K}_p$ must guarantee that $K_p = \bar{K}_p$ when $\delta = 0$. This mapping rule also requires that the limit line be straight to avoid mapping to points ou side it.

Since a radial line connects the current stress state ($\underset{\sim}{\sigma}$) with the image state ($\bar{\underset{\sim}{\sigma}}$), we can write

$$\bar{\underset{\sim}{\sigma}} = \beta \underset{\sim}{\sigma} , \quad \beta \geq 1 , \tag{3.8.1.2}$$

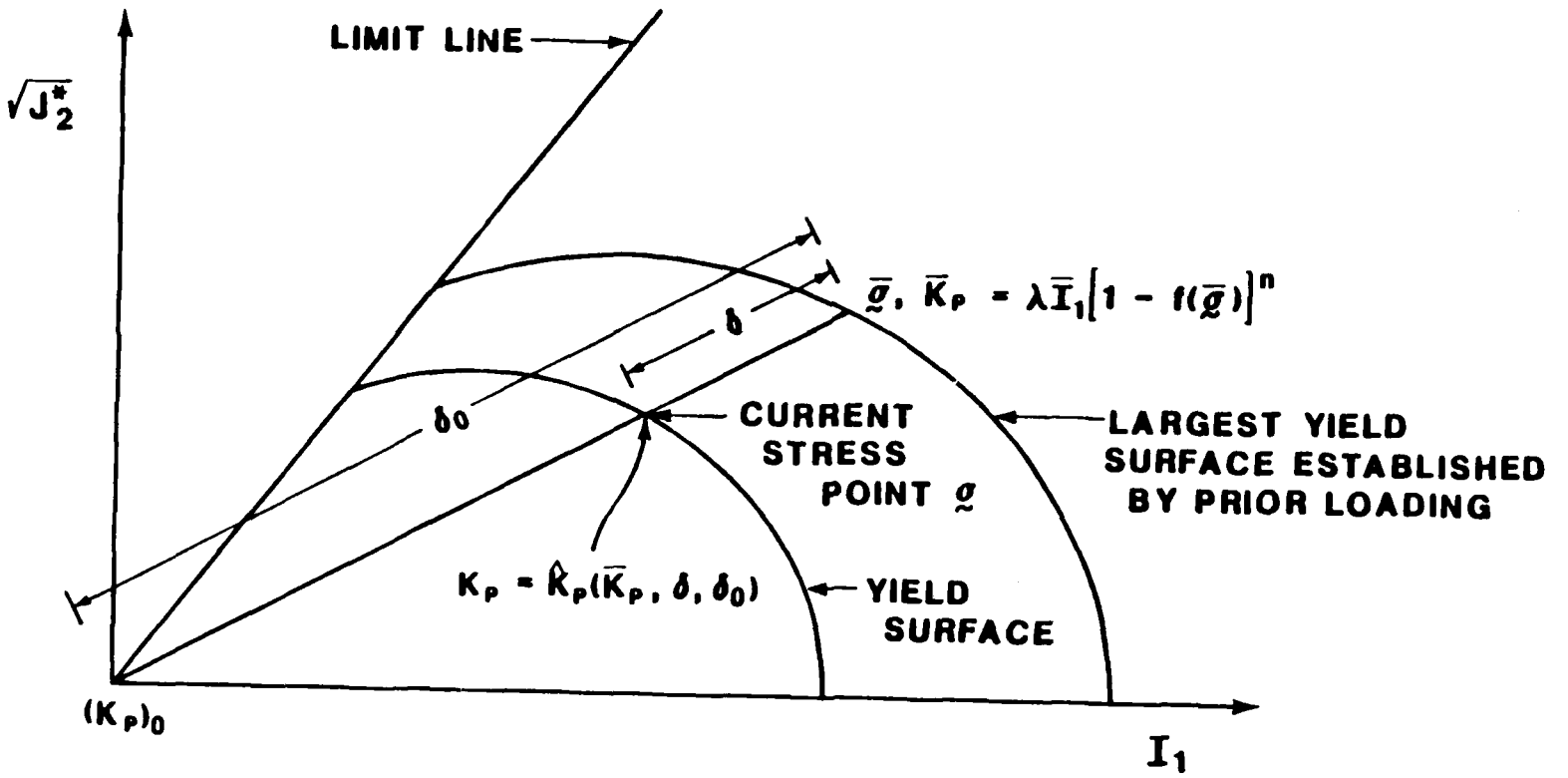

Figure 3.42 Conventional bounding surface adaptation with radial mapping rule

where β is a postitive scalar. The equations for computing the mapping quantity β directly from the current state of stress and the size of the bounding surface are presented in Appendix F.

The Euclidean distance between the origin and the image point (δ_o) , and the distance between the current stress state and the image point (δ) are

$$\delta_o = \beta \sqrt{(\sigma_{ij}\sigma_{ij})} \tag{3.8.1.3}$$

and

$$\delta = (\beta - 1) \sqrt{(\sigma_{ij}\sigma_{ij})} \quad , \tag{3.8.1.4}$$

respectively.

Therefore, once β is computed from a knowledge of the size of the boundary surface $(I_o)_p$ and the current stress point. the stress state $\bar{\sigma}$ can be located and used to compute the "virgin" bounding plastic modulus $\bar{K}_p$. For this stress-dependent formulation only $\bar{\sigma}$ is needed to calculate $\bar{K}_p$.

To complete the formulation a specific form for the function $\hat{K}_p$ (Equation 3.8.1.1) must now be selected. Zienkiewicz and Mroz (1984) proposed the form

$$K_p = \bar{K}_p \left[\delta_o/(\delta - \delta)\right]^{\gamma} = \bar{K}_p \beta^{\gamma} \quad , \tag{3.8.1.5}$$

which is adopted bereobecause it adds only one more parameter (γ) to the existing list. If γ is constant, plastic response is cyclically stable, but in general, it may be considered a function of the number of load repetitions, etc. to simulate cyclic hardening or softening. Notice from Equation 3.8.1.5 that $(K_p) \to \infty$ as $\delta \to \delta_o$.

On the hydrostatic axis, observe that

$$\beta = (I_o)_p / I_1 \quad ,$$

where $(I_o)_p$ is the size (or intersection with the hydrostatic axis) of the boundary surface. Using the plastic modulus formula (Equation 3.4.7) and the previous equation, the plastic modulus at the bound on the hydrostatic axis is found to be

$$\bar{K}_p = \lambda\ (I_o)_p = \lambda\ \beta\ I_1\ . \qquad (3.8.1.6)$$

Substituting this equation into the mapping function (Equation 3.8.1.5) gives

$$K_p = \lambda\ I_1\ \ (\beta)^{\gamma+1} = \lambda\ I_1\ [(I_o)_p/I_1]^{\gamma+1}\ , \qquad (3.8.1.7)$$

which in turns yields the following equation for the plastic volumetric strains generated on spherical reloading:

$$\varepsilon^p_{kk}\ \ \frac{1}{\lambda\ x}\ (A^x\ -\ B^x)\ ,\ A\ >\ B \qquad (3.8.1.8)$$

where

$A = [I_1/(I_o)_p]$ at the end of reloading,

$B = [I_1/I_o)_p]$ at the start of reloading

ε^p_{kk} = plastic volumetric strain caused by reloading from B to A, and

$x = \gamma + 1$.

This equation provides a simple method for initializing γ. Although one might exist, a closed-form solution for "x" ($= \gamma + 1$) in Equation 3.8.1.8, was not available so a trial and error procedure was adopted.

3.8.2 Prediction of Cavity Expansion Tests

With two additional refinements, the version of the bounding surface theory described in the previous section has been implemented in a finite element routine to predict a series of cavity expansion tests. The first improvement is the freedom accorded the parameter R (of Equation 3.3.1.6) to match the deviatoric shape of the failure surface. It is no longer forced to coincide with the Mohr-Coulomb criterion in extension. Instead, R is now a material constant which is calculated directly from the (generally unequal) friction angles observed in compression (ϕ_c) and extension (ϕ_e) tests,

$$R = [\sin \phi_e / \sin \phi_c] \; [(3 - \sin \phi_c)/(3 + \sin \phi_e)] \quad . \qquad (3.8.2.1)$$

A second modification was effected to predict a softer response in extension tests, as the data of Saada et al. (1983) suggests. To accomplish this, the exponent "n" of the plastic modulus equation (Equation 3.4.7) was made a function of Lode's parameter θ,

$$n = n^*/g(\theta) \quad , \qquad (3.8.2.2)$$

where n^* is the exponent applicable to compression tests and $g(\theta)$ is as defined in equation 3.3.1.6. This change causes the shape of the iso-plastic moduli contours on the deviatoric plane to differ from the trace of the specified failure locus.

In retrospect, the writers must admit that these modifications were perhaps not necessary; they do not seem to have as much an impact on the predictions as originally thought. Therefore, in future studies, consideration should be given to omitting both of them.

A self-boring pressuremeter probe, implanted in a large-scale triaxial chamber, provided the necessary experimental data for this study (Davidson,

1983). The soil tested, Reid-Bedford Sand, was the same as that investigated by Saada et al. (1983) and Chapter 1, except that the relative density was about 7% higher.

Table 3.8 summarizes from Davidson (1983) essential information regarding the five pressuremeter tests analyzed. Included in this table are the initial vertical and horizontal stresses, and the elastic stress-strain and strength parameters [derived from the data using the elastic-perfectly frictional "plastic" method of interpretation proposed by Hughes et al. (1977)] Notice that tests #2 adn #3 as well as tests #4 and #5 were nominally replicate experiments. The reproducibility of these data (later see Figures 3.45 and 3.46 for example) gave the researchers the needed confidence to proceed with such a rigorous solution.

Table 3.9 lists the model parameters used in the finite element analysis, and these were selected on the following basis:

1. The strength parameter k used in all simulations was computed from an average of the friction angles listed in Table 3.8.
2. A unique (constant) elastic shear modulus was input for each numerical prediction, and these were calculated directly from the small unload-reload loop common to all pressuremeter tests (Table 3.8 provides this information).
3. The material constants, N, Q, b, and n were assumed to be the same as that for Reid-Bedford sand at 75% relative density (see Table 3.4). Judging from Table 3.5, these parameters do not seem to be affected much by changes in the relative density. Note that in this theory the slope of the zero dilation line, N, does not vary at all with porosity.

Table 3.8 Summary of Pressuremeter Tests in Dense Reid-Bedford Sand

	TEST IDENTIFICATION				
	#1	#2	#3	#4	#5
Initial relative density D_r (%)	83.2	84.8	85.8	83.2	81.1
Initial vertical stress (kPa)	45.5	155.	157.	265.	265.
Initial horizontal stress (kPa)	20.7	46.2	51.7	84.8	92.4
Observed lift-off pressure (kPa)	35.9	46.2	51.7	84.8	92.4
Estimated shear modulus (MPa)	45.6	55.2	55.2	82.7	82.7
Friction angle, ϕ	39.5°	41.7°	41.3°	41.2°	39.2°

Source: Davidson, 1983

Note: Test #2 and #3 as well as #4 and #5 were intended to be replicate experiments

Table 3.9 Model Constants Used to Simulate Pressuremeter Tests

PARAMETER	MAGNITUDE
Elastic Constants:	
Elastic shear modulus, G for test #1	45,610 kPa
for test #2 & #3	55,160 kPa
for test #4 & #5	82,740 kPa
(extracted from Table 3.7)	
Poisson's ratio, ν	0.2
Flow Parameters:	
Slope of zero dilation line, N	.218
Shape controlling parameter of consolidation portion of yield surface, Q	2.60
Shape controlling parameter of dilation portion of yield surface, b	15.0
Plastic Modulus Parameters:	
Plastic compressibility parameter, λ	580
Strength parameter, k	.325
Parameter to model curvature of failure meidian, m	0
Shape hardening controlling exponent n	2
Non-standard Parameters:	
Ratio of radius of failure surface in extension to compression, R	.7
Bounding surface reload modulus parameter, γ	15

Note: the parameters G and k were calculated from data reported by Davidson (1983), λ and γ from Linton (1986), and the remainder from Saada et al. (1983).

4. The reload modulus parameter γ was reckoned from a series of unload-reload hydrostatic compression tests reported in Chapter 1. Also calculated from Chapter 1 was the plastic bulk modulus parameter λ; it was found to be about twice as large as that computed from a similar test by Saada (see Table 3.4 and Figure 3.18). However, as the results in Chapter 1 were from many repeated tests, using different types and combinations of strain measuring devices, all of which gave consistent results, its characterization was chosen.
5. Finally, the parameter R was estimated from the constant mean pressure compression and extension tests (GC 0 and GT 90) of the series of experiments reported by Saada et al. (1983).

Figure 3.43 gives the nodal point and element information of the finite element idealization of the expanding cavity problem. Observe from this figure that the radius of the pressuremeter's cavity is equal to 40.8 mm, and the distance from the centerline of the cavity to the lateral boundary of the chamber is equal to 607 mm. Also, note the assumption of plane strain for the boundary conditions and the fact that the lateral periphery of the calibration chamber does not move. Studies by Laier et al. (1975), Hartmann and Schmertmann (1975), and Hughes et al. (1977) support the hypothesis that the pressuremeter cavity expands under conditions of axial symmetry and plane strain.

The numerical results of the five tests are superposed with the experimentally measured data in Figures 3.44 to 3.48. Cavity strain in these plots is defined as the average radial displacement of three symmetrically positioned "feeler" arms, divided by the radius of the undeformed cavity. In each prediction, 200 load steps were used for the initial loading, 50 steps for the small unloading, and 300 steps for the final loading.

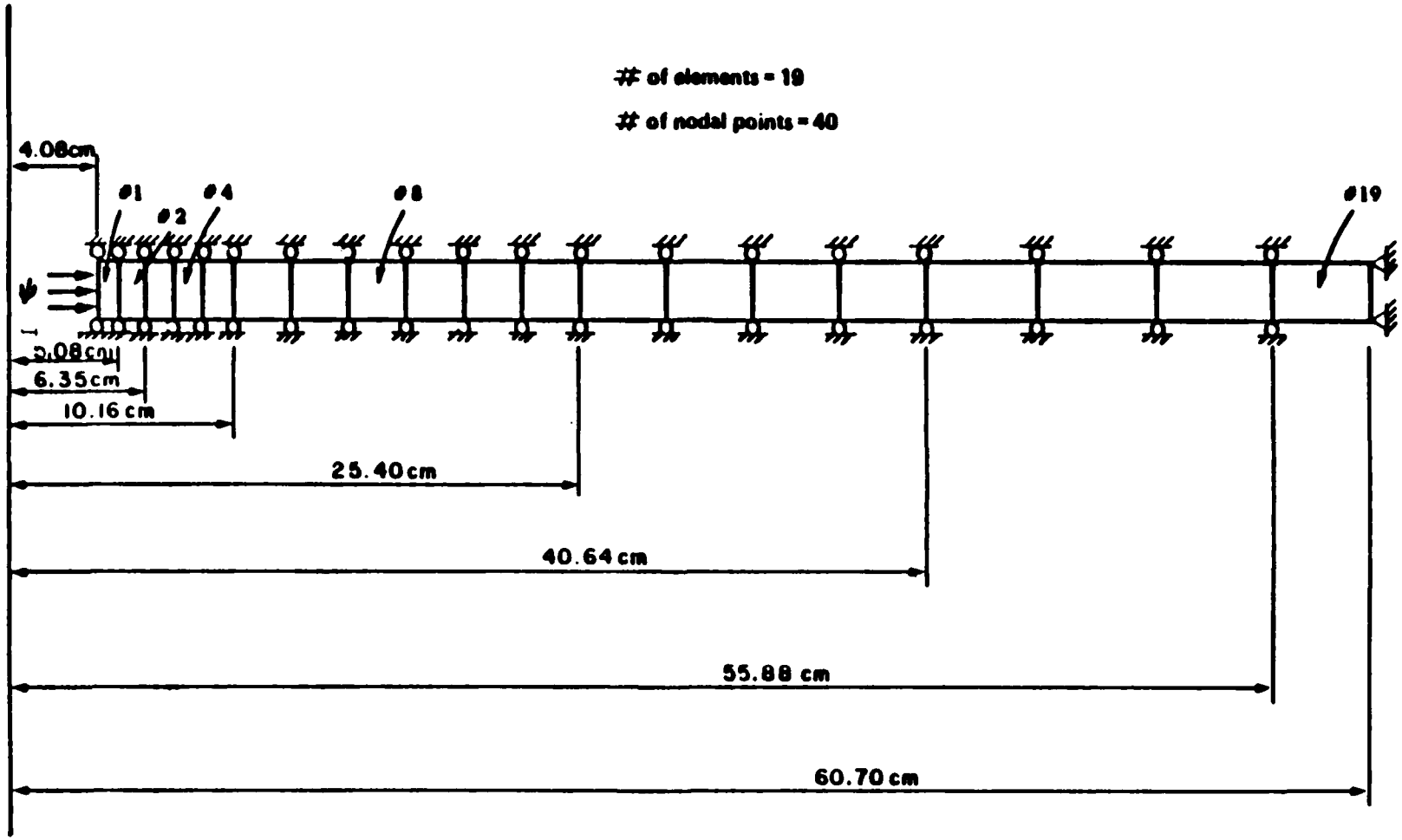

Figure 3.43 Finite element mesh used in pressuremeter analysis

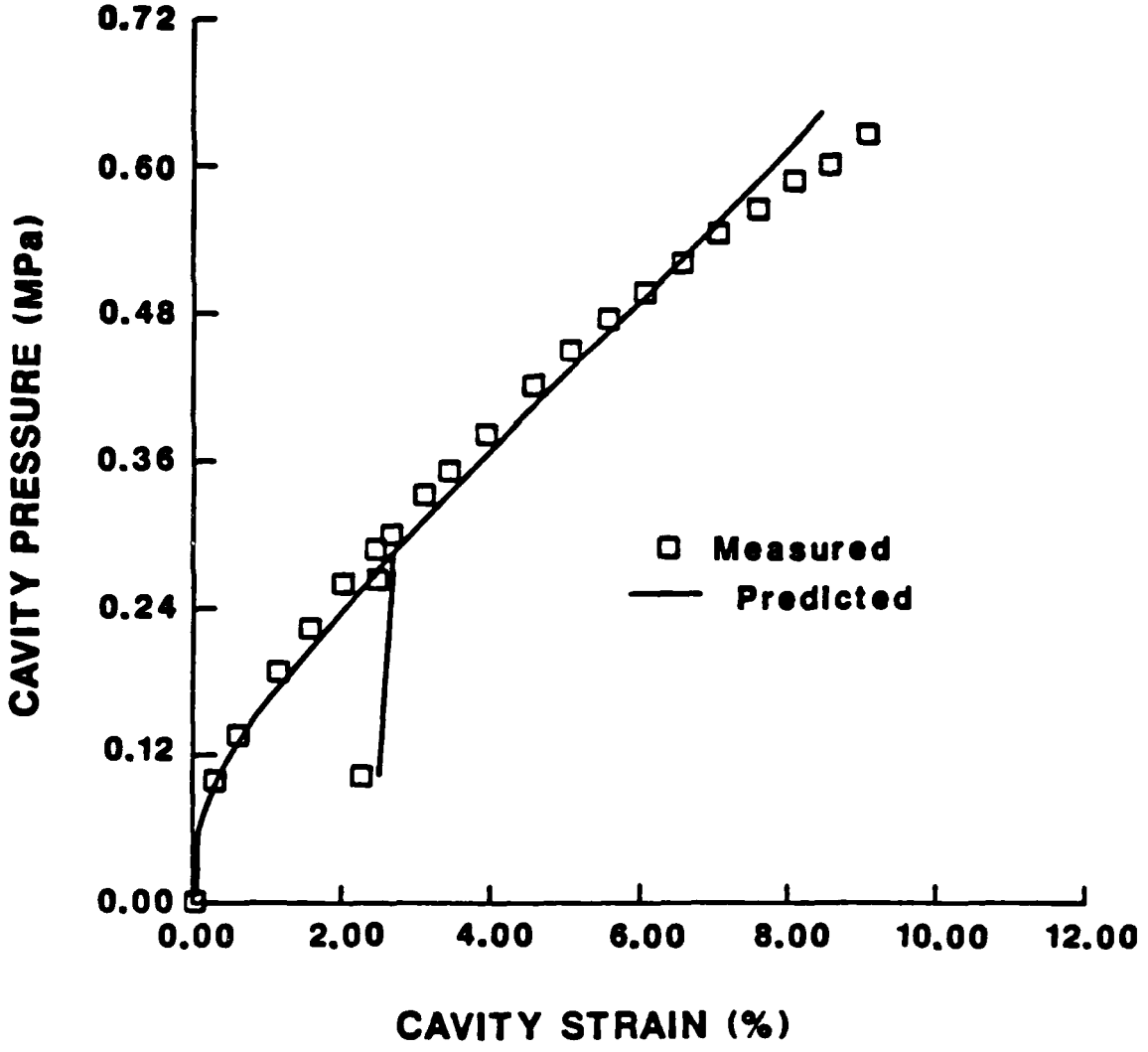

Figure 3.44 Measured vs. predicted response for pressuremeter test #1

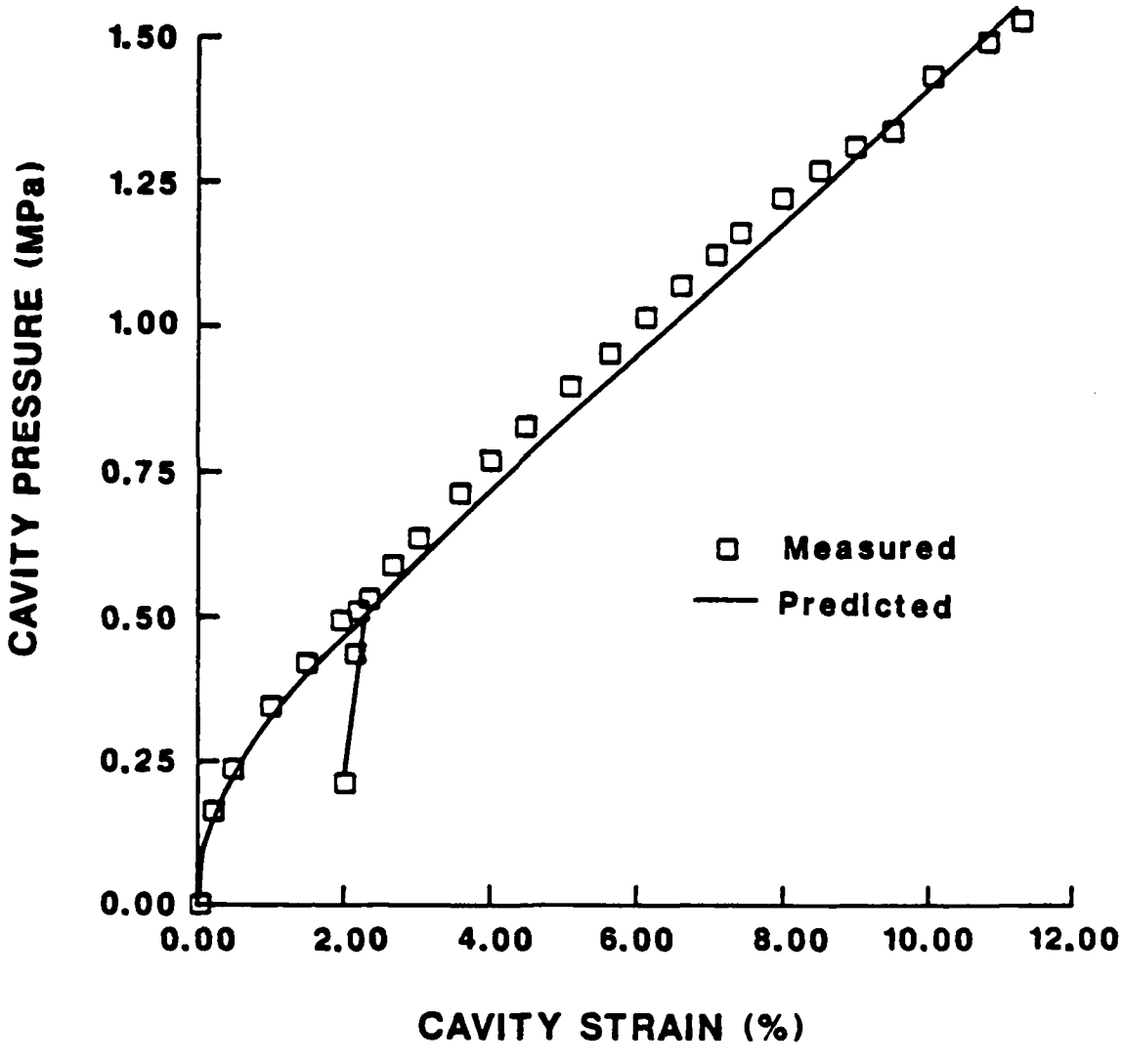

Figure 3.45 Measured vs. predicted response for pressuremeter test #2

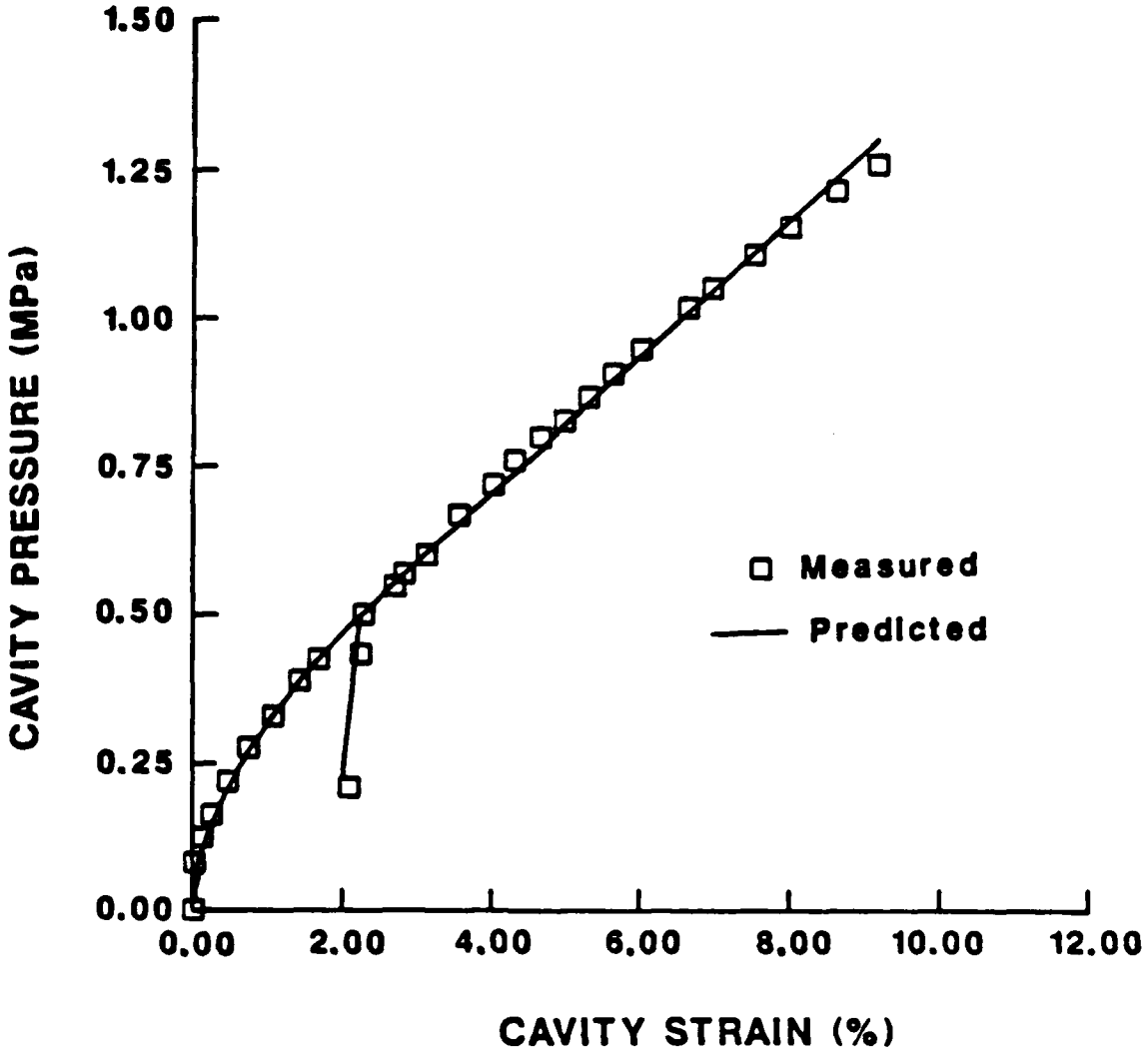

Figure 3.46 Measured vs. predicted response for pressuremeter test #3

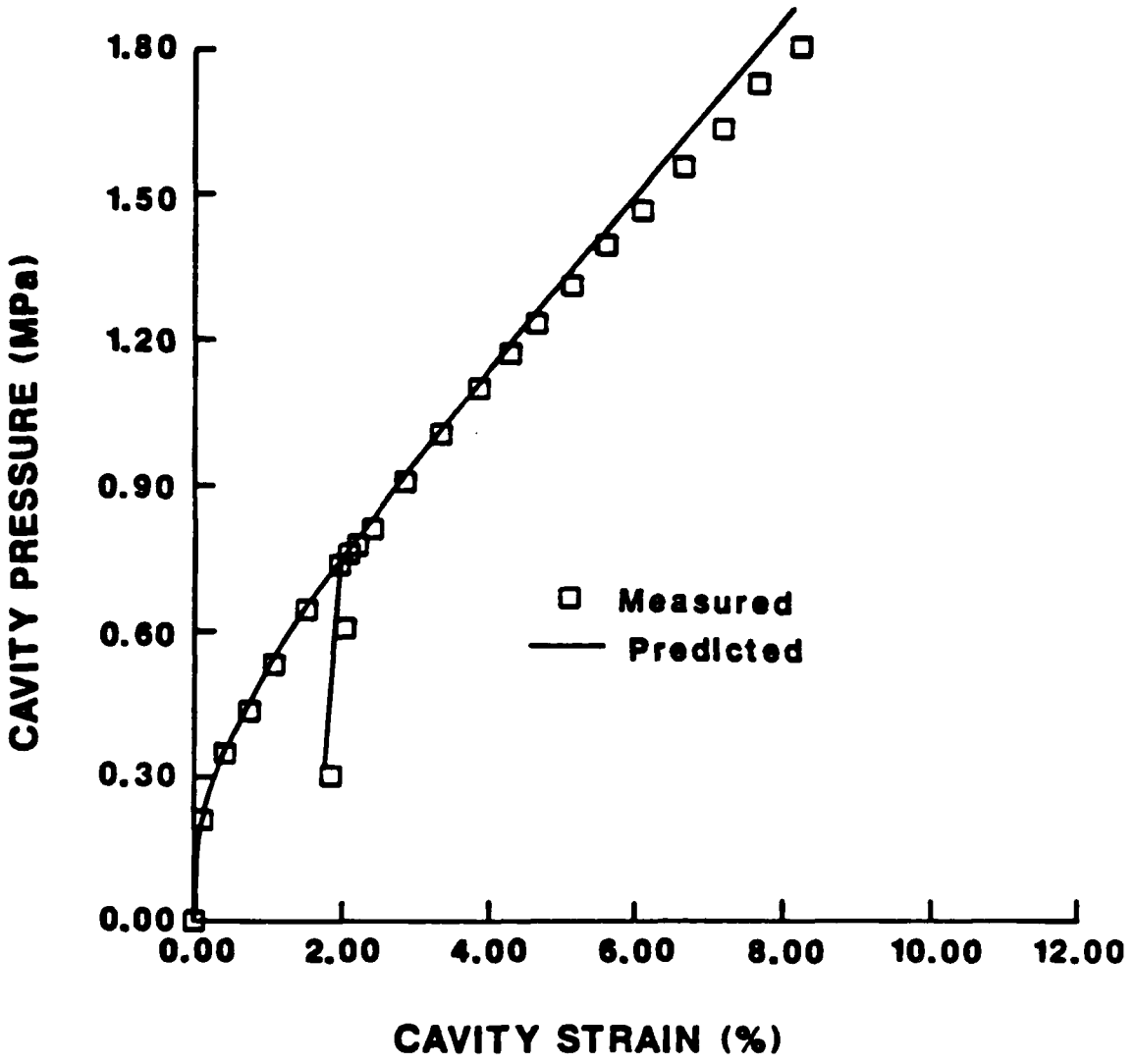

Figure 3.47 Measured vs. predicted response for pressuremeter test #4

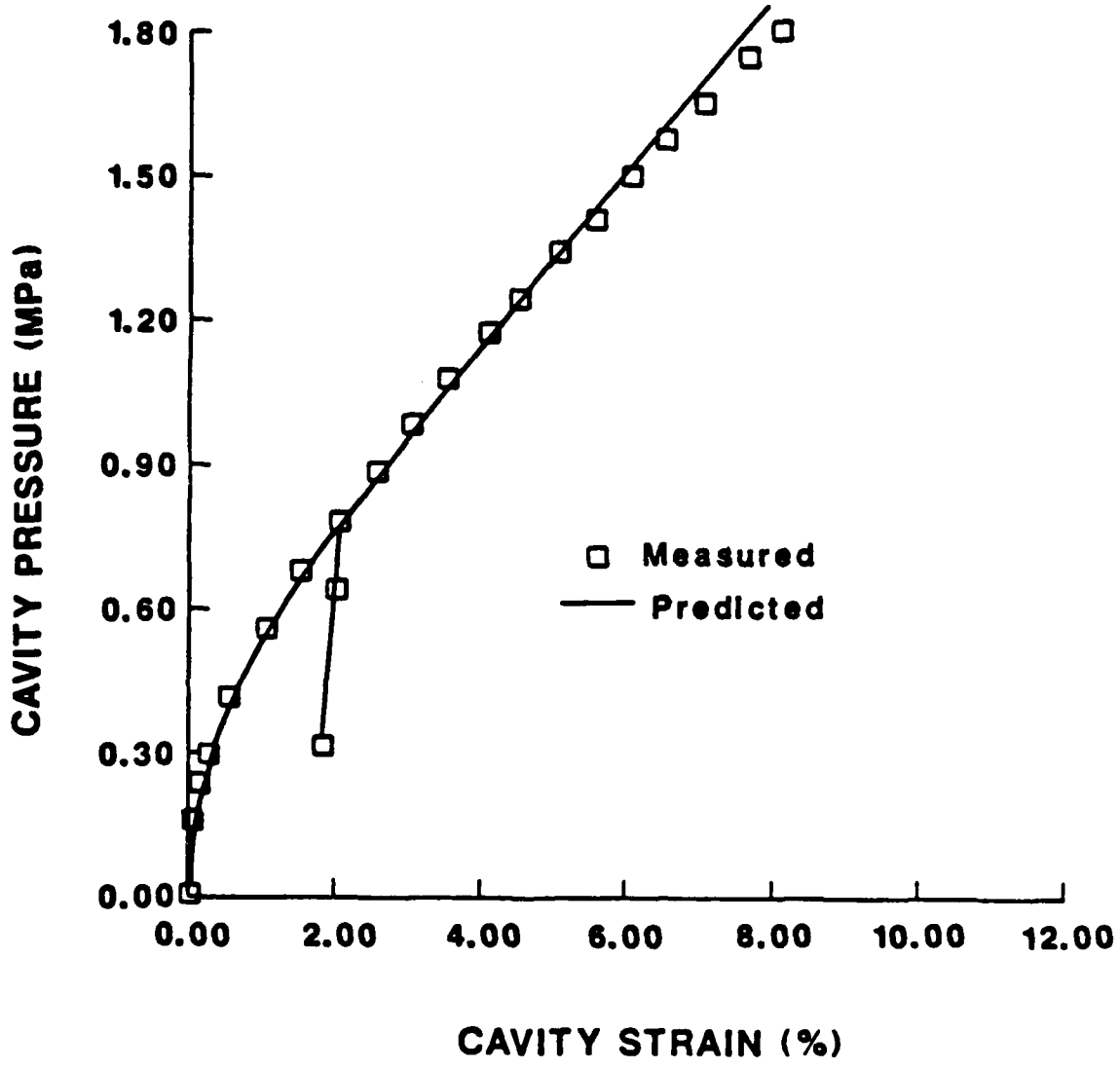

Figure 3.48 Measured vs. predicted response for pressuremeter test #5

The remarkably close agreement between the measured and predicted curves suggests that: a) the constitutive idealization is indeed a good approximation to reality for this test path, b) the assumption of plane strain is valid, c) the pressure-expansion tests are free to any major sources of experimental error, and d) the conventional procedure for computing the friction angle ϕ from pressuremeter data, as outlined in Davidson (1983), is rational.

Detailed results, originating from the finite element output, permitted an inspection of the typical predicted stress path and the stress distribution in the zone of influence of expanding cylindrical cavity. In the graphs that follow, σ_r , σ_z , and σ_θ denote respectively the radial, axial, and circumferential components of the stress tensor in cylindrical coordinates. Figure 3.49 shows the typical variation of the principal stresses with monotonically increasing cavity pressure. The variation of the predicted Lode angle θ, an indicator of the relative magnitude of the intermediate principal stress, is also shown on this plot. Its significance becomes apparent when related to Figure 3.50, which shows the variation of plastic stiffness in selected elements. Notice that the material response is softest when the Lode angle is minus 30°, or alternatively, when $\sigma_r = \sigma_z$ $(\sigma_1 = \sigma_2)$. This spectular drop in stiffness is a direct consequence of the connection imposed between the exponent "n" and the Lode angle θ in Equation 3.8.2.2. The stiffness increases as the Lode angle increases toward a steady magnitude of about +15°, and once there, the plastic modulus decreases again.

Figure 3.51 gives an alternate view of the stress path in which its relative position with respect to the zero dilatancy line and the failure envelope is emphasized. It appears that, for this particular boundary condition, the soil element does not undergo plastic dilation, but compacts as it is being sheared. Also note from this figure that the reloading path more

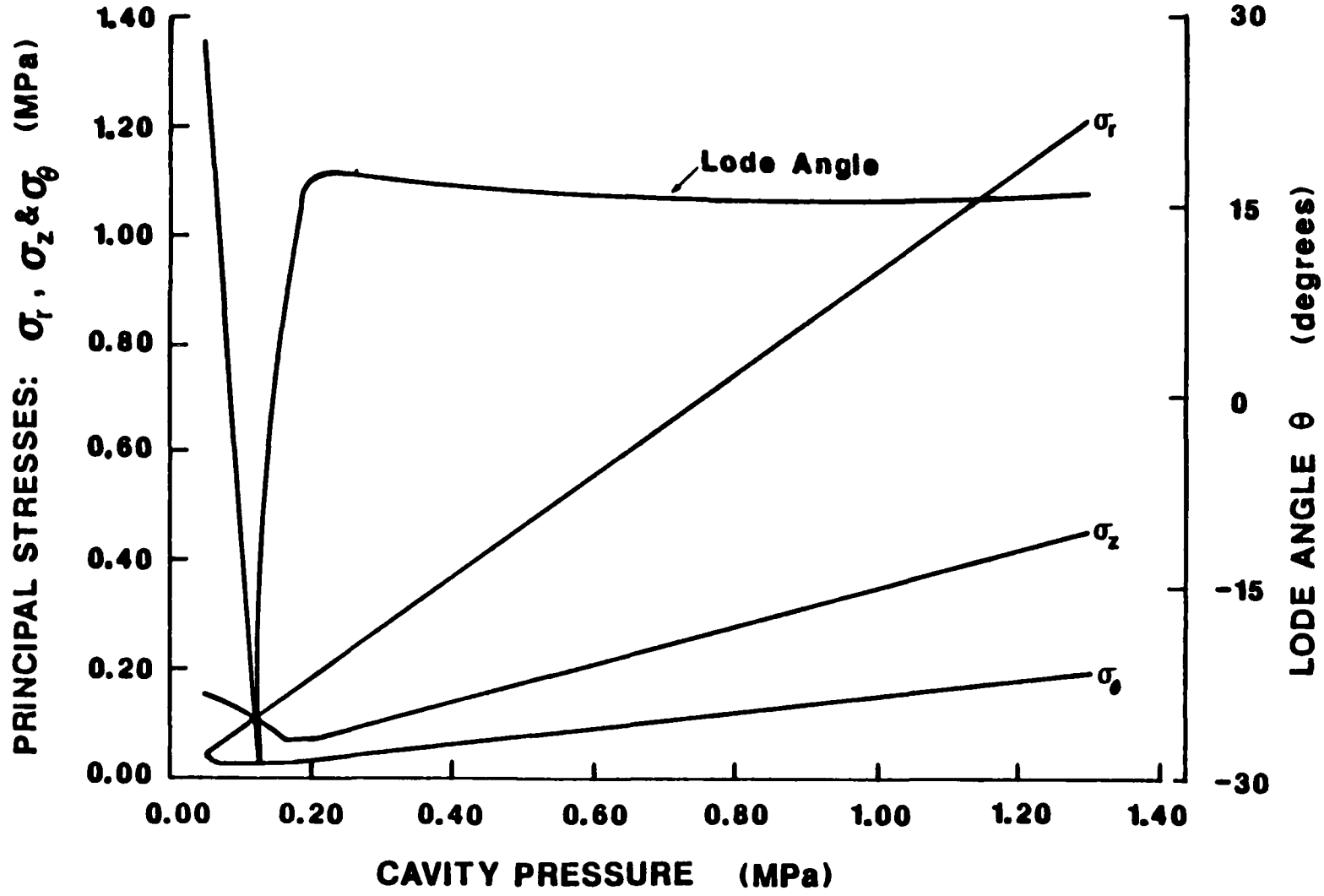

Figure 3.49 Variation of principal stresses and Lode angle with cavity pressure for element #1 and pressuremeter test #2

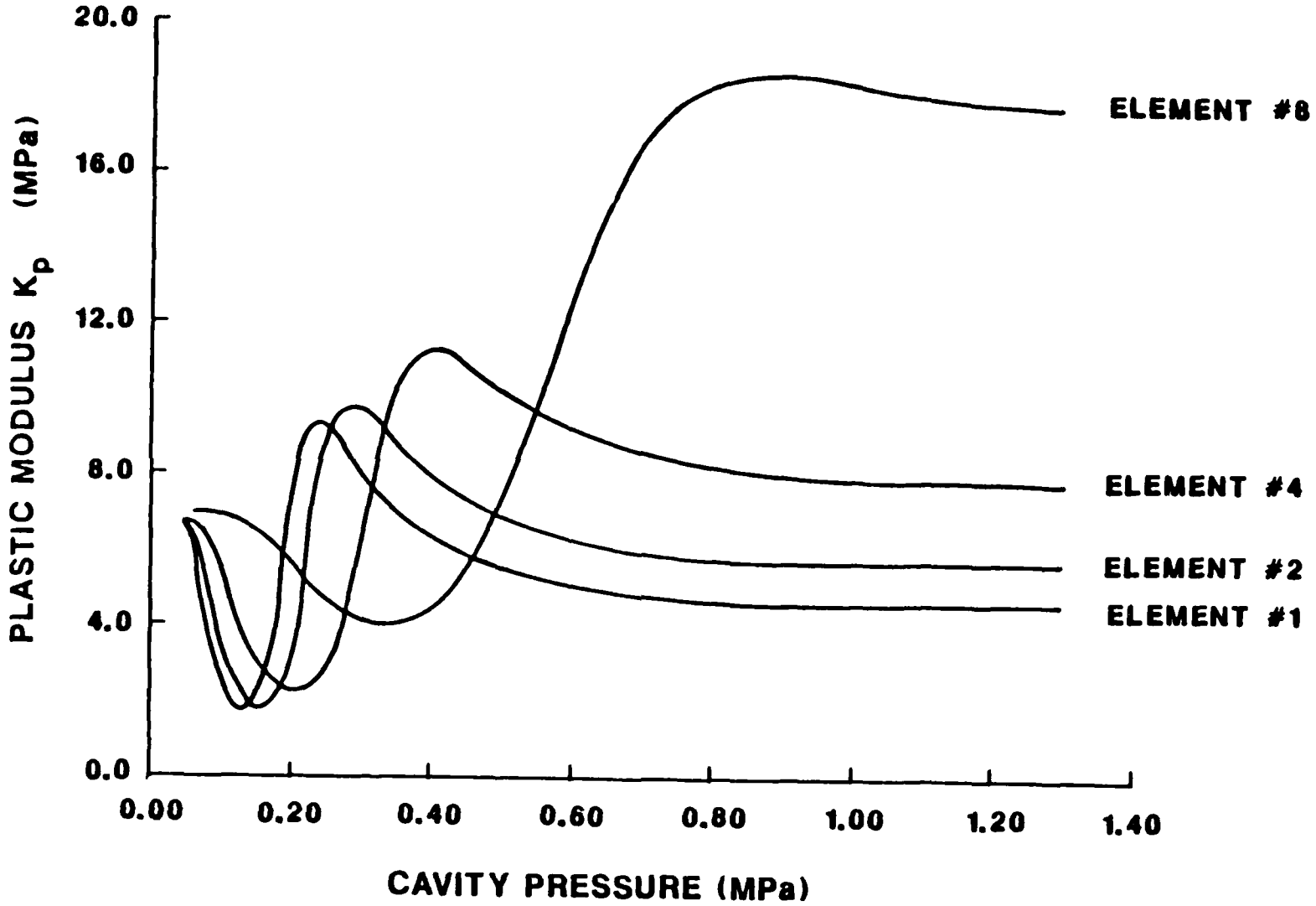

Figure 3.50 Variation of plastic modulus with cavity pressure for pressuremeter test #2

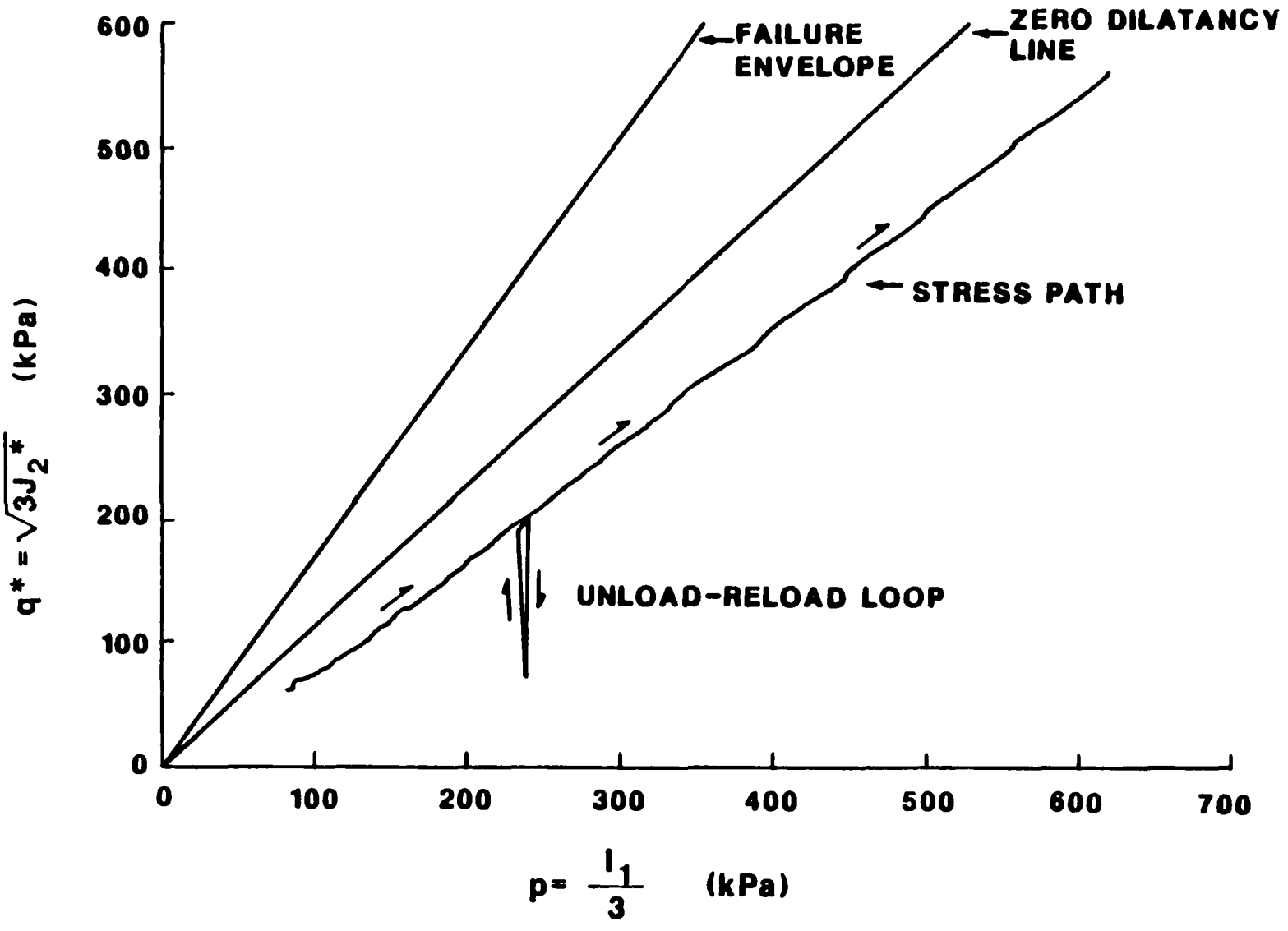

Figure 3.51 Meridional projection of stress path for element #1, pressuremeter test #2

or less retraces the unloading path, and so the actual shape of the bounding surface does not really matter--virgin response reinitiates at the point of unloading.

The importance of minimizing disturbance to the surrounding soil is emphasized in Figure 3.52, which shows the distribution of principal stresses with radial distance from the cavity wall. Very high stress gradients exist in the small annular region of soil within a few centimeters of the probe. Any significant remoulding in this region due to the field drilling procedure may result in meaningless pressure-expansion data.

3.8.3 Proposed Hardening Modification

Recall that a hardening control surface is defined here as a surface which encloses the totality of points where the purely stress-dependent plastic moduli are higher than their virgin loading magnitudes. As pointed out previously, experimental studies indicate that the shape of the hardening control surface does not resemble the shape of the yield surface relevant to the simple theory. Poorooshasb et al. (1967) and Tatsuoka and Ishihara (1974a) have found, using a variety of experimental stress probes, that these surfaces have shapes similar to that of the limit surface.

Using the stress paths drawn in Figure 3.53, together with a Taylor-Quinney (1931) definition of "yield" (as depicted in Figure 2.7), Tatsuoka and Ishihara (1974a) have sketched the family of hardening control surfaces shown in Figure 3.54. For simplicity, it is assumed that these surfaces are smaller versions of the limit surface. So, for a straight line failure envelope, a hardening control surface F_p is defined by the maximum q/p ratio established by the loading history.

For the more general form of the failure surface (Equation 3.4.9), the current mobilized stress ration k_{mob} is

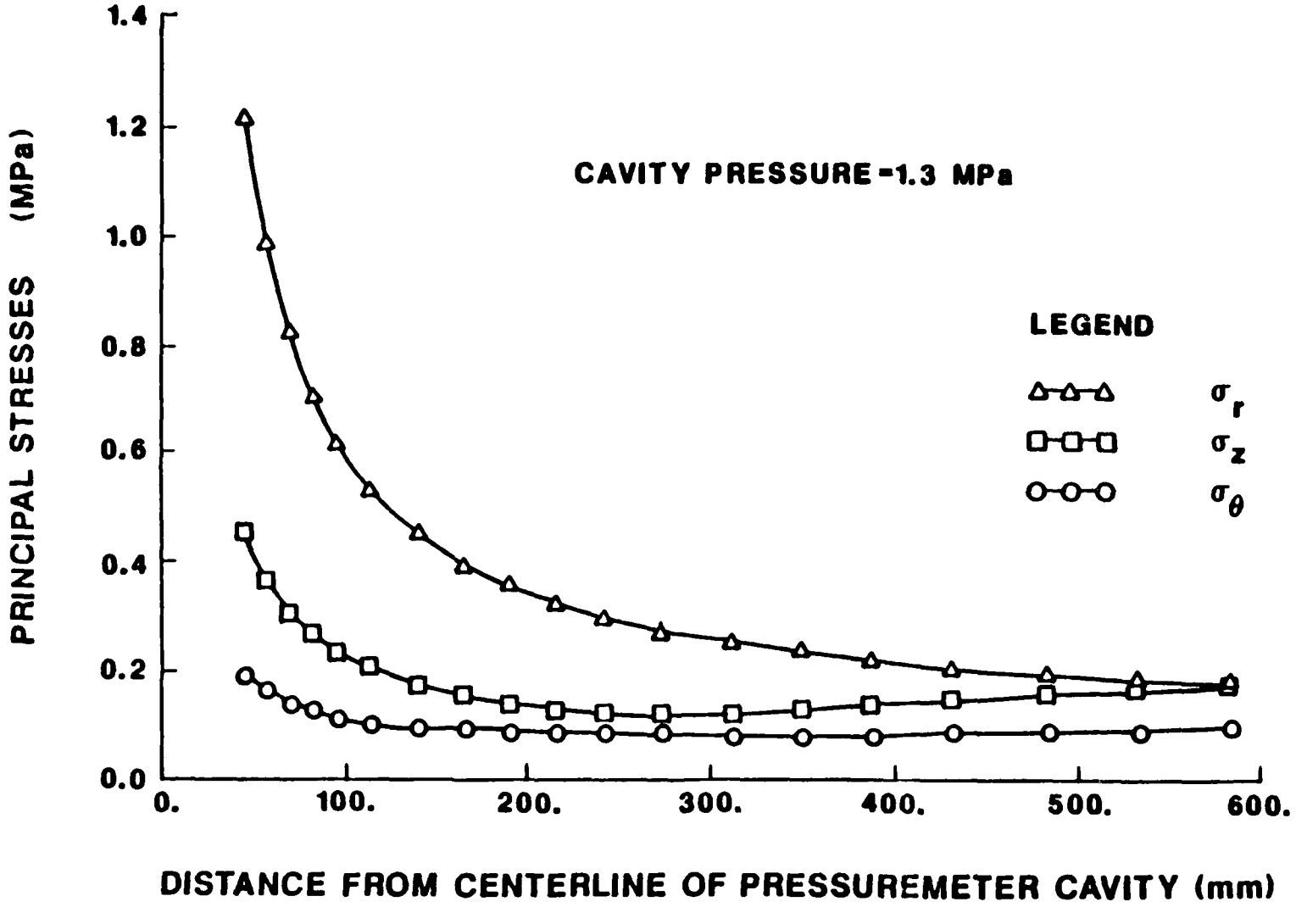

Figure 3.52 Principal stresses as a function of radial distance from axis of cavity at end of pressuremeter test #2

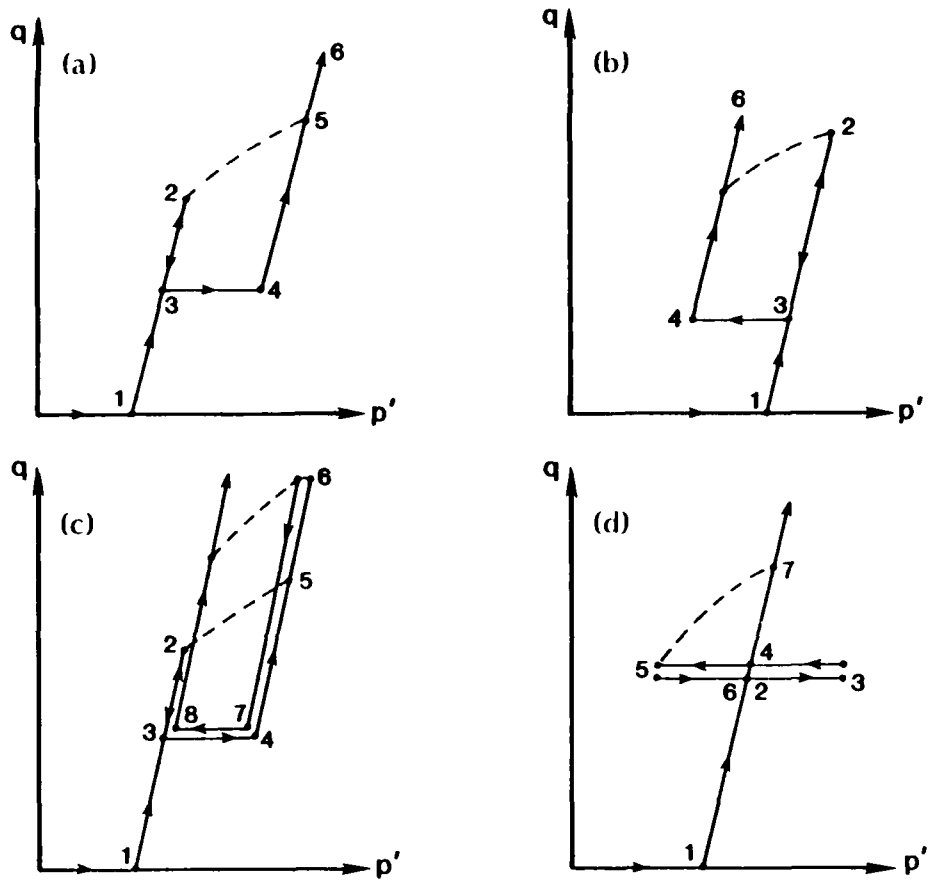

Figure 3.53 Experimental stress probes of Tatsuoka and Ishihara (1974b)

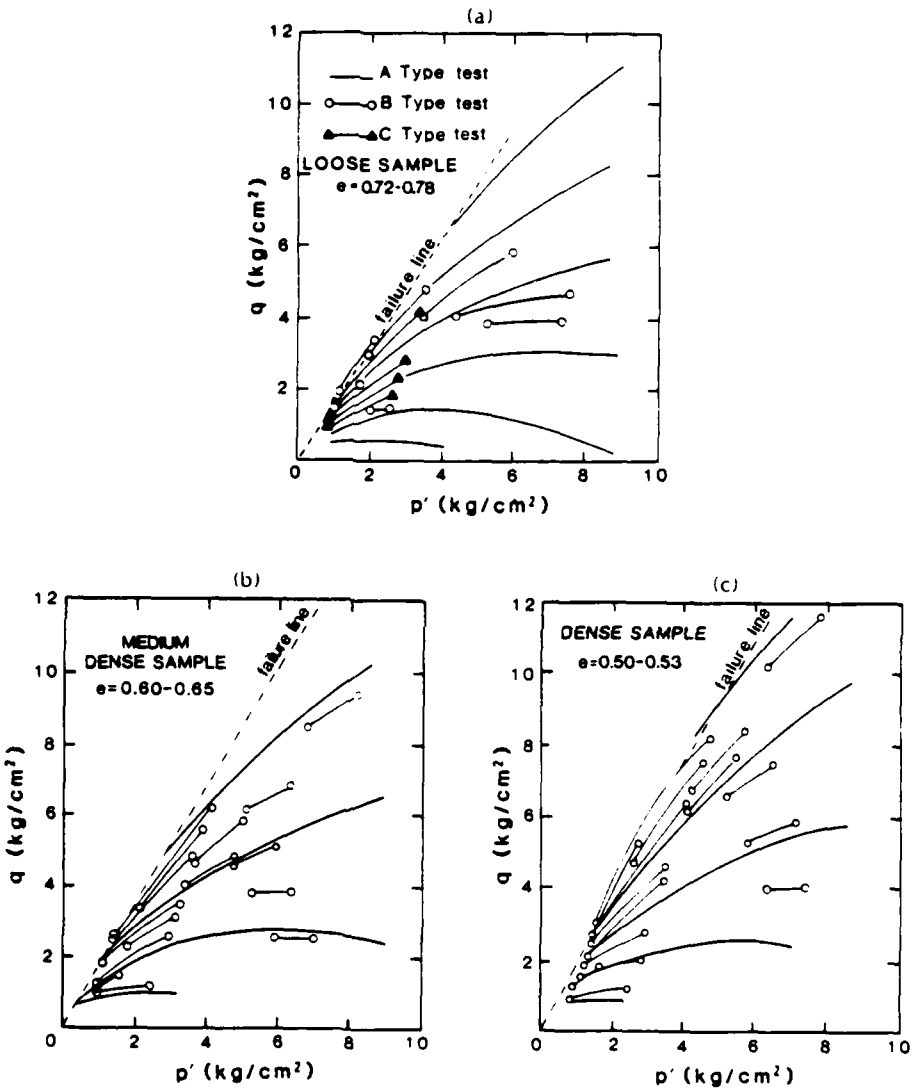

Figure 3.54 Shapes of the hardening control surfaces as evidenced by the study of Tatsuoka and Ishihara (1974b) on Fuji River sand

$$k_{mob} = (I_1/p_a)^m \frac{\sqrt{J_2^*}}{I_1} \quad . \tag{3.8.3.1}$$

As the stress point approaces the limit envelop, $k_{mob} \rightarrow k$. If unloading takes place (i.e., k_{mob} decreases), the maximum magnitude of k_{mob} is recorded and labeled the memorized stress ratio k_{mem}. This magnitude then specifies the size of the "boundary" or hardening control surface.

At any instant therefore, three stress ratios are known: i) a fixed magnitude k (which is the size of the stationary limit surface, ii) the current mobilized stress ratio k_{mob}, and iii) the memorized stress ratio k_{mem} (or the historical maximum of k_{mob}). Id $K_{mob} = k_{mem}$, the virgin plastic modulus given by Equation 3.4.7 is applicable, but if $k_{mob} < k_{mem}$ (a shear preloading), a stiffer modulus must be stipulated.

Equation 3.8.1.1 is again used to specify the reload modulus, and it is specialized here to

$$K_p = [(K_p)_o - \bar{K}_p] \left(\frac{\delta}{\delta_o}\right)^{\gamma_1} + \bar{K}_p \quad , \tag{3.8.3.2}$$

where γ_1 is a model constant. Observe that, as required, $K_p = \bar{K}_p$ when $\delta = 0$, and $K_p = (K_p)_o$ when $\delta = \delta_o$. In contrast to the previous bounding surface formulation, the original of mapping is slected as the hydrostatic state on the octahedral plane containing the current stress point, Figure 3.55.

From Equation 3.4.7, note that the virgin or prime plastic modulus $\bar{K}_p$ at the conjugate point $(\bar{I}_1 = I_1, \sqrt{\bar{J}_2^*})$ is simply

$$\bar{K}_p = \lambda I_1 [1 - (k_{mem} + k)]^n \quad . \tag{3.8.3.3}$$

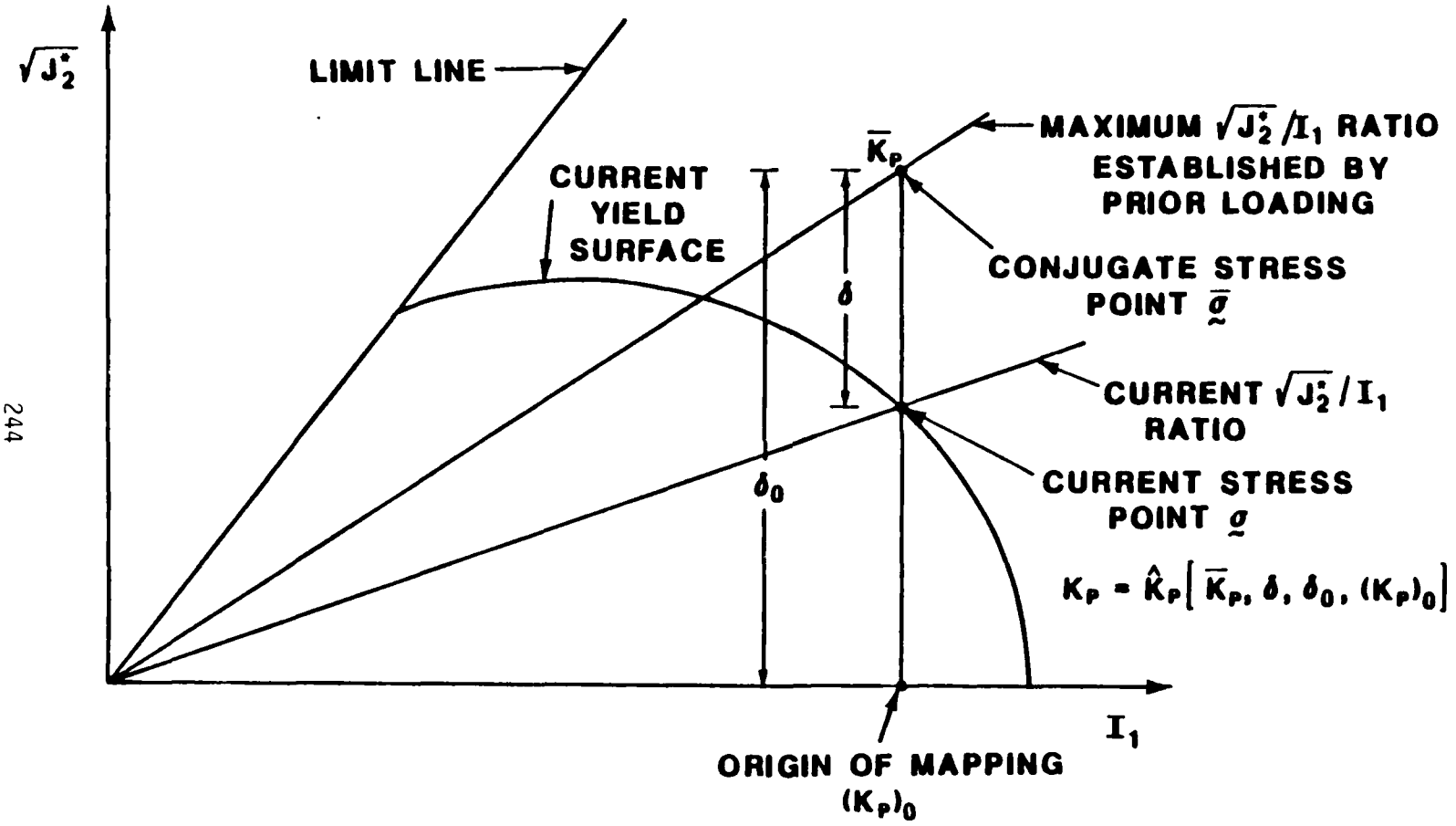

Figure 3.55 Illustration of proposed hardening control surface and interpolation rule for reload modulus

Also, recollect from Equation 2.5.2.3 that the radius on the deviatoric plane is equal to $\sqrt{(2J_2)}$ so

$$\frac{\delta}{\delta_o} = (\sqrt{\bar{J}_2} - \sqrt{J_2})/\sqrt{\bar{J}_2} = [(k_{mem} - k_{mob})/k_{mem}] \quad . \tag{3.8.3.4}$$

As in the first hardening option, the magnitude of the reload plastic modulus on the hydrostatic axis, $(K_p)_o$, is given by (cf. Equation 3.8.1.7)

$$(K_p)_o = \lambda\, I_o\, [(I_o)_p/I_o]^{\gamma+1} = \lambda\, I_1\, [(I_o)_p/I_1]^{\gamma+1} \quad , \tag{3.8.3.5}$$

where $(I_o)_p$ is the point at which the largest yield surface intersects the hydrostatic axis, Figure 3.56. With $\bar{K}_p$, δ/δ_o, and $(K_p)_o$ detailed in Equations 3.8.3.3, 3.8.3.4, and 3.8.3.5 respectively, only the parameter γ_1 is needed to completely specify the reload modulus interpoltion rule (Equation 3.8.3.2).

But before completing the formulation, a shortcoming of Equation 3.8.3.2 must be alluded to and amended. It occurs for shear paths following pure hydrostatic preconsolidation. Since in such a case k_{mem} is zero, no hardening is predicted for any subsequent shear path. The data of Hettler et al. (1984) in Figure 3.57 for a subsequent axial compression path contradicts this statement. Although any differences in the shear stress vs. axial strain and the dilative behavior are imperceptible, a conspicous hardening effect shows up in the compaction volumetric strain. Consequently, a modification is sought to recognize isotropic or nearly isotropic preloading and to recover Equation 3.8.3.5 as a special case for cyclic hydrostatic compression tests.

Since the preconsolidation process does not seem to have any effect on response in the dilation domain, it is not unreasonable to postulate that the

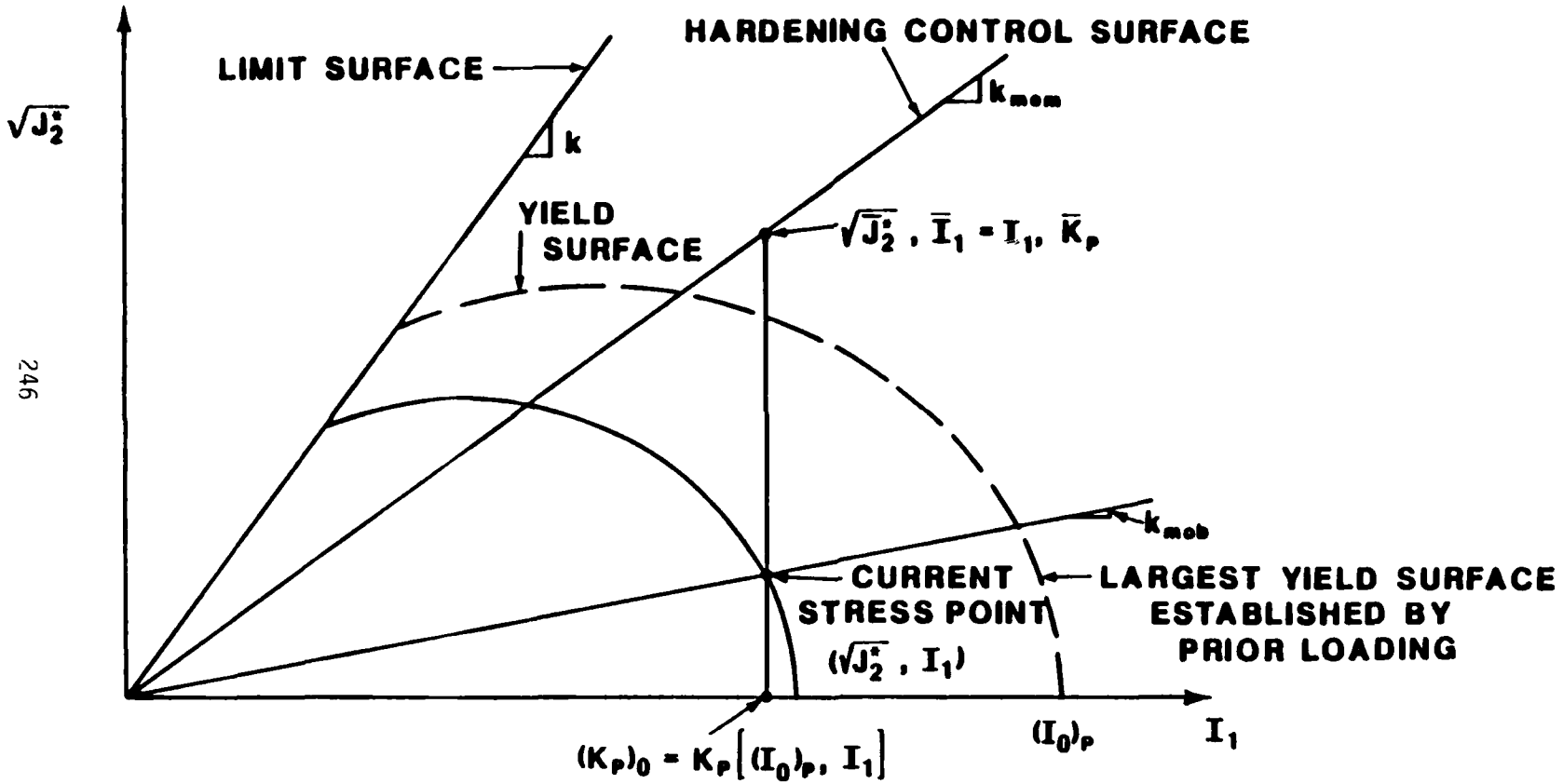

Figure 3.56 Illustration of the role of the largest yield surface (established by the prior loading) in determining the reload plastic modulus on the hydrostatic axis

effects of isotropic preloading should be ignored at some radial line at or below the zero dilation line. Such a modification can be effected by rewriting the plastic modulus formula (Equation 3.4.7) as:

$$K_p = \lambda I_1 (\beta')^{\gamma+1} \{1 - [f(\sigma)/k]\}^n \quad , \qquad (3.8.3.6)$$

where

$$\beta' = \beta \left[1 - \frac{\sqrt{J_2^*}}{X I_1 N}\right] + \frac{\sqrt{J_2^*}}{X I_1 N} \quad ,$$

X N = slope of the radial line beyond which "isotropic" preloading effects are ignored ($0 < X \leq 1$) ,

and β is the scalar radial mapping factor defined in Equation 3.8.1.2. In other words, the largest yield surface established by the prior loading acts somewhat like a cap to the "q/p" hardening control surface.

To test this hypothesis, the isotropically preloaded data of Figure 3.57 for Karlsruhe sand at 99% relative density was predicted using the relevant simple model parameters of Table 3.6 and the assumptions that: a) the entire elliptical portion of the yield surface acts as a cap to the hardening control surface (i.e., X = 1), and b) $\gamma = 15$ (as for Reid-Bedford sand in Table 3.9). Since there was no shear preloading, the parameter γ_1 was not needed. Figure 3.58 shows the calculated and experimental results; the correspondence is excellent.

Figure 3.59 shows the axial strain accumulation in a constant amplitude stress-controlled cyclic axial compression test (Chapter 1). The material tested was Reid-Bedford sand prepared at an initial relative density of 75%,

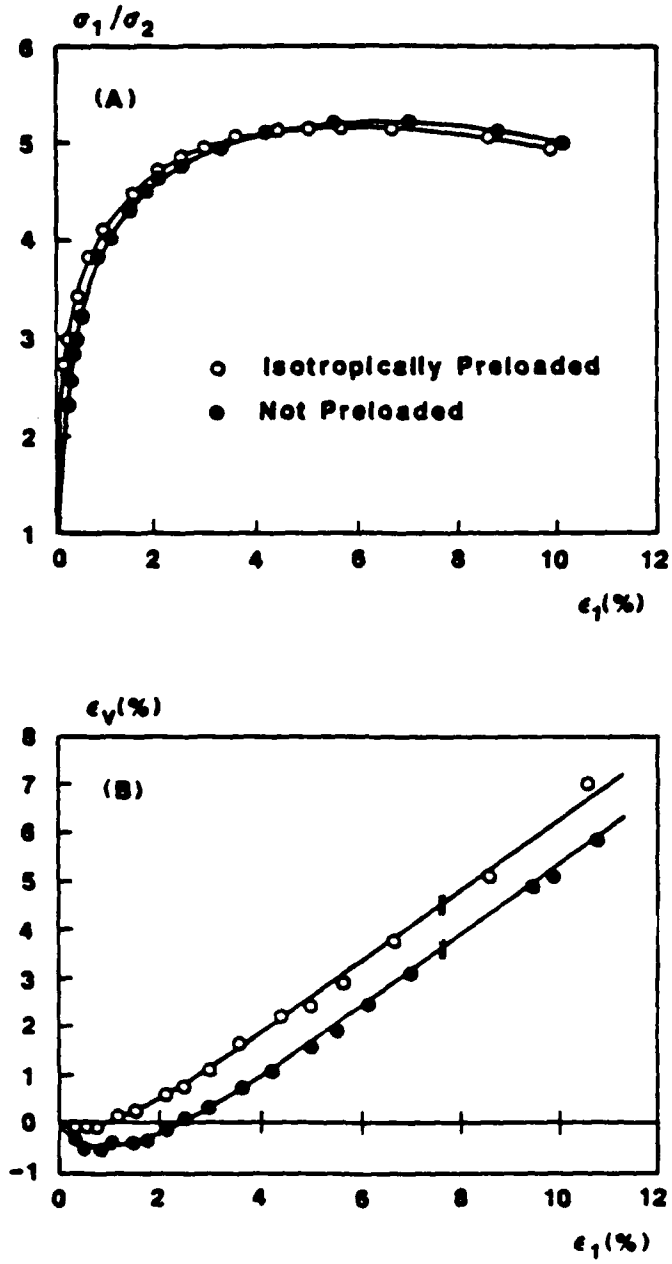

Figure 3.57 Influence of isotropic preloading on an axial compression test (σ_3 = 200 kN/m^2) on Karlsruhe sand at 99% relative density (after Hettler et al., 1984)

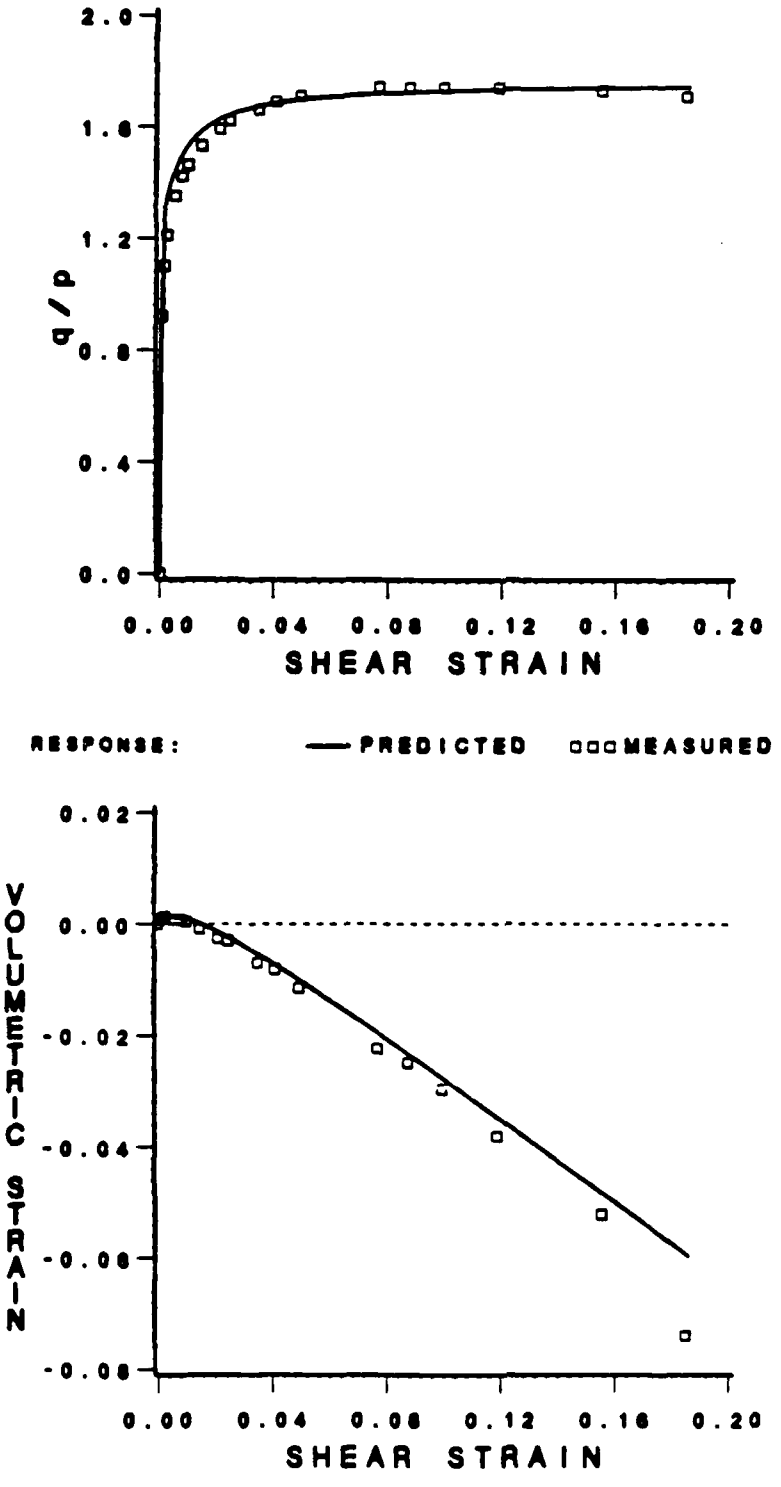

Figure 3.58 Predicted vs. measured results for hydrostatic preconsolidation followed by axial shear (measured data after Hettler et al., 1984; see Fig. 3.57)

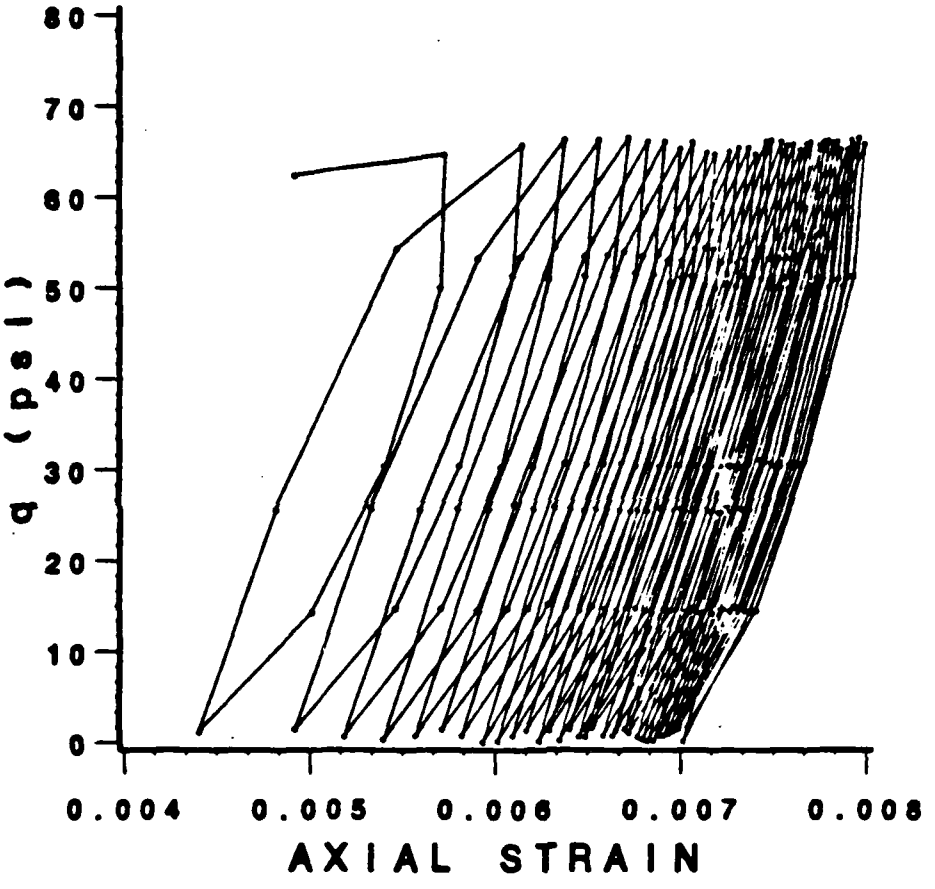

Figure 3.59 Shear stress vs. axial strain data for a cyclic axial compression test on Reid-Bedford sand at 75% relative density. Nominal stress amplitude q = 70 psi, and confining pressure σ_3 = 30 psi (after Linton, 1986)

and the external axial load was cycled between nominally fixed stress limits of 0 and 100 psi with an ambient pressure of 30 psi.

Granular base course and subbase course materials undergo this type of continued (or cyclic) hardening under repeated loads for as many as 10^4 cycles (Brown, 1974), beyond which point there is cyclic stability, or plastic shakedown, or sometimes a sudden degradation. Only a crude formulation for cyclic hardening is implemented here to demonstrate the versatility of the model to predict this ratchetting. The interested reader is referred to Eisenberg (1976) and Drucker and Palgen (1982) for examples of more general descriptions of cyclic hardening and cyclic softening, and to Mroz and Norris (1982) for an example of a cyclic degradation option for sand.

To simplify the theory, the response in cyclic hydrostatic compression is assumed to be immediately stable. That is, the parameter γ is assumed to be constant and the reload modulus on the hydrostatic axis, $(K_p)_o$, is unaffected by the number of load repetitions. This is not a bad assumption when one considers the relatively small plastic strains occuring in this non-critical region of stress space. With this assumption, cyclic hardening (or softening) effects are controlled solely by the exponent γ_1 of the reload modulus equation (Equation 3.8.3.2). Note that high magnitudes γ_1 produce a softer response.

Factors which affect the accumulation of permanent strain in cohesionless material have been reported to be the number of load repetitions, stress history, confining pressure, stress level, and density (Lentz and Baldi, 1980). All but the number of load repetitions and the stress history are implicit in the simple theory. Stress history effects have been included by the introduction of the hardening control surface, and now cyclic hardening is incorporated by replacing the parameter γ_1 with the empirical equation

$$\gamma_1 = \gamma_2 \ (N_{REP})^{\gamma_3} \ , \qquad (3.8.3.7)$$

where N_{REP} is the number of load repetitions, γ_2 is the magnitude of γ_1 for the first loading (N_{REP}=1), and γ_3 (a negative quantity) models the decrease in γ_2, or the stiffening of the response with increasing numbers of load cycles. By assigning an approriate magnitude of γ_1 for each cycle, log (γ_2) and γ_3 can be determined as the intercept and slope respectively of a straight line fit to a plot of log (γ_1) vs. log (N_{REP}).

The permanent strain accumulation of Figure 3.59 was predicted using as approriate: a) the simple model plastic parameters and the reload modulus parameter γ of Table 3.9, b) the elastic constants of Table 3.4, and c) back-computed magnitudes for the cyclic hardening parameters γ_2 and γ_3 . To get a more precise prediction of the axial strain for the first (or virgin) loading, the strength parameter k was reduced slightly from .300 to .295. The parameters γ_2 and γ_3 were computed to be 5.23 and -0.11 respectively, and cyclic stability was assumed after 25 cycles. Figure 3.60 shows how precisely the representation predicts this buildup of axial strain.

3.9 Limitations and Advantages

In conclusion, a number of limitations and advantages of the proposed theory are summarized.

At this early stage in the development of the model, its main limitations appear to be following:

1. As shown in Figure 3.61, an unusual range of stress paths, moving from region A into region B, can penetrate the limit surface as elastic unloading or neutral loading paths.

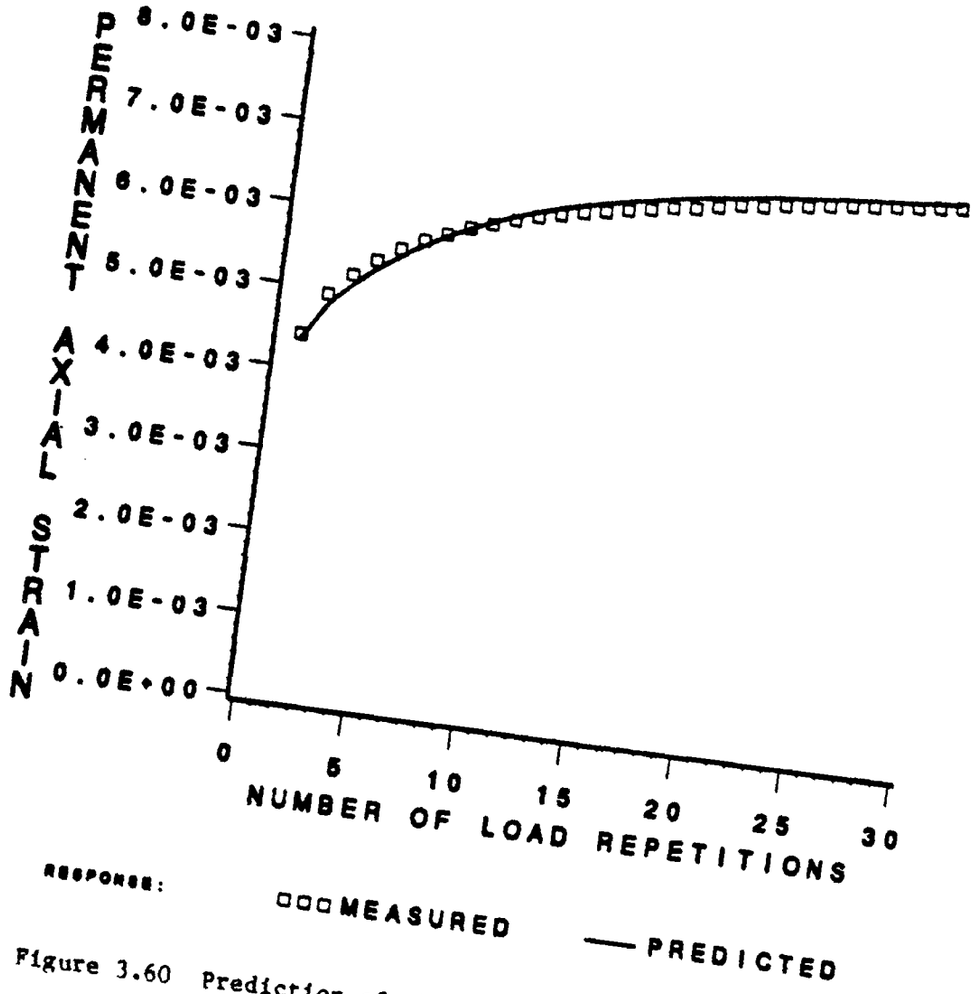

Figure 3.60 Prediction of the buildup of the axial strain data of Figure 3.59 using proposed cyclic hardening representation

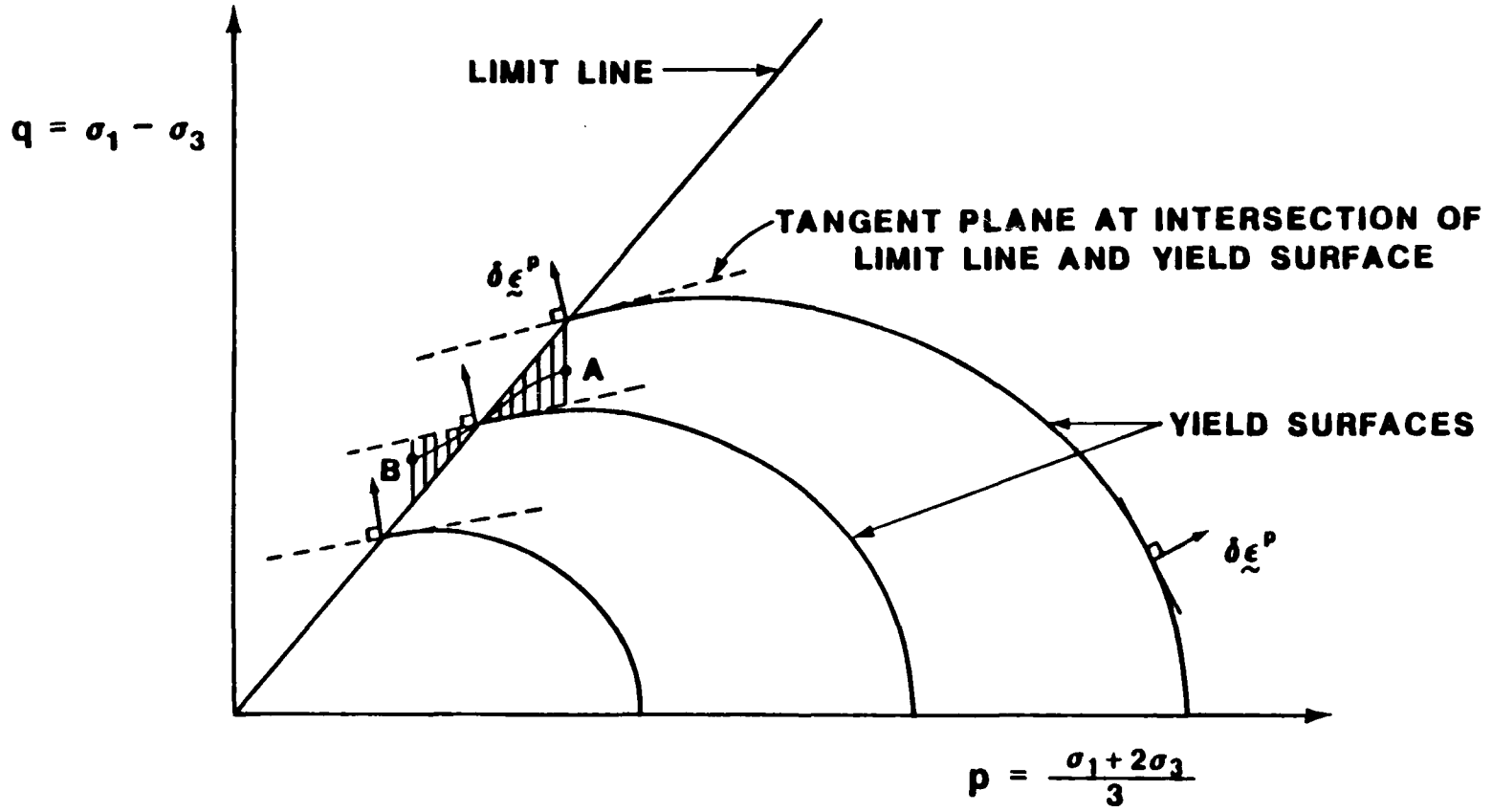

Figure 3.61 Any loading starting in the region A and moving to region B can go beyond the limit line as an elastic unloading or a neutral loading path

2. The interpolation rule used to model the decrease in K_p as the stress point moves from the hydrostatic axis to the limit surface needs refinement. It is not capable of matching stress-strain curves which become soft at the lower stress ratios.
3. The proposed hardening options give up the ability to predict virgin response in extension following a prior loading in compression. Thismay be corrected by adding a degree of stress reversal variable similar to the ones used by Eisenberg (1976) and Ghaboussi and Momen (1982).

The model proposed here appears to be significantly more rational, more attractive, and more manageable than many of the present theories because

1. of the separate and independent status accorded the yield surface, the limit surface, and the hardening control surface;
2. of the simplifications resulting from the automatic satisfaction of the consistency condition which therefore does not enter into the determination of the plastic modulus;
3. each parameter has a physical significance and each can be correlated to a stress-strain-strength concept in routine use by geotechnical engineers;
4. experiments used for model calibration are the standard triaxial test and a hydrostatic compression test;
5. the initialization procedure is straightforward and can be carried out expeditiously;
6. varying degrees of sophistication can be achieved by adding model constants and by assuming numbers for, instead of rigorously calibrating, certain less-critical material parameters;

7. the model could predict reasonably accurately a wide variety of monotonic stress paths over a range of densities and sands of different genesis, and in its crudest form, it could also qualitatively simulate the more complicated type "A", type "B", and compression-extension stress paths of Tatsuoka & Ishihara (1974a, 1974b);
8. the model very precisely predicts the expansion of a cylindrical cavity, which, although not particularly complicated, is a boundary value problem of growing importance in soil mechanics;
9. satisfies the requirements of Drucker's postulate of stability in the small in the forward (or monotonic) sense, which contributes to computational stability;
10. an associative flow rule results in symmetric stiffness matrices in finite element calculations which are much more economical than the non-symmetric ones that emanate from non-assocative flow rules;
11. it is computationally economical and easy to implement since there is no need to keep track of the evolution of any so-called plastic internal variables (such platic volumetric strain, plastic work, etc.) during the deformation;
12. by using some straightforward modifications (which are familiar to those acquainted with the bounding surface concept), the theory can be set up to model (cyclic) hardening aspects of sand behavior; and
13. the consolidation yield surface can be easily modified to model anisotropic plastic flow as a deviation from normality to the "isotropic" yield surface using the method suggested by Dafalias (1981).

CHAPTER 4

CONCLUSIONS AND RECOMMENDATIONS

4.1 Introduction

A number of extremely important developments and conclusions were obtained from both the analytical and the laboratory study reported herein. The experimental investigation will be presented first, since it had a significant influence on the theoretical work as well as any planned future development.

4.2 Laboratory Results

Basically, besides the hollow cylinder data of Saada (1985), the University of Florida conducted three separate series of triaxial tests on the identical sand and initial conditions as was performed by Saada (1985). The tests encompassed: cyclic hydrostatic compression, cyclic conventional triaxial compression (CTC) experiments with different initial cell pressures and deviatoric loads, and special triaxial tests which involved both extension and compression loading.

Based on the monotonic hydrostatic response it was realized that for appreciable monotonic mean pressure increases, Reid Bedford sand developed an isotropic strain field, whereas in cyclic loading the sand exhibited significant stress-induced anisotropy. It was also discovered in the course of this study that the magnitude of strains measured with the conventional burette shaft displacement measuring system were on the same order as those associated with membrane penetration effects. Since the local DCDT monitoring system spanned the soil grains, resulting in little, if any membrane

penetration problems, it was believed to be a better monitoring system than the conventional approach.

From the conventional triaxial stress paths, a number of stress-strain-strength characteristics of Reid Bedford sand were gleaned. First, a comparison of the CTC response which involved prior hydrostatic compression with virgin monotonic loading, revealed that prior loading of a hydrostatic nature induced only minor anisotropic strain influences. However, cyclic CTC loading induced both alterations in the strain rate directions and the strength. These latter changes were associated with the rearrangement of the soil fabric, i.e., densification - volumetric compression. Secondly, the conventional triaxial tests which involved a combination of different axial stress levels and initial cell pressures on the same specimen resulted in the information that both the virgin and reloading stress-strain characteristics, if normalized with respect to the initial mean stress, are quite similar. Finally, the latter series of tests also suggested that the assumption of the yield surface being attached to the stress state is not a bad first approach, i.e., the plastic modulus on reloading is similar to its virgin counterpart.

Based on a special series of triaxial tests performed to replicate the hollow cylinder representation of a passing moving wheel, comes some of the most startling results. In a comparison of a triaxial test which reproduces the magnitudes of the principal stresses of a moving wheel versus a conventional cyclic compression test, it was observed that the standard cyclic CTC exhibited more permanent axial strains, but less volumetric strains than the triaxial version of the moving wheel. This difference was attributed to the fabric rearrangement, in particular the densification due to particle rotation and sliding in the latter test over its former counterpart. Also, the smaller permanent axial strains generated in the special test compared to

those obtained in the conventional cyclic CTC were associated with the denser fabric in the case of the former over the latter. A study of Ishihara's (1983) correlation of a hollow cylinder representation of a moving wheel with the conventional cyclic CTC on Toyoura sand reveals similar conclusions: significant fabric rearrangement is occurring (particle sliding, rotating, volumetric compression) in the case of the former over the latter. However, contrary to the previous study (see Section 1.3.3), Ishihara's study showed not only less permanent volumetric strains, but significantly less axial strains for the conventional CTC experiment compared to those measured in the hollow cylinder representation (a factor of three). This response was attributed to the fact that when all the fabric rearrangement was occurring in the hollow cylinder representation of a moving wheel, the axial loads were also increasing, whereas the previous study (see Section 1.3.3), they were either constant or decreasing. In light of the above study, the representation of a moving wheel stress path within a triaxial device is not recommended.

In a study of Saada's hollow cylinder experimental investigation of the stress-strain-strength characteristics of Reid Bedford sand incorporating rotation of principal planes (see Chapter 3), a number of very important observations were noted. A correlation of strength measured in the hollow cylinder device to a number of past proposed strength envelopes (Lade, Matsuoka, etc.), Table 3.5, revealed that in all instances the experimental hollow cylinder results were significantly different than the proposed strength criteria (a strength criteria which was developed from true triaxial experiments). Moreover in the hollow cylinder test, as the principal planes rotated, significant amounts of volumetric compression was occurring, and in most instances exceeded the peak values recorded in the conventional tests

(CTC). Correlation of CTC results to true triaxial results at different Lode angles (see Chapter 2) for Ottawa sand at a recent Workshop, "Limit Equilibrium, Plasticity and Generalized Stress-Strain In Geotechnical Engineering" (Yong et. al., 1980), revealed that there was almost an order of magnitude less volumetric compression if the Lode angle (see Chapter Two) were to be rotated away from vertical. Given the above results, it is a belief of the investigators that significant amounts of fabric structure change are occurring in the case of the hollow cylinder tests over and above what possibly could occur in a true triaxial device. Moreover, it is suggested that this fabric rearrangement is associated not as much with stress path and/or anistropy, but with the applied stress tractions (shear stresses in particular).

The above conclusions raises an interesting question as to the significance of anisotropy. If a soil specimen which was subject to a stress traction resulting in a particular rotation of principal planes in a hollow cylinder device, was tested at the same principal stresses in a true triaxial device and gave dissimilar stress-strain-strength response as the hollow cylinder test, should it be attributed to anisotropy or to the particulate nature of the material? In the truest sense, anisotropy effects are those associated with the rotation of the material reference under a given set of boundary tractions. The above testing scenario does not meet this criteria, and to the investigators' knowledge there does not presently exist a series of experimental tests which address this problem. However, it is the opinion of the investigators that the application of shear tractions on the boundary will alter the soil's fabric more significantly than any rotation of the material reference (anisotropy); consequently there is a distinct possibility that

soil, sand in particular, may not be feasible to characterize as a continuum, i.e., it violates the Principle of Material Frame Indifference (Objectivity). (See Section 2.1).

From all of the above discussions, it is concluded that there is a significant need for laboratory experimentation to probe the influence of anisotropy and boundary tractions, independently of one another, for various rotated principal directions. The former should be undertaken in a cubical triaxial device and the latter with hollow cylinder equipment. Also, it is extremely important that an experimental program be initiated to investigate the influence of boundary tractions on a soil's fabric (in particular a photoelastic study of micro stresses, particle sliding, rotation, etc.).

4.3 Theoretical Results

Judging from its performance in predicting response for numerous stress paths, its intrinsic features, and its relative simplicity, the proposed constitutive model for granular material does seem to be an attractive new approach. With regard to its effectiveness in predicting stress paths, the following conclusions are drawn:

1. The representation predicted remarkably well a comprehensive series of axial compression paths over a wide range of densities and confinement pressures (data from Hettler et. al., 1984). This attests to the rationality of the formulation in two respects: a) the density dependence of the material parameters, and b) the pressure sensitivity of the material response. The remaining data sets test the rationale for its extension to more general paths of loading.
2. Very realistic simulations were generated for a wide variety of linear monotonic stress paths emanating from a fixed point on the

hydrostatic axis (data from Saada et. al., 1983, and Chapter 1). From this particular test series, it was noted that further laboratory investigation of the influence of boundary tractions versus anistropy is warranted.

3. The pressuremeter simulation showed that the model performs sensibly along a stress path which in general non-linear and non-proportional and which rotates on the octahedral plane (data from Davidson, 1983). However, it should be recognized that the principal plane rotation are those associated with changing normal stresses not shear tractions.

4. The stress paths of Tatsuoka and Ishihara (1974a, 1974b) demonstrated, primarily in a qualitative sense, the realistic aspects of the simple representation for the relatively complicated load-unload-reload loading programs shown in Figure 3.36. The simple model, with no hardening, appears to be particularly appropriate for reloading paths in which the direction of the shear stress is completely reversed (data from Tatsuoka and Ishihara, 1974b). Quantitatively, the calculated stress-strain curves are about 15% stiffer than the measured data. The source of this problem is the one-parameter from the interpolation rule used to model the decrease of the plastic modulus from its bulk modulus magnitude on the hydrostatic axis to zero at the limit line.

5. Using some straightforward hardening modifications. the flexibility of the formulation was illustrated by predicting: a) the influence of istropic preloading on a subsequent axial compression path (data from Hettler et. al., 1984), and b) the accumulation of permanent

strain (or cyclic hardening) in a cyclic uniaxial compression test (data from Chapter 1).

From a practical viewpoint, the model is conceptually easy to understand and to implement, and it is also very economical from the computational standpoint. Its parsimony is a direct consequence of:

1. the use of a stress dependent plastic modulus, which marks a break in the trend of placing the consistency condition central to the determination of the plastic modulus;
2. permitting the material to remain at yield during unloading;
3. hypothesizing that no change in state is a useful first approximation for sand;
4. using an infinitesimal strain definition of yield instead of the traditional offset or Taylor-Quinney (1931) definition; and
5. according independent status to the yield surface, the limit surface, and the hardening control surface.

A number of factors dealing with the material constants also lend credibility to the proposal, and among these are:

1. the ability to correlate each constitutive parameter to one of the "fundamental" geotechnical parameters;
2. the dependence of each parameter only on the initial porosity, as should be expected for sands; and
3. the straightforward initialization procedure which, because of the implicit linear mena pressure normalization necessitates only input data from two standard experiments: an axial compression test and a hydrostatic compression test.

Despite the many positive comments, the seriousness of the model's limitations remain to be probed, and many avenues of research and possible

improvements are still to be explored. The main issues presented in order of importance, are:

1. How significant are the differences associated with boundary tractions and those associated with anisotropy. Moreover, it is possible to characterize the soil's fabric alterations through the boundary tractions. This is a necessity, if one plans on representing the hollow cylinder behavior with the true triaxial response, even if one has accounted for anisotropy. It may be possible to keep tract of the latter's influence through a second order phenomenological fabric tensor. However, the former is only possible if a micro mechanical fabric study is undertaken.
2. Presently, little is known on influence of cyclic loading on the alteration of the soil's fabric. For instance, is strength and plastic flow significantly altered? The preliminary study in Chapter 1 for cyclic CTC data does show appreciable variations. Moreover, how can such influences be incorporated into the simple model? Maybe the same second order fabric tensor discussed above.
3. How serious is the limitation of Figure 3.61 showing the range of stress increments which can penetrate the limit surface as elastic unloading or neutral loading paths? What class of practical problems (if any) will it affect? And if it does prove to be a major drawback, how can it be circumvented or corrected? With the theory in its present form, a check should be included in finite element applications to detect the possibility of stress points straying into the forbidden zone outside the limit surface.

In a less general context, many other aspects of the model may be improved; for example:

1. A more complicated interpolation rule may be selected for the field of plastic moduli to simulate stress-strain curves in which the plastic modulus decreases more rapidly below the zero dilation line.
2. Degradation effects as well as a stress path memory variable to monitor the degree of stress reversal may also be used to improve the hardening option. If one follows the approach used in this study, these variables will only influence the plastic modulus.

LIST OF REFERENCES

Aboim, C.A., and W. H. Roth. "Bounding-Surface Plasticity Theory Applied to Cyclic Loading of Sand." In International Symposium on Numerical Methods in Geomechanics, (held in Zurich, Switzerland, 13-17 September, 1982), edited by R. Dungar, G. N. Pande, and J. A. Studer. P. O. Box 1675, 3000 BR Rotterdam, Netherlands: A. A. Balkema, 1982.

Akivis, M. A., and V. V. Goldenberg. An Introduction to Linear Algebra and Tensors. Translated and edited by R. A. Silverman. 180 Varick Street, New York, N.Y.: Dover Publications, Inc., 1972.

Al-Hussaini, M. M. and F. C. Townsend. Investigation of K_o Testing in Cohesionless Soils. Technical Report S-75-16, Vicksburg, Mississippi: Soils and Pavements Laboratory, U. S. Army Engineers Waterways Experiment Station, 1975.

Anandarajah, A., Y. F. Dafalias, and L. R. Hermann. "A Bounding Surface Plasticity Model for Anisotropic Clays." In Proceedings of the ASCE Fifth Engineering Mechanics Divison Speciality Conference, (held in Laramie, Wyoming, 1-3 August, 1984), edited by A. P. Boresi and K. P. Chong. 345 East 47th Street, New York, N.Y.: American Society of Civil Engineers (ASCE), 1984.

Baltov, A., and A. Sawczuk. "A Rule of Anisotropic Hardening." Acta Mechanica, Vol. 1, No. 2 (1965): 81-92.

Bauschinger, J. "Ueber die Veraenderunge.. der Elasticitaetsgrenze von Eisen und Stahl." Dingler's Polytechnisches Journal, Vol. 266 (1887): 216-220.

Beyer, W. H., Editor. CRC Standard Mathematical Tables. 26th Edition. Boca Raton, Florida: CRC Press, Inc., 1981.

Bishop, A. W. "The Strength of Soils as Engineering Materials." Geotechnique, Vol. 16, No. 2 (June, 1966): 91-128.

Bishop, A. W., and D. J. Henkel. The Measurement of Soil Properties in the Triaxial Test. London, U.K.: William Arnold, 1975.

Boyce, J. R., (1983) "Measurement of Stress and Strain During Repeated Load Triaxial Tests on a Crushed Rock," UROMECH 157 - Quality of Mechanical Observations on Particulate Media.

Bridgman, P. W., "Flow and Fracture." Transactions of the American Institute of Mining, Metallurgical, and Petroleum Engineers (AIME), Iron and Steel Division, Vol. 162 (1945): 569-583.

Bristol Industries & Research Associates, Ltd. Non-Contact Measurements P. O. Box 2, Portishead, Bristol BS20, 9JB.

Brown, S. F. "Repeated Load Testing of a Granular Material." Journal of the Geotechnical Engineering Division, ASCE, Vol. 100, No. GT7 (July, 1974): 825-841.

Cambou, B. "Orientational Distributions of Contact Forces as Memory Parameters in a Granular Material." In IUTAM Conference on Deformation and Failure of Granular Materials, (held in Delft, Netherlands, 31 Aug. - 3 Sept., 1982), edited by P. A. Vermeer and H. J. Luger. P. O. Box 1675, 3000 BR Rotterdam, Netherlands: A. A. Balkema, 1982.

Casagrande, A. "The Determination of the Preconsolidation Load and Its Practical Significance." In Proceedings First International Conference on Soil Mechanics and Foundation Engineering, Vol. III, (June 22-26, 1936) Cambridge, Massachusetts: Graduate School of Engineering, Harvard University, 1936.

Casagrande, A., and N. Carillo. "Shear Failure of Anisotropic Materials." Journal of the Boston Society of Civil Engineers, Vol. 31 (1944): 74-87.

Cherian, T. V., P. Pietrokowsky, and J. E. Dorn. "Some Observations on the Recovery of Cold Worked Aluminum." Transactions of the American Institute of Mining, Metallurgical, and Petroleum Engineers (AIME), Iron and Steel Division, Vol. 185 (1949): 948-956.

Clough, R. W., and R. J. Woodard, III. "Analysis of Embankment Stresses and Deformations." Journal of Soil Mechanics and Foundation Engineering, ASCE, Vol. 93, No. SM4 (July, 1967): 529-549.

Coulomb, C. A. "Essai sur une application des regles de maximis et minimis a quelques problemes de statique, relatifs a l'architecture." Memoires de Mathematique et de Physique, presentes a l'Academie Royale des Sciences, par divers savans, & lus dan ses assemblees, Vol. 7 (1773): 343-382.

Cowin, S. C. "Microstructural Continuum Models for Granular Materials." In Proceedings of the U.S. - Japan Seminar on Continuum Mechanical and Statistical Approaches in the Mechanics of Granular Materials, (held in Sendai, Japan, June 5-9, 1978), edited by S. C. Cowin and M. Satake. Gakujutsu Bunken Fukyukai, Tokyo, Japan: The Kajima Foundation, 1978.

Cowin, S. C., and M. Satake, Editors. Proceedings of the U. S. - Japan Seminar on Continuum Mechanical and Statistical Approaches in the Mechanics of Granular Materials (held in Sendai Japan, June 5-9, 1978), Gakujutsu Bunken Fukyukai, Tokyo, Japan: The Kajima Foundation, 1978.

Dafalias, Y. F. "Initial and Induced Anistropy of Cohesive Soils by Means of a Varying Non-Associated Flow Rule." In Proceedings sur Le Comportement Plastique des Solides Anisotropes, Colloque International du C.N.R.S. No. 319, Villard-de-Lans, France: N. P., 1981.

Dafalias, Y. F. "Modelling Cyclic Plasticity: Simplicity Versus Sophistication ." Mechanics of Engineering Materials, edited by C. S. Desai and R. H. Gallagher. New York, N. Y.: John Wiley & Sons Ltd., 1984.

Dafalias, Y. F., and E. P. Popov. "A Model of Nonlinearly Hardening Materials for Complex Loadings." Acta Mechanica, Vol. 21 (1975): 173-192.

Dafalas, Y. F., and E. P. Popov. "Cyclic Loading for Materials With a Vanishing Elastic Region." Nuclear Engineering and Design, Vol. 41 (1977): 293-302.

Dafalias, Y. F., and L. R. Herrmann. "A Bounding Surface Soil Plasticity Model." In Proceedings of the International Symposium on Soils Under Cyclic and Transient Loading, (held in Swansea, Wales, 7-11 January, 1980), edited by G. N. Pande and O. C. Zienkiewicz. P. O. Box 1675, 3000 BR Rotterdam, Netherlands: A. A. Balkema, 1980.

Davidson, J. L. "Self-Boring Pressuremeter Testing in Sand in the University of Florida Calibration Chamber." Final Report, EIES Project No. 245*W516, Gainesville, Florida: Department of Civil Engineering, University of Florida, 1983.

Davis, R. O., and G. Mullenger. "A Rate-Type Constitutive Model for Granular Media with a Critical State." International Journal of Numerical and Analytical Methods in Geomechanics, Vol. 12 (1978): 255-282.

Desai, C. S. "A General Basis for Yield, Failure and Potential Functions in Plasticity." International Journal of Numerical and Analytical Methods in Geomechanics, Vol. 4 (1980): 361-375.

Desai, C. S., and H. J. Siriwardane. " A Concept of Correction Functions to Account for Non-associative Characteristics of Geologic Media." International Journal of Numerical and Analytical Methods in Geomechanics. Vol. 4 (1980): 377-387.

Desai, C. S. and R. H. Gallagher, Editors. International Conference on Constitutive Laws for Engineering Materials (Theory and Applications), (held in Tucson, Arizona, January 10-14, 1983), published in book form as Mechanics of Engineering Materials. New York, N. Y.: John Wiley & Sons, 1984.

Desai, C. S., and H. J. Siriwardane. Constitutive Laws For Engineering Materials With Emphasis On Geologic Mateials. Englewood Cliffs, New Jersey: Prentice-Hall Inc., 1984.

DiMaggio, F. L., and I. S. Sandler. "Material Models for Granular Soils." Journal of the Engineering Mechanics Division, ASCE, Vol. 97, No. EM3 (1971): 936-950.

Drucker, D. C. "Stress-Strain Relations in the Plastic Range - a Survey of Theory and Experiment." Office of Naval Research (ONR) Technical Report, Contract N7-onr-358, Providence, Rhode Island: Graduate Division of Applied Mathematics, Brown University, 1950a.

Drucker, D. S. "Some Implications of Work-Hardening and Ideal Plasticity." Quarterly of Applied Mechanics, Vol. 7 (1950b): 411-418.

AD-A173 976 GENERALIZED PHENOMENOLOGICAL CYCLIC STRESS-STRAIN-STRENGTH CHARACTERIZATI (U) FLORIDA UNIV GAINESVILLE DEPT OF CIVIL ENGINEERING M C MCVAY ET AL. 4/4

UNCLASSIFIED 02 SEP 84 AFOSR-TR-86-0918 AFOSR-84-0108 F/G 8/13 NL

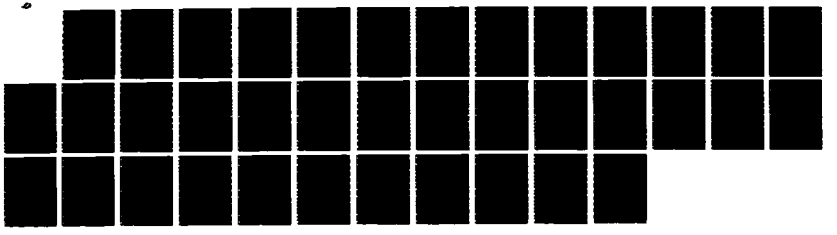

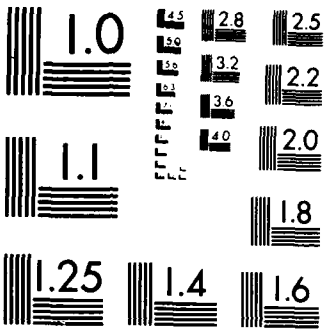

MICROCOPY RESOLUTION TEST CHART
NATIONAL BUREAU OF STANDARDS-1963-A

Drucker, D. C. "A More Fundamental Approach to Stress-Strain Relations." In Proceedings of the 1st U. S. National Congress for Applied Mechanics, ASME (1951): 487-491.

Drucker, D. C. "Coulomb Friction, Plasticity, and Limit Loads." Journal of Applied Mechanics, Vol. 21, No. 4 (1954): 71-74.

Drucker, D. C. "On Uniqueness in the Theory of Plasticity." Quarterly of Applied Mathematics, Vol. 14, No. 1 (1956): 35.42.

Drucker, D. C. "Plasticity." In First Symposium on Naval Structural Mechanics, Report C11-41, Providence, Rhode Island: Division of Applied Mathematics, Brown University, 1958.

Drucker, D. C. "Concept of Path Independence and Material Stability for Soils." In Proceedings of the IUTAM Symposium on Rheology and Mechanics of Soils, (held in Grenoble, France), edited by J. Kravtchenko and P. M. Sirieys Berlin, Germany: Springer, 1966.

Drucker, D. C. and W. Prager. "Soil Mechanics and Plastic Analysis or Limit Design." Quarterly of Applied Mathematics, Vol. 10, No. 157 (1952): 157-165.

Drucker, D. C., R. E. Gibson, and D. J. Henkel. "Soil Mechanics and Work-Hardening Theories of Plasticity." ASCE Transactions, Paper No. 2864, Vol. 22 (1957): 338-346.

Drucker, D. C., and L. Palgen. "On Stress-Strain Relations Suitable for Cyclic and Other Loading." Journal of Applied Mechanics, Vol. 48 (September, 1981): 479-485.

Drucker, D. C., and D. Seereeram. "Remaining at Yield During Unloading and Other Unconventional Elastic-plastic Response." Journal of Applied Mechanics, submitted for publication, 1986.

Duncan, J. M., and C. Y. Chang. "Non-linear Analysis of Stress and Strain in Soils." Journal of Soil Mechanics and Foundation Engineering, ASCE, Vol. 96, No. SM5 (September 1970): 1629-1653.

Eisenberg, M. A. "A Generalization of Plastic Flow Theory With Application to Cyclic Hardening and Softening Phenomena." Journal of Engineering Materials and Technology, ASME, Vol. 98 (July, 1976): 221-228.

Eringen, A. C. Nonlinear Theory of Continuous Media. New York, N. Y.: McGraw-Hill, Inc., 1962.

Gerrard, G. M. "Background to Mathematical Modelling in Geomechanics: The Role of Fabric and Stress History." Chapter 2 in Finite Elements in Geomechanics, edited by G. Gudehus. London, England: John Wiley & Sons Ltd., 1977.

Ghaboussi, J., and H. Momen. "Modelling and Analysis of Cyclic Behaviour of Sands." Chapter 12 in Soil Mechanics - Transient and Cyclic Loads, edited by G. N. Pande and O. C. Zienkiewicz. Chichester, England: John Wiley & Sons Ltd., 1982.

Girijavallabhan, C. V., and L. C. Reese. "Finite Element Method Applied to Some Problems in Soil Mechanics." Journal of Soil Mechanics and Foundation Engineering, ASCE, Vol. 94, No. SM2 (March, 1968): 473-496.

Goldscheider, M. "True Triaxial Tests on Dense Sand" In Results of the International Workshop on Constitutive Relations for Soils, (held in Grenoble, France, 6-8 September, 1982), edited by G. Gudehus, F. Darve, and I. Vardoulakis. P. O. Box 1675, 3000 BR Rotterdam, Netherlands: A. A. Balkema, 1984.

Goodman, M. A., and S. C. Cowin. "A Continuum Theory for Granular Materials." Archive for Rational Mechanics and Analysis, Vol. 44 (1972): 321-339.

Gudehus, G. "Gedanken zur Statistischen Boden Mechanik." Baningenieur, Vol. 43 (1968): 320-326.

Gudehus, G. "Elastoplastische Stoffgleichugen fur trockener Sand." Ingenieur Archiv., Vol. 42 (1973): 151-169.

Gudehus, G., and F. Darve, Editors International Workshop on the Constitutive Behavior of Soils, (Grenoble, 6th - 8th September, 1982), P. O. Box 1675, 3000 BR Rotterdam, Netherlands.: A. A. Balkema, 1984.

Habib, P., and M. P. Luong. "Cohesionless Soils Under Cyclic Loadings." In Materiaux et Structures sous Chargement Cyclique, Palaiseau, France: Association Amicale des Ingenierur Anciens Eleves de l'Ecole Nationale des Ponts et Chausses, 1978.

Hartmann, J. P., and J. H. Schmertmann. "FEM Study of Elastic Phase of Pressuremeter Test." In Proceedings of the ASCE Specialty Conference on Insitu Testing, Vol. 1, pp. 190-207. 345 East 47th Street, New York, N. Y.: American Society of Civil Engineers (ASCE), 1975.

Hay, G. E. Vector and Tensor Analysis. 180 Varick Street, New York, N. Y.: Dover Publications, Inc., 1953.

Herceg, E.E., (1985) Handbook of Measurement and Control, Schaevitz Engineering, Pennsauken, N. J. pp. 3-14.

Hettler, A., I. Vardoulakis, and G. Gudehus. "Stress-Strain Behavior of Sand in Triaxial Test." In Results of the International Workshop on Constitutive Relations for Soils, (held in Grenoble, France, 6-8 September, 1982), edited by G. Gudehus, F. Darve, and I. Vardoulakis. P. O. Box 1675, 3000 BR Rotterdam, Netherlands: A. A. Balkema, 1984.

Hill, R. The Mathematical Theory of Plasticity. Ely House, London: Oxford University Press, 1950.

Horne, M. R. "The Behavior of an Assembly of Rotund, Rigid, Cohesionless Particles (I & II)." Proceedings of the Royal Society of London, Vol. 286 (1964): 62-97.

Hughes, J. M. O., Wroth, C. P., and Windle, D. "Pressuremeter Tests in Sands." Geotechnique, Vol. 27, No. 4 (1977): 455-477.

Hughes, T. J. R., and J. H. Prevost. "DIRT II -- A Nonlinear Quasi-Static Finite Element Analysis Program." Pasadena, California: California Institute of Technology. 1979.

Ishihara, K., "Soil Response in Cyclic Loading Induced by Earthquakes, Traffic and Waves." Lecture presented to the 7th Asian Regional Conference on Soil Mechanics and Foundation Engineering, Haifa, Israel, August, 1983.

Ishihara, K., F. Tatsuoka, and S. Yasuda. "Undrained Deformation and Liquefaction of Sand Under Cyclic Stresses." Soils and Foundations, Vol. 15, No. 1 (1975): 29-44.

Ivey, H. J. "Plastic Stress-Strain Relations and Yield Surfaces for Aluminum Alloys." Journal of Mechanical Engineering Sciences, Vol. 3 (1961): 15-31.

Iwan, W. S. "On a Class of Models for the Yielding Behavior of Continuous and Composite Systems." Journal of Applied Mechanics, Trans. ASME, Vol. 89, Series E (1967): 612-617.

Jain, S. K. Fundamental Aspects of the Normality Rule. P. O. Box 302, Blacksburg, Virginia: Engineering Publication, 1980.

Jamal, A. K. "Triaxial Extension Tests on Hollow Cylinder Sand Specimens." Canadian Geotechnical Journal, Vol. 8, No. 1 (February, 1971): 119-133.

Janbu, N. "Soil Compressibility as Determined by Oedometer and Triaxial Tests." European Conference on Soil Mechanics and Foundation Engineering, Wiesbaden, German, Vol. 1 (1963): 19-25.

Jaunzemis, W. Continuum Mechanics. 866 Third Ave., New York, N. Y.: Macmillan Publishing Co., Inc., 1967.

Kirkpatrick, W. M. "Discussion on Soil Properties and their Measurement." In Proceedings 5th International Conference on Soil Mechanics, Vol. III, (17-22 July, 1961) Paris, France: Dunod, 1962

Ko, H. Y., and S. Sture. "State of the Art: Data Reduction and Application for Analytical Modeling." In Proceedings of the Symposium on Laboratory Shear Strength of Soil, (held in Chicago, Illinois, 25 June, 1980), edited by R. N. Yong and F. C. Townsend. 1916 Race Street, Philadelphia, Pa.: ASTM STP 740, 1980.

Krieg, R. D. "A Practical Two-Surface Plasticity Theory." Journal of Applied Mechanics, Transactions ASME, Vol. 42, Series E (1975): 641-646.

Linton, P. F. "A Study of a Sand in the Standard Triaxial Chamber Equipped With a Computerized Data Acquisition System." Master's Thesis, Department of Civil Engineering, University of Florida, Gainesville, Florida, May, 1986.

Lode, W. "Versuche ueber den Einfluss der mittleren Hauptspannung auf das Fliessen der Metalle Eisen, Kupfer, und Nickel." Zeitschrift fur Physik. Vol. 36 (1926): 913-939.

Loret, B. "On the Choice of Elastic Parameters for Sand." Short Communications, International Journal for Numerical and Analytical Methods in Geomechanics, Vol. 9, No. 3 (1985): 285-292.

Lubliner, J. A. "A Simple Theory of Plasticity." International Journal of Solids and Structures. Vol. 10 (1974): 313-319.

Luong, M. P. "Stress-Strain Aspects of Cohesionless Soils Under Cyclic and Transient Loading." In Proceedings of the International Symposium on Soils Under Cyclic and Transient Loading, (held in Swansea, Wales, 7-11 January, 1980), edited by G. N. Pande and O. C. Zienkiewicz. P. O. Box 1675, 3000 BR Rotterdam, Netherlands: A. A. Balkema, 1980.

Malvern, L. E. Introduction to the Mechanics of a Continuous Medium. Englewood Cliffs, New Jersey: Prentice Hall Inc., 1969.

Matsuoka, H.. and T. Nakai. "Stress-Deformation and Strength Characteristics of Soil Under Three Different Principal Stresses." Proceedings of the Japanese Society of Civil Engineers, Vol. 232 (1974): 59-70.

Melan, E. "Zur Plastizitaet des raeumlichen Kontinuums." Ingenieur Archiv., Vol. 9 (1938): 116-126.

von Mises, R. "Mechanik der plastischen Formaenderung von Kristallen." Zeitschrift fur Angewandte Mathematik und Mechanik, Vol. 8 (1928): 161-185.

Mould, J. C., S. Sture, and H. Y. Ko. "Modeling of Elastic-Plastic Anistropic Hardening and Rotating Principal Stress Directions in Sand." In IUTAM Conference on Deformation and Failure of Granular Materials, (held in Delft, Netherlands, 31 Aug.-3 Sept., 1982), edited by P. A. Vermeer and H. J. Luger. P. O. Box 1675, 3000 BR Rotterdam, Netherlands: A. A. Balkema, 1982.

Mroz, Z. "On The Description of Anistropic Work Hardeing." Journal of Mechanics and Physics of Solids, Vol. 15 (1967): 163-175.

Mroz, Z. "On Isotropic Hardening Constitutive Models in Soil Mechanics." In Results of the International Workshop on Constitutive Relations for Soils. (held in Grenoble, France, 6-8 September, 1982), edited by G. Gudehus, F. Darve, and I. Vardoulakis. P. O. box 1675, 3000 BR Rotterdam, Netherlands: A. A. Balkema, 1984.

Mroz, Z., and V. A. Norris. "Elastoplastic and Viscoplastic Constitutive Models for Soils with Application to Cyclic Loading." Soil Mechanics - Transient and Cyclic Loads, edited by G. N. Pande and O. C. Zienkiewicz. New York, N. Y.: John Wiley & Sons, 1982.

Naghdi, P. M. "Stress-Strain Relations in Plasticity and Thermoplasticity." In Plasticity, Proceedings of the 2nd Symposium on Naval Structural Mechanics, edited by E. H. Lee and P. S. Symonds. Oxford, England: Pergamon Press, 1960.

Naghdi, P. M., F. Essenburg, and W. Koff. "An Experimental Study of Initial and Subsequent Yield Surfaces in Plasticity." Journal of Applied Mechanics, Vol. 25 (1958): 201-209.

Nayak, G. C., and O. C. Zienkiewicz. "Convenient Form of Stress Invariants for Plasticity." Journal of the Structural Division, ASCE, Vol. 98, No. ST4 (April, 1972): 949-954.

Nemat Nasser, S. "On Dynamic and Static Behaviour of Granular Materials." Soil Mechanics - Transient and Cyclic Loads, edited by G. N. Pande and O. C. Zienkiewicz. New York, N. Y.: John Wiley & Sons, 1982.

Nemat-Nasser, S., and M. M. Mehrabadi. "Micromechanically Based Rate Constitutive Descriptions for Granular Materials." Chapter 23 in Mechanics of Engineering Materials, edited by C. S. Desai and R. H. Gallagher. New York, N. Y.: John Wiley & Sons, 1984.

Nova, R., and D. M. Wood. "A Constitutive Model for Sand in Traixial Compression." International Journal for Numerical and Analytical Methods in Geomechanics, Vol. 3 (1979): 255-278.

Oda, M. "The Mechanism of Fabric Change During Compressional Deformation of Sand." Soils and Foundations, Vol. 12, No. 2 (June, 1972): 1-18.

Oda, M. "Fabric Tensor for Discontinuous Geological Materials." Soils and Foundations, Vol. 22, No. 4 (December, 1982): 96-108.

Oda, M., J. Konishi, and S. Nemat-Nesser. "Some Experimentally Based Fundamental Results on the Mechanical Behaviour of Granular Materials." Geotechnique, Vol. 30, No. 4 (1980): 479-495.

Odqvist, F. K. G. "Die Verfestigung von flusseisenaehnlichen Koerpern." Zeitschrift fur Angewandte Mathematik und Mechanik, Vol. 13 (1933): 360-363.

Pande, G. N., and O. C. Zienkiewicz, Editors. Proceedings of the International Symposium on Soils Under Cyclic and Transient Loading, (held in Swansea, Wales, 7-11 January, 1980). P. O. Box 1675, 3000 BR Rotterdam, Netherlands: A. A. Balkema, 1980.

Parkin, A. K., C. M. Gerrard, and D. R. Willoughby. "Discussion on Deformation of Sand in Hydrostatic Compression." Journal of Soil Mechanics and Foundation Engineering, ASCE, Vol. 94, No. SM1 (1968): 336-340.

Phillips, A., and G. J. Weng. "An Analytical Study of an Experimentally Verified Hardening Law." Journal of Applied Mechanics, Transactions ASME, Vol. 42, No. 2, Series E (1975): 375-378.

Pietrusczak, St., and Z. Mroz. "On Hardening Anisotropy of K_o Consolidated Clays." International Journal for Numerical and Analytical Methods in Geomechanics, Vol. 7 (1983): 19-38.

Podgorski, J. "General Failure Criterion for Isotropic Media." Journal of Engineering Mechanics, ASCE, Vol. 111, No. 2 (February 1985): 188-201.

Poorooshasb, H. B., I. Holubec, and A. N. Sherbourne. "Yielding and Flow of Sand in Triaxial Compression: Part I." Canadian Geotechnical Journal, Vol III, No. 4 (November 1966): 179-190.

Poorooshasb, H. B., I. Holubec, and A. N. Sherbourne. "Yielding and Flow of Sand in Triaxial Compression: Parts II and III." Canadian Geotechnical Journal, Vol. IV, No. 4 (November 1967): 376-397.

Poorooshasb, H. B., R. N. Yong, and B. Lelievre. "Anisotropic Hardening Yield Locii for Sand." In IUTAM Conference on Deformation and Failure of Granular Materials, (held in Delft, Netherlands, 31 Aug.-3 Sept., 1982), edited by P. A. Vermeer and H. J. Luger. P. O. Box 1675, 3000 BR Rotterdam, Netherlands: A. A. Balkema, 1982.

Prager, W. "Recent Developments in the Mathematical Theory of Plasticity." Journal of Applied Physics, Vol. 20, No. 3 (March, 1949): 235-241.

Prager, W., "The Theory of Plasticity: A Survey of Recent Achievements." In Proceedings of the Institution of Mechanical Engineers, (James Clayton Lecture), Vol. 169, No. 21 (1955): 41-57.

Prevost, J. H. "Plasticity Theory for Soil Stress-Strain Behavior." Journal of the Engineering Mechanics Division, ASCE, Vol. 104, No. EM5 (October, 1978): 1177-1194.

Prevost, J. H. "Nonlinear Anisotropic Stress-Strain-Strength Behaviour of Soils." In Proceedings of the Symposium on Laboratory Shear Strength of Soil, (held in Chicago, Illinois, 25 June, 1980 , edited by R. N. Yong and F. C. Townsend. 1916 Race Street, Philadelphia, Pa.: ASTM STP 740, 1980.

Romano, M. "A Continuum Theory for Granular Media with a Critical State." Archive for Rational Mechanics and Analysis, Vol. 26 (1974): 1011-1028.

Roscoe, K. H., and J. B. Burland. "On the Generalized Stress-Strain Behavious of 'Wet' Clay." In Engineering Plasticity, edited by J. Heyman and F. A. Leckie. Bentley House, P. O. Box 92, 200 Euston Road, London: Cambridge University Press, 1968.

Rowe, P. W. "The Stress-Dilatancy Relation for Static Equilibrium of an Assembly of Particles in Contact." Proceedings of the Royal Society of London, Vol. 269 (1962): 500-527.

Saada, A. S., (1985) Personnal communication.

Saada, A. S. and F. C. Townsend. "State of the Art: Laboratory Strength Testing of Soils." In Proceedings of the Symposium on Laboratory Shear Strength of Soil, (held in Chicago, Illinois, 25 June, 1980), edited by R. N. Yong and F. C. Townsend. 1916 Race Street, Philadelphia, Pa.: ASTM STP 740, 1980.

Saada, A. S., G. Bianchi and P. Puccini. "The Mechanical Properties of Anisotropic Granular Soils." In Colloque International du C.N.R.S. No. 351. Grenoble, France: N. P., 1983.

Saleeb, A. F., and W. F. Chen. "Nonlinear Hyperelastic (Green) Constitutive Models for Soils: Theory and Calibration." In Proceedings of the Workshop on Limit Equilibrium, Plasticity and Generalized Stress-Strain in Geotechnical Engineering, (held in Montreal, Canada, 28-30 May, 1980), edited by R. N. Yong and H. Y. Ko. 345 East 47th Street, New York, N. Y.: American Society of Civil Engineers (ASCE), 1984.

Salkind, M. October 23, 1984 (Comments from Air Force Office of Scientific Research). Personal Correspondence.

Sandler, I. S., F. L. DiMagio, and G. Y. Baladi. "Generalized Cap Model for Geologic Materials." Journal of the Geotechnical Engineering Division, ASCE, Vol. 102, No. GT7 (July, 1976): 683-699.

Satake, M. "Constitution of Mechanics of Granular Materials through the Graph Theory." In Proceedings of the U. S. - Japan Seminar on Continuum Mechanical and Statistical Approaches in the Mechanics of Granular Materials, (held in Sendai, Japan, June 5-9, 1978), edited by S. C. Cowin and M. Satake. Gakujutsu Bunken Fukyukai, Tokyo, Japan: The Kajima Foundation, 1978.

Schmidt, R. "Ueber den Zusammenhang von Spannungen und Formaenderungen im Verfestigungsarbeit." Ingenieur Archiv., Vol. 3 (1932): 215-235.

Schofield, A., and C. P. Wroth. Critical State Soil Mechanics. London: McGraw-Hill, 1968.

Scott, R. F. "Plasticity and Constitutive Relations in Soil Mechanics." 19th Terzaghi Lecture, Journal of Geotechnical Engineering, ASCE, Vol. 111, No. 5 (May, 1985): 563-605.

Seereeram, D., M. C. McVay, and P. F. Linton. "Generalized Phenomenological Cyclic Stress-Strain-Strength Characterization of Anisotropic Granular Media." Annual Report, Grant No. AFOSR-84-0108, Gainesville, Florida: Department of Civil Engineering, Division of Soil Mechanics, University of Florida 1985.

Shield, R. T. "On Coulomb's law of Failure in Soils." Journal of Mechanics and Physics of Solids, Vol. 4 (1955): 10-10.

Sture, S., J. C. Mould, and H. Y. Ko. "Elastic-Plastic Anisotropic Hardening Constitutive Model and Prediction of Behavior for Dry Quartz Sand." In Results of the International Workshop on Constitutive Relations for Soils, (held in Grenoble, France, 6-8 September, 1982), edited by G. Gudehus, F. Darve, and I. Vardoulakis. P. O. Box 1675, 3000 BR Rotterdam, Netherlands: A. A. Balkema, 1984.

Synge, J. L., and A. Schild. Tensor Calculus. Toronto, Canada: University of Toronto Press, 1949.

Tatsuoka, F. "A Fundamental Study on the Deformation of a Sand by Triaxial Tests." Doctoral Dissertation (in Japanese), Department of Civil Engineering, University of Tokyo, Bunkyo-ku, Tokyo 113, Japan, 1972.

Tatsuoka, F., and K. Ishihara. "Yielding of Sand in Triaxial Compression." Soils and Foundations, Vol. 14, No. 2 (1974a): 63-76.

Tatsuoka, F., and K. Ishihara. "Drained Deformation of Sand Under Cyclic Stresses Reversing Directions." Soils and Foundations, Vol. 14, No. 3 (1974b): 51-65.

Taylor, G. I., and H. Quinney. "The Plastic Distortion of Metals." Philosophical Transactions of the Royal Society (London) ser. A, Vol. 230 (1931): 323-362.

Tresca, H. "Memoire sur l'ecoulement des corps solides soumisa de fortes pressions." Comptes Rendus hebdomadaires des seances de l'Academie des Sciences (Paris) Vol. 59 (1864): 754-760.

Truesdell, C. "Hypoelasticity." Archive for Rational Mechanics and Analysis, Vol. 4 (1955): 83-133.

Vermeer, P. A. and H. J. Luger, Editors. IUTAM Conference on Deformation and Failure of Granular Materials, (held in Delft, Netherlands, 31 Aug.-3 Sept., 1982). P. O. Box 1675, 3000 BR Rotterdam, Netherlands: A. A. Balkema, 1982.

Wiedemann, G. "Ueber die Torsion, die Biegung und den Magnetismus." Verhandlungen der naturforschenden Gesselschaft in Basel, Vol. II (1860): 168-247.

William, K. J., and E. P. Warnke. "Constitutive Model for the Triaxial Behavior of Concrete." In Proceedings of the International Association of Bridges and Structural Engineers Seminar on Concrete Structures Subjected to Triaxial Stresses. Bergamo, Italy: N. P., 1974.

Wrede, R. C. Introduction to Vector and Tensor Analysis. 180 Varick Street, New York, N. Y.: Dover Publications, Inc., 1972.

Wu, T. H., A. K. Loh, and L. E. Malvern. "Study of the Failure Envelope of Soils." Proceedings of the American Society of Civil Engineers, Vol. 89, No. SM1 (1963): 145-181.

Wylie, C. R., and L. C. Barrett. Advanced Engineering Mathematics. New York, N. Y.: McGraw-Hill Book Co., 1982.

Yong, J. E., (1974) The New Science of Skin and Scuba Diving, Follett Publishing Company, pg. 26.

Yong, R. N., and H. Y. Ko, Editors. Workshop on Limit Equilibrium, Plasticity and Generalized Stress-Strain in Geotechnical Engineering, (held in Montreal, Canada, 28-30 May, 1980). 345 East 47th Street, New York, N. Y.: American Society of Civil Engineers (ASCE), 1980a.

Yong, R. N., and H. Y. Ko. "Soil Constitutive Relationships and Modelling of Soil Behavior." In Workshop on Limit Equilibrium, Plasticity and Generalized Stress-Strain in Geotechnical Engineering, (held in Montreal, Canada, 28-30 May, 1980), edited by R. N. Yong and H. Y. Ko. 345 East 47th Street, New York, N. Y.: American Society of Civil Engineers (ASCE), 1980b.

Ziegler, H. "A Modification of Prager's Hardening Rule." Quarterly of Applied Mathematics, Vol. 17, No. 1 (1959): 55-65.

Zienkiewicz, O. C., and Z. Mroz. "Generalized Plasticity Formulation and Applications to Geomechanics." Chapter 33 in Mechanics of Engineering Materials, edited by C. S. Desai and R. H. Gallagher. New York, N. Y.: John Wiley & Sons, 1984.

APPENDIX A

DERIVATION OF ANALYTICAL REPRESENTATION OF THE DILATION PORTION OF THE YIELD SURFACE

Start by considering the following general seçond order equation (defined for convenience in an arbitrary rectangular Cartesian x-y coordinate system) to which the relevant constraints shall be subsequently applied:

$$F = a\,x^2 + b\,y^2 + c\,xy + d\,y + e\,x + f = 0\ . \qquad (A.1)$$

As a first step, equation A.1 can be divided by the coefficient of x^2, "a", and then the constants can be renamed such that b = b/a, c = c/a, etc.; this algebraic operation results in

$$F = x^2 + b\,y^2 + c\,xy + d\,y + e\,x + f = 0\ . \qquad (A.2)$$

Inserting the stress invariant variables in place of x and y in equation A.2 yields

$$F = I_1^2 + b\,J_2^* + c\,I_1\sqrt{J_2^*} + d\,\sqrt{J_2^*} + e\,I_1 + f = 0\ . \qquad (A.3)$$

Equation A.3 is now subjected to four consecutive constraints to ensure that the function is continuous with the ellipse and satisfies certain boundary stipulations.

Constraint #1: F = 0 at $I_1 = \sqrt{J_2^*} = 0$; this implies that the constant f is equal to zero, and as a result, equation A.3 reduces to

$$F = I_1^2 + b\,J_2^* + c\,I_1\sqrt{J_2^*} + d\,\sqrt{J_2^*} + e\,I_1 = 0\ . \qquad (A.4)$$

Constraint #2: at $I_1 = \sqrt{J_2^*} = 0$, $d\sqrt{J_2^*}/dI_1 = S$, and this condition establishes that

$$d\sqrt{J_2}^*/dI_1 = -\partial F/\partial I_1 + \partial F/\partial\sqrt{J_2}^*$$

$$= -(2I_1 + c\sqrt{J_2}^* + e) + (2b\sqrt{J_2}^* + cI_1 + d) = S,$$

from which we see

$$e = -S\,d \quad . \tag{A.5}$$

Substitution of equation A.5 into equation A.4 gives

$$F = I_1^2 + b J_2^* + c I_1\sqrt{J_2}^* + d\sqrt{J_2}^* - S\,d\,I_1 = 0 \quad . \tag{A.6}$$

Constraint #3: at $I_1 = (I_0/Q)$, $\sqrt{J_2}^* = N(I_0/Q)$. Substituting this information into equation A.6 shows that

$$d = (I_0/Q)[1 + bN^2 + cN] + [S - N] \quad . \tag{A.7}$$

And now we can substitute A.7 into equation A.6 to obtain

$$F = I_1^2 + b J_2^* + c I_1\sqrt{J_2}^* + (I_0/Q)\frac{[1 + bN^2 + cN]}{[S - N]}\{\sqrt{J_2}^* - S I_1\} \quad . \tag{A.8}$$

Constraint #4: at the zero dilation point $[I_1 = I_0/Q,\ \sqrt{J_2}^* = N(I_0/Q)]$,

$$d\sqrt{J_2}^*/dI_1 = -\partial F/\partial I_1 + \partial F/\partial\sqrt{J_2}^* = 0 \ ,$$

which implies that $\partial F/\partial I_1 = 0$. Using these requirements in equation A.8 results in

$$2 I_1 + c\sqrt{J_2}^* - S(I_0/Q)\frac{[1 + bN^2 + cN]}{[S - N]} = 0 \ ,$$

from which we then see that

$$c = (S/N^2) - (2/N) - S\,b \quad . \tag{A.9}$$

Finally, the substitution of equation A.9 into equation A.8 gives the following expression for the yield surface characterizing the meridional section between the limit line and the zero dilation line:

$$F = I_1^2 + b J_2^* + \left[\frac{S}{N^2} - \frac{2}{N} - Sb\right] I_1\sqrt{J_2}^* + (I_0/Q)\left[\frac{1}{N} - bN\right]\{\sqrt{J_2}^* - S I_1\} = 0 \quad . \tag{A.10}$$

After exhausting all available constraints, inspection of equation A.10 reveals that we have eliminated all but one independent parameter (i.e., "b") from the original set (i.e., "a", "b", "c", "d", "e", & "f"). The slope S is usually fixed at a magnitude of 1.5.

Range of the parameter "b"

Following the standard procedure outlined by Beyer (1981, p. 250), the restrictions on the parameter b are investigated by looking at how its magnitude affects the nature of the graph of this quadratic in I_1 and $\sqrt{J_2^*}$. Table A.1 gives the details of the general procedure. For the particular function derived here, equation A.10,

$$\Delta = -\frac{1}{4}(I_o/Q)^2 \left(\frac{1}{N} - bN\right)^2 \left(\frac{S}{N} - 1\right)^2 ,$$

$$J = b - \frac{1}{4}\left[\frac{S}{N^2} - \frac{2}{N} - Sb\right]^2 ,$$

$$I = 1 + b \quad , \text{ and}$$

$$K = -(1 + S^2)\frac{1}{4}(I_o/Q)^2 \left(\frac{1}{N} - bN\right)^2 .$$

From these equations, we see that

$$b = \left(\frac{1}{N} - \frac{2}{S}\right)^2 \qquad (A.11)$$

identifies a parabolic conic section. Magnitudes of b greater than that specified by equation A.11 gives ellipses and those smaller than this magnitude give hyperbolas. Furthermore, to ensure that $\Delta \neq 0$, b must not be exactly equal to $\frac{1}{N^2}$. In fact, if $b = \frac{1}{N^2}$ the quadratic equation degenerates to case 9 of Table A.1 to give the equation of the zero dilation line $\sqrt{J_2^*}/I_1 = N$. As $b \to -\infty$, the equation of the yield surface, equation A.10, simplifies to

Table A.1 Formulas for Use in Inspecting the Nature of the Quadratic Function Describing the Dilation Portion of the Yield Surface

General quadratic in x and y: $ax^2 + 2hxy + by^2 + 2gx + 2fy + c = 0$

Definitions: $\Delta = a(bc - f^2) - h(hc - gf) + g(hf - bg)$
$J = ab - h^2$
$I = a + b$
$K = ac - g^2 + bc - f^2$

CASE	Δ	J	Δ/I	K	CONIC
1	$\neq 0$	> 0	< 0		real ellipse
2	$\neq 0$	> 0	> 0		imaginary ellipse
3	$\neq 0$	< 0			hyperbola
4	$\neq 0$	0			parabola
5	0	< 0			real intersecting lines
6	0	> 0			conjugate complex intersecting lines
7	0	0		< 0	real distinct parallel lines
8	0	0		> 0	conjugate complex parallel lines
9	0	0		0	coincident lines

Source: Beyer, 1981

$$F = J_2^* - S\, I_1 \sqrt{J_2^*} - (I_0/Q)\, N \{\sqrt{J_2^*} - S\, I_1\} = 0 ,$$

or alternatively,

$$F = (\sqrt{J_2^*} - S\, I_1)\, (\sqrt{J_2^*} - N\, \frac{I_0}{Q}) = 0,$$

which shows that it represents two straight line portions: the horizontal line $\sqrt{J_2^*} = N\, (I_0/Q)$ intersecting the line $\sqrt{J_2^*}/I_1 = S$. Therefore, from these two extreme cases, we see that the parameter b must lie in the range

$$-\infty < b < \frac{1}{N^2} . \qquad \text{(A.12)}$$

APPENDIX B

COMPUTATION OF THE GRADIENT TENSOR TO THE YIELD SURFACE

The gradient to the yield surface is

$$\frac{\partial F}{\partial \underline{\sigma}} = \frac{\partial F}{\partial I_1}\frac{dI_1}{d\underline{\sigma}} + \frac{\partial F}{\partial \sqrt{J_2}}\frac{d\sqrt{J_2}}{d\underline{\sigma}} + \frac{\partial F}{\partial \theta}\frac{d\theta}{d\underline{\sigma}} \quad , \tag{B.1}$$

where (cf. equation 2.2.2.33)

$$\sin 3\theta = \left[\frac{3\sqrt{3}}{2}\left(J_3/\sqrt{J_2}^3\right)\right] \quad . \tag{B.2}$$

From equation B.2 we find that

$$\frac{d\theta}{d\underline{\sigma}} = \frac{\sqrt{3}}{2\cos 3\theta}\left\{\frac{\partial J_3}{\partial \underline{\sigma}}\frac{1}{[\sqrt{J_2}]^3} - \frac{3J_3}{[\sqrt{J_2}]^4}\frac{\partial \sqrt{J_2}}{\partial \underline{\sigma}}\right\} \quad . \tag{B.3}$$

Substitution of equation B.3 into equation B.1 yields (in indicial notation)

$$\frac{\partial F}{\partial \sigma_{ij}} = \nabla \underline{F} = \frac{\partial F}{\partial I_1}\frac{\partial I_1}{\partial \sigma_{ij}} + \left\{\frac{\partial F}{\partial \sqrt{J_2}} - \frac{\sqrt{3}}{2\cos 3\theta}\frac{3J_3}{[\sqrt{J_2}]^4}\frac{\partial F}{\partial \theta}\right\}\frac{\partial \sqrt{J_2}}{\partial \sigma_{ij}} + \left\{\frac{\sqrt{3}}{2\cos 3\theta}\frac{1}{[\sqrt{J_2}]^3}\frac{\partial F}{\partial \theta}\right\}\frac{\partial J_3}{\partial \sigma_{ij}} \tag{B.4}$$

where

$$\frac{dI_1}{d\sigma_{ij}} = \delta_{ij} \tag{B.5}$$

$$\frac{d\sqrt{J_2}}{d\sigma_{ij}} = \frac{1}{2\sqrt{J_2}}s_{ij} \tag{B.6}$$

$$\frac{dJ_3}{d\sigma_{ij}} = \{a'_3\}^T + \frac{1}{3}J_2\,\delta_{ij} \tag{B.7}$$

and

$$\{a'_3\}^T = \{(s_{22}s_{33} - s_{23}^2),\ (s_{11}s_{33} - s_{13}^2),(s_{11}s_{22} - s_{12}^2),$$

$$(s_{23}s_{13} - s_{33}s_{12}),(s_{13}s_{12} - s_{11}s_{23}),(s_{12}s_{23} - s_{22}s_{13})\} \ .$$

In order to find the gradient tensor, we need therefore only to compute the partial derivatives $\frac{\partial F}{\partial I_3}$, $\frac{\partial F}{\partial \sqrt{J_2}}$, and $\frac{\partial F}{\partial \theta}$ of equations 3.3.3.1 and 3.3.4.1. We find from equation 3.3.3.1,

$$\frac{\partial F}{\partial I_3} = 2(I_3 - \frac{I_0}{Q}) \qquad (B.8)$$

$$\frac{\partial F}{\partial \sqrt{J_2}} = 2\ \frac{\{(Q-1)/N\}^2\ \sqrt{J_2}}{[g(\theta)]^2} \qquad (B.9)$$

and

$$\frac{\partial F}{\partial g(\theta)} = -\ 2\ \frac{\{(Q-1)/N\}^2\ J_2}{[g(\theta)]^3} \ . \qquad (B.10)$$

Also, from equation 3.3.1.8, recognize that

$$\frac{dg(\theta)}{d\theta} = \frac{6R\ (1-R)\ \cos 3\theta}{\{[1+R] - [1-R]\ \sin 3\theta\}^2} \qquad (B.11)$$

which is to be used in the following:

$$\frac{\partial F}{\partial \theta} = \frac{\partial F}{\partial g(\theta)}\ \frac{dg(\theta)}{d\theta} \ .$$

And for the more complicated choice of $g(\theta)$ (equation 3.3.1.6),

$$\frac{dg(\theta)}{d\theta} = \frac{v\ \frac{du}{d\theta} - u\ \frac{dv}{d\theta}}{v^2} \ , \qquad (B.12)$$

where

$$u = A\ (1-R^2) + (2R-1)\ \sqrt{[(2+B)\ (1-R^2) + 5R^2 - 4R]},$$

$$v = (1-2R)^2 + 2(1-R^2) + B(1-R^2) \ ,$$

$$\frac{du}{d\theta} = (1-R^2)\ \frac{dA}{d\theta} + \frac{1}{2}\ \frac{(2R-1)\ (1-R^2)\ \frac{dB}{d\theta}}{\sqrt{[(2+B)(1-R^2) + 5R^2 - 4R]}} \ ,$$

$$\frac{dv}{d\theta} = (1-R^2)\ \frac{dB}{d\theta} \ ,$$

$$A = \sqrt{3}\ \cos\theta - \sin\theta \ ,$$

$$B = \cos 2\theta - \sqrt{3}\sin 2\theta ,$$

$$\frac{dA}{d\theta} = -\sqrt{3}\sin\theta - \cos\theta ,$$

and

$$\frac{dB}{d\theta} = -2\sin 2\theta - 2\sqrt{3}\cos 2\theta .$$

Similarly, from equation 3.3.4.1, we find that

$$\frac{\partial F}{\partial I_1} = 2 I_1 + \left[\frac{S}{N^2} - \frac{2}{N} - Sb\right]\sqrt{J_2}\,\frac{1}{[g(\theta)]} - (I_0/Q)\left[\frac{1}{N} - bN\right] S \qquad (B.13)$$

$$\frac{\partial F}{\partial \sqrt{J_2}} = 2\,\frac{b}{[g(\theta)]^2}\sqrt{J_2} + \left[\frac{S}{N^2} - \frac{2}{N} - Sb\right] I_1\,\frac{1}{[g(\theta)]} + (I_0/Q)\left[\frac{1}{N} - bN\right]\frac{1}{[g(\theta)]} , \qquad (B.14)$$

and

$$\frac{\partial F}{\partial g(\theta)} = -\frac{2b}{[g(\theta)]^3} J_2 - \left[\frac{S}{N^2} - \frac{2}{N} - Sb\right] I_1\sqrt{J_2}\,\frac{1}{[g(\theta)]^2} - (I_0/Q)\left[\frac{1}{N} - bN\right]\frac{1}{[g(\theta)]^2}\sqrt{J_2} . \qquad (B.15)$$

APPENDIX C

EQUATIONS FOR UPDATING THE SIZE OF THE YIELD SURFACE

When the stress state resides on the consolidation portion of the surface (i.e., when $\frac{\sqrt{J_2^*}}{I_1} \leq N$),

$$I_0 = \max \left\{ \frac{-B_1 \pm \sqrt{(B_1^2 - 4 A_1 C_1)}}{2 A_1} \right\} \quad \text{if } Q > 2 \qquad (C.1)$$

$$= -C_1/B_1 \quad \text{if } Q = 2 \qquad (C.2)$$

$$= \min \left\{ \frac{-B_1 \pm \sqrt{(B_1^2 - 4 A_1 C_1)}}{2 A_1} \right\} \quad \text{if } Q < 2 \qquad (C.3)$$

where

$$A_1 = \frac{2}{Q} - 1 \ ,$$

$$B_1 = -2 I_1/Q \ ,$$

and

$$C_1 = I_1^2 + \frac{(Q-1)^2}{N^2} J_2^* \ .$$

For the dilation portion of the yield surface, when $\frac{\sqrt{J_2^*}}{I_1} > N$, we have

$$I_0 = -\frac{D_1}{E_1} \ , \qquad (C.4)$$

where

$$D_2 = I_1^2 + b J_2^* + \left[\frac{S}{N^2} - \frac{2}{N} - Sb\right] I_1 \sqrt{J_2^*} ,$$

and

$$E_2 = \frac{1}{Q}\left(\frac{1}{N} - bN\right)\left(\sqrt{J_2^*} - SI_1\right) .$$

APPENDIX D

PREDICTION OF HOLLOW CYLINDER TESTS USING PROPOSED MODEL

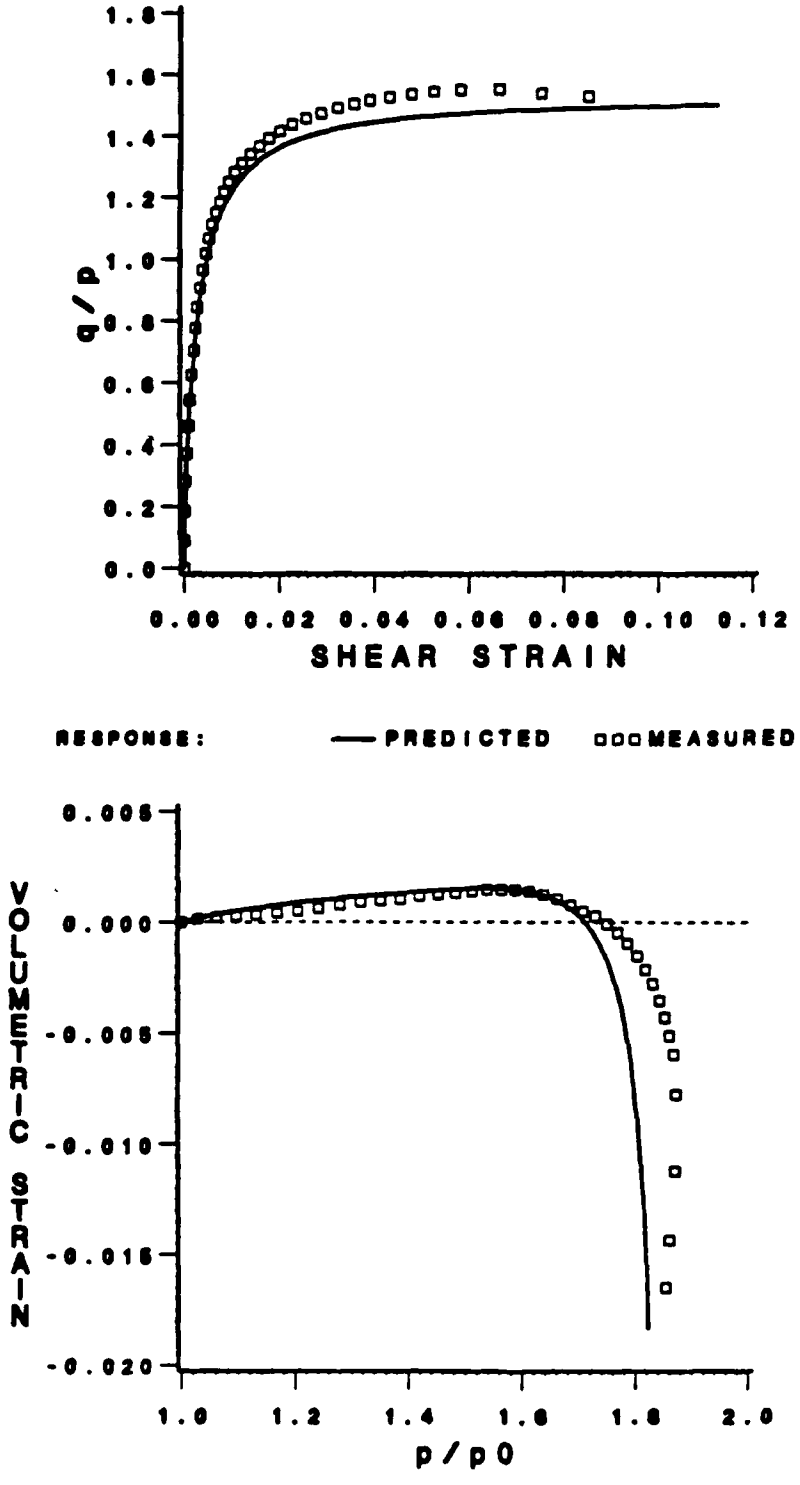

Figure D.1 Measured vs. predicted stress-strain response for DCR 15 stress path using proposed model

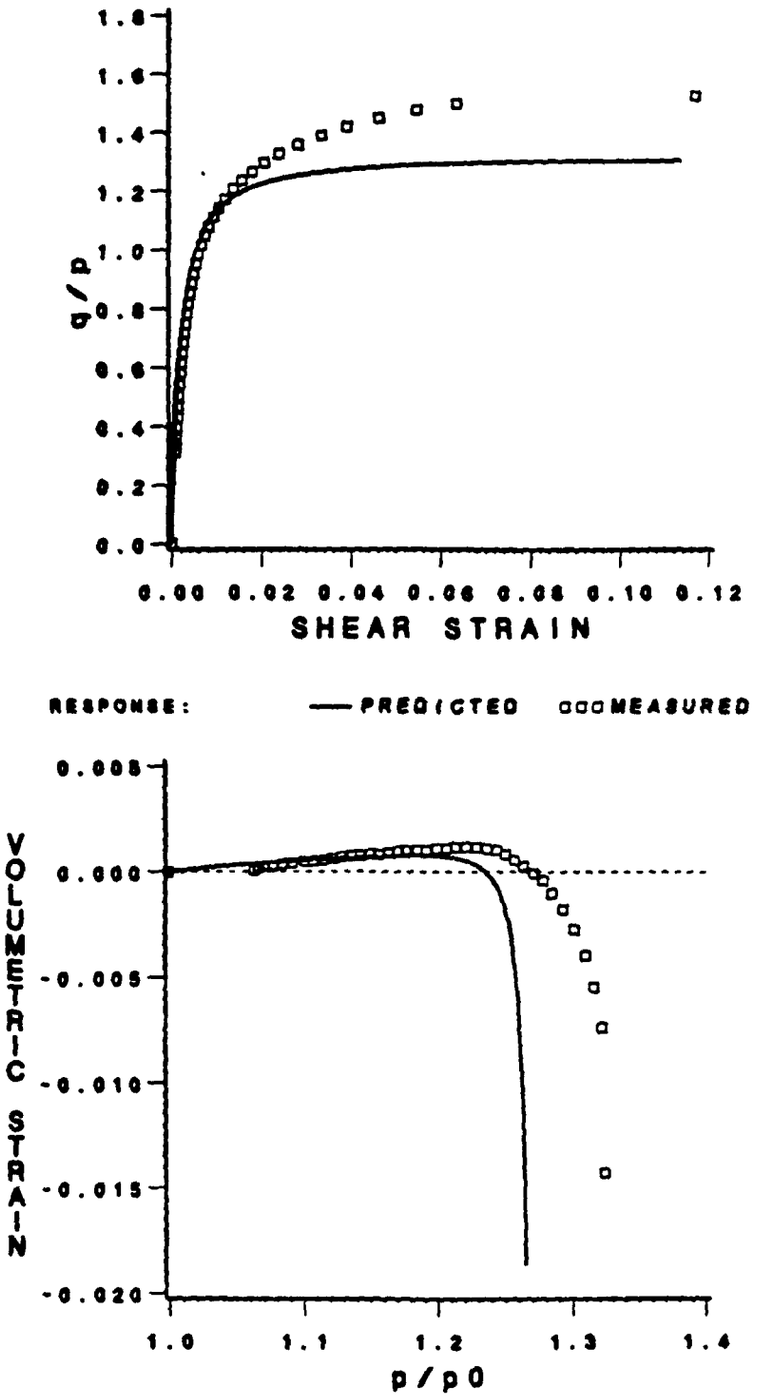

Figure D.2 Measured vs. predicted stress-strain response for DCR 32 stress path using proposed model

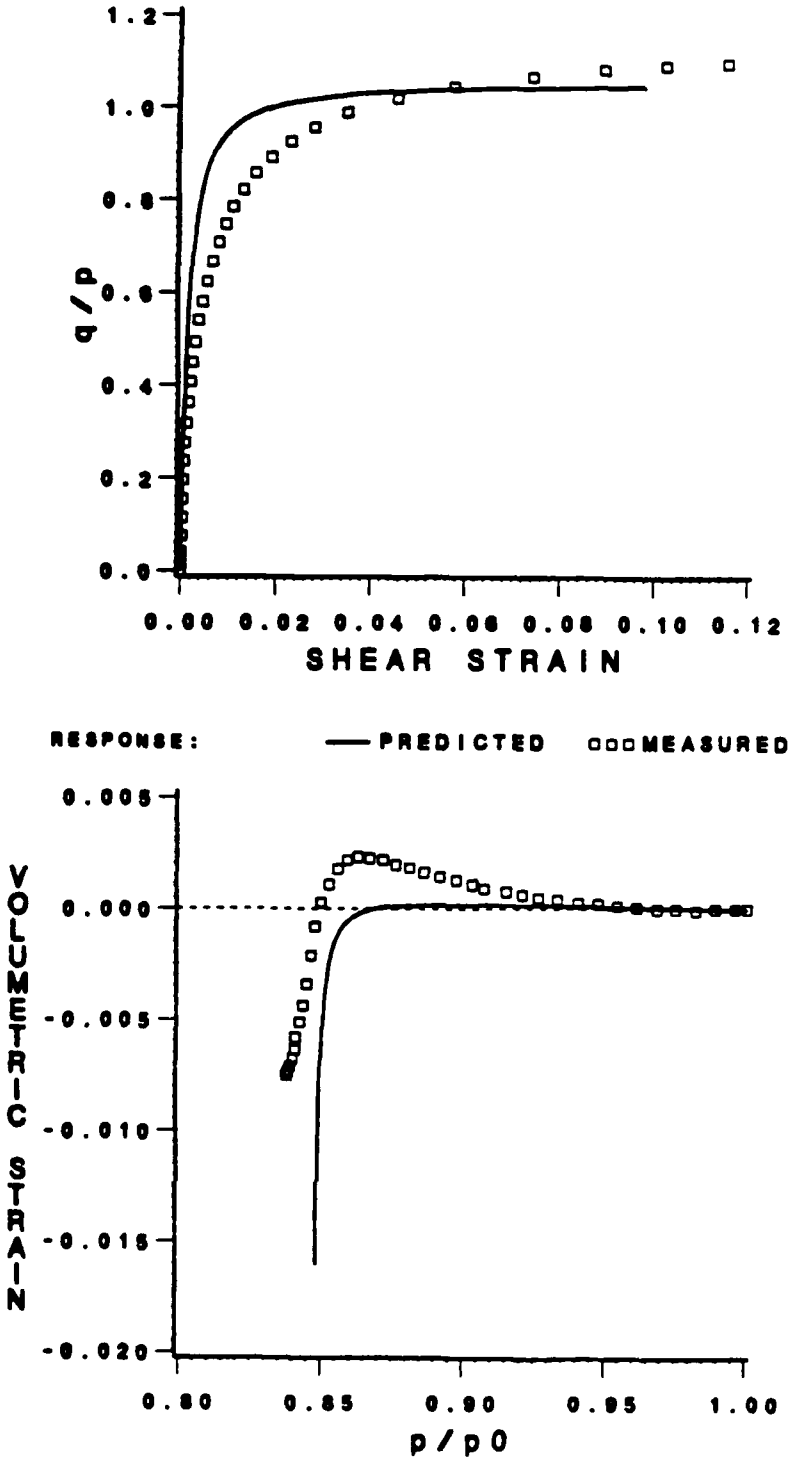

Figure D.3 Measured vs. predicted stress-strain response for DTR 58 stress path using proposed model

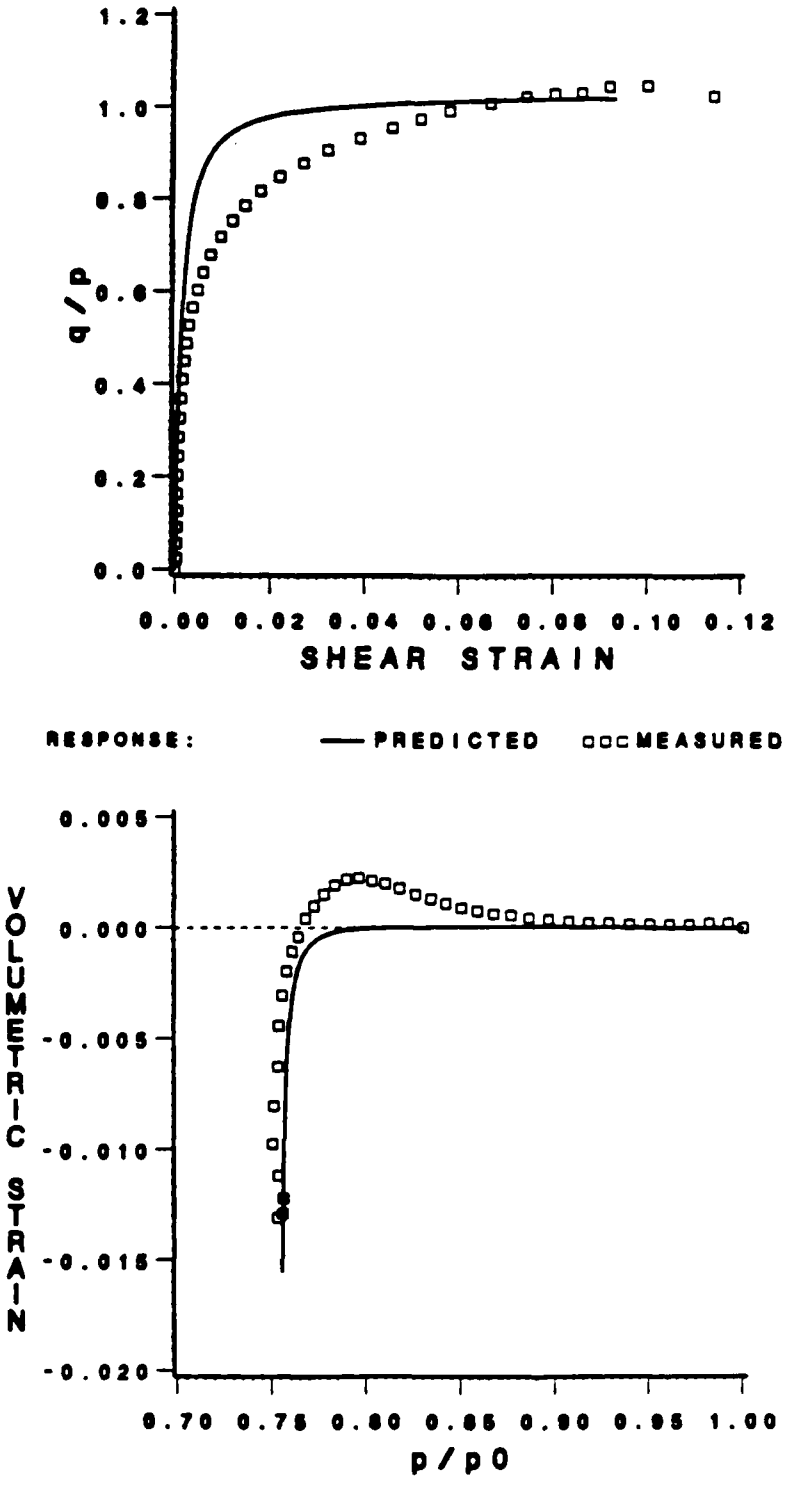

Figure D.4 Measured vs. predicted stress-strain response for DTR 75 stress path using proposed model

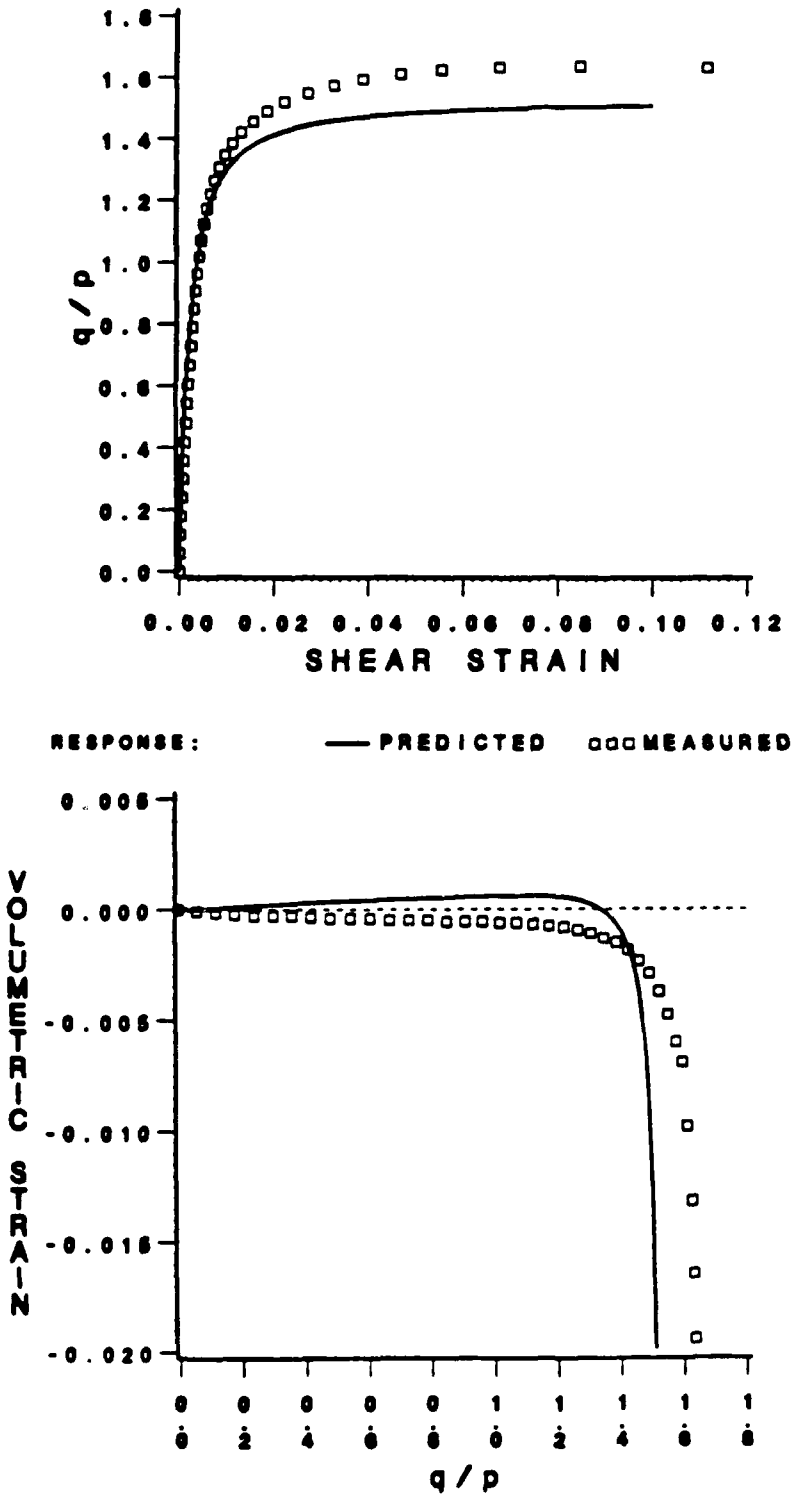

Figure D.5 Measured vs. predicted stress-strain response for GCR 15 stress path using proposed model

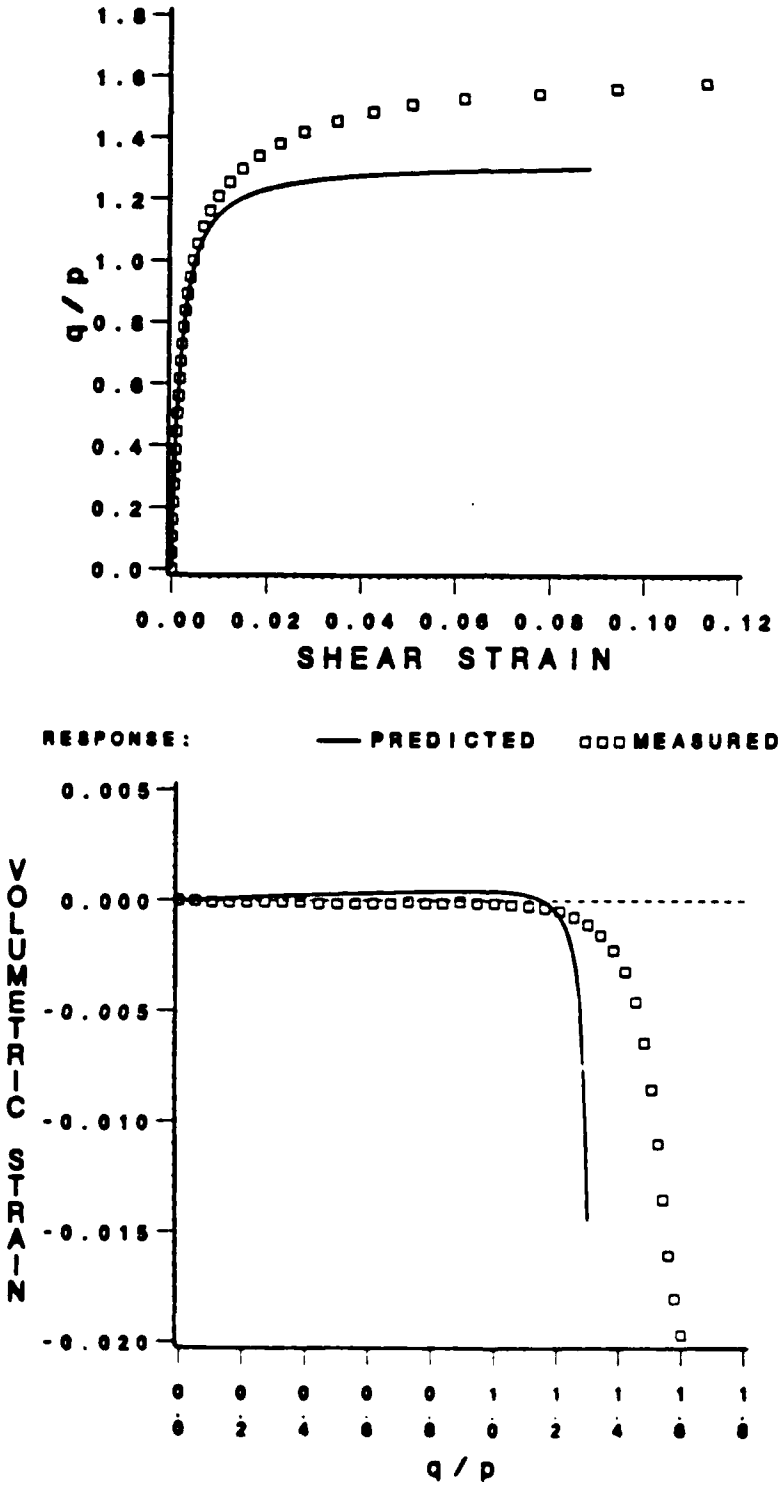

Figure D.6 Measured vs. predicted stress-strain response for GCP 32 stress path using proposed model

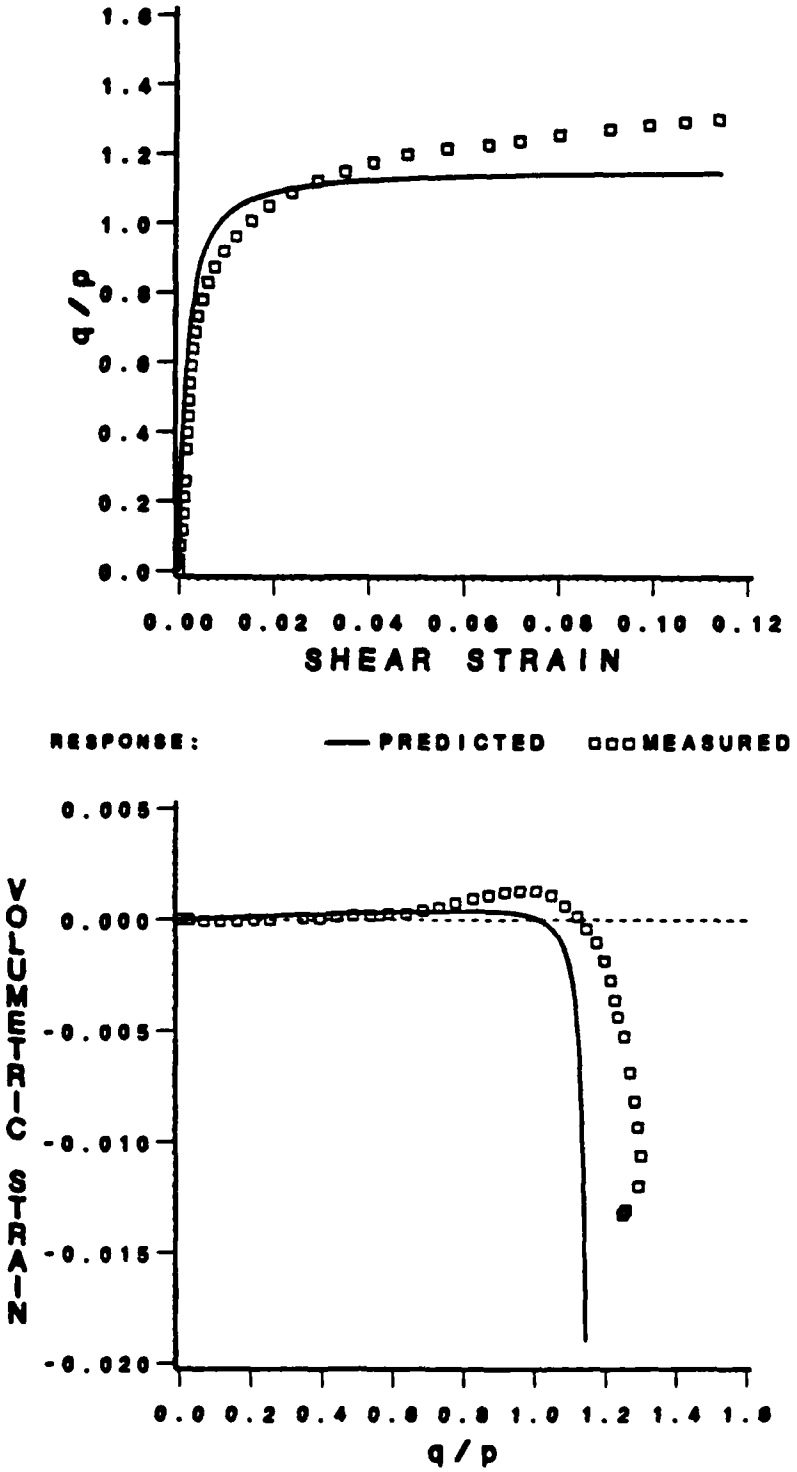

Figure D.7 Measured vs. predicted stress-strain response for R 45 (or pure torsion) stress path using proposed model

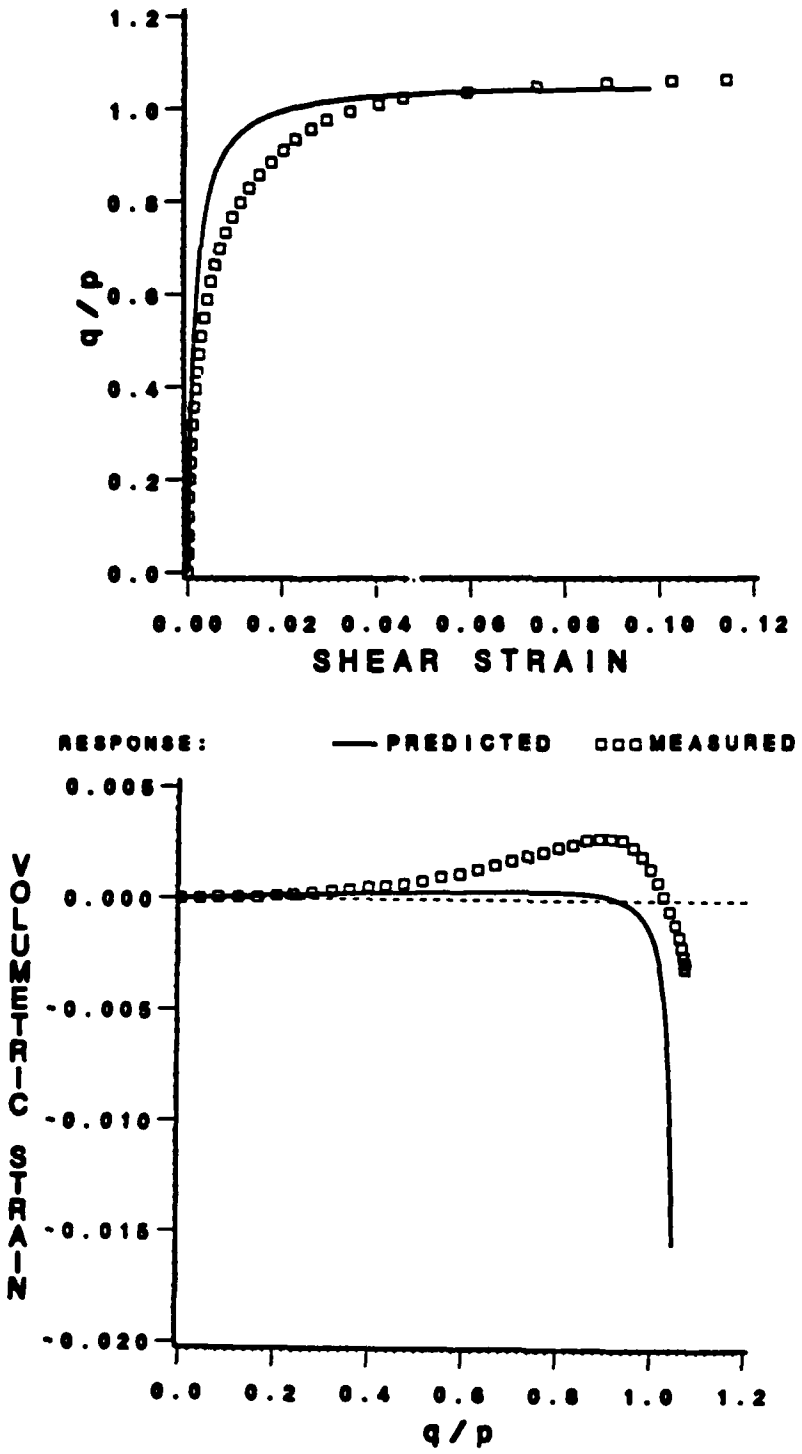

Figure D.8 Measured vs. predicted stress-strain response for GTR 58 stress path using proposed model

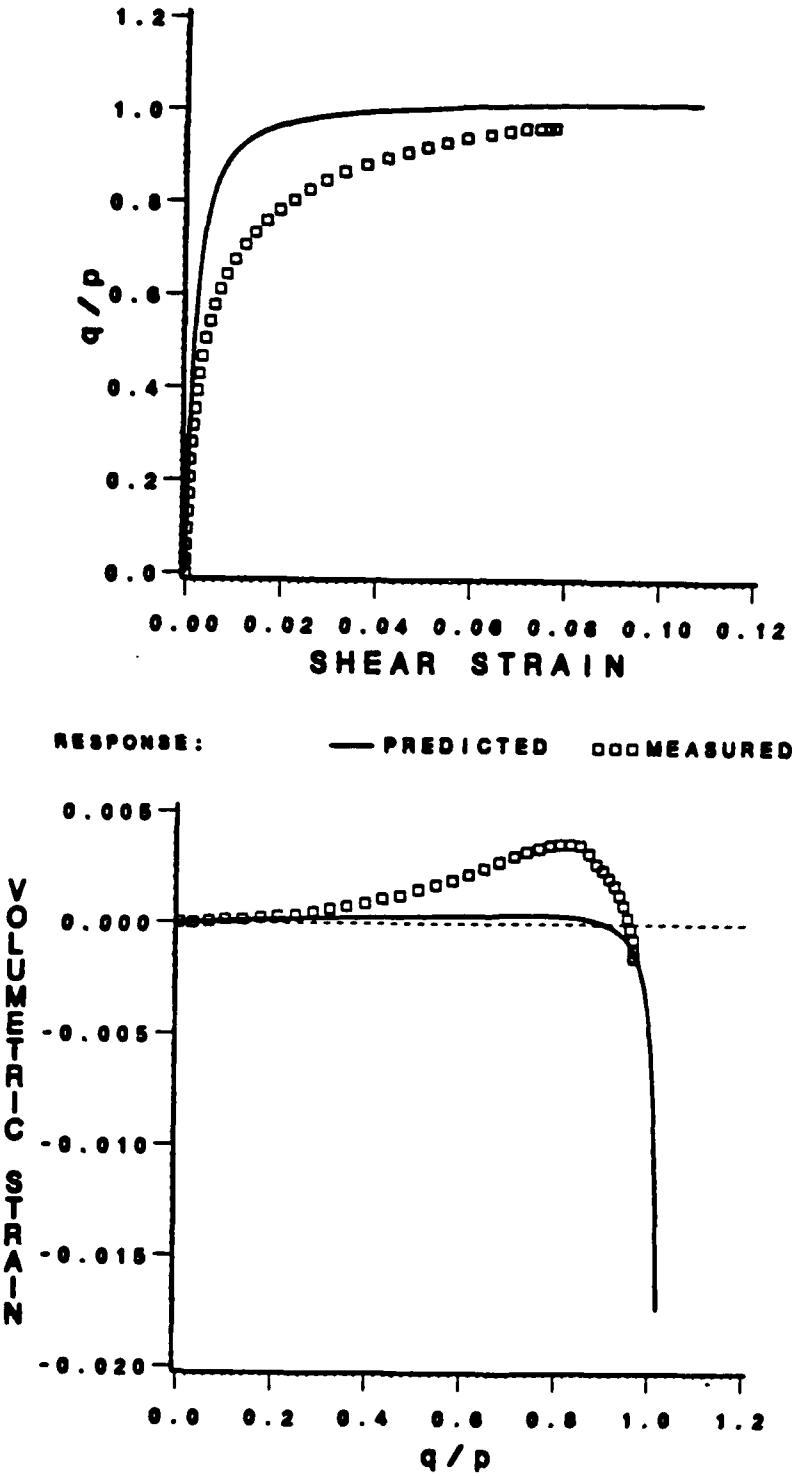

Figure D.9 Measured vs. predicted stress-strain response for GTR 75 stress path using proposed model

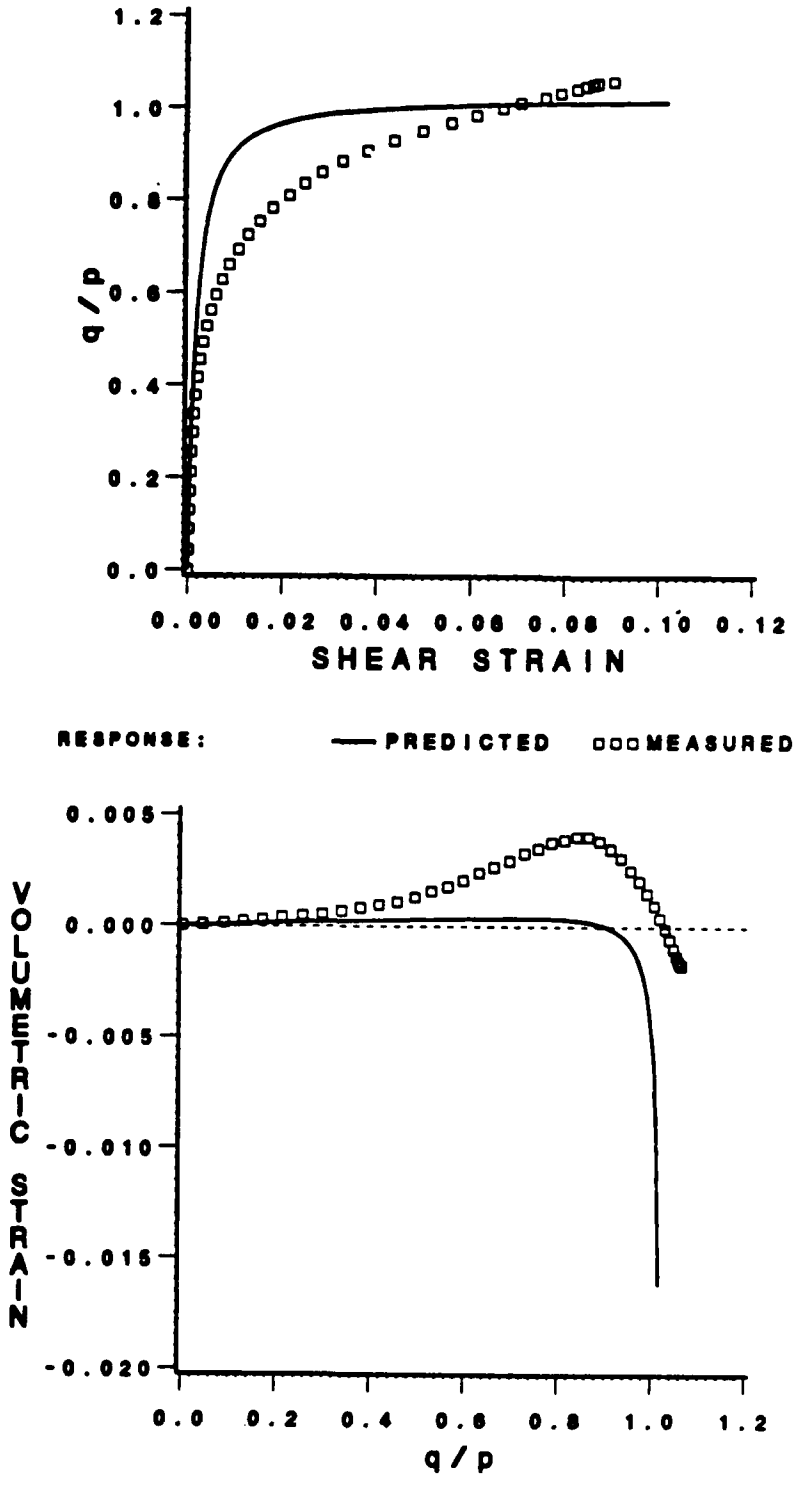

Figure D.10 Measured vs. predicted stress-strain response for GT 90 stress path using proposed model

APPENDIX E

PREDICTION OF HETTLER'S DATA USING PROPOSED MODEL

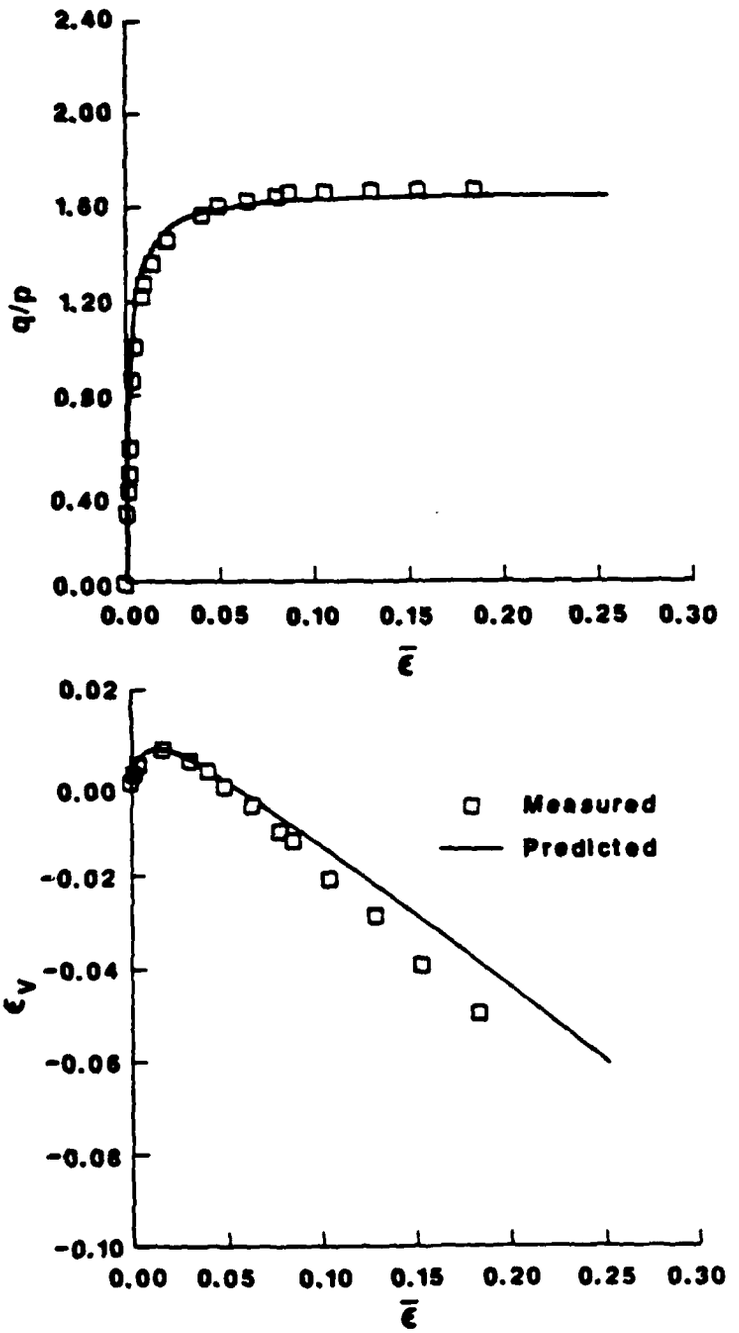

Figure E.1 Measured and predicted response for axial compression test (σ_3 = 400 kN/m^2) on Karlsruhe sand at 92.3% relative density (measured data after Hettler et al., 1984)

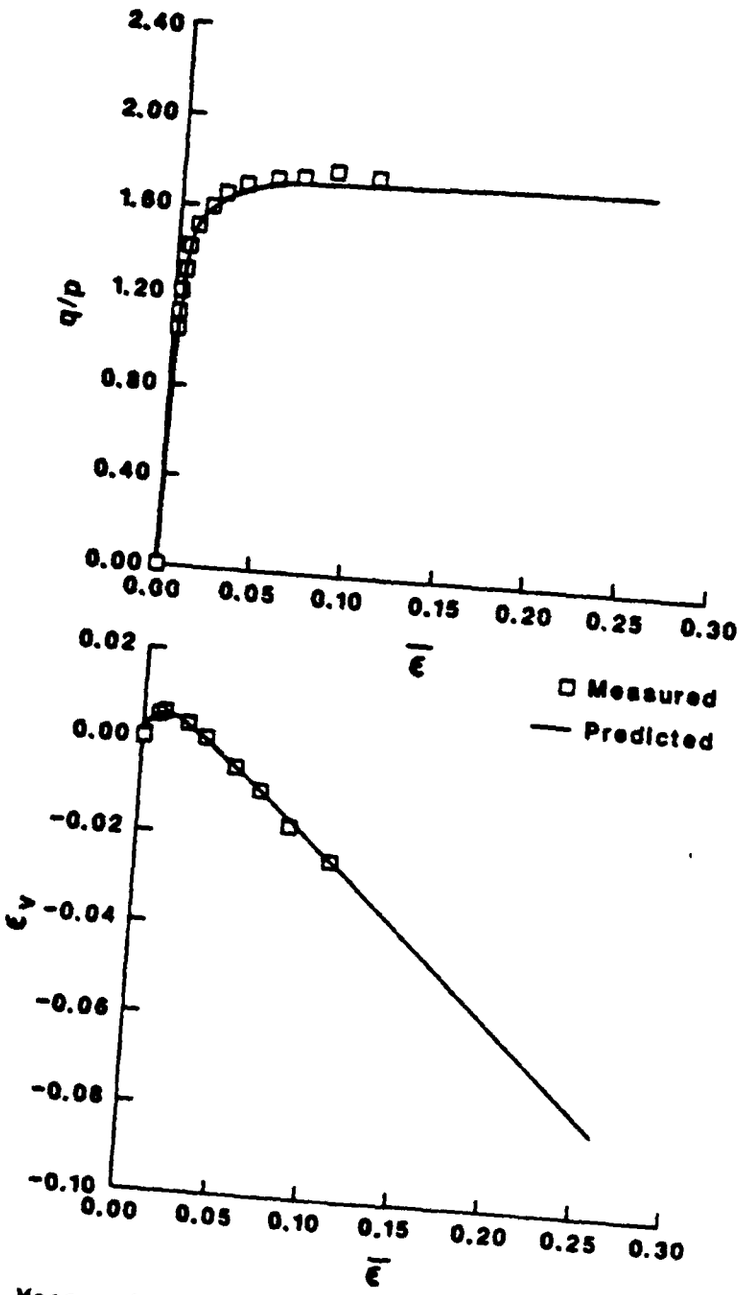

Figure E.2 Measured and predicted response for axial compression test (σ_3 = 80 kN/m^2) on Karlsruhe sand at 99.0% relative density (measured data after Hettler et al., 1984)

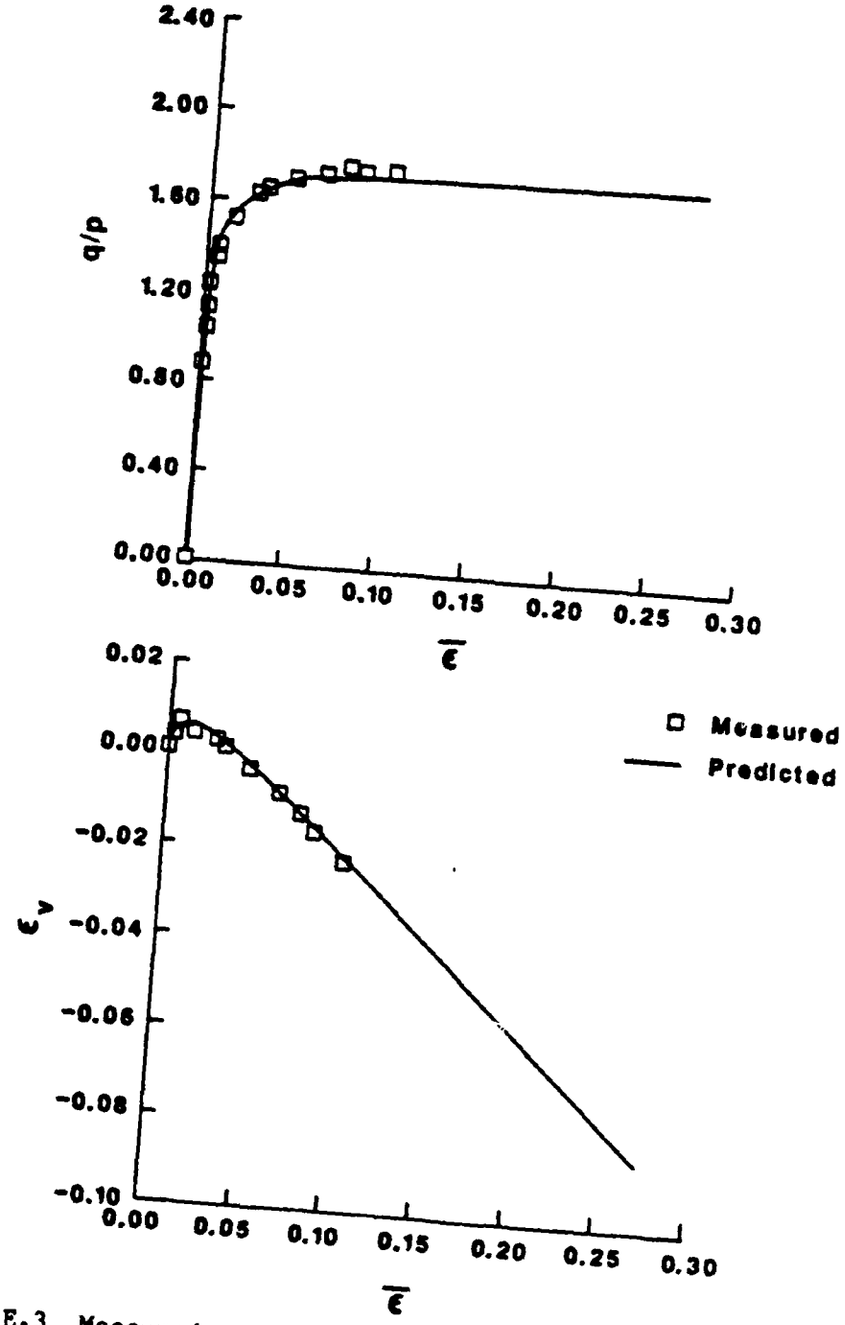

Figure E.3 Measured and predicted response for axial compression test (σ_3 = 200 kN/m^2) on Karlsruhe sand at 99.0% relative density (measured data after Hettler et al., 1984)

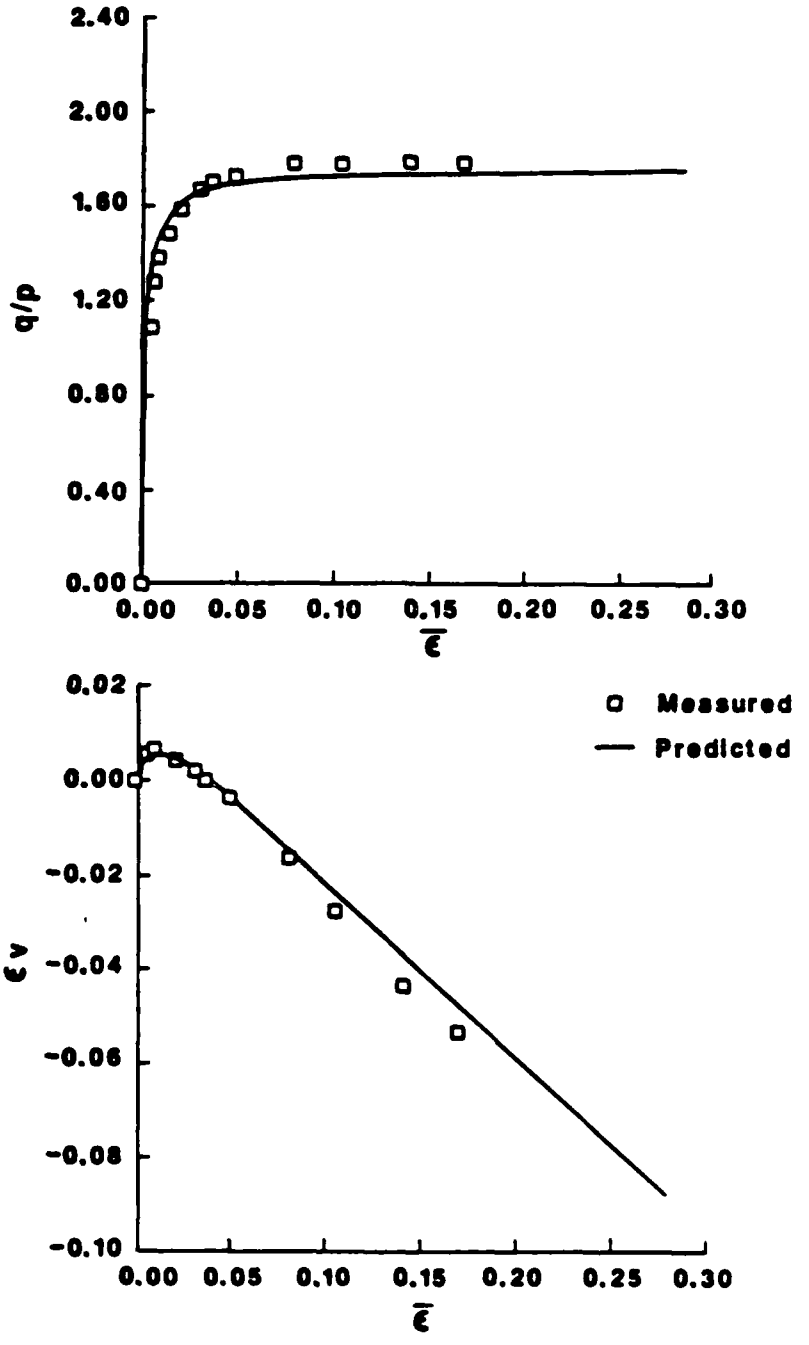

Figure E.4 Measured and predicted response for axial compression test (σ_3 = 300 kN/m^2) on Karlsruhe sand at 99.0% relative density (measured data after Hettler et al., 1984)

APPENDIX F

COMPUTATION OF THE BOUNDING SURFACE SCALAR MAPPING PARAMETER β

When the stress state resides on the consolidation surface (i.e., when $\frac{\sqrt{J_2^*}}{I_1} \leq N$),

$$\beta = \frac{-B_2 \pm \sqrt{(B_2^2 - 4 A_2 C_2)}}{2A_2} \quad , \quad 1 \leq \beta \leq \infty$$

where

$$A_2 = I_1^2 + \frac{\{(Q-1)/N\}^2}{[g(\theta)]^2} J_2 \quad ,$$

$$B_2 = -2 (I_0/Q) I_1 \quad ,$$

and

$$C_2 = I_0^2 \{(2/Q)-1\} \quad .$$

For the dilation surface, when $\frac{\sqrt{J_2^*}}{I_1} > N$, we have

$$\beta = \frac{D_2}{E_2} \quad ,$$

where

$$D_2 = -(I_0/Q)\left[\frac{1}{N} - bN\right] \left\{\frac{1}{[g(\theta)]} \sqrt{J_2} - S I_1\right\} \quad ,$$

and

$$E_2 = I_1^2 + \frac{b}{[g(\theta)]^2} J_2 + \left[\frac{S}{N^2} - \frac{2}{N} - S b\right] I_1 \sqrt{J_2} \frac{1}{[g(\theta)]} \quad .$$

END

12-86

DTIC